PROGRESS TOWARDS A PRECISION MEASUREMENT OF THE 2^3P_0-TO-2^3P_1 TRANSITION IN ATOMIC HELIUM

TAYLOR DAVID GRANT SKINNER

A DISSERTATION SUBMITTED TO THE FACULTY OF GRADUATE STUDIES
IN PARTIAL FULFILMENT OF THE REQUIREMENTS
FOR THE DEGREE OF
DOCTOR OF PHILOSOPHY

GRADUATE PROGRAM IN PHYSICS AND ASTRONOMY
YORK UNIVERSITY
TORONTO, ONTARIO

DECEMBER 2023

Abstract

Significant progress towards a high-precision measurement of the 29.6 GHz 2^3P_1-to-2^3P_0 fine-structure interval in helium at an intended precision of 20 Hz is presented. The measurement is performed using a thermal beam of metastable helium atoms, and the transition is measured using the frequency-offset separated oscillatory fields (FOSOF) method, where the transition is driven by a pair of temporally separated microwave pulses. The two pulses are at slightly different frequencies, which can be viewed as a continuously advancing phase difference between the pulses. The advancing phase difference leads to a sinusoidally varying atomic signal due to quantum interference between atoms excited during the two pulses. The phase difference between the sinusoidal atomic signal and a reference signal generated by combining the two microwave frequencies is zero at resonance and approximately proportional to the difference between the applied microwave frequency and the centre frequency of the transition.

A large number of experiment parameters which could lead to systematic effects have been investigated and shown to be sufficiently well-managed at the intended precision level of the intended measurement. One effect which causes the measured linecentre to depend on the range of microwave frequencies at which data is taken has been thoroughly investigated in both experiments and in a numerical simulation developed to investigate systematic effects. This effect is still not sufficiently wellunderstood or controlled to allow completion of a measurement at the 20 Hz level of precision.

A completed measurement, at a precision of 20 Hz, would be able to be combined with our previous 25 Hz measurement of the 2.3 GHz $2^3\mathrm{P}_2$-to-$2^3\mathrm{P}_1$ interval to obtain a part-per-billion (ppb) determination of the combined 31.9 GHz $2^3\mathrm{P}_2$-to-$2^3\mathrm{P}_0$ interval. When compared to a sufficiently-precise theoretical calculation, the combined interval would allow a 0.5 ppb determination of the fine-structure constant, the most precise determination of the fine-structure constant in a two-electron system and within an order of magnitude of the most precise determinations of the fine-structure constant. This 0.5 ppb determination could be compared with other fine-structure constant determinations to test beyond-the-Standard-Model physics.

Acknowledgements

Firstly I would like to thank my supervisor Eric Hessels for sharing with me his years of experience with precision measurement and invaluable guidance in learning to become an experimental physicist.

I would also like to thank Kosuke Kato for developing the current generation of the experimental apparatus, which took many years of hard work through trial and error to find a configuration which works so well, and training me on how to use it. Alongside Kosuke I thank Nikita Bezginov and Travis Valdez for many hours of enjoyment both in and out of the lab. Thanks to Farshad Heydarizadmotlagh for completing a measurement and letting me leave knowing that the experiment is in safe hands.

For enduring my countless complaints over the years and helping me distract myself from them I thank Michelle, Dylan, Jack, Jim, Jamie, and Alex.

Finally, and most importantly, I would like to thank my family, and in particular my parents Mark and Jo-Anne. You made me who I am, and none of this would have been possible without you.

Table of Contents

List of Tables

List of Figures

1 Introduction

1.1 The Fine-Structure Constant

The fine-structure constant α is a fundamental physical constant which describes the strength of electromagnetic interactions. It was first introduced by Sommerfeld in his extension of the Bohr model of the hydrogen atom to explain the fine structure which had been observed in precise spectroscopy of atomic hydrogen, splitting the lines into doublets [1]. It was later interpreted as a coupling constant for the strength of interactions between charged particles and photons in work which led to the development of the theory of quantum electrodynamics (QED) to describe these interactions. The value of α cannot be calculated within QED, instead it is a free parameter in the theory which must be measured experimentally. In SI units its value is given by [2]

$$\alpha = \frac{1}{4\pi\epsilon_0}\frac{e^2}{\hbar c} = \frac{1}{137.035\,999\,084(21)}, \tag{1.1}$$

where ϵ_0 is the permittivity of free space, e is the elementary charge, $\hbar$ is the reduced Planck constant, and c is the speed of light. Under the 2019 redefinition of SI units [3], all of these are constants with fixed values except the permittivity of free space ϵ_0 and so a measurement of α is equivalent to a measurement of ϵ_0 (or of the permeability of free space μ_0, as they are related by $\mu_0\epsilon_0 = 1/c^2$).

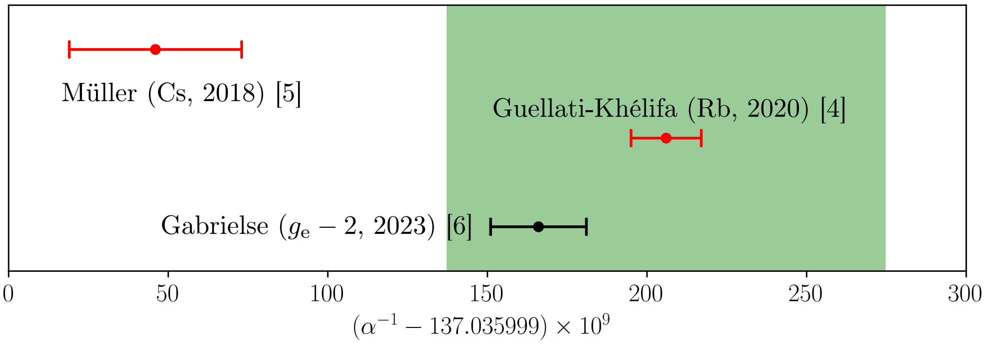

Figure 1.1: The most precise determinations of the fine-structure constant. The points in red are from atom recoil measurements, the black point is from the electron magnetic moment measurement. The green shaded area (which is centred at an arbitrary point) covers 0.5 ppb, corresponding to the uncertainty in determining α from a 1 ppb measurement of the 2^3P_0-to-2^3P_2 helium interval.

QED has become the most precisely tested theory in physics. These tests use measurements hinging on the value of α, because QED predictions of measurable properties are given in terms of power series of α. As a result, a single high-precision measurement cannot both determine α and be used to test QED without using other independent determinations of α with similar precision. Tests of QED in different systems probe different aspects of QED and different possible extensions of QED, making high-precision measurements in a variety of systems extremely valuable.

The results of the highest-precision α determinations are shown in Fig. 1.1. A measurement of the recoil of ^{87}Rb atoms in a matter-wave interferometer [4] determines α to 81 parts per trillion (ppt). The previous best atomic recoil measurement had a 200 ppt uncertainty using ^{133}Cs [5]. These measurements show a 5.5σ (1.2 ppb) disagreement which is currently unresolved.

Another precise determination of α comes from a measurement of the electron's anomalous magnetic moment ($g_e - 2$) in a one-electron quantum cyclotron [6]. This measurement can then be used to determine the value of α by comparing to QED calculations [7]. This determination gives an uncertainty of 110 ppt, which lies between the two recoil results: 3.9σ above the ^{133}Cs determination and 2.1σ below the ^{87}Rb determination.

Previous determinations of α in other systems include the quantum Hall effect [8] and laser spectroscopy of the same helium fine-structure states presented in this thesis [9], though both are more than an order of magnitude lower in precision than the leading determinations.

1.2 Structure of Helium

Helium has two stable isotopes: ^{3}He and ^{4}He. The natural abundance of ^{3}He is approximately one million times lower than that of ^{4}He, so its concentration is negligible except in expensive isotopically-enriched samples. Thus we use ^{4}He in this work, and hereafter "helium" will refer to ^{4}He. ^{4}He is an atom with a nucleus consisting of two protons and two neutrons, with a total nuclear spin of zero, and two orbiting electrons. The non-relativistic Hamiltonian describing this system is

$$\hat{H} = -\frac{\hbar^2}{2\mu}\nabla_1^2 - \frac{\hbar^2}{2\mu}\nabla_2^2 + \frac{e^2}{4\pi\epsilon_0}\left(-\frac{Z}{r_1} - \frac{Z}{r_2} + \frac{1}{r_{12}}\right) - \frac{\hbar^2}{M}\nabla_1 \cdot \nabla_2, \tag{1.2}$$

where M is the nuclear mass, μ is the electron-nucleus reduced mass $\mu = \frac{m_e M}{m_e + M}$, $\mathbf{r_i}$ is the vector from the nucleus to the i-th electron, $\mathbf{r_{12}}$ is the vector between the electrons, ∇_i is the gradient operator with respect to $\mathbf{r_i}$, and Z is the nuclear charge number ($Z = 2$ for helium). The electron-electron repulsion term involving $r_{12} = |\mathbf{r}_1 - \mathbf{r}_2|$ causes the Schrödinger equation associated with this Hamiltonian to be inseparable, and so it cannot be solved analytically. A very rough approximation can be made by discarding the final term (a small correction, because $M \gg m_e$) and the electron-electron repulsion

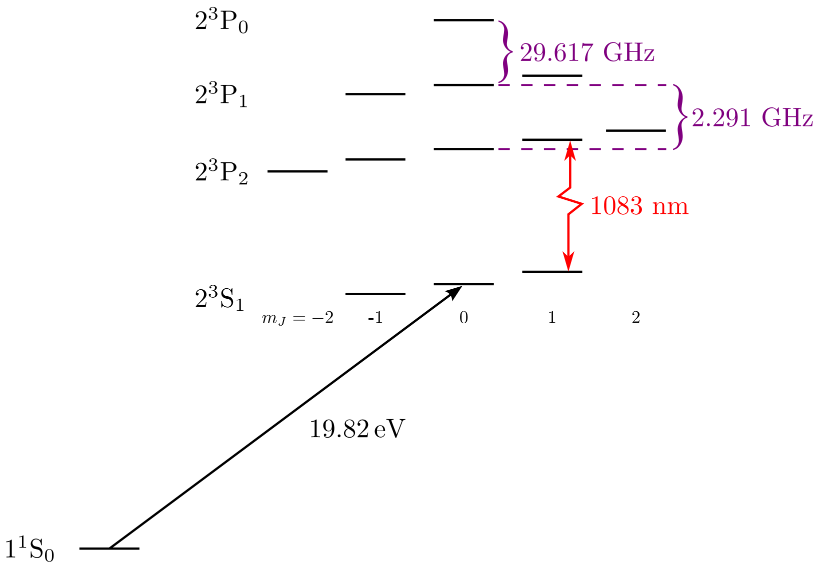

Figure 1.2: Diagram of the relevant energy levels of helium for this experiment (not to scale).

term, so that each electron independently populates hydrogenic states described by four quantum numbers: the principal quantum number $n = 1, 2, \ldots,$ the azimuthal quantum number (corresponding to the orbital angular momentum of the state) $\ell = 0, 1, \ldots, n-1$, the magnetic quantum number $m_\ell = -\ell, -\ell+1, \ldots, \ell-1, \ell$, and the projection of the electron spin on the z-axis $m_s = \pm\frac{1}{2}$. The real wavefunctions of the electrons in the atom can be represented as modifications of these hydrogenic wavefunctions, and so any state of the helium atom can be written in the properly symmetrized $|(n_1, \ell_1, m_{\ell 1}, m_{s1})\,(n_2, \ell_2, m_{\ell 2}, m_{s2})\rangle$ states where 1 and 2 refer to each of the two electrons. We are unconcerned with doubly-excited states because they are very short-lived, and are not populated by our lasers, so we consider only states where one electron is in the ground state: $|(1, 0, 0, m_{s1})(n, l, m_l, m_{s2})\rangle$.

1.2.1 LS Coupling

The state of the helium atom can be described in the LS coupling scheme (where the sum of the orbital angular momenta, $\mathbf{L} = \sum_i \boldsymbol{\ell}_i$, and the sum of the spin angular momenta, $\mathbf{S} = \sum_i \mathbf{s}_i$ are added to form a total angular momentum vector $\mathbf{J} = \mathbf{L} + \mathbf{S}$) by five quantum numbers n, S, L, J, and m_J. These quantum numbers can be combined to create a term symbol of the form $n^{2S+1}L_J$, where $L = 0, 1, 2, 3$ are represented by S, P, D, and F, and $2S + 1$ has values of 1 (singlet state) or 3 (triplet state). In terms of this notation the lowest-lying states are $1^1\mathrm{S}_0$ (the ground state), $2^3\mathrm{S}_1$ (a long-lived metastable state since it is the lowest-lying $S = 1$ state, and transitions to $S = 0$ states are strongly forbidden), $2^3\mathrm{P}_2$, $2^3\mathrm{P}_1$, and $2^3\mathrm{P}_0$. The metastable $2^3\mathrm{S}_1$ state forms a pseudo-ground state and is also commonly denoted as He*. If the degeneracy of the magnetic sublevels is lifted by a dc magnetic field (as described in Sec. 4.4.1), m_J is included to fully define the state as $n^{2S+1}L_J(m_J)$ where m_J ranges from $-J$ to J in integer steps. The energy level diagram for these states is shown in Fig. 1.2.

1.3 Previous Measurements

In 1964 Schwartz presented a calculation [16] of the fine structure of helium accurate to 1 part per million (ppm), anticipating experimental measurements at the same level of precision in order to provide a new determination of α more accurate than any previously available. This was followed [17] in 1971 with a 36 kHz (1 ppm) measurement of the 29.6 GHz $2^3\mathrm{P}_1$-to-$2^3\mathrm{P}_0$ interval. More recent measurements [9–14] are summarized in Fig. 1.3. These measurements use a range of methods to measure this interval. They all use thermal beams of metastable helium, except for Ref. [13], which uses a variable pressure of helium in a discharge cell.

As discussed in Sec. 1.1, it is essential to use several different systems to measure α, not only to test for consistency, but because a single measurement which involves a QED calculation cannot both determine α and test QED at the same time. Furthermore, measurements in multiple systems also allow for tests of beyond-the-standard-model

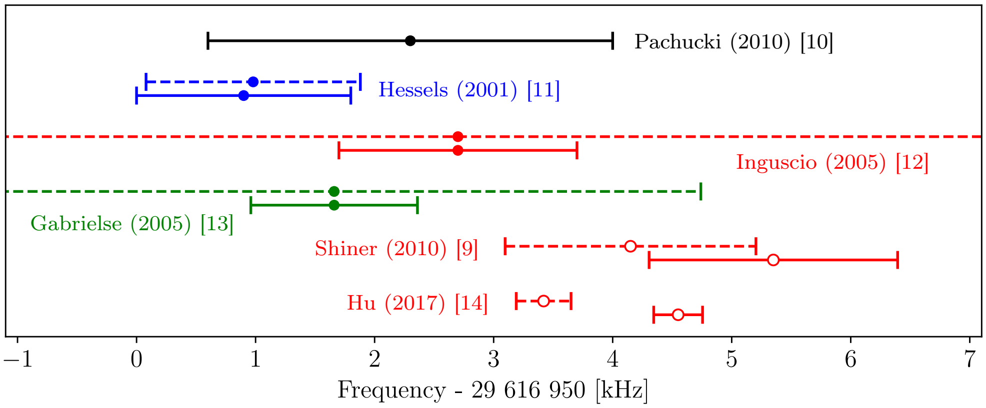

Figure 1.3: Summary of previous measurements to determine the $2^3\mathrm{P}_1$-to-$2^3\mathrm{P}_0$ transition frequency, and the best theoretical prediction. Black is the theoretical calculation, the colours of the other points denote the spectroscopy type: red is laser spectroscopy with an atomic beam, green is saturated absorption spectroscopy in a low-pressure cell, and blue is direct microwave spectroscopy. Empty circles denote indirect measurements, where ν_{10} is determined by taking the difference between measured values of ν_{20} and ν_{21}. Points with dashed error bars are corrected for quantum interference effects described in [15]. The Hu measurement accounted for this effect in the published result, the uncorrected value is included here only to show the size of the effect in that measurement.

physics in these systems. For example, this helium measurement when completed will test for spin-dependent interactions between the two electrons in the atom [18]. These interactions arise in theories which predict new bosons such as axions, a dark matter candidate particle [19].

For helium, the energy difference between the $2^3\mathrm{P}_0$ and $2^3\mathrm{P}_2$ states can be calculated more accurately than either of the sub-intervals ($2^3\mathrm{P}_2$ to $2^3\mathrm{P}_1$ and $2^3\mathrm{P}_1$ to $2^3\mathrm{P}_0$) due to the lack of triplet-singlet mixing which affects the $2^3\mathrm{P}_1$ state [10]. Exciting the $2^3\mathrm{P}_2$-to-$2^3\mathrm{P}_0$ transition directly with microwaves would require extremely high microwave power as it is magnetic-dipole forbidden without the application of a magnetic field, which mixes J states. Instead, we measure both sub-intervals and sum them in order to get the highest possible precision when comparing theory and experiment. The $2^3\mathrm{P}_2$-to-$2^3\mathrm{P}_1$ interval has already been measured by our group [20], and progress towards a measurement of the $2^3\mathrm{P}_1$-to-$2^3\mathrm{P}_0$ interval which uses the same apparatus modified to enable the use of 29.6 GHz microwaves is the subject of this dissertation.

2 Experimental Technique

2.1 Introduction to FOSOF

Figure 2.1: Timing diagram for microwave pulses in the Separated Oscillatory Fields (SOF) and Frequency-Offset Separated Oscillatory Fields (FOSOF) techniques. The pulses are of duration D and their starting edges are separated by a time T.

The measurement technique used in this experiment is known as frequency-offset separated-oscillatory fields (FOSOF) [21], which is a refinement of the Ramsey separated-oscillatory fields (SOF) technique [22]. In the Ramsey SOF technique, the linewidth of a transition between two atomic states is narrowed by exposing atoms to two pulses of microwaves (each of duration D separated by time T, as shown in Fig. 2.1) and measuring the population which has undergone a transition as a function of frequency ($f = \frac{\omega}{2\pi}$) when these pulses are in phase ($\phi_1 = \phi_2$ in Fig. 2.1) and π out of phase ($\phi_1 = \phi_2 \pm \pi$). The lineshapes from these two configurations (shown in Fig. 2.2(a)) are then subtracted from each other (Fig. 2.2(b)), resulting in a lineshape

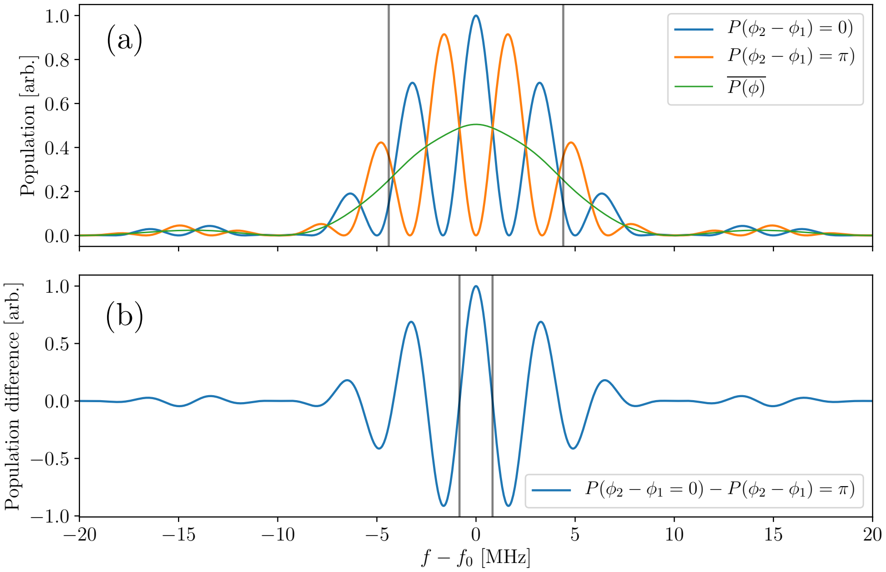

Figure 2.2: (a) SOF lineshapes (Eqn. (2.8)) for $T = 300\,\text{ns}, D = 100\,\text{ns}$ (see Fig. 2.1). Lineshapes are for in-phase pulses ($\phi_2 - \phi_1 = 0$, blue), out-of-phase pulses ($\phi_2 - \phi_1 = \pi$, orange), and the average of all phases (green). The full width at half maximum of the phase-averaged lineshape, indicated by the vertical lines, is $\Delta f \approx \frac{0.886}{D}$. (b) The difference between the $\phi_2 - \phi_1 = 0$ and $\phi_2 - \phi_1 = \pi$ SOF lineshapes (Eqn. (2.10)), showing a full width of $\Delta f = \frac{1}{2T}$.

where the central peak has a width of $1/(2T)$ (where T — see Fig. 2.1 — is the time separation of the pulses), independent of, and potentially narrower than, the natural linewidth of the transition. The SOF lineshape is due to quantum interference between atoms which are excited during the first pulse and those which are excited during the second pulse, making this technique a form of interferometry. If the lifetimes of the two states are different, the interference will only be partial, as some of the atoms excited in the first pulse will undergo radiative decay before they encounter the second pulse. In this experiment, the lifetimes of the two atomic states are the same (98 ns; both decaying down to the 2^3S_1 state) and so the effect of radiative decay is only to decrease the total amplitude of the signal, but the degree of interference is not affected.

The main drawbacks of the Ramsey SOF method are that this interference signal is often a small perturbation on the lineshape (due to the aforementioned lifetime effect), so a careful subtraction is needed, and that it is susceptible to all sources of transition amplitude noise across the whole frequency spectrum (e.g. laser frequency instability, laser amplitude noise, helium source intensity instability, etc.).

In FOSOF, instead of having fixed relative phases between the pulses, all relative phases are sampled by slightly offsetting the microwave frequencies of the two pulses by $f_{\mathrm{ofs}} = f_2 - f_1$. If the inverse of the frequency offset $1/f_{\mathrm{ofs}}$ is large compared to the pulse duration (D), then within each individual pulse the phase can be approximated as constant. If the experiment pulse cycle of Fig. 2.1 is continually repeated, the fraction of the population which undergoes a transition will vary sinusoidally in time at the offset frequency, as the atomic signal cycles through constructive and destructive interference. The resulting lineshapes are derived in the next section.

2.1.1 Time-Dependent Perturbation Theory SOF and FOSOF Lineshapes

The two-level SOF and FOSOF lineshapes can be solved analytically (see Sec. 3.1 of [23]), but an approximation using time-dependent perturbation theory (TDPT) illustrates most of the pertinent physics. The time-dependent wavefunction is written as the linear combination $|\psi(t)\rangle = c_{\mathrm{l}}(t)\,|l\rangle + c_{\mathrm{u}}(t)\,|u\rangle$, where $|l\rangle$ and $|u\rangle$ are the lower and upper states. It is assumed that at time $t = 0$ the atom is in the lower state and we calculate the amplitude $c_u(t)$ for driving the population up to the upper state. If H'_{lu} is the element of the perturbing Hamiltonian coupling the two states, the first-order perturbation theory solution is given by [24]

$$c_{\mathrm{u}}(t) = -\frac{i}{\hbar}\int_0^t H'_{\mathrm{lu}}(\tau)e^{i\omega_0\tau}\,\mathrm{d}\tau, \tag{2.1}$$

where $\omega_0 = \Delta E/\hbar$ and ΔE is the energy difference between the $|l\rangle$ and $|u\rangle$ states. For the two microwave pulses of Fig. 2.1,

$$H'_{\mathrm{lu}}(t) = \begin{cases} V\cos(\omega t + \phi_1) & 0 \leq t \leq D \\ 0 & D < t < T \\ V\cos(\omega t + \phi_2) & T \leq t \leq T + D \\ 0 & t > T + D. \end{cases} \tag{2.2}$$

Inserting this into Eqn. (2.1) and evaluating at $t = T + D$ to find the amplitude for being in the upper state after the two pulses gives

$$\begin{aligned} c_{\mathrm{u}}(T+D) &= -\frac{i}{\hbar}\bigg[\int_0^D V\cos(\omega\tau + \phi_1)e^{i\omega_0\tau}\mathrm{d}\tau + \\ &\qquad \int_T^{T+D} V\cos(\omega\tau + \phi_2)e^{i\omega_0\tau}\mathrm{d}\tau\bigg] \qquad (2.3) \\ &= -\frac{iV}{2\hbar}\bigg[\int_0^D e^{i((\omega+\omega_0)\tau+\phi_1)} + e^{-i((\omega-\omega_0)\tau+\phi_1)}\mathrm{d}\tau \\ &\qquad + \int_T^{T+D} e^{i((\omega+\omega_0)\tau+\phi_2)} + e^{-i((\omega-\omega_0)\tau+\phi_2)}\mathrm{d}\tau\bigg], \qquad (2.4) \end{aligned}$$

with Eqn. (2.4) using the identity $\cos(x) = (e^{ix} + e^{-ix})/2$. The first term in each integral oscillates very rapidly at $\omega + \omega_0 \gg \omega - \omega_0$ (where $\Delta\omega = \omega - \omega_0$ is known as the detuning), so it will average to zero during the integration and can be discarded (the rotating wave approximation). This leaves

$$c_{\mathrm{u}}(T+D) = -\frac{iV}{2\hbar}\left[ie^{-i\phi_1}\frac{e^{-i\Delta\omega D}-1}{\Delta\omega} + ie^{-i\phi_2}\frac{e^{-i\Delta\omega(T+D)}-e^{-i\Delta\omega T}}{\Delta\omega}\right], \tag{2.5}$$

$$c_{\mathrm{u}}(T+D) = \frac{Ve^{-i\phi_1}}{2\hbar\Delta\omega}\left[e^{-i\Delta\omega D}-1+e^{-i(\phi_2-\phi_1)}(e^{-i\Delta\omega(T+D)}-e^{-i\Delta\omega T})\right]. \tag{2.6}$$

The population, after simplifying, is given by

$$P(T,D,V,\Delta\omega,\phi) = |c_{\mathrm{u}}(T+D)|^2 = \frac{4V^2}{\hbar^2}\cos^2\left(\frac{T\Delta\omega+\phi_2-\phi_1}{2}\right)\frac{\sin^2(D\Delta\omega/2)}{\Delta\omega^2} \tag{2.7}$$

$$= \left(\frac{DV}{\hbar}\right)^2\cos^2\left(\frac{T\Delta\omega+\phi_{21}}{2}\right)\mathrm{sinc}^2\left(\frac{D\Delta\omega}{2}\right), \tag{2.8}$$

where $\phi_{21} = \phi_2 - \phi_1$ is the phase difference between the pulses. The sinc^2 part is the standard lineshape of atoms exposed to a pulse of radiation, with zeros at $\Delta\omega = \pm 2n\pi/D$, where n is any nonzero integer. The cosine squared term effectively modulates the amplitude of this lineshape by a factor ranging from 0 to 1 as one of the terms in its argument is varied.

It is illustrative to consider some particular cases here. If $\phi_{21} = 0$, the two pulses are in phase and their contributions add constructively on resonance ($\Delta\omega = 0$). If $\phi_{21} = \pi$, the interference is destructive on resonance. At any other phase the interference will be somewhere between constructive and destructive, according to the cosine term of Eqn. (2.8). The same behaviour will be observed at every detuning, reaching a maximum when the cosine argument $T\Delta\omega + \phi_{21} = 2n\pi$ and a minimum at $T\Delta\omega + \phi_{21} = (2n+1)\pi$.

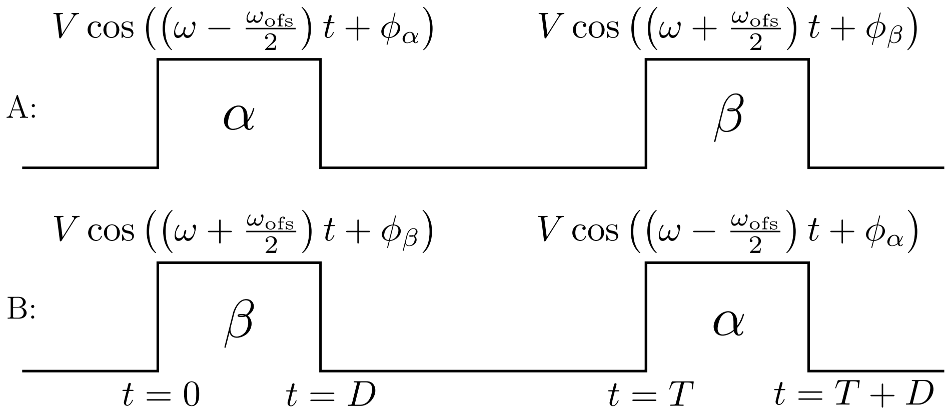

Figure 2.3: The pulse orders for the two configurations of FOSOF experiment, A and B. In configuration A, the pulse at frequency $\omega - \omega_{\text{ofs}}/2$ from source α is first, and in configuration B, the pulse at frequency $\omega + \omega_{\text{ofs}}/2$ from source β is first.

Subtracting the $\phi_{21} = \pi$ case from the $\phi_{21} = 0$ case gives

$$P(0) - P(\pi) = \frac{1}{2}\left(\frac{DV}{\hbar}\right)^2 \operatorname{sinc}^2(D\Delta\omega/2)\left[(\cos(T\Delta\omega) + 1) - (\cos(T\Delta\omega + \pi) + 1)\right] \tag{2.9}$$

$$= \left(\frac{DV}{\hbar}\right)^2 \operatorname{sinc}^2(D\Delta\omega/2)\cos(T\Delta\omega), \tag{2.10}$$

which can be considered the time-dependent-perturbation-theory approximation to the SOF lineshape.

For FOSOF, the two pulses of Fig. 2.1 have slightly different frequencies $f \pm f_{\text{ofs}}/2$, where f_{ofs} is the offset frequency (as shown in configuration A of Fig. 2.3). The FOSOF signal can be analyzed by replacing $\phi_{21} \to \omega_{\text{ofs}}t + \phi_{21}^0 = 2\pi f_{\text{ofs}}t + \phi_{21}^0$ (where ϕ_{21}^0 is the phase difference between the microwave fields at $t = 0$) in Eqn. (2.8) to give

$$P(t) = \frac{1}{2}\left(\frac{DV}{\hbar}\right)^2 (\cos(\omega_{\text{ofs}}t + T\Delta\omega + \phi_{21}^0) + 1)\operatorname{sinc}^2(D\Delta\omega/2), \tag{2.11}$$

that is, the population varies sinusoidally at the offset frequency as the two-pulse experiment cycle of Fig. 2.3(A) is continually repeated. This variation of signal size ranges between zero and some maximum value at each detuning, and the phase of this cosine is given by $T\Delta\omega + \phi_{21}^0$, i.e. ϕ_{21}^0 on resonance with an additional term proportional to the detuning away from resonance, as shown in Fig. 2.4. In the ideal case, it can be assumed that $\phi_{21}^0 = 0$. In any real experiment there will be many extra phase terms; the cancellation of these extra phase terms is discussed in Sec. 2.1.2. In order to determine the phase unambiguously in an experiment, a stable reference cosine is generated at the offset frequency by beating the two microwave frequencies together and this reference cosine is recorded simultaneously alongside the atomic response. This is necessary because the value of any given phase is determined by the arbitrary choice of defining the time where $t = 0$, but the phase difference between two signals at the same frequency is independent of the time chosen to correspond to $t = 0$. This reference (in the artificial ideal case with no extra phases) gives a signal of the form

$$R(t) = R_0 \cos(\omega_{\text{ofs}} t). \tag{2.12}$$

In order to determine the centre frequency of the transition being measured, the FOSOF phase $\Delta\theta$ (relative to the reference phase, i.e. the phase difference between $P(t)$ and $R(t)$) is measured at a range of applied microwave frequencies, and (in the TDPT approximation and with no extra phase terms in $P(t)$ or $R(t)$) this phase is simply proportional to the pulse repetition period T and the detuning $\Delta\omega$, so that the idealized TDPT FOSOF lineshape is given by

$$\Delta\theta = T\Delta\omega. \tag{2.13}$$

The centre of the transition can then be found by simply fitting a straight line to the phase vs. frequency data and determining the zero-phase ($\Delta\theta = 0$) point.

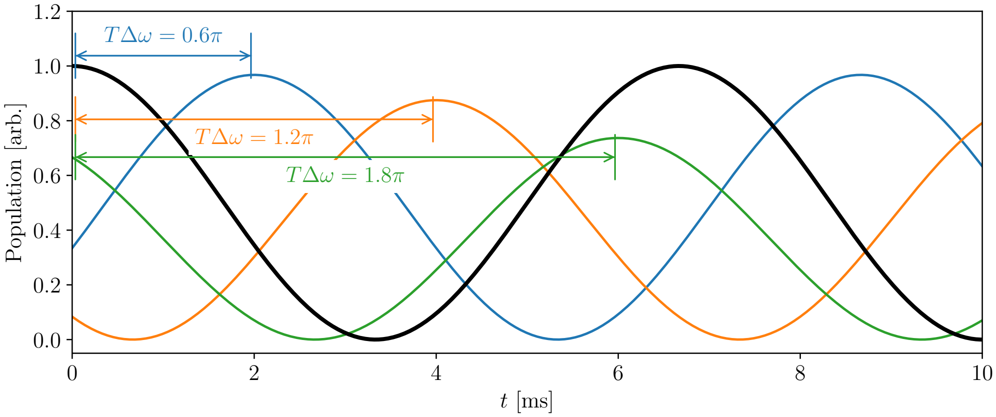

Figure 2.4: FOSOF cosines showing the atomic response signal at different detunings (blue = 1 MHz, orange = 2 MHz, and green = 3 MHz), relative to a perfect reference cosine (black), according to Eqn. (2.11) for $\omega_{\text{ofs}} = 2\pi \times 150\,\text{Hz}, T = 300\,\text{ns}$ and $D = 100\,\text{ns}$.

2.1.2 Additional Phases and Reversed Experiment Configuration

In a real experiment, there will be multiple extra phase imperfections which will complicate the FOSOF signal. Firstly, the sources that produce the two frequencies $f \pm f_{\text{ofs}}/2$ will each have some arbitrary overall phases, ϕ_α and ϕ_β, which will remain constant if the sources are perfectly synchronized. There will also be a time delay η due to any delays and phase shifts in the detection system, such as the time difference between when the atoms reach the end of the second pulse and when the signal from their detection reaches the recording device, or phase shifts due to the finite bandwidth of signal amplifiers. Altogether the signal given by Eqn. (2.11) becomes (after gathering the amplitude terms into one factor S_0)

$$S(t) = S_0(\cos(\omega_{\text{ofs}}(t - \eta) + T\Delta\omega + \phi_{\beta\alpha}) + 1), \tag{2.14}$$

where $\phi_{\beta\alpha} = \phi_\beta - \phi_\alpha$.

It is also not feasible to obtain a reference sine where the phase exactly matches the phase of the radiation that the atoms see, so the reference of Eqn. (2.12) will take the form

$$R(t) = R_0 \cos(\omega_{\mathrm{ofs}}(t - \gamma) + \phi_{\beta\alpha}). \tag{2.15}$$

The time delay γ is due primarily to imperfectly matched paths from the two sources to the point where they are combined to form the reference signal. The phase shift due to this path length will vary with detuning frequency (as a different number of wavelengths will fit along the length, an effect referred to as electrical length) and temperature as thermal expansion will change the physical lengths of the paths. The phase of the reference is thus

$$\phi_{\mathrm{R}} = -\omega_{\mathrm{ofs}}\gamma + \phi_{\beta\alpha}, \tag{2.16}$$

and the phase of the signal is

$$\phi_{\mathrm{S}} = -\omega_{\mathrm{ofs}}\eta + T\Delta\omega + \phi_{\beta\alpha}. \tag{2.17}$$

The phase difference (the atomic signal phase relative to the reference phase) is then

$$\Delta\theta = \phi_{\mathrm{S}} - \phi_{\mathrm{R}} = T\Delta\omega + \omega_{\mathrm{ofs}}(\gamma - \eta). \tag{2.18}$$

Confounding phases due to γ, η, and $\phi_{\alpha\beta}$ can be cancelled by repeating the experiment with the order of the microwave pulses reversed, as shown in Fig. 2.3(B), as long as this reversal is done in such a way that it does not affect the pulses in any other way or the reference signal. The initial configuration is then known as configuration

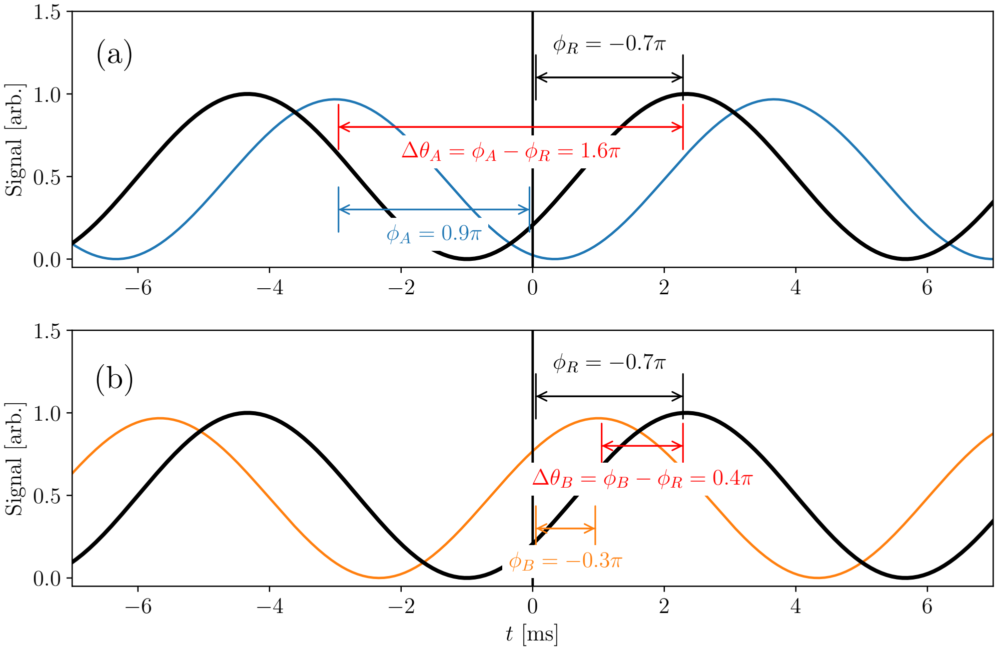

Figure 2.5: FOSOF signals $S(t)$ (blue, orange) and reference $R(t)$ (black) for (a): configuration A, (b): configuration B of Fig. 2.3, showing the phase shifts caused by imperfections which are described in the text. The phases are given by Eqns. (2.16), (2.22) and (2.23), with $\omega_{\text{ofs}} = 2\pi \times 150\,\text{Hz}, \gamma = 0.6/f_{\text{ofs}}, \eta = -0.1/f_{\text{ofs}}, \phi_{\beta\alpha} = 0.5\pi, \Delta\omega = 2\pi \times 1\,\text{MHz}$, and $T = 300\,\text{ns}$.

A, which has the same form as Eqn. (2.14):

$$S_{\text{A}}(t) = S_0(\cos(\omega_{\text{ofs}}(t-\eta) + T\Delta\omega + \phi_{\beta\alpha}) + 1). \tag{2.19}$$

After reversing the order of the pulses, the signal for configuration B is

$$S_{\text{B}}(t) = S_0(\cos(-\omega_{\text{ofs}}(t-\eta) + T\Delta\omega - \phi_{\beta\alpha}) + 1) \tag{2.20}$$

$$= S_0(\cos(\omega_{\text{ofs}}(t-\eta) - T\Delta\omega + \phi_{\beta\alpha}) + 1), \tag{2.21}$$

where the sign of ω_{ofs} flips because the first pulse is now at $\omega + \omega_{\text{ofs}}/2$ and the second at $\omega - \omega_{\text{ofs}}/2$. The phase difference between the pulses $\phi_{\beta\alpha}$ becomes $\phi_{\alpha\beta} = -\phi_{\beta\alpha}$ due to the reversed ordering. All of the signs are flipped again in the second line using the evenness of the cosine function, $\cos(-x) = \cos(x)$.

For the two configurations, the FOSOF signal phases are then

$$\theta_{\mathrm{A}} = -\omega_{\mathrm{ofs}}\eta + T\Delta\omega + \phi_{\beta\alpha}, \tag{2.22}$$

$$\theta_{\mathrm{B}} = -\omega_{\mathrm{ofs}}\eta - T\Delta\omega + \phi_{\beta\alpha}., \tag{2.23}$$

and the phases relative to the reference are

$$\Delta\theta_{\mathrm{A}} = T\Delta\omega + \omega_{\mathrm{ofs}}(\gamma - \eta), \tag{2.24}$$

$$\Delta\theta_{\mathrm{B}} = -T\Delta\omega + \omega_{\mathrm{ofs}}(\gamma - \eta). \tag{2.25}$$

Taking the averaged difference $\overline{\Delta\Theta} = (\Delta\theta_{\mathrm{A}} - \Delta\theta_{\mathrm{B}})/2$ gives

$$\overline{\Delta\Theta}(\mathrm{TDPT}) = T\Delta\omega = 2\pi(f - f_0), \tag{2.26}$$

which has all of the confounding phase terms removed. The two configurations of the experiment are measured immediately subsequent to each other (with the order of the two configurations randomly chosen each time), over a time period short enough for each of the cancelled phase terms to be stable, ensuring that the cancellation is not impaired by the phase terms drifting between the measurements.

The simple straight-line result of Eqn. (2.26) is the time-dependent perturbation theory approximation of the FOSOF lineshape. For larger driving field powers and pulse durations, this FOSOF lineshape is slightly distorted as the transition is driven closer to saturation, where the TDPT approximation is no longer good, and the full

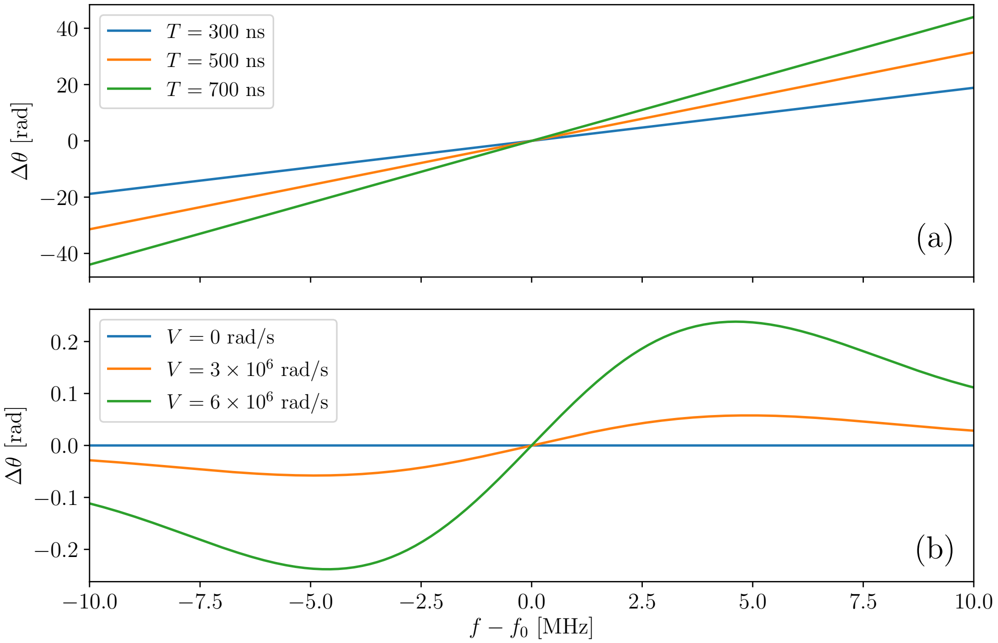

Figure 2.6: (a) Analytic FOSOF lineshape Eqn. (2.27) for a range of T with $D = 100\,\text{ns}$, $V = 10^6\,\text{rad/s}$. (b) The deviation of the lineshape from a straight line for $T = 300\,\text{ns}, D = 100\,\text{ns}$, given by subtracting the TDPT solution $\Delta\theta = 2\pi(f - f_0)T$ from Eqn. (2.27).

analytical solution for the FOSOF phase:

$$\Delta\theta(T, D, V, \Delta\omega) = \Delta\omega(T - D) + 2\tan^{-1}\left[\frac{\Delta\omega \tan\left(\sqrt{4V^2 + \Delta\omega^2}D/2\right)}{\sqrt{4V^2 + \Delta\omega^2}}\right] \tag{2.27}$$

must be used (a detailed derivation is given in Sec. 3.1 of [23]). It can be seen that Eqn. (2.27) simplifies to the TDPT lineshape in both far-below-saturation limits: $V \to 0$ and $D \to 0$.

The phase subtraction of the reversed pulse order in Eqn. (2.26) works exactly the same way for cancelling phase imperfections with this lineshape, only with the RHS of Eqn. (2.26) replaced by the RHS of Eqn. (2.27).

Because this technique depends on measuring the phase of a sinusoid at a frequency f_{ofs}, the measurement is only affected by noise in a very narrow frequency band around

f_{ofs}. If f_{ofs} is chosen to lie in a low-noise region of the detected signal's spectrum, a significant increase in signal-to-noise ratio is achieved.

3 Apparatus

3.1 Experiment Scheme

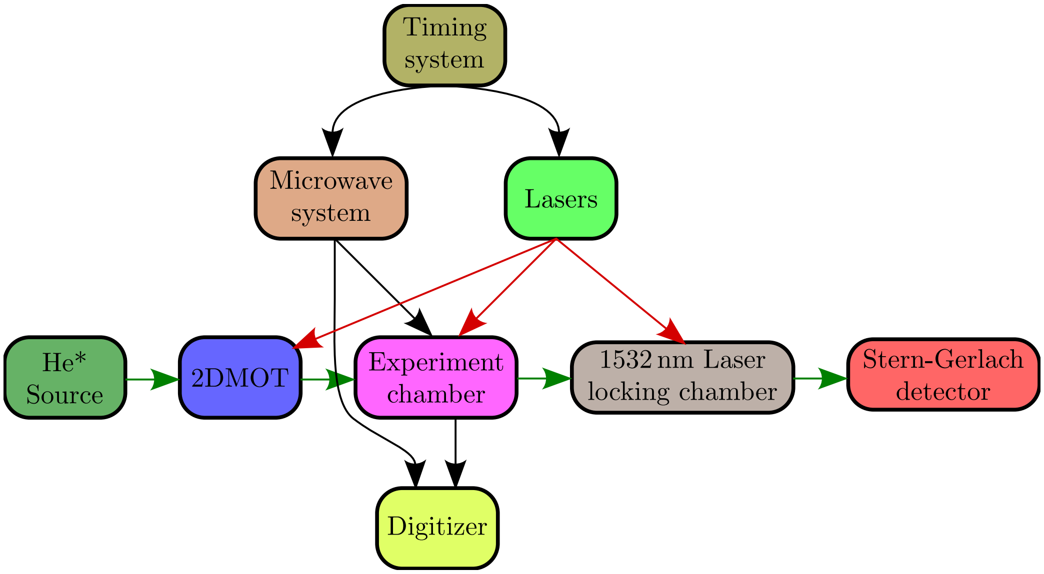

Figure 3.1: A schematic overview of the apparatus. Green arrows denote the path of the He* beam, black arrows electrical signals, and red arrows lasers.

In this experiment, (schematic overview shown in Fig. 3.1 and the physical layout shown in Fig. 3.2), metastable helium atoms are generated in a liquid-nitrogen-cooled constant-current dc-discharge source (described in Sec. 3.2.1). This source produces a thermal beam of metastable helium atoms (with a slow average speed, due to the cryogenic cooling), which is further concentrated and collimated by a two-stage

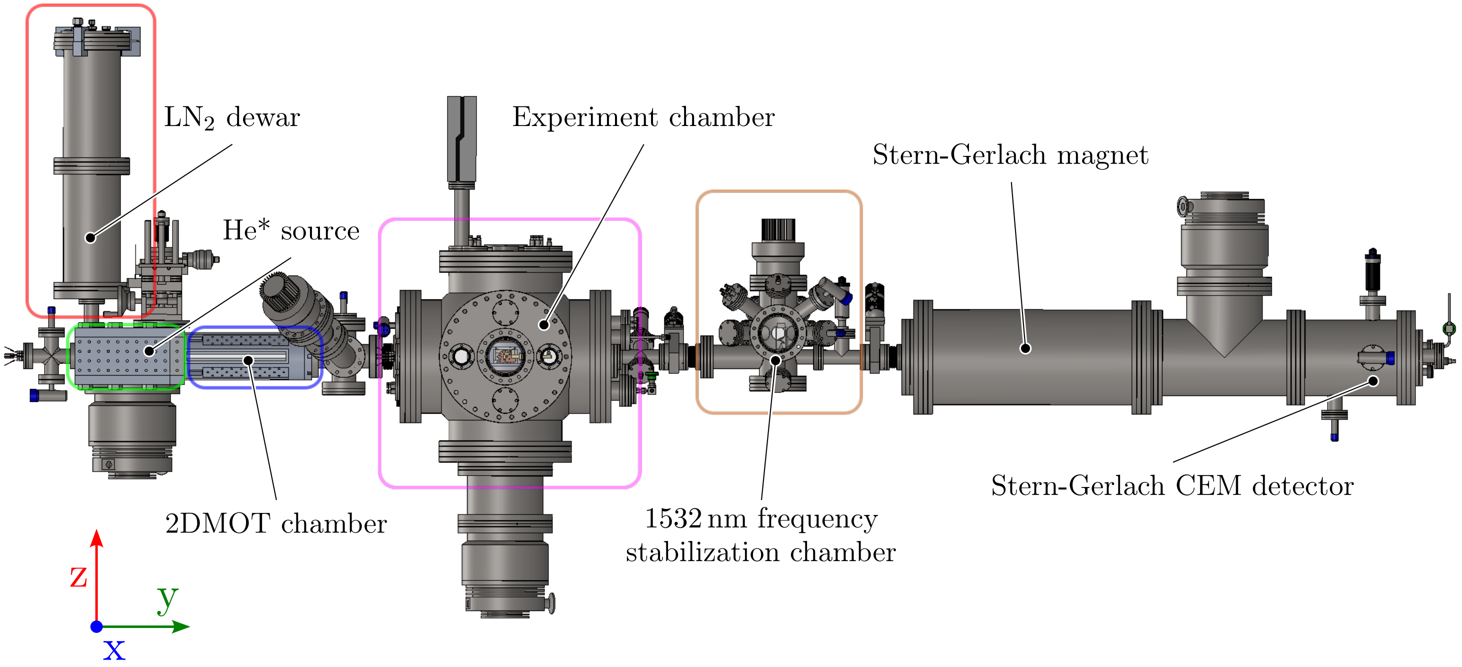

Figure 3.2: Side view of the experiment beamline identifying the main sections.

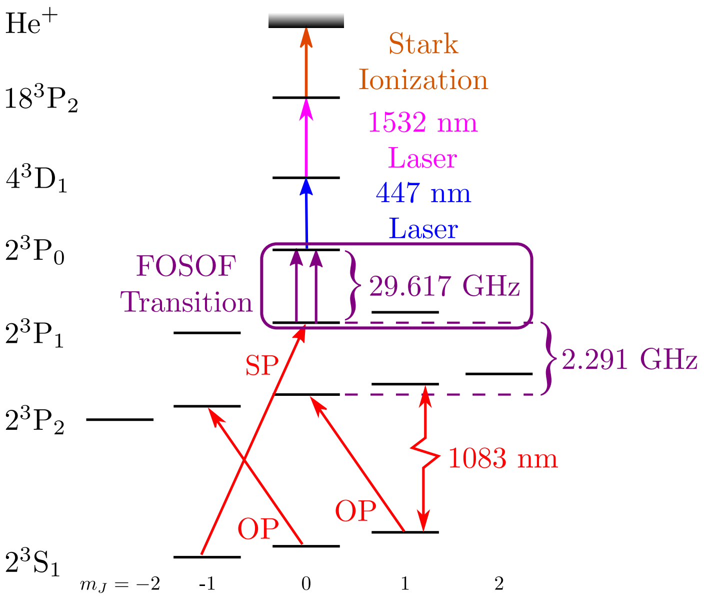

Figure 3.3: Selected energy levels and transitions used in the experiment (not to scale). SP = state-preparation laser, OP = optical pumping.

2-dimensional magneto-optical trap (2DMOT, described in Sec. 3.2.2).

The collimated atoms travel through a 10 cm-long tube which acts as a < 1 L/s pumping restriction between the 2DMOT chamber and the experiment chamber. Upon entering the experiment chamber, the atoms are in an arbitrary distribution of m_J sublevels of 2^3S$_1$. They are optically pumped (as described in Sec. 3.2.3) into either $m_J = +1$ or $m_J = -1$ in order to maximize the signal size and to avoid possible systematic effects due to interference from driving some atoms into the detection state via unintended transitions (which are described in Sec. 4.6).

Next, the atoms are exposed to a series of laser and microwave pulses (as shown in Figs. 3.3 and 3.4) within a section of WR-28 rectangular waveguide, as illustrated in Fig. 3.8. First the state-preparation laser pulse excites the metastable He atoms to 2^3P$_1$($m_J = 0$), and then a pair of microwave pulses drive a FOSOF transition to 2^3P$_0$. This is followed by a 447 nm laser pulse driving atoms to the 4^3D$_1$ state, from which a 1532 nm laser pulse drives them to the 18^3P$_2$ Rydberg state. The laser and

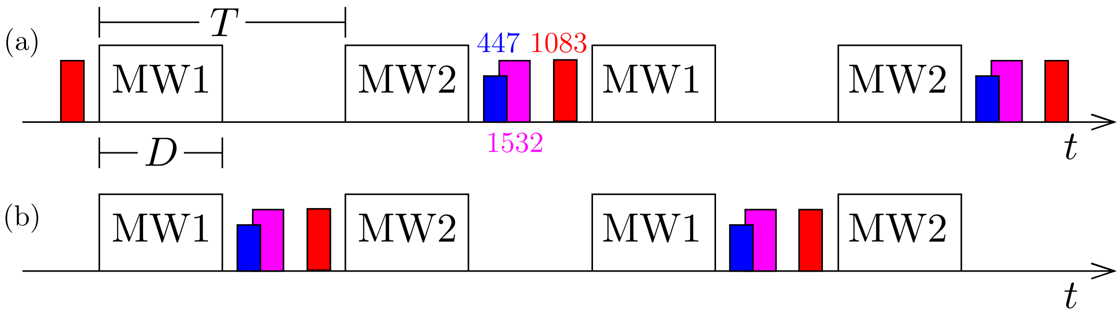

Figure 3.4: (a) Timing diagram for an experiment with repetition period T and microwave pulse duration D. MWn = pulse from microwave generator n. Coloured rectangles represent laser pulses of the labelled wavelength. (b) Timing diagram for alternate experiment configuration (configuration B of Fig. 2.3), with reversed microwave pulse order so that atoms see MW2 immediately after the state-preparation pulse, to cancel phase imperfections as described in Sec. 2.1.2.

microwave systems which generate these pulses are described in Sec. 3.4 and Sec. 3.3.1 respectively.

Upon exiting the waveguide region, the He* beam enters a wire-grid ionizer, which is further described in Sec. 3.2.6, where the atoms which have been excited to the $n = 18$ Rydberg state are Stark ionized. The resulting ions are guided to a CEM (channel electron multiplier) which multiplies the He^+ ion current into a measurable electrical current.

The remainder of the atoms, which are not ionized, continue on to the 1532 nm laser frequency stabilization chamber. Here the metastable atoms are driven by lasers to the 18^3P state and ionized to provide a signal with which to stabilize the frequency of the 1532 nm laser as described further in Sec. 3.4.2.

Finally, the beam passes through a Stern-Gerlach magnet which allows the population in each m_J state to be determined. Additionally, using a chopper wheel in the beam, the speed of the He* atoms is determined by comparing their time of flight with that of UV photons from the source. This system is described further in Sec. 3.2.9.

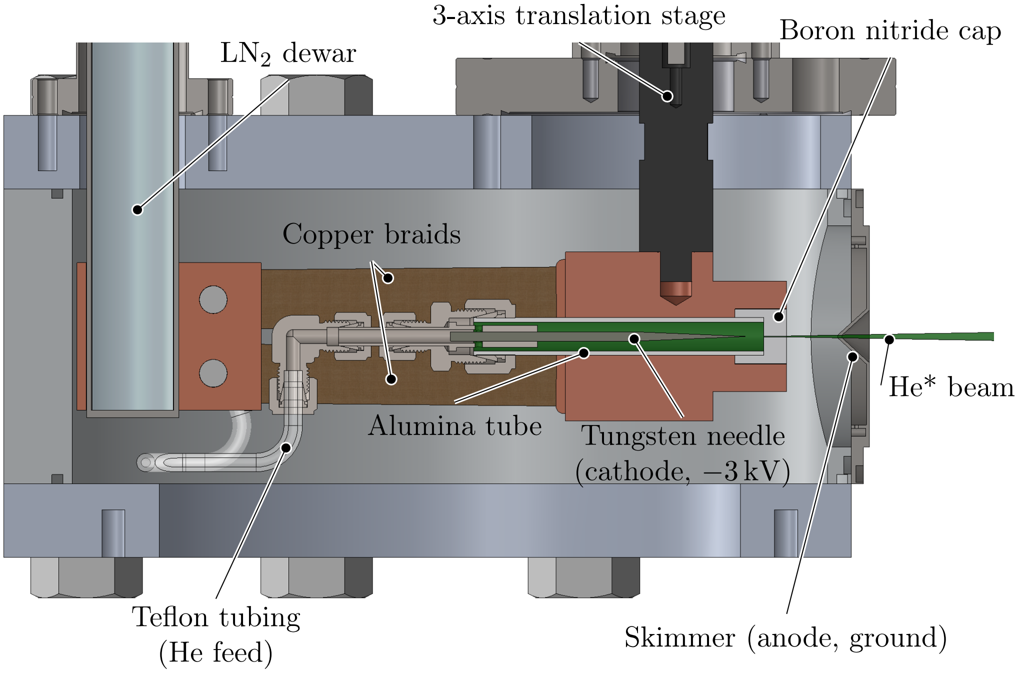

Figure 3.5: Bisected view of the metastable-helium source.

3.2 Beamline

3.2.1 Metastable-Helium Source

Transitions from the singlet states of helium to the triplet state are electric-dipole forbidden, so triplet helium atoms cannot be generated in significant numbers using laser-driven transitions as is common in atomic state preparation. Instead, collisional excitations are used which can more readily mix singlet and triplet states.

In this experiment a 25 mA dc-discharge source is used where free electrons accelerated by a large potential drive the collisional excitation of helium atoms. The source (shown in Fig. 3.5) consists of a tungsten needle anode, which creates a large electric field due to its sharpness, and a grounded skimmer plate with a hole in the centre which acts as an cathode. The diameter of the hole in the skimmer, along with the lower pressure near this skimmer, constrains the divergence of the beam. Between the needle and skimmer there is an insulating boron nitride cap with a 1 cm-long, 0.3 mm-diameter hole drilled through it to allow helium to pass through while maintaining a high pressure in the vicinity of the needle. In this space 99.999% purity helium is introduced through PTFE tubing, at a rate of approximately 100 sccm set by a mass flow controller (MKS 1179A51CS1BV-S) to maintain the pressure at around 25 torr as measured on a capacitive pressure transducer (Edwards 600AB 100TR) just before the feedthrough from external tubing to vacuum. The narrow hole through which the helium exits the high-pressure region functions as a significant pumping restriction, maintaining a large pressure differential between this inner source region and the outer region, which is evacuated by a turbopump with a pumping speed of 900 L/s for He (Agilent Turbo-V 1001 Navigator) to a pressure of around 5×10^{-5} torr while the source is operating.

The pressurized inner source region is surrounded by an alumina tube (see Fig. 3.5), which is held in a copper heatsink block attached to a 3-axis linear translation stage to allow fine tuning of the source position and angle. This block is connected, via copper braids, to another copper block which is clamped to a cold finger at the bottom of a 10 L liquid-nitrogen dewar. The flexible braids allow the critical region of the source to be maintained at cryogenic temperature while still allowing its position and angle to be adjusted. This cooling decreases the velocity of the He* atoms in the beam. The beam intensity is approximately 10^{15}/sr/s for atoms in the 2^3S_1 state.

The power source for the discharge is a high-voltage power supply (Glassman PS/FR06R50.0GA1), operating in constant-current mode with a set current of 25 mA and a maximum voltage of 5 kV. A 100 kΩ resistor bank in series with the discharge helps to stabilize the current. To start the source, the supply is switched on, rapidly ramping the voltage to the set 5 kV until a discharge ignites and current starts flowing, after which the voltage settles to a steady value in the range of 3–3.2 kV. Of this voltage, 2.5 kV is the voltage drop over the resistor bank and 500–700 V powers the discharge between the needle and grounded skimmer.

The combination of materials used in the source discharge region (tungsten needle, boron nitride cap, alumina insulating tube) have been carefully chosen and refined over time. Other combinations which were previously used resulted in source failure after a few months of constant operation due to the formation of an insulating layer on the needle which inhibited arc formation. This insulating layer is also responsible for the voltage required to maintain the arc increasing from 500 V to 700 V throughout the lifetime of a needle. With the current combination of materials this source has functioned for over five years without maintenance, while being operated continuously for the majority of that period. From time to time the discharge will not ignite at the usual operating pressure, but this can be remedied by supplying a short burst of higher helium pressure while the high voltage is applied. It has also been found that after exposing the source to atmosphere (which is sometimes necessary due to the lack of an isolation valve between it and the experiment region), sometimes the arc will extinguish a few hours after being initiated when run at 25 mA. This can be remedied by running at 30 mA for a day or two, and then decreasing the current to the typical 25 mA again.

3.2.2 Laser Cooling

After passing the skimmer the beam is collimated in a 25 cm-long 2-dimensional magneto-optical trap (2DMOT). The 2DMOT is described in detail of Sec. 2.9 of [23] and so only a brief description is given here. Circularly-polarized laser beams are red-detuned by 20 MHz relative to the 2^3S_1-to-2^3P_2 transition. These laser beams

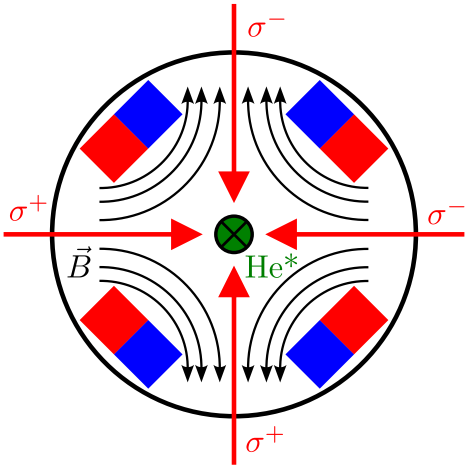

Figure 3.6: Cross Section of the 2DMOT, showing magnetic field lines (black arrows) and laser beams of the two circular polarizations (red arrows) acting on the beam going into the page (central green circle).

illuminate the helium beam from the four directions transverse to its axis in a region containing a quadrupolar magnetic field, that has zero field along the axis and an increasing field away from the axis. Doppler shifts cause atoms with a velocity component transverse to the atomic beam direction to become on-resonance with the detuned laser, and Zeeman shifts similarly cause atoms located away from the magnetic field axis to become on-resonance with the detuned laser. Absorption of red-detuned photons due to the Zeeman and Doppler shifts results in the helium beam being compressed and intensified. The intensification as measured at the end of the beamline is approximately a factor of 25 as it was in the previous measurement.

3.2.3 Optical Pumping

In order to shift the atoms into one of the $2^3\mathrm{S}_1(m_J = \pm 1)$ states, a circularly polarized beam from a 1083 nm laser (tuned to the $2^3\mathrm{S}_1$-to-$2^3\mathrm{P}_2$ transition) is directed into the experiment from above (such that the k-vector for the laser is aligned with the magnetic field), immediately prior to the microwave region.

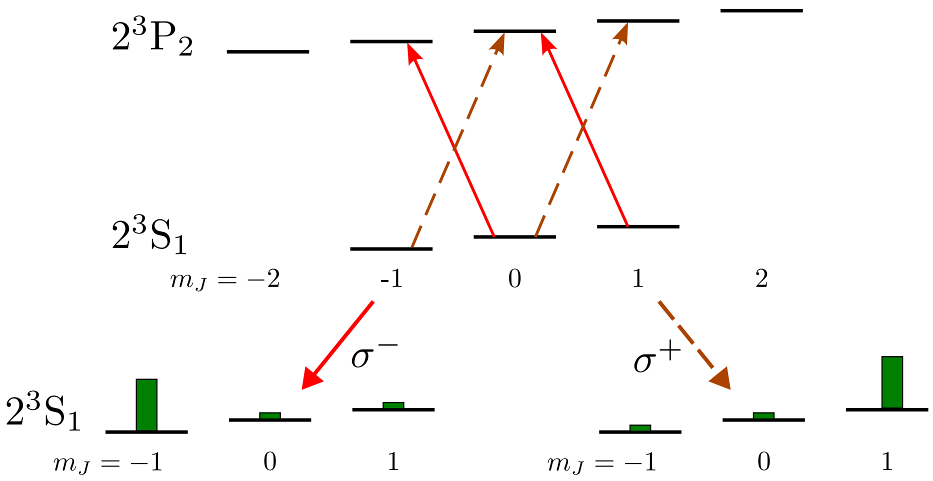

Figure 3.7: Transitions used to optically pump atoms into $2^3S_1(m_J = -1)$ (red solid arrows) and resulting population distributions. Dashed brown lines represent optical pumping into the opposite magnetic sublevel $m_J = +1$, when either the magnetic field direction or optical pumping laser polarization is reversed.

The two optical pumping transitions shown in Fig. 3.7 (the two solid red lines when optically pumping to the $m_J = -1$ state, or the two dashed brown lines when pumping to the $m_J = +1$ state) have different Zeeman shift rates and so two laser frequencies are required to drive them. Details of how these frequencies are obtained are given in Sec. 3.4.1.

The optical pumping scheme is unchanged from the previous measurement[23]. It was shown in Sec. 2.8 of Ref. [23] that approximately 99 % of the population could be pumped into the desired magnetic sublevel. This level of performance has been maintained and periodically verified during the current measurement.

3.2.4 State Preparation

A state-preparation beam travelling parallel to the x axis (a component of the blue beam shown in Fig. 3.8), linearly polarized along the y axis (and thus perpendicular to the magnetic field along the z axis) can drive both $\Delta m_J = +1$ and $\Delta m_J = -1$ transitions to excite atoms into $2^3P_1(m_J = 0)$ after the atoms are optically pumped into $2^3\mathrm{S}_1(m_J = -1)$ or $2^3\mathrm{S}_1(m_J = +1)$ (the $m_J = -1$ case is shown in Fig. 3.3). Care must be taken to minimize the linear polarization component along z as this can lead to excitation to the $2^3\mathrm{P}_1(m_J = \pm 1)$ states and cause unintended interference effects, as described in Sec. 4.6.

3.2.5 Microwave Waveguide

After optical pumping, the atoms enter a custom-machined section of gold-plated copper WR-28 waveguide (shown in Fig. 3.8) which is held in a three-part clamshell assembly (top, bottom, and the waveguide short, which doubles as an endcap). This assembly has outer dimensions which match the GR900 airline used in the previous $2^3\mathrm{P}_2$-to-$2^3\mathrm{P}_1$ measurement in order to make the WR-28 waveguide compatible with the assembly used in that measurement. WR-28 is a specification for rectangular cross-section waveguide with long and short inner dimensions of $a = 0.280\,\text{inches} = 7.112\,\text{mm}$ and $b = 0.140\,\text{inches} = 3.556\,\text{mm}$ respectively, which is used to carry microwaves in the $\mathrm{K_a}$ band (26.5 GHz to 40 GHz). The helium beam enters and exits this waveguide through a pair of 0.5 mm-diameter holes drilled through both walls in one operation in order to ensure that they are aligned with each other.

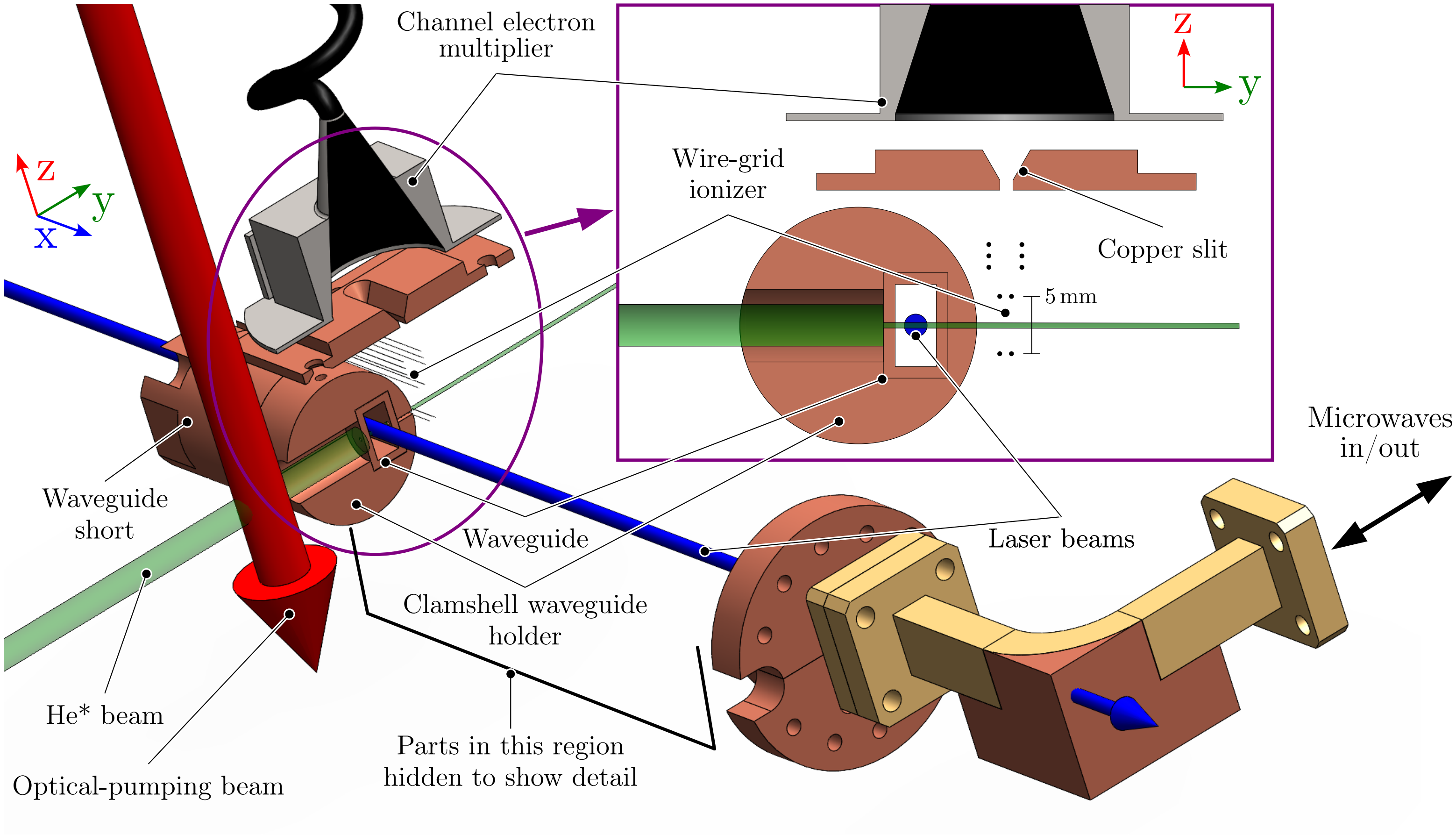

Figure 3.8: Cutaway view of the experiment region, with cross section shown in box.

In order to minimize Doppler shifts, the waveguide is oriented perpendicular to the axis of the atomic beam so that the component of He* beam velocity along the direction of travel of the microwaves is very close to zero. In addition, a microwave short is created at the end of the waveguide section by the endcap, which is held against the flat-cut end of the waveguide by screws. This short causes the microwaves incident on it to be almost completely reflected (with some small loss due to ohmic heating in the waveguide walls), which ensures that there is approximately equal microwave power incident on the atoms from both directions. Further detail on possible Doppler shifts is given in Sec. 4.13.

The distance between the hole in the waveguide through which atoms pass and the short is carefully chosen so that at the resonant frequency of the transition, the hole is a half wavelength away from the short. The incident and reflected microwaves create an antinode of the microwave magnetic field where the He* beam passes, doubling the amplitude (and quadrupling the intensity) of the field which drives the $2^3\mathrm{P}_1 \rightarrow 2^3\mathrm{P}_0$ transition. There is a node of the microwave electric field at the same point, which suppresses ac Stark shifts (discussed in Sec. 4.2) and depopulation of atoms in the Rydberg state (discussed in Sec. 4.8). The wavelength of microwaves within a waveguide is given by

$$\lambda_{\mathrm{WG}} = \frac{c/f}{\sqrt{1 - \left(\frac{c}{2af}\right)^2}}, \tag{3.1}$$

where c is the speed of light in vacuum, f is the microwave frequency, and $a = 7.112\,\mathrm{mm}$ is the length of the long side of the rectangular waveguide cross-section. At 29.617 GHz, Eqn. (3.1) gives $\lambda_{\mathrm{WG}} = 14.409\,\mathrm{mm}$, and so the hole is centred at $\lambda_{\mathrm{WG}}/2 = 7.204\,\mathrm{mm}$ from the short.

As they pass through this waveguide, the atoms are exposed to the laser and microwave pulses shown in Fig. 3.4, which drive the transitions shown in Fig. 3.3. Driving the transitions is accomplished by spatially overlapping the three laser beams before sending them into the waveguide along its axis (blue arrow in Fig. 3.8). Laser access through the waveguide is provided by a pair of 1.5 mm-diameter holes, the laser entry hole drilled in the waveguide short and the exit hole drilled through the wall of the waveguide elbow connected to the end of the experiment waveguide section (as can be seen in the bottom right of Fig. 3.8). These holes are made so that their diameter is much smaller than λ_{WG} and their lengths are at least ten times their diameters in order to minimize their impact on the microwave transmission properties of the waveguide and to ensure that no microwave power is transmitted through the holes. For the waveguide elbow an extra copper piece was machined and brazed on before drilling in order to provide material for a sufficiently long hole.

The rest of the microwave system which generates and transmits the pulses is described in Sec. 3.3.1, and the laser systems are described in Sec. 3.4.

3.2.6 Stark-Ionization Detector

After being excited to the $n = 18$ Rydberg state by the series of laser and microwave pulses (see Fig. 3.3 and Fig. 3.4), the atoms exit the waveguide and enter a wire-grid ionizer, as shown in the inset of Fig. 3.8. This is the same ionizer described in Sec. 2.7 of [23], and so only a brief description is given here.

The ionizer (Fig. 3.9) consists of a series of wires strung between insulators, to which high voltages (up to 3 kV, actual voltages used are given in Table 3.1) are applied. The bottom two wires have positive potentials applied and the ones directly above them are negative, such that a large electric field is directed vertically upwards.

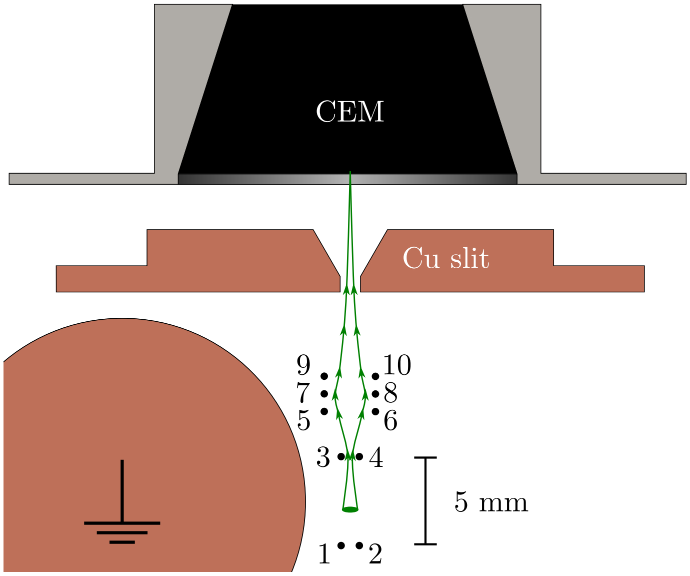

Figure 3.9: Wire-grid ionizer with wires labelled 1-10. Green arrows depict paths of helium atoms which have been ionized in between wires 1, 2, 3, and 4. The potentials applied to the wires and other ionizer components are given in Table 3.1.

Component	1	2	3	4	5	6	7	8	9	10	Cu Slit	CEM
Applied Voltage [V]	2300	1700	-2300	-1700	-200	350	200	350	-70	350	-2300	-1200

Table 3.1: Voltages applied to the components of the ionizer.

This field both Stark ionizes the Rydberg helium atoms and directs them upwards through the other six wires, which act as an electrostatic lens to focus the ions through the 1 mm-wide copper slit and into the channel electron multiplier (CEM, Photonis 30075). The background signal from the CEM is dominated by collisionally ionized helium atoms from the small amount (3×10^{-9} torr) of gas remaining in the experiment chamber. The narrow copper slit decreases this background signal level by rejecting ions created away from the intended ionization point, as they will be placed on a trajectory which does not pass through the slit and into the CEM. The output current of the CEM is fed into a low-noise transimpedance amplifier (Femto DLPCA-200) with a gain of 10^9 V/A, and the output of this amplifier is recorded on one of the two channels of a digitizer (Agilent L4352A). These digitizer traces constitute the atomic FOSOF signal for the experiment.

3.2.7 Magnetic Field Coils

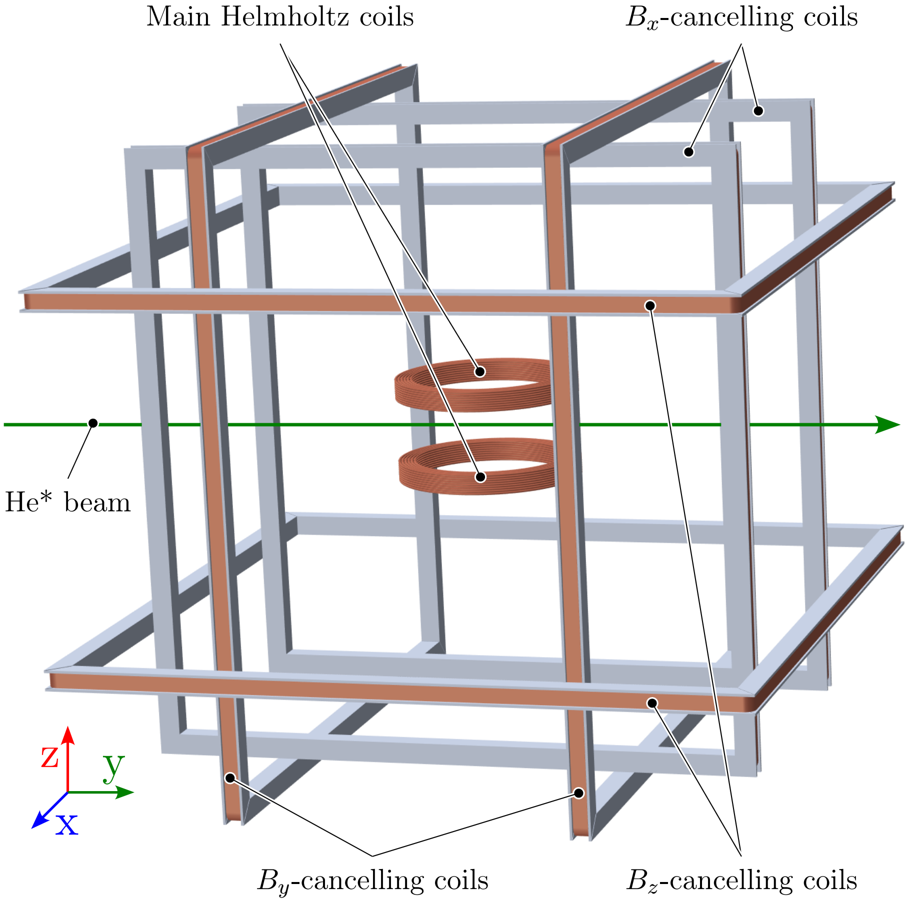

Figure 3.10: Magnetic field coils used in the experiment. The inner pair of circular loops are the main Helmholtz coils for applying the dc magnetic field along the z axis. The components shown in Fig. 3.8 are located in the centre of these coils. The three pairs of square coils are background-cancelling coils, one pair for each axis.

The coils used to generate a dc magnetic field along the z axis and those used to cancel the ambient background field are shown in Fig. 3.10. To cancel the background field (the earth's field and other local fields present in the laboratory) there are three pairs of square coils outside the vacuum chamber, one for each component of $\mathbf{B}_{\text{background}} = (B_x, B_y, B_z)$. Because the interaction volume in which atoms are excited within the waveguide is very small (at most a cylinder of 0.5 mm diameter due to the He* access hole and 3.6 mm length due to the distance between waveguide walls, in practice even less because the laser excitation to the state from which the microwave transition is driven occurs at approximately the midpoint between the waveguide walls), variation of the magnetic field due to field gradients is minimal. The current through these coils is recorded via precision 10 mΩ shunt resistors (IET Labs DCCS-0.01) on the data logger (Keithley 2701 with 7708 multiplexer) with every data acquisition (every 1-10 seconds, depending on experiment parameters), in order to allow correcting for any drift in current from the power supplies.

The main dc bias field is supplied by a pair of water-cooled solenoids in a Helmholtz configuration (see Fig. 3.10) inside the vacuum chamber, which are capable of providing fields up to 30 G. The current through these coils, which are wired in series, is also recorded on a 10 mΩ shunt resistor. The voltages across all coils are recorded as well so that their total resistances can be monitored, and any possible electrical short between windings which might develop due to damage would be detected as a drop in resistance.

Further details on the calibration and operation of these coils are given in Sec. 4.4.

3.2.8 1532 nm Locking Detector

In a separate chamber further down the beamline (labelled "1532 nm frequency stabilization chamber" in Fig. 3.2), a simplified copy of the Stark-ionization detector is used to provide a signal with which to stabilize the 1532 nm laser. Because there are no microwaves to excite the atoms in this region, CW power from a laser tuned to excite the $2^3\mathrm{S}_1 \rightarrow 2^3\mathrm{P}_0$ transition (laser 1083C, described in Sec. 3.4.1) and the two detection

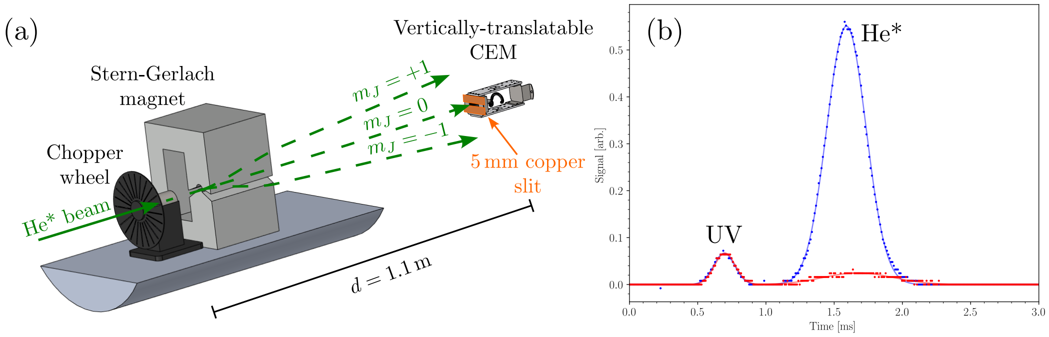

Figure 3.11: (a) Stern-Gerlach apparatus, with chopper wheel and drift distance used to determine the beam velocity shown. (b) Signals from the Stern-Gerlach CEM detector, with the 2DMOT on (blue) and off (red) showing a signal size increase by a factor of approximately 25. Each line is a fit to a sum of two Gaussian profiles, one for the initial UV peak and one for the later He* peak.

lasers (447 nm and 1532 nm) are used to excite atoms to the 18^3P state through the sequence $2^3\mathrm{S}_1 \rightarrow 2^3\mathrm{P}_0 \rightarrow 4^3\mathrm{D}_1 \rightarrow 18^3\mathrm{P}$. Other than using a different 1083 nm laser, this scheme is unchanged from the previous measurement, and is described in detail in Sec. 2.6.2 of [23].

3.2.9 Stern-Gerlach Detector

The final element of the beamline is a Stern-Gerlach detector, consisting of a long permanent magnet with a large vertical field gradient followed by a CEM on a vertical translation stage (see Fig. 3.11(a)). The magnetic field gradient causes a net force to be exerted on the atoms according to their magnetic dipole moment $\boldsymbol{\mu}$ (which is determined by the value of m_J):

$$\mathbf{F} = \nabla(\boldsymbol{\mu} \cdot \mathbf{B}) = |\mu|\nabla\mathbf{B}. \tag{3.2}$$

The atoms are thus spatially separated along the z axis according to which m_J sublevel of $2^3\mathrm{S}_1$ they are in, and the population in each sublevel can be sampled by adjusting the height of the CEM with the translation stage.

The metastable helium source also generates UV photons which have sufficient energy to liberate photoelectrons from the surface of the CEM (when it is situated on the beam axis), resulting in a measurable signal. To separate the signals due to the UV light and the metastable atoms, a 2 % duty cycle chopper wheel (Stanford Research Systems SR540) is placed inside the vacuum system in front of the Stern-Gerlach magnet, 1.1 m from the CEM. The chopper causes the continuous signals to be split into pulses, with the pulse from the UV separated in time from that of the much slower metastable atoms. These signals allow the speed of the beam to be monitored, giving a typical mean value of approximately 1100 m/s.

3.3 Microwave and Timing Systems

3.3.1 Microwave System

An overview of the timing-critical components of the experiment is shown in Fig. 3.12. The microwaves used for the FOSOF pulses of Fig. 3.4 originate from two 40 GHz generators (Wiltron/Anritsu 68369A/NV and HP 83640A). These are run in CW output mode, at frequencies separated by the FOSOF offset frequency f_{ofs}. Their outputs are fed into a system which produces alternating pulses from the two generators (as in Fig. 3.4), as well as a reference sine wave at the offset frequency ($R(t)$ of Eqn. (2.15)). This system is described in detail in Sec. 3.3.2. The reference sine is amplified by a low-noise preamp (Stanford Research Systems SR560), before being fed into one channel of a digitizer (Agilent L4352A). The other channel of the digitizer records the atomic signal (the ionization signal from the CEM), giving traces of $R(t)$ and $S(t)$ (Eqns. (2.14) and (2.15)) similar to those shown in Fig. 2.5.

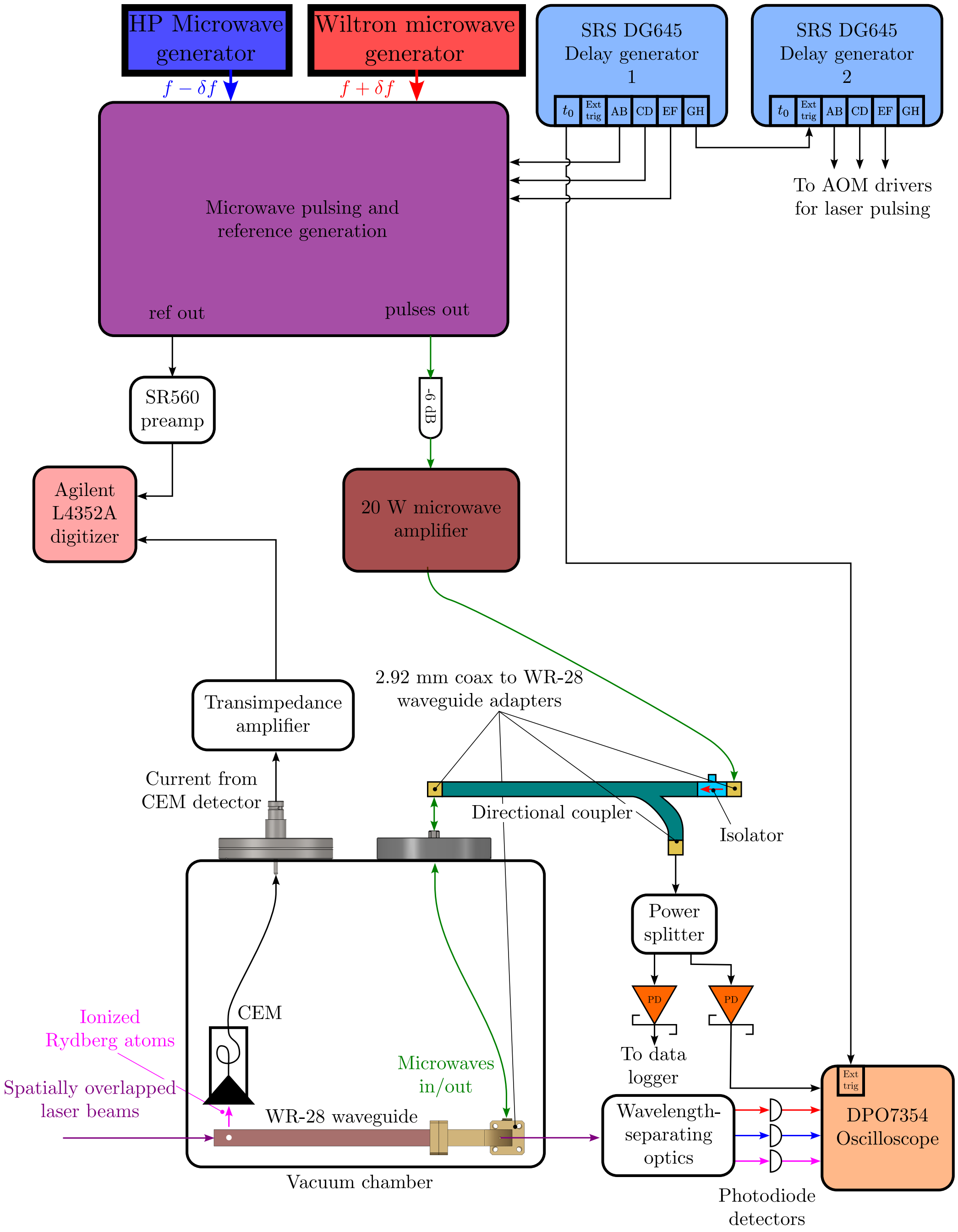

Figure 3.12: Schematic of the microwave and detector systems. Green arrows represent microwave path, PD = Schottky diode power detector. The microwave generator frequencies are separated by the FOSOF offset frequency $f_{\text{ofs}} = 2\delta f$.

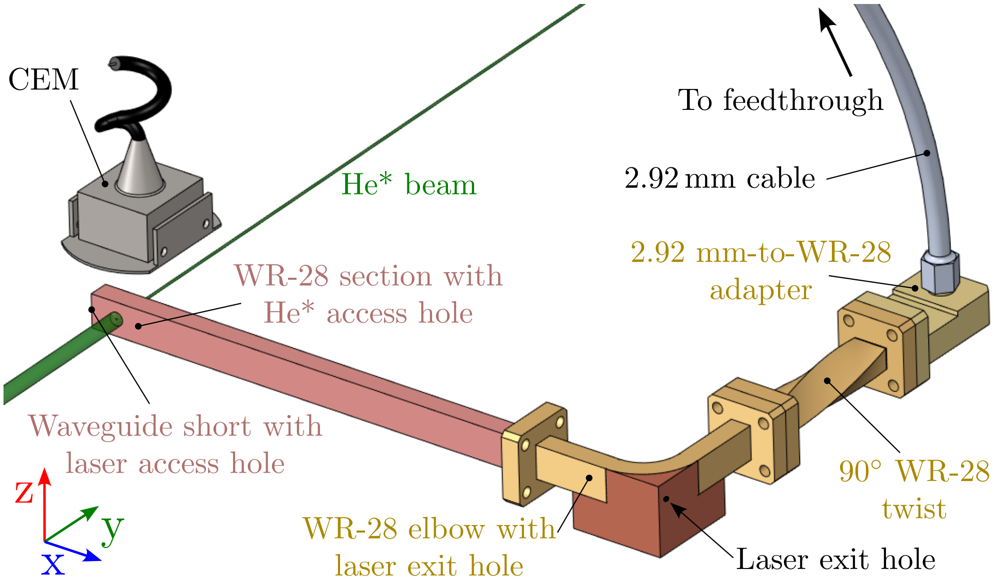

Figure 3.13: The in-vacuum microwave components.

The microwave pulses from this system go to an amplifier (RF-Lambda RFLUPA27G34GB), which has a saturation power of 15 W. A 6 dB attenuator at the input of the amplifier attenuates reflections from the input of the amplifier that would otherwise reflect back and forth between the output port of the system which generates the pulses and the input of the amplifier. These reflections would distort the phase and amplitude of the microwaves at the turn-on and turn-off of the pulses (as compared to a perfect rectangular amplitude profile with constant phase). The output of the amplifier is connected to a 2.92 mm coax-to-WR-28 waveguide adapter (Quinstar QWA-28S29F00), which is attached to a waveguide isolator (Pamtech RYG2031) and 20 dB directional coupler (HP R752D) and then via another waveguide-to-coax adapter connected to a vacuum feedthrough. These adapters are a compromise because waveguide isolators and directional couplers have significantly better performance than coaxial ones, but coaxial vacuum feedthroughs are significantly simpler and more robust than waveguide vacuum feedthroughs.

After the vacuum feedthrough another coaxial cable (in vacuum) leads to another coax-to-waveguide adapter and finally the experiment waveguide section. The in-vacuum microwave components are shown in Fig. 3.13, and in the context of the ionizer in Fig. 3.8. The waveguide section (Fig. 3.13) consists of a 90° twist (to rotate the microwave polarization to lie along the z axis while orienting the adapter to minimize the cable length required), and then a 90° elbow followed by a straight section of waveguide with an electrical short at the end. The elbow and waveguide section are further described in Sec. 3.2.5, and essentially consist of waveguide segments with holes drilled along the x axis and y axis to allow lasers and the helium beam, respectively, to enter the waveguide.

The amount of microwave power which reaches the atoms when the amplifier is at its maximum power is approximately $P_{\mathrm{Max}} = 1\,\mathrm{W}$. The fits of FOSOF data to Eqn. (2.27) give a value of approximately $V = 2\,\mathrm{rad/\mu s}$ at full power, which can be related to the microwave ac magnetic field amplitude B_0 by Eqn. (5.6). This field amplitude can then be converted to microwave power in the waveguide with Eqn. (5.7). A measurement of the saturation behaviour of the $2^3\mathrm{P}_1$-to-$2^3\mathrm{P}_0$ transition versus microwave power for a single pulse with duration ranging from $D = 300\,\mathrm{ns}$ to $D = 900\,\mathrm{ns}$ also gave results consistent with $P_{\mathrm{Max}} = 1\,\mathrm{W}$.

The microwaves reflected from the short retrace their path back out of the vacuum region and into the $-20\,\mathrm{dB}$ directional coupler shown in Fig. 3.12. The majority of the reflected microwave power is absorbed in the isolator (which protects the amplifier). The portion from the $-20\,\mathrm{dB}$ directional coupler is divided in two by a power splitter (RF-Lambda RFLT2W6G40G) and then fed into two zero-bias Schottky diode power detectors (Krytar 203BK). The output voltage of one detector is recorded on a data logger once each time the frequency or experiment configuration (between the two configurations shown in Fig. 2.3) is changed when taking FOSOF data. The output of the other goes to the 3.5 GHz bandwidth oscilloscope (Tektronix DPO7354) which is used to record traces of the microwave pulses. This oscilloscope also records traces of the laser pulses, which are detected on photodiodes after passing through the waveguide of of Fig. 3.8 and out of the experiment chamber of Fig. 3.2.

The timing of all microwave and laser pulses is controlled by a pair of delay generators (Stanford Research Systems DG645). The first three outputs of the first delay generator provide the TTL signals for the microwave pulses shown in Fig. 3.15, while the fourth is used to trigger the second delay generator. The second delay generator outputs signals to the AOM drivers which create the pulse configurations shown in Fig. 3.4. The delay generator outputs for a $T = 300\,\mathrm{ns}, D = 100\,\mathrm{ns}$ FOSOF experiment are shown in Fig. 3.16. The signal from the first generator, which is used to trigger the second, is a pulse which has a rising edge at the start of the experiment cycle and a falling edge exactly halfway through the cycle. Constructing the synchronization pulse in this way allows for a switch between configurations A and B of Fig. 2.3 by simply switching the second generator from triggering on the rising edge of the synchronization pulse to the falling edge, placing the laser pulses in the positions shown in Fig. 3.4(a) and (b). Crucially, this change does not affect the microwave pulses or reference signal in any way, allowing the FOSOF reversal which cancels phase imperfections as described in Sec. 2.1.2.

3.3.2 Generation of Microwave Pulses and Reference Signal

The microwave pulse train and reference signal are generated in a temperature-stabilized box (to 32(1) °C), as shown in Fig. 3.14. The output of each generator is first fed into a directional coupler (Marki C13-0140) which splits off $-13\,\mathrm{dB}$ of the input power to the reference-signal-generation arm. In both the HP and Wiltron sections of this arm there are two $20\,\mathrm{dB}$ isolators (Fairview Microwave SFI2731) in

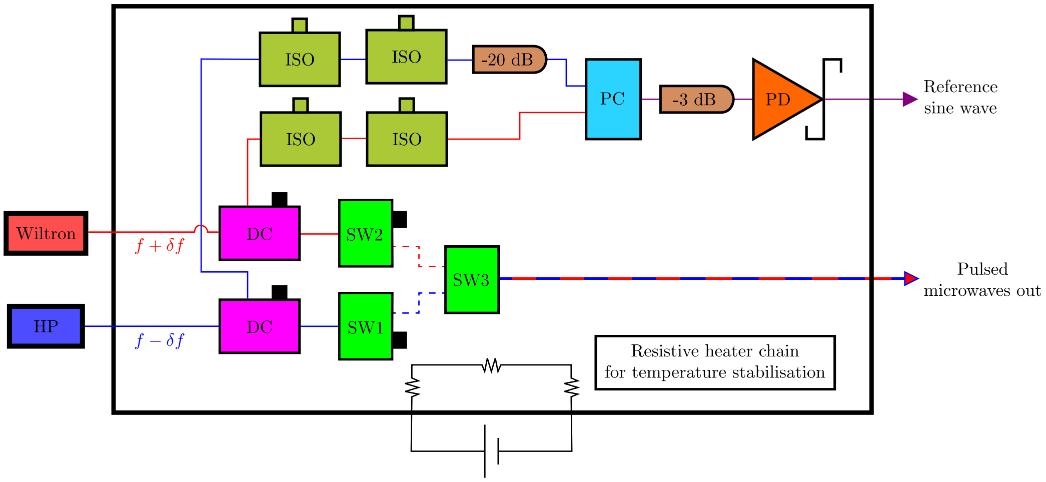

Figure 3.14: Schematic of microwave pulse generation system. HP & Wiltron are the two microwave generators, DC = directional coupler, SW = switch, ISO = isolator, PC = power combiner, PD = Schottky diode power detector. Attenuators are labelled with their attenuation value. Small black squares represent 50 Ω terminated ports.

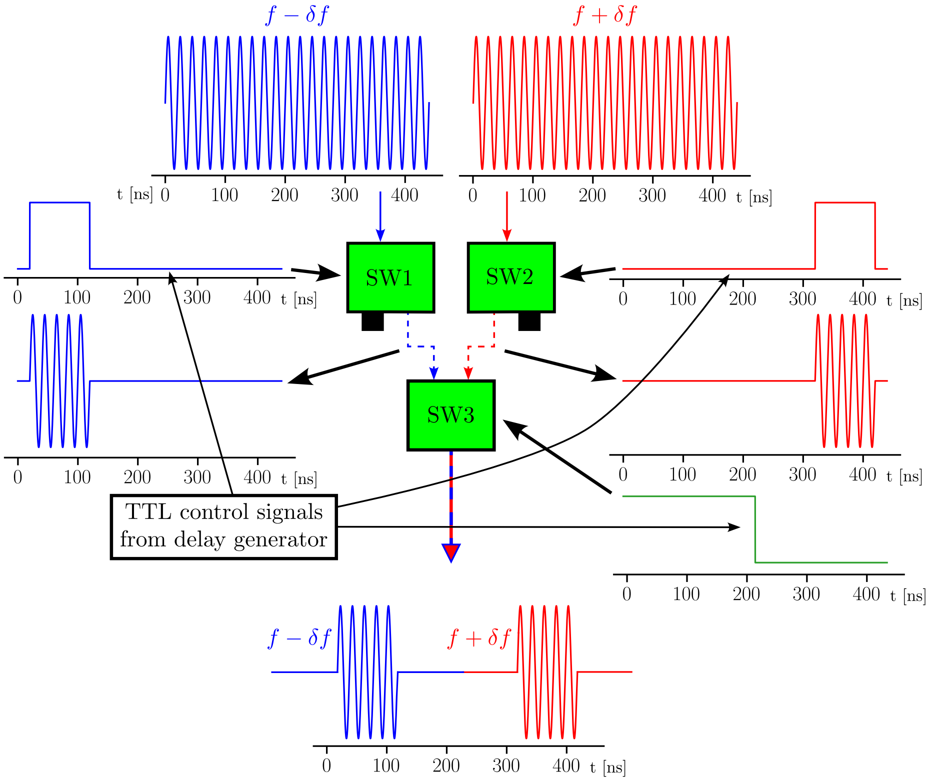

Figure 3.15: One period of the continuously repeating TTL control signals which are sent to the switches to generate microwave pulses, and the resulting microwave pulses throughout the system. The frequencies of the sine waves have been reduced to make them visible at this scale.

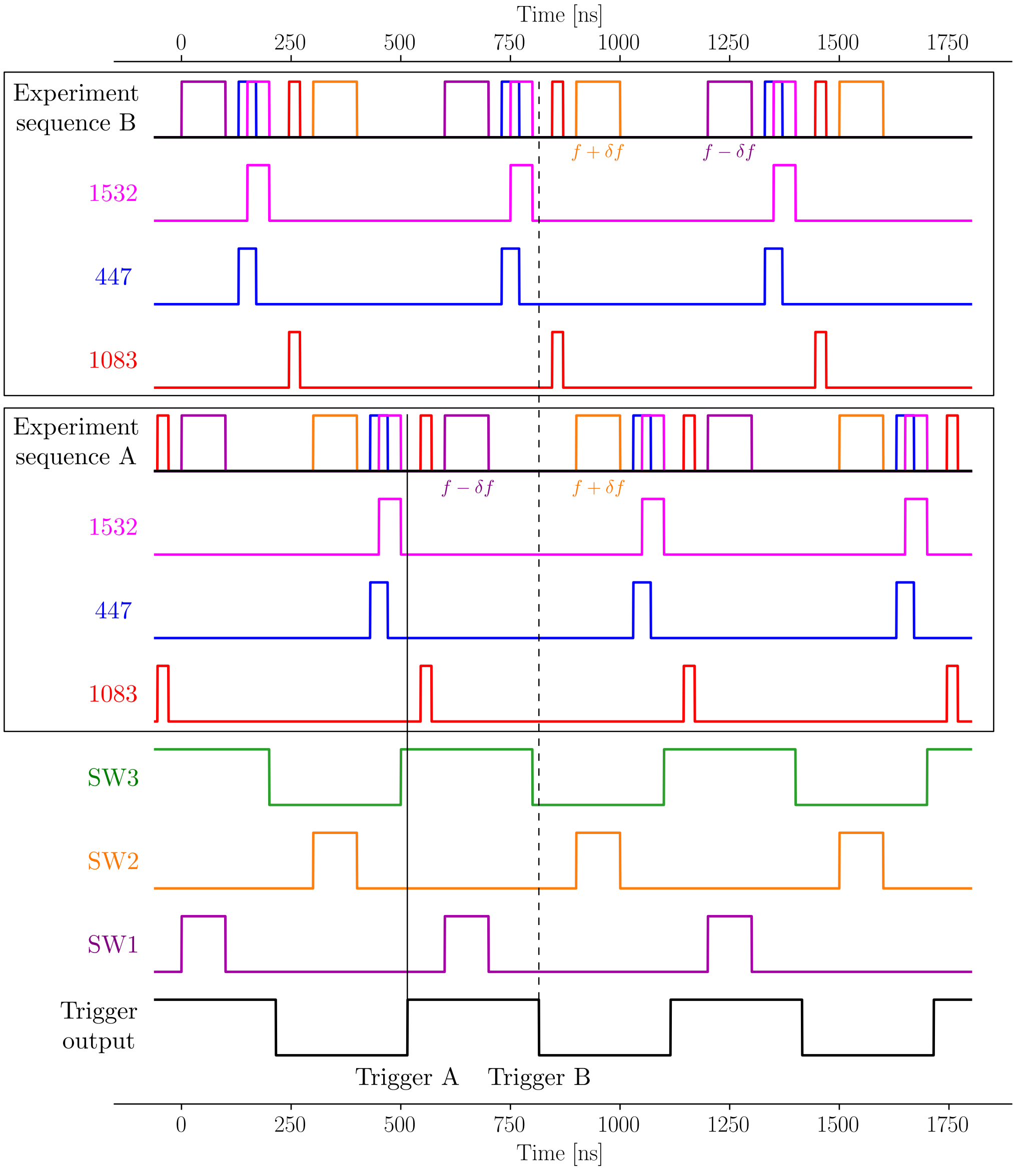

Figure 3.16: The outputs of the delay generators used to control the timing of pulses in the experiment. The pulses labelled SW1-3 come from the first delay generator and are used to control the microwave switches in Figs. 3.14 and 3.15. The pulses labelled 1083, 447, and 1532 are the signals which control the pulsing of the corresponding lasers via AOMs (shown in Figs. 3.23, 3.26 and 3.27). Experiment sequences A and B comprise the reversal described in Sec. 2.1.2 (which is used to cancel phase imperfections), implemented by shifting the timing of only the laser pulses. The laser switching pulses are generated by a second delay generator, which is triggered by the trigger output of the first delay generator (which generators the microwave switch pulses). The start of an experiment cycle is determined by the timing of the 1083 nm laser pulse, and the experiment type by whether a microwave pulse at $f+\delta f$ or $f-\delta f$ is the first after this laser pulse.

order to stop any possible microwaves leaking from one generator's path into the other in the switching arm, due to back reflections from the imperfect impedance matching most components have at this frequency. All cables used inside the box are made with Pasternack PE-SR402FL coax which is rated to 110 dB of shielding. The 2.92 mm connectors are also rated to >100 dB of shielding. Both arms are then combined in a power combiner (RF-Lambda RFLT2W6G40G), the output of which passes through a 3 dB attenuator which both allows the Schottky diode power detector (Krytar 203BK) to operate in the low-power regime where its output voltage is proportional to input power (also known as the square-law region, as the output voltage of these devices is approximately proportional to the square of the input rf electric field at low power) and attenuates reflections from the input of the power diode, which has a very poor VSWR (voltage standing-wave ratio). Operating in the linear region suppresses harmonics of the offset frequency. The HP path of the reference arm has an extra 20 dB attenuator to ensure linearity: if a beat note is formed between two waves of equal amplitude, the peak power can become large enough to drive the Schottky diode power detector beyond the linear region, leading to distortion of the reference sine.

A beat note is generated when two sinusoidal waves close in frequency are added together:

$$E(t) = E_0 \left(\cos(\omega_1 t) + \cos(\omega_2 t)\right) = 2E_0 \cos\left(\frac{\omega_1 + \omega_2}{2} t\right) \cos\left(\frac{\omega_1 - \omega_2}{2} t\right). \qquad (3.3)$$

The Schottky diode power detector outputs a voltage which is proportional to the square of the input field, averaged over a time period which is short on the scale of the offset frequency but long compared to the period of the microwaves. Thus $V_{\text{out}} \propto \langle E^2 \rangle$, and the sum-frequency part of Eqn. (3.3) averages out to leave

$$V_{\mathrm{out}}(t) \propto \left(E_0 \cos\left(\frac{\omega_1 - \omega_2}{2} t\right)\right)^2 = \frac{E_0^2}{2} \left(\cos((\omega_1 - \omega_2)t) + 1\right). \tag{3.4}$$

Eqn. (3.4) shows that the output of the power detector is a voltage oscillating sinusoidally at the offset frequency as required for a FOSOF reference signal, with a dc offset which can be easily filtered out.

From the other output of each of the directional couplers (the one that transmits the majority of the power) in Fig. 3.14, the microwaves from the two generators each enter an SPDT (single-pole, double-throw) switch (Quinstar QSC-ADH000), with one of the three ports terminated such that they can act as simple on/off SPST (single-pole, single-throw) switches. Both paths are then fed into a third switch, which improves the isolation so that the amount of unwanted power from a given generator reaching the output is further decreased when the switches are configured to pass power from the other generator to the output. Each switch is specified to provide 50 dB of isolation between input and output ports when in the off state, so this configuration provides a total isolation of 100 dB.

3.3.3 Microwave Power Detection

Two types of power detectors are used to measure the power level of microwaves in this experiment, a thermal power detector (HP 436A meter with HP R8486A sensor) and Schottky diode power detectors (Krytar 203BK). The Schottky diode detectors have a large bandwidth and can respond to power changes on the scale of nanoseconds, but their output voltage is not linear with input power across their whole power range, and so must be calibrated. Thermal power detectors utilize a thermocouple which monitors the temperature of a load as it is heated by incident microwave power and

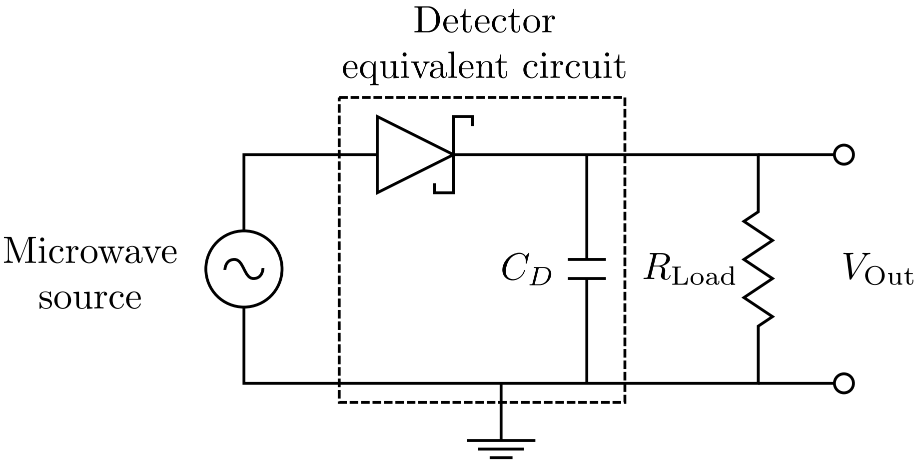

Figure 3.17: Electrical schematic of a Schottky diode power detector.

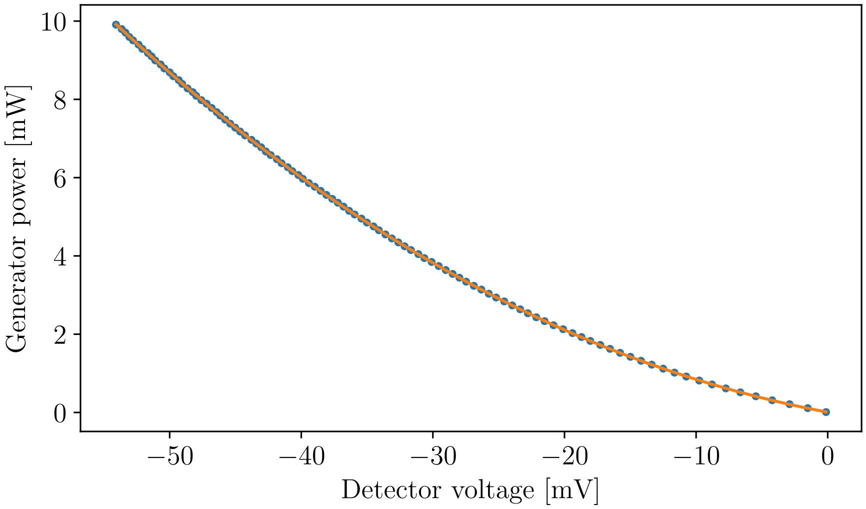

Figure 3.18: Calibration curve for a Schottky diode microwave power detector with 50 Ω termination on the output. The y axis is thermal power meter readings at a given generator power, the orange line is a smoothed cubic spline fit to the data. This spline converts the measured detector output voltage to the corresponding microwave power incident upon the diode.

are very linear, but respond relatively slowly to changes in incident power. Using the thermal power meter as a reference to calibrate the diodes allows the benefits of both types of detector to be exploited. Linearity of the detector's output voltage as a function of input power is especially important, because the measured linecentres are extrapolated to zero microwave power in our analysis to suppress many systematic effects (which are linearly proportional to the microwave power) as described in Sec. 4.2.

A representative schematic of a Schottky diode power detector is shown in Fig. 3.17. The signals from this detector can be analyzed in the small-signal regime using the Shockley diode equation

$$I_D = I_S \left(e^{\frac{V_D}{nV_T}} - 1 \right), \tag{3.5}$$

where I_D is the current through the diode, I_S is the reverse-bias saturation current (a property of a particular diode), V_D is the voltage across the diode, $V_T = k_B T/q$ is the thermal voltage, and n is the ideality factor of the particular diode. If we assume that $V_S = V\cos(\omega t)$ (the voltage output of the microwave source) is much larger than V_{Out} (which is defined in Fig. 3.17), then $V_D \approx V_S$ and we can series expand Eqn. (3.5), dropping terms beyond the second order to give

$$\begin{aligned} I_{\mathrm{D}} &= I_{\mathrm{S}} \left(\frac{V}{nV_T}\cos(\omega t) + \frac{1}{2}\left(\frac{V\cos(\omega t)}{nV_T}\right)^2 + \dots \right) && (3.6) \\ &\approx I_{\mathrm{S}} \left(\frac{V}{nV_T}\cos(\omega t) + \frac{1}{4}\left(\frac{V}{nV_T}\right)^2 (1+\cos(2\omega t)) \right). && (3.7) \end{aligned}$$

At microwave frequencies, the oscillating terms $\cos(\omega t)$ and $\cos(2\omega t)$ will average to zero and the output voltage is approximately

$$V_{\mathrm{Out}} = I_{\mathrm{D}} R_{\mathrm{Load}} = \frac{I_{\mathrm{S}} R_{\mathrm{Load}}}{4(nV_T)^2} V^2 \propto P_{\mathrm{MW}}, \tag{3.8}$$

where P_{MW} is the microwave power. That is, the output voltage is proportional to the input microwave power for small signals.

In the large-signal regime, this circuit can be thought of as a half-wave rectifier for the microwave input (due to the diode), followed by a low-pass filter or integrator so that the output voltage is the average rectified microwave voltage, and proportional to the square root of the input microwave power.

The external load resistance R_{load} affects the bandwidth of the detector; all measurements in this experiment are taken with $R_{\mathrm{Load}} = 50\,\Omega$ which gives an RC time constant of 1.5 ns when combined with the specified capacitance of our detectors $C_D = 30\,\mathrm{pF}$. This 1.5 ns detector response time is faster than the 5 ns switching time of the microwave switches used in this experiment, and so this configuration can be used to accurately record the power profiles of the microwave pulses on an oscilloscope.

Both types of sensor typically have poor VSWRs (1.4 for the thermal sensor, 1.5 for the diodes) and so it would be very difficult to eliminate or correct for effects due to reflections in power measurements to obtain an absolute measure of power seen by the helium atoms. However, since proportionality is our main concern (as the only purpose for the power measurement is performing a linear extrapolation of the linecentre to zero power as described in Sec. 4.2), increasing the output power of the amplifier by a factor will increase the power at the input of the sensor by the same factor, no matter how large and numerous the reflections are.

To calibrate the diode power detectors, the power output of the HP generator was first confirmed to be proportional to its front-panel setting using the thermal

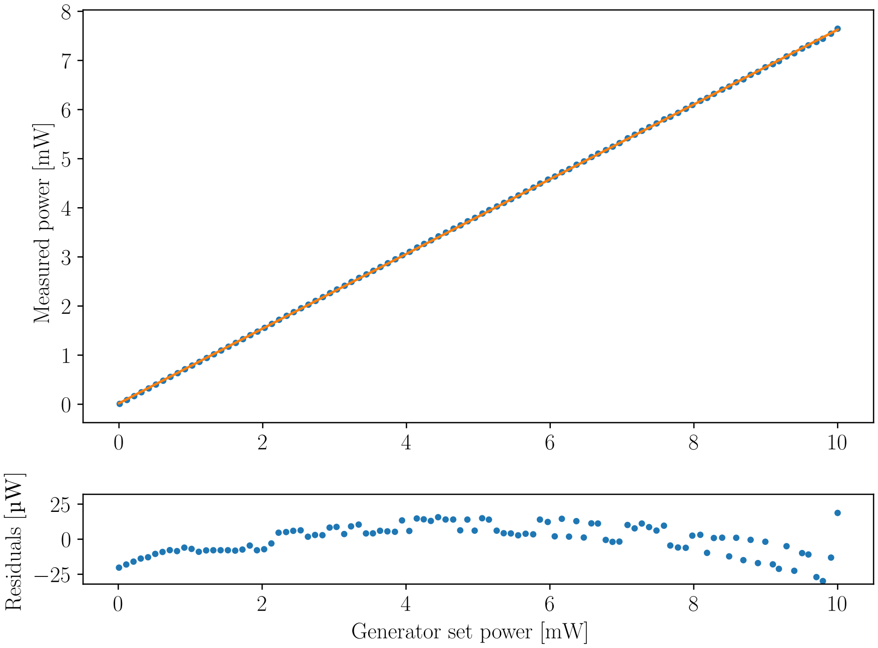

Figure 3.19: A measurement of the HP generator's output power with a thermal power meter, which confirms that it is proportional to the front panel power setting.

power meter, as shown in Fig. 3.19. This allows the generator front-panel setting to be used as a proportional power standard to compare the diode against. The results of the calibration procedure are shown in Fig. 3.18. The curve does not closely follow an obvious analytical function, so a cubic spline with a small amount of smoothing ($s = 5 \times 10^{-3}$ in the Python function `scipy.interpolate.splrep`) is used to interpolate this curve to convert measured diode voltages from the experiment to the corresponding power value. Because the data logger only records average voltages, it is important to convert this measured voltage to the voltage at the peak of the pulse by dividing by the duty cycle D/T before applying the calibration function. This is because the calibration function is nonlinear, and $f(\overline{x}) \neq \overline{f(x)}$ in general if f is not linear.

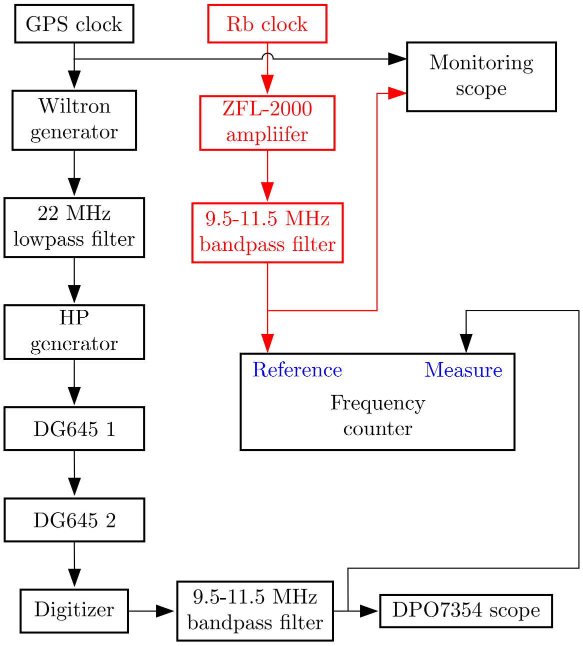

Figure 3.20: Schematic of the timing reference chain and monitoring system.

3.3.4 Frequency Reference Chain

In order to measure a transition frequency on the part-per-billion scale, the applied frequency must be known to better than a part per billion. This is achieved by locking all frequency and timing-sensitive devices in this experiment to a GPS-disciplined oscillator (Trimble Thunderbolt E), which is regularly checked against a Rubidium frequency reference (FEI Communications FE-5680A).

The GPS clock works as a GPS receiver: on initial startup it uses the signal from at least four GPS satellites to solve for its position (which is stationary) so that it can use the signal from a single satellite to find t after this initial setup. The GPS satellites carry a redundant combination of rubidium and caesium clocks, which are steered in frequency every 12 hours (once per orbit) to stay in agreement with the US Naval Observatory Master Clock, and are specified to have a frequency stability much better than a part per trillion between these steering events [25]. The GPS clock uses this signal to maintain the frequency of an oven-controlled crystal oscillator to similar stability, the model used in this experiment is specified as accurate to 1 ppt when averaged over a day. It also has extended hold-over functionality, so that if satellite signal is lost, known parameters determining the frequency drift of the crystal oscillator with temperature and time can be used as inputs to an algorithm to maintain the frequency to a limited extent.

Both the rubidium and the GPS clocks output a 10 MHz sine wave (which is a standardized reference signal) that is used for a frequency reference for the devices shown in Fig. 3.20. Each device has an internal crystal oscillator which can be locked to an external reference via a phase-locked loop, and each also outputs the signal from this internal oscillator to allow more devices to be locked in a daisy-chain configuration. The DPO7354 oscilloscope does not have a 10 MHz reference output and thus must be at the end of the chain. Some of these devices output a reference signal with significant harmonics of 10 MHz, which can affect the quality of the lock for the next device on the daisy chain. These devices were identified by looking at the signal output by each device on an oscilloscope, and filters were placed after these devices in order to remove the harmonics.

To ensure that the GPS clock has not lost satellite signal and drifted too far in frequency, two separate measurements comparing its frequency to that of the rubidium clock are used. Firstly, a frequency counter (TTi TF960) measures the frequency of the GPS clock using the rubidium clock as a reference. The frequency counter is run with a 100 s integration time which allows a 10 MHz signal to be determined to 2 mHz of precision, or 0.2 ppb. This value is recorded as an element of every data acquisition event in the experiment (every 1-10 seconds), and any data taken while the clocks disagree is excluded from our analysis. Typically the clocks show no disagreement at the millihertz level, though due to the position of the antenna the clock does sometimes

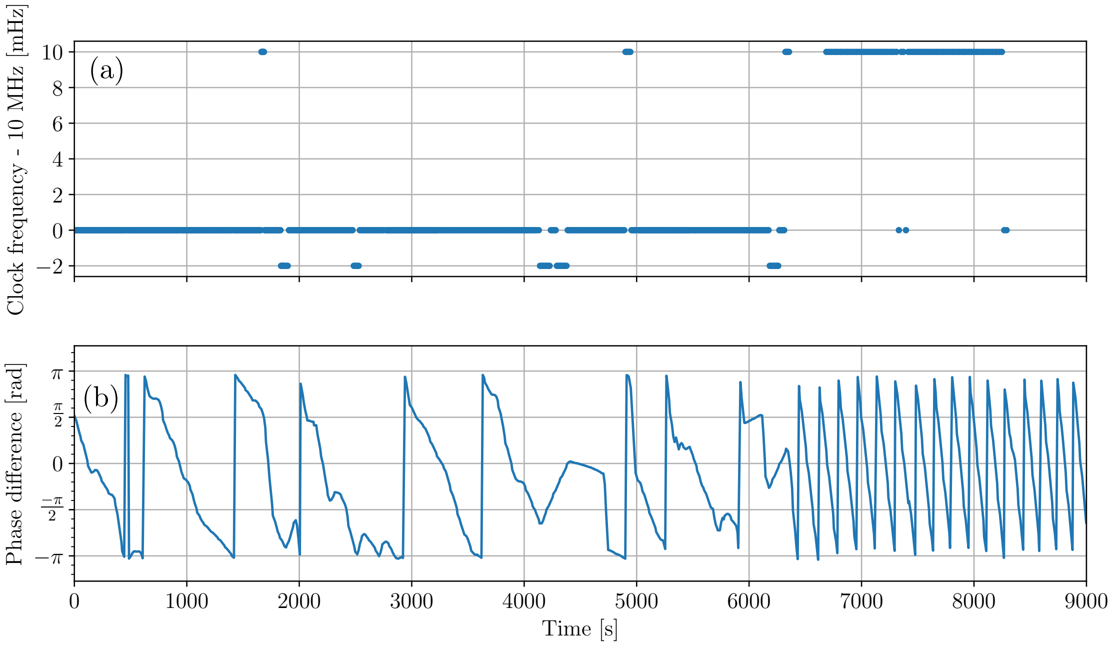

Figure 3.21: (a) A plot of frequency counter measurements recorded during a set of experiment runs. (b) A plot of the recorded phase difference between clock signals during approximately the same time period. At the beginning, the clocks are very close in frequency, taking hundreds of seconds to drift in phase by a full 2π period. Around $t = 6500\,\mathrm{s}$, however, the relative frequency of the clocks is seen to jump in both plots, shifting the measured frequency significantly on the frequency counter in (a) and causing the phase to advance much more rapidly in (b).

lose satellite signal for long enough to cause a measurable drift (see latter part of Fig. 3.21), making a small amount of collected data unusable.

The other clock monitoring system is an oscilloscope which acquires traces of each of the 10 MHz signals simultaneously approximately every 10 seconds. From these traces, the phase difference is extracted using an inner product method as described in Sec. 5.1.2 and saved alongside a timestamp. Because a small difference Δf in frequencies is equivalent to a phase advancing over time at a rate $\Delta\theta = 2\pi\Delta f t$, the frequency difference between the two clocks (as determined by measuring a phase

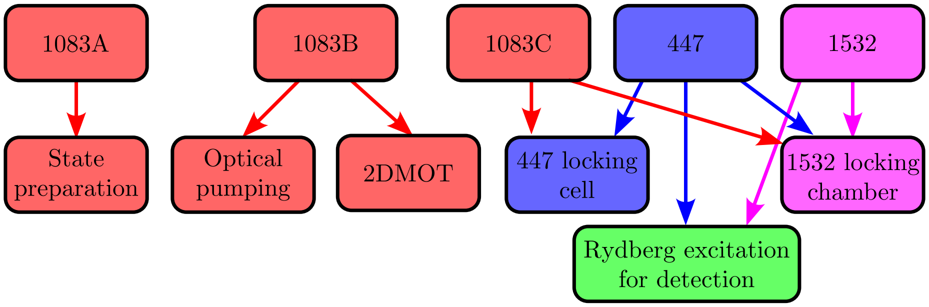

Figure 3.22: Diagram showing the five lasers used in the experiment (top row), and what each is used for.

difference $\Delta\theta$ at two points separated in time by Δt) is

$$\Delta f = \frac{\Delta\theta}{2\pi\Delta t}. \tag{3.9}$$

Due to the very high signal-to-noise ratio of this data, it is possible to determine frequency differences with much higher resolution than the frequency counter. This measurement does typically show a 1–2 mHz discrepancy (0.1–0.2 ppb) in regular operation, but this can be attributed to the aging of the rubidium clock: its frequency drift specification is 0.2 ppb/yr, and it is at least a decade old.

3.4 Laser Systems

As shown in Fig. 3.22, there are five lasers used in this experiment: three 1083 nm diode lasers tuned to each of the $2^3\mathrm{S}_1 \rightarrow 2^3\mathrm{P}_J$ transitions, a 447 nm diode laser tuned to the $2^3\mathrm{P}_0 \rightarrow 4^3\mathrm{D}_1$ transition, and a 1532 nm diode laser tuned to the $4^3\mathrm{D}_1 \rightarrow 18^3\mathrm{P}$ transition. For the most part, the laser systems are unchanged from the previous experiment and detailed descriptions can be found in Secs. 2.5 and 2.6 of [23]. However that experiment did not make use of the $2^3\mathrm{P}_0$ state, and so a third 1083 nm laser (1083C of Fig. 3.22) tuned to the $2^3\mathrm{S}_1 \rightarrow 2^3\mathrm{P}_0$ transition was added.

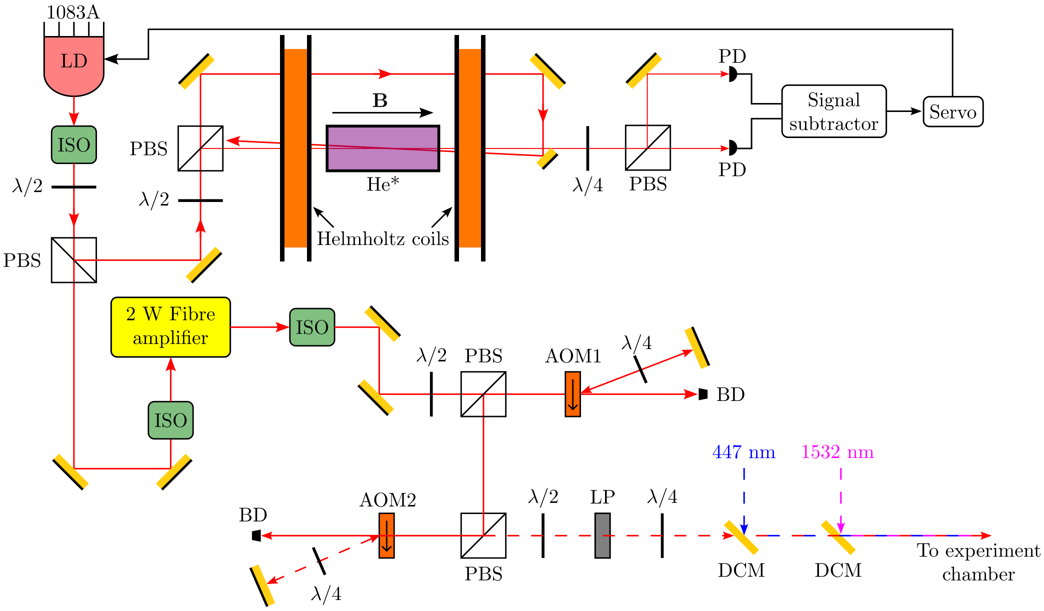

Figure 3.23: 1083A Laser system. LD = Laser diode, ISO = 30 dB isolator, λ/2 = half-wave plate, PBS = polarizing beamsplitter, PD = photodiode, He* = metastable helium discharge cell, DCM = dichroic mirror, AOM = acousto-optic modulator.

3.4.1 1083 nm Lasers

There are three 1083 nm lasers used in this experiment, referred to as 1083A, 1083B, and 1083C, which all use the same model of distributed Bragg reflector (DBR) laser diode (Photodigm PH1083DBR), driven by the same model of laser driver (Melles Griot 06DLD203A).

1083 nm Laser A

Laser 1083A provides the state-preparation pulse (labelled SP in Fig. 3.3 and 1083 in Fig. 3.4) which defines the start of an experiment sequence, exciting atoms from $2^3\mathrm{S}_1(m_J = \pm 1)$ to $2^3\mathrm{P}_1(m_J = 0)$ using light linearly polarized along the y axis that is travelling along the x axis (see Fig. 3.8 for definitions of the axes).

As shown in Fig. 3.23, the light is initially generated by a laser diode, after which part of the beam is split off by a polarizing beamsplitter (PBS) and sent to a sub-

Doppler dichroic atomic vapour laser locking (DAVLL) [26–28] setup. This setup consists of a standard saturated absorption spectroscopy setup with counterpropagating pump and probe beams to interrogate only the zero-velocity Doppler group. A magnetic field perpendicular to the polarization axis is applied via a pair of Helmholtz coils to separate the $\Delta m_J = +1$ and $\Delta m_J = -1$ transitions due to their linear Zeeman shifts. The light in the pump beam can be considered a linear combination of σ^+ and σ^- polarizations, which are split into different paths by a quarter wave plate followed by a PBS. One photodiode then receives the absorption signal from the $\Delta m_J = +1$ transition and the other from the $\Delta m_J = -1$ transition, and an error signal is generated by subtracting the signals from the two photodiodes. A 100 kHz-bandwidth analog PID (proportional, integral, and derivative) controller (SRS SIM960) then processes this error signal to produce a correction which is applied to the current modulation input of the diode laser controller.

The other branch of the diode's output is fed into a 2 W Keopsys fibre amplifier. The output of this amplifier passes through two dual-pass AOM (acousto-optic modulator) setups, the latter fed by a pulsed rf input. Each of these setups reverses the linear polarization of the beam via two passes through the quarter-wave plate, so that beams which were transmitted by a PBS before entering the AOM are instead reflected and vice versa. The CW AOM (AOM1) is aligned to the -1 order, shifting the frequency of the beam by a total of $-2f_{\mathrm{AOM1}}$ where f_{AOM1} is the rf driving frequency. The pulsing AOM (AOM2) is aligned to the $+1$ order and provides a shift of $+2f_{\mathrm{AOM2}}$, leading to no net shift if $f_{\mathrm{AOM1}} = f_{\mathrm{AOM2}}$. Because the DAVLL setup stabilizes the frequency of the laser to the $\Delta m_J = 0$ transition, f_{AOM1} and f_{AOM2} are offset slightly to account for the linear Zeeman shift corresponding to the magnetic field applied in the experiment chamber, where this laser drives $\Delta m_J = \pm 1$ transitions.

The pulsed beam leaves the second AOM setup and passes through a half-wave plate and linear polarizer. The linear polarizer aligns the polarization of the beam with the axis of the magnetic field in the experiment, and the half-wave plate before the polarizer allows the power which passes through the polarizer to be adjusted. A quarter-wave plate then follows to correct for dichroism of the further optical elements and windows between the linear polarizer and the point where the 1083A laser beam interacts with the atoms in the metastable helium beam. Two dichroic mirrors are used to spatially overlap the 1083A beam with the 447 nm and 1532 nm beams. The overlapped beams then pass through a series of lenses which focus the beams to a waist at the overlap point with the helium beam, and enter the experiment chamber through a vacuum window. After entering the vacuum chamber, the combined beams pass through the hole in the waveguide short to enter the waveguide, as shown in Fig. 3.8. Upon exiting the far end of the waveguide through the hole in the elbow, the beams are separated by another set of dichroic mirrors so that the pulse timings can be monitored on independent photodiodes, as shown in Fig. 3.12.

1083 nm Laser B

Laser 1083B, tuned to the 2^3S_1-to-2^3P_2 transition, provides light for the 2DMOT and optical pumping. As shown in Fig. 3.24, light from the diode is fed into a 15 W fibre amplifier (Nufern NuAmp NUA-1064-PB-0015-C2). Some of the light from the output of the amplifier is split off by a half-wave plate and PBS, then split into four beams (not shown) and sent to the 2DMOT (described in Sec. 3.2.2) via cylindrical lenses to expand the beams along one axis and quarter-wave plates to provide the appropriate circular polarizations.

The remainder of the beam is sent to reflect off another PBS, entering AOM1 where the first positive order is selected in a double-pass AOM configuration and then sent to AOM2, where the first negative order of the AOM is selected. The frequencies f_{AOM1}

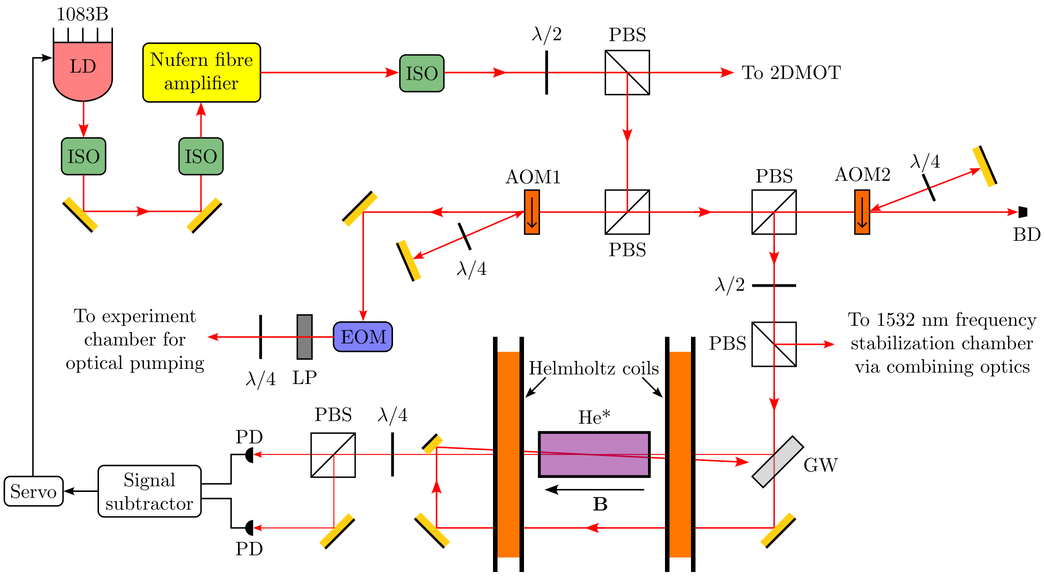

Figure 3.24: 1083B Laser system. LD = Laser diode, ISO = 30 dB isolator, λ/2 = half-wave plate, λ/4 = quarter-wave plate, PBS = polarizing beamsplitter, PD = photodiode, He* = metastable helium discharge cell, DCM = dichroic mirror, GW = glass wedge, AOM = acousto-optic modulator, EOM = electro-optic modulator.

and f_{AOM2} of these AOMs are offset such that the light reflected into the frequency stabilization arm is shifted in frequency 20 MHz above that which is emitted from the diode, which ensures that the light going to the 2DMOT is red-detuned by 20 MHz.

Because this laser is locked 20 MHz away from the central transition to provide red-detuned light for the 2DMOT, and two transitions (the two dashed lines in Fig. 3.7) must be driven to optically pump using $2^3\mathrm{P}_2$ ($2^3\mathrm{S}_1(m_J = \pm 1) \longleftrightarrow 2^3\mathrm{P}_2(m_J = \pm 2)$ is a cycling transition which does not contribute to optical pumping), two sidebands must be generated to excite the corresponding Zeeman-shifted transitions.

The light which passes through AOM1 without being deflected is sent through a fibre-coupled electro-optic modulator (EOM, EOSPACE PM-0K5-10-PFA-PFA-106). Sine waves at two rf frequencies are generated by an arbitrary waveform generator (AWG, Rigol 4162), the output of which is fed into an rf amplifier (Minicircuits ZHL-6A+) before being sent into the rf port of the EOM. This combination of rf

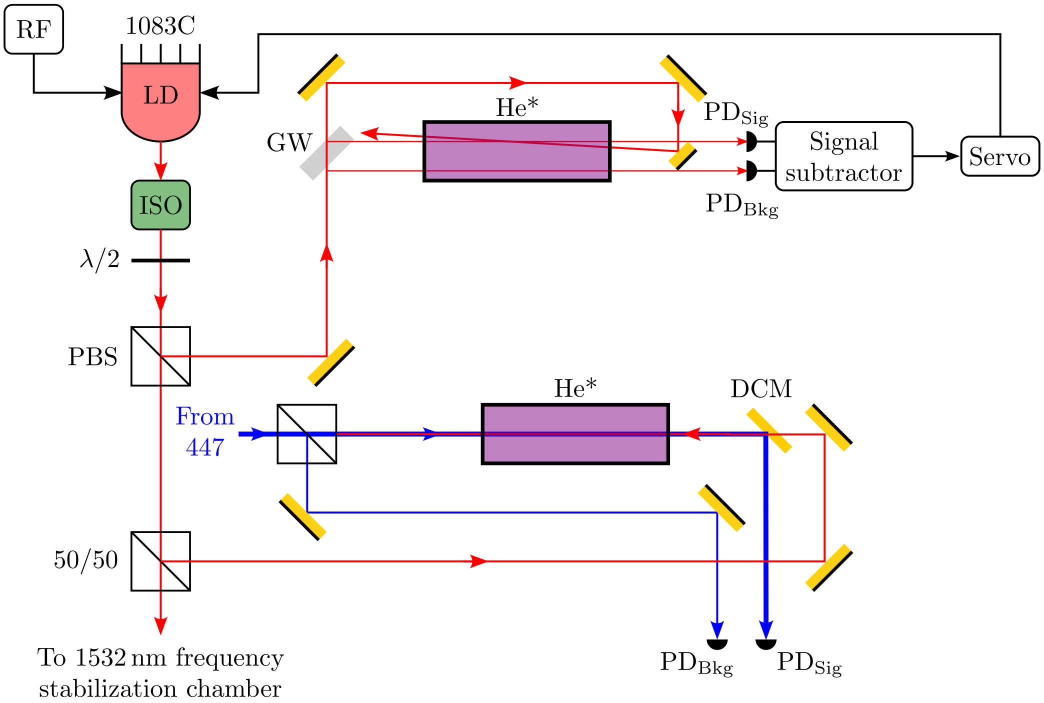

Figure 3.25: 1083C Laser system. LD = Laser diode, ISO = 30 dB isolator, $\lambda/2$ = half-wave plate, $\lambda/4$ = quarter-wave plate, PBS = polarizing beamsplitter, 50/50 = 50/50 beamsplitter, PD = photodiode, He* = metastable helium discharge cell, DCM = dichroic mirror, GW = glass wedge.

frequencies in the EOM generates sidebands on the laser beam at the appropriate frequencies to drive the transitions shown in Fig. 3.7, which are adjusted according to the applied magnetic field and optical pumping direction (into $2^3S_1(m_J = +1)$ or $2^3S_1(m_J = -1)$) to account for the Zeeman shifts.

1083 nm Laser C

1083C is a laser which has been added since the previous experiment, and excites atoms from 2^3S_1 to 2^3P_0 in order to provide locking signals for the detection lasers: for the 447 nm laser in a gas-filled discharge cell, and for the 1532 nm laser in the second ionization detector (see Fig. 3.25).

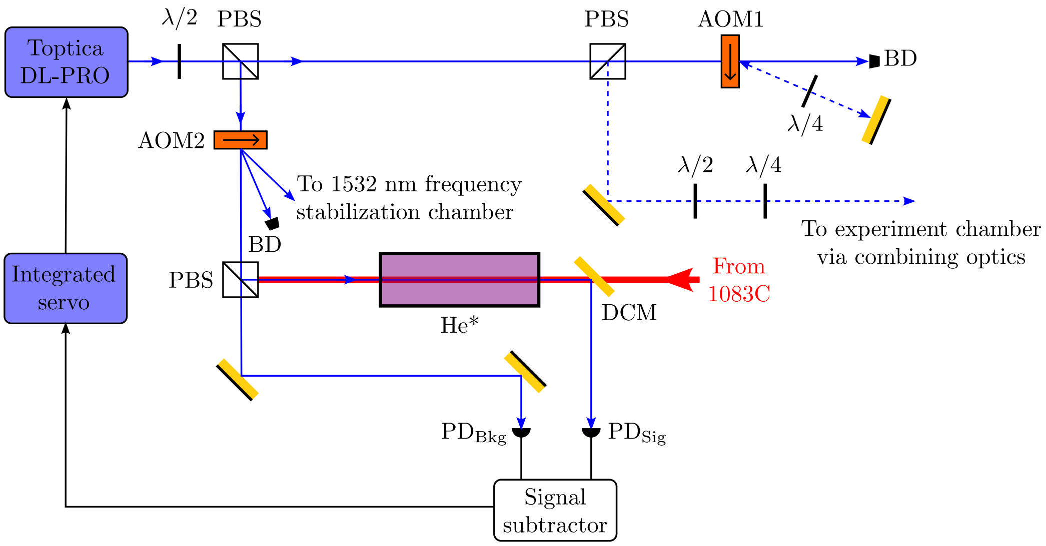

Figure 3.26: 447 nm Laser system. LD = Laser diode, ISO = 30 dB isolator, $\lambda/2$ = half-wave plate, $\lambda/4$ = quarter-wave plate, PBS = polarizing beamsplitter, 50/50 = 50/50 beamsplitter, PD = photodiode, He* = metastable helium discharge cell, DCM = dichroic mirror, GW = glass wedge.

3.4.2 Detection Lasers

There are two lasers required to excite the atoms into the Rydberg detection state after the atoms undergo a microwave transition. A 447 nm laser first excites atoms from $2^3\mathrm{P}_0$ to $4^3\mathrm{D}_1$, and then a 1532 nm laser excites the atoms from $4^3\mathrm{D}_1$ to the $18^3\mathrm{P}$ Rydberg state. After this final excitation the Rydberg helium atoms exit the waveguide and are ionized by the high-voltage wire grid.

447 nm Laser

The 447 nm laser is used to excite atoms from $2^3\mathrm{P}_0$ to $4^3\mathrm{D}_1$ in both the main experiment chamber and the 1532 nm frequency stabilization chamber. As shown in Fig. 3.26, the light from a Topica DL-PRO external cavity diode laser (ECDL) is split into two paths by a PBS, with the transmitted part travelling through another PBS and into a pulsed AOM in a double-pass retroreflecting configuration, AOM1. The two AOM passes shift the frequency of the light by $+2f_{\mathrm{AOM1}}$. The light shifted by the AOM has its linear polarization rotated 90° by two passes through the quarter-wave plate, and is now reflected from the PBS it was previously transmitted through. A combination of half- and quarter-wave plates are then used to adjust the polarization of this pulsed beam which is sent to the experiment chamber via the combining optics shown in Fig. 3.23.

The light which was reflected from the first PBS passes through a CW AOM, AOM2, and the second order (shifted by $+2f_{\mathrm{AOM2}}$) is selected to be directed to the 1532 nm frequency stabilization chamber via a separate set of combining optics, shown in Fig. 3.27. The light which is not deflected by AOM2 continues to a saturated absorption spectroscopy frequency stabilization setup, where the pump beam is supplied by the 1083 nm laser C.

Because the 447 nm laser path sent to the experiment is pulsed using a double-pass AOM at 200 MHz, it acquires a shift of 400 MHz relative to the locking cell. This shift is compensated for by applying 165 MHz sidebands to 1083C, and locking the 447 nm laser to the population excited by one of these sidebands. The sidebands are created by injecting 165 MHz rf into the laser diode drive current via a bias tee (Minicircuits ZFBT-4R2G-FT+). This sideband of the 1083 nm laser addresses atoms in a certain velocity group within the broad (approximately 1.7 GHz) Doppler width of the $2^3\mathrm{S}_1$-to-$2^3\mathrm{P}_0$ transition, and a 165 MHz shift at 1083 nm corresponds to a $165\,\mathrm{MHz} \times \frac{1083\,\mathrm{nm}}{447\,\mathrm{nm}} = 400\,\mathrm{MHz}$ shift in at 447 nm(as the frequency of the Doppler shift is inversely proportional to wavelength). Because the beams are counter-propagating the atoms have opposite velocities relative to the direction of propagation of the two lasers so the two shifts have opposite signs, which can be accounted for by selecting the correct sideband (-165 MHz rather than 165 MHz).

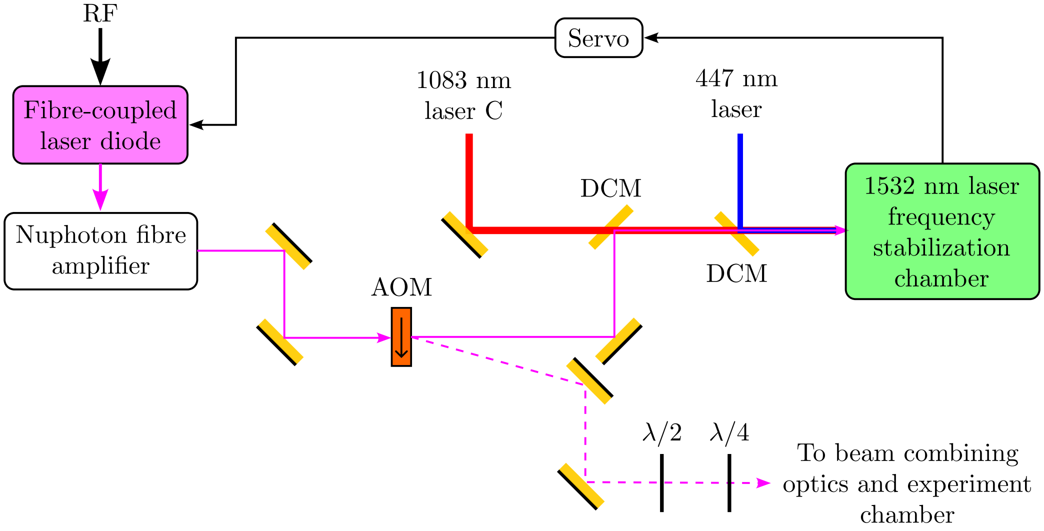

Figure 3.27: 1532 nm Laser system. LD = Laser diode, ISO = 30 dB isolator, λ/2 = half-wave plate, λ/4 = quarter-wave plate, PBS = polarizing beamsplitter, 50/50 = 50/50 beamsplitter, PD = photodiode, He* = metastable helium discharge cell, DCM = dichroic mirror, GW = glass wedge.

1532 nm Laser

The 1532 nm laser is used to provide the final excitation to drive the helium atoms to the 18^3P Rydberg state, as shown in Fig. 3.4 and Fig. 3.3. The layout of the 1532 nm laser system is shown in Fig. 3.27. Light is initially produced in a fibre-coupled DFB (Distributed Feedback) laser (Alcatel A1905LMI), which is sent directly to the input of a 27 dBm amplifier (Nuphoton EDFA-CW-1532-PM-SMR-27-17-FCA). The output of this amplifier is coupled to free space where it enters an AOM which is powered by a pulsed 200 MHz rf signal in order to create the 1532 nm laser pulses of Fig. 3.4. The pulsed first order output of this AOM is sent through a HWP and QWP to control its polarization, and then through the dichroic mirrors which spatially overlap it with the 1083A state-preparation beam and the 447 nm laser beam.

The undiffracted output of the AOM is sent to another set of combining optics, where it is combined with a beam from laser 1083C and another from the 447 nm laser (which are labelled "To 1532 nm frequency stabilization chamber" in Fig. 3.25 and Fig. 3.26). This combined CW beam is sent to the frequency stabilization chamber shown in Fig. 3.2, where it interacts with the He* beam inside a Stark ionizer similar to the one shown in Fig. 3.9. The helium atoms are excited from 2^3S_1 to 2^3P_0 by 1083C, then from 2^3P_0 to 4^3D_1 by the 447 nm laser, and finally to 18^3P by the 1532 nm laser, after which the atoms are Stark ionized and detected by the CEM within the ionizer. This signal is then used to stabilize the frequency of the 1532 nm laser via current feedback with a PID controller.

Because the 1532 nm beam sent to the experiment chamber is shifted 200 MHz by the AOM relative to the undiffracted beam which goes to the frequency stabilization chamber, sidebands are generated on the output of the laser diode by injecting 200 MHz rf power into its drive current with a bias tee. The 1532 nm laser is then stabilized such that the higher-frequency sideband is on resonance with the atomic transition in the frequency-stabilization chamber, making the centre frequency of the laser below the atomic resonance, so that the frequency shift from the AOM places the centre frequency of the laser back on resonance in the pulsed beam which travels to the experiment chamber.

3.5 Data Analysis

The raw data from the experiment is recorded as a pair of simultaneous digitizer traces (a very small section of each is shown in Fig. 3.28), one of the reference signal (which is created by beating the two microwave frequencies as described in Sec. 3.3.2) and one of the atomic FOSOF signal (as described in Sec. 3.2.6). The relative phase of these two signals is the primary measured quantity used for a FOSOF measurement. The traces are all recorded at a sample rate of 10 kHz, with the duration of each trace

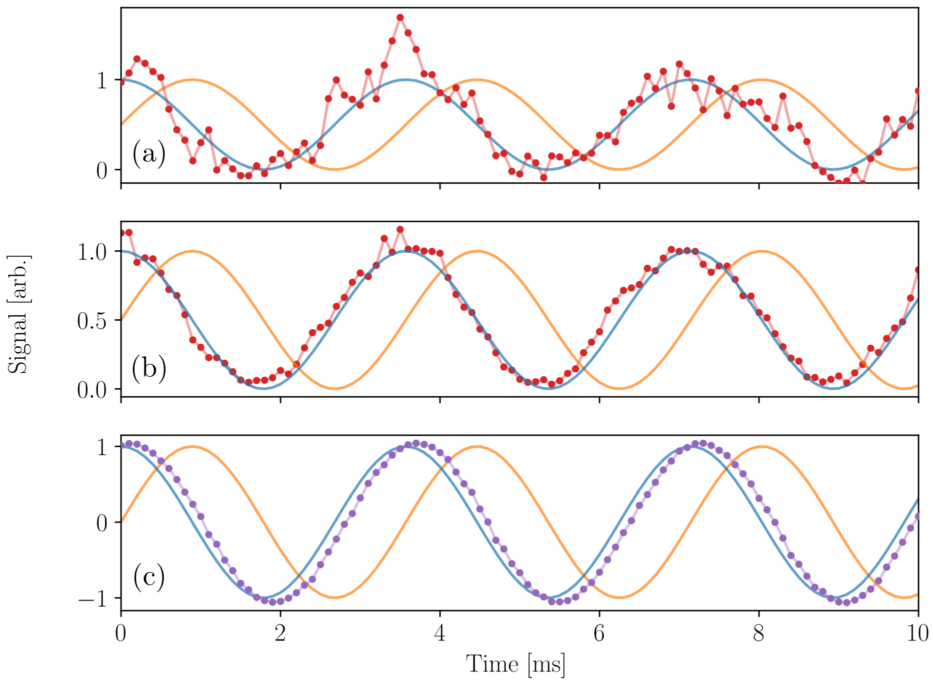

Figure 3.28: Signals used to determine phase in a $T = 300, D = 150, P = 100\%$ experiment. (a) shows the raw atomic data from a digitizer trace in red. (b) shows the same as (a) but with each point being the average of ten points at the equivalent time in subsequent periods. The 10 ms trace of averaged points represents the same amount of data as one green dot in Fig. 3.29. (c) shows the measured FOSOF reference signal in purple. The blue and orange curves in each plot are unit cosines and sines used to calculate inner products for phase determination. Only the first 10 ms of a 5 s trace is shown.

ranging from 1 to 20 seconds (longer traces are required when the SNR of the data is low). For analysis, these traces are split into smaller segments, with each segment covering an integer multiple of the period of the offset frequency. This process is carried out for multiple segment lengths, which are defined by dividing the trace into 5, 10, and 50 segments.

For each segment, using sines and cosines at the offset frequency as shown in Fig.

3.28, the discrete inner products

$$X = \sum_{i=1}^{N} S_i \cos(2\pi f_{\mathrm{ofs}} t_i), \tag{3.10}$$

$$Y = \sum_{i=1}^{N} S_i \sin(2\pi f_{\mathrm{ofs}} t_i) \tag{3.11}$$

are calculated to find the in-phase and quadrature components X and Y, where the S_i are the sampled signal voltages, t_i are the sample times, and N is the number of samples. From X and Y the amplitude A and phase ϕ can be determined:

$$A = \frac{2}{N}\sqrt{X^2 + Y^2}, \tag{3.12}$$

$$\phi = \mathrm{arctan2}(Y, X), \tag{3.13}$$

where arctan2 returns the angle from the positive x axis to the vector (X, Y) in the range $(-\pi, \pi]$. This process is carried out for both signal trace $\mathbf{V}_{\mathrm{S}}$ and reference trace $\mathbf{V}_{\mathrm{R}}$, and the FOSOF phase (corresponding to Eqn. (2.18)) is given by

$$\Delta\theta_{\mathrm{FOSOF}} = \phi_{\mathrm{S}} - \phi_{\mathrm{R}}. \tag{3.14}$$

This process gives results which are independent of the trigger time of the digitizer.

For each microwave frequency used during a scan over microwave frequencies (which constitutes one run of the experiment), the two pulse order configurations (A and B, described in Sec. 2.1.2) are recorded in succession, with the order randomly chosen for each frequency (and the order of frequencies randomized for each run). The phase used for further analysis is the averaged difference between the phases obtained

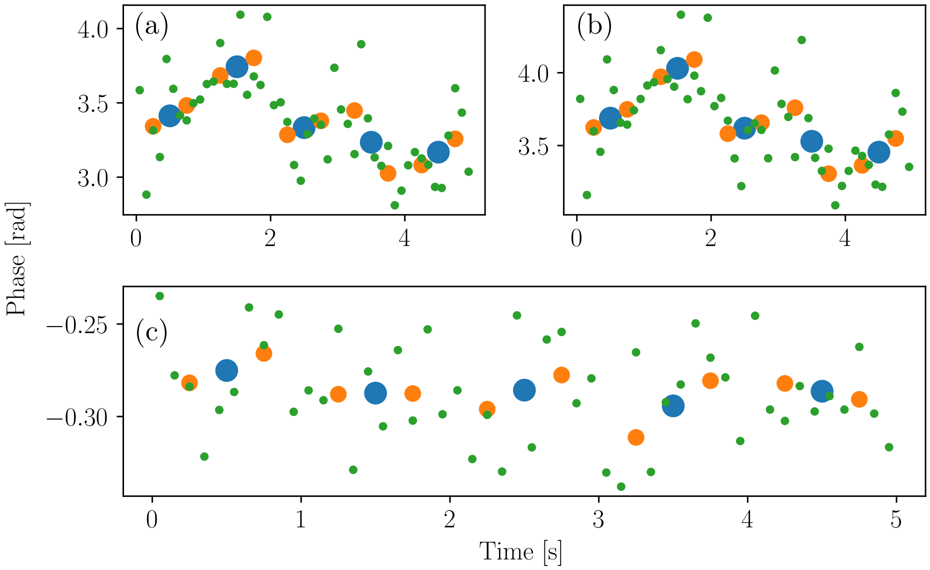

Figure 3.29: Phases determined from the traces which are partially shown in Fig. 3.28. (a) Shows the results ϕ_{S} from the atomic trace, (b) shows ϕ_{R} from the reference trace, and (c) is the phase difference between atomic signal and reference $\Delta\theta_{\mathrm{FOSOF}} = \phi_{\mathrm{S}} - \phi_{\mathrm{R}}$. Green points are the result of splitting the traces into 0.1 s segments, orange 0.5 s, and blue 1 s. Areas of the dots are proportional to the time which they represent.

with the two experiment configurations,

$$\overline{\Delta\Theta} = (\theta_A - \theta_B)/2. \tag{3.15}$$

The uncertainty in $\overline{\Delta\Theta}$ is then taken to be the standard error in the mean of the phases calculated from the segments of the trace, which are shown in Fig. 3.29(c).

The phases $\overline{\Delta\Theta}$ of Eqn. (3.15) are then unwrapped from the $(-\pi, \pi]$ range returned by the arctan2 function to the continuous, approximately linearly increasing value expected from Eqn. (2.27) (the results of the process are shown in Fig. 3.30(a-b), with a detailed description given in Sec. 2.13 of [23]). A cut is applied to the data at this point, where any frequency for which the range of $\overline{\Delta\Theta}$ determinations from different segments exceeds a threshold of 0.85 rad is discarded, to reduce to a negligible level the possibility that any point is assigned to the wrong multiple of 2π in the phase

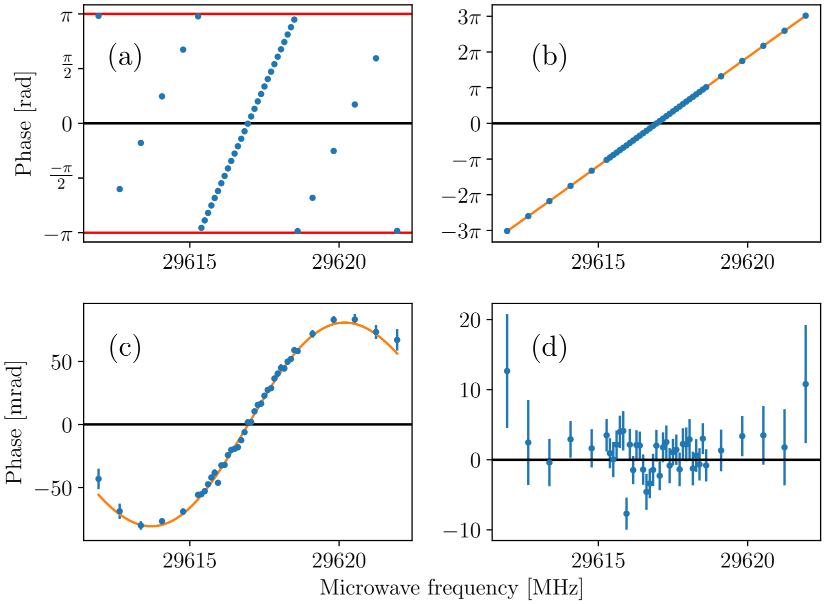

Figure 3.30: An illustration of the phase stitching and curve fitting procedure with data from a $T = 300\,\mathrm{ns}, D = 150\,\mathrm{ns}$ experiment. (a) $\overline{\Delta\Theta}$ data before phase stitching, showing discontinuities at phase values of $\pm\pi$. (b) The approximately linear FOSOF lineshape (Eqn. (2.27)) which is recovered when the appropriate multiple of 2π is added to each point. Error bars are smaller than the data points at this scale. (c) The lineshape from (b) with the TDPT approximation $\overline{\Delta\Theta} = T\Delta\omega$ subtracted. (d) The residuals of the fit shown in (b).

unwrapping process. Each run is then fit to Eqn. (2.27) (as shown in Fig. 3.30(b-d)), with the phase $\overline{\Delta\Theta}$ for each frequency weighted according to its uncertainty, in order to extract a linecentre from the fit parameters. If the fitting routine fails to converge (usually because too many frequencies have been discarded due to low SNR resulting in an uncertainty of greater than the 0.85 rad threshold), the procedure is repeated with the trace divided into longer segments so that the phases uncertainty is decreased and data points taken at fewer frequencies are discarded. The mean of the reduced chi square values for the individual fits to each run of the data taken for this dissertation is 1.05, indicating that the phase errors are not significantly over- or under-estimated.

The results of these fits are then collated in a summary table along with numerous other parameters relating to possible systematic effects, allowing easy plotting of the measured linecentre as a function of those parameters in order to look for unanticipated shifts due to systematic effects as described in Chapter 4. When performing the fits, a blind offset (a single randomly generated number between $-4\,\text{kHz}$ and $4\,\text{kHz}$) is added to every frequency to shift the linecentre determined from the fit by the blind offset. The purpose of this blind offset is to remove any bias towards making the result of the current measurement agree with previously measured values of the same interval. The blind offset will only be revealed and removed from the measured value after all systematic effects have been investigated and accounted for.

4 Systematic Effects and Preliminary Results

4.1 Summary of Systematic Effects

In order to test for systematic effects in this experiment, a large number of parameters were varied, and their effects on the measured linecentres were investigated. The results for the main parameters which have been investigated are listed in Table 4.1 and shown in Fig. 4.1. A table listing the results for each set of experiment parameter values, totalling 904 different configurations, is provided in Appendix A. Those parameters which are known to shift the measured linecentre must be determined to sufficient precision so that their effect can be corrected for at a level below the overall precision of the measurement. Other parameters which are not known to directly shift the linecentre but could feasibly do so were tested over as wide a range of parameters as was feasible in order to verify that any potential shift related to these parameters is smaller than the precision of this measurement.

To test for all possible systematic effects, each time a trace is recorded from the experiment, a large set of parameters (such as ambient temperature, measured microwave power, source discharge current, etc.) are recorded and stored for later

Experimental Parameter	Parameter Value	$\Delta\nu$ [Hz]	Section
Magnetic Field Direction	$+\hat{z}$	-8(11)	Sec. 4.4
	$-\hat{z}$	9(11)	
Magnetic Field Magnitude [G]	$\|B\| < 5$	-1(9)	
	$5 \leq \|B\| \leq 10$	22(17)	
	$\|B\| > 10$	-10(35)	
Microwave Timing (T, D) [ns]	(300, 50)	-11(25)	Sec. 4.15.3
	(300, 100)	-9(10)	
	(300, 150)	-14(25)	
	(400, 50)	37(42)	
	(400, 100)	5(16)	
	(400, 150)	70(27)	
	(400, 200)	16(21)	
	(500, 100)	15(24)	
	(500, 200)	20(55)	
	(600, 100)	-14(73)	
Microwave Separation T [ns]	300	-8(10)	
	400	16(14)	
	500	13(23)	
Microwave Duration D [ns]	50	-5(23)	
	100	-3(9)	
	150	22(21)	
	200	13(21)	
Optical Pumping m_J State	-1	-1(11)	Sec. 4.6
	1	1(11)	
Offset Frequency [Hz]	-280	-4(11)	Sec. 4.12
	+280	3(10)	
Analysis Frequency Range	$\|f - f_0\| < 3/(4D)$	3(9)	Sec. 4.15
	$\|f - f_0\| < 1/(2D)$	—	
	$\|f - f_0\| < 1/(4D)$	3(10)	
	$\|f - f_0\| < 1/(8D)$	112(12)	
Decreased Laser Powers	25% 1083 nm	-11(20)	Sec. 4.7
	25% 447 nm	22(22)	
Rydberg Detection State	18^3F	21(16)	Sec. 4.9
Microwave Transition Direction	$2^3\mathrm{P}_0$ to $2^3\mathrm{P}_1$	-31(18)	Sec. 4.10

Table 4.1: Results for different parameters in the experiment. $\Delta\nu = \nu - \nu_{\mathrm{Ref}}$ is the difference from the linecentre determined when including all data within the $|f - f_0| < 1/(2D)$ frequency range.

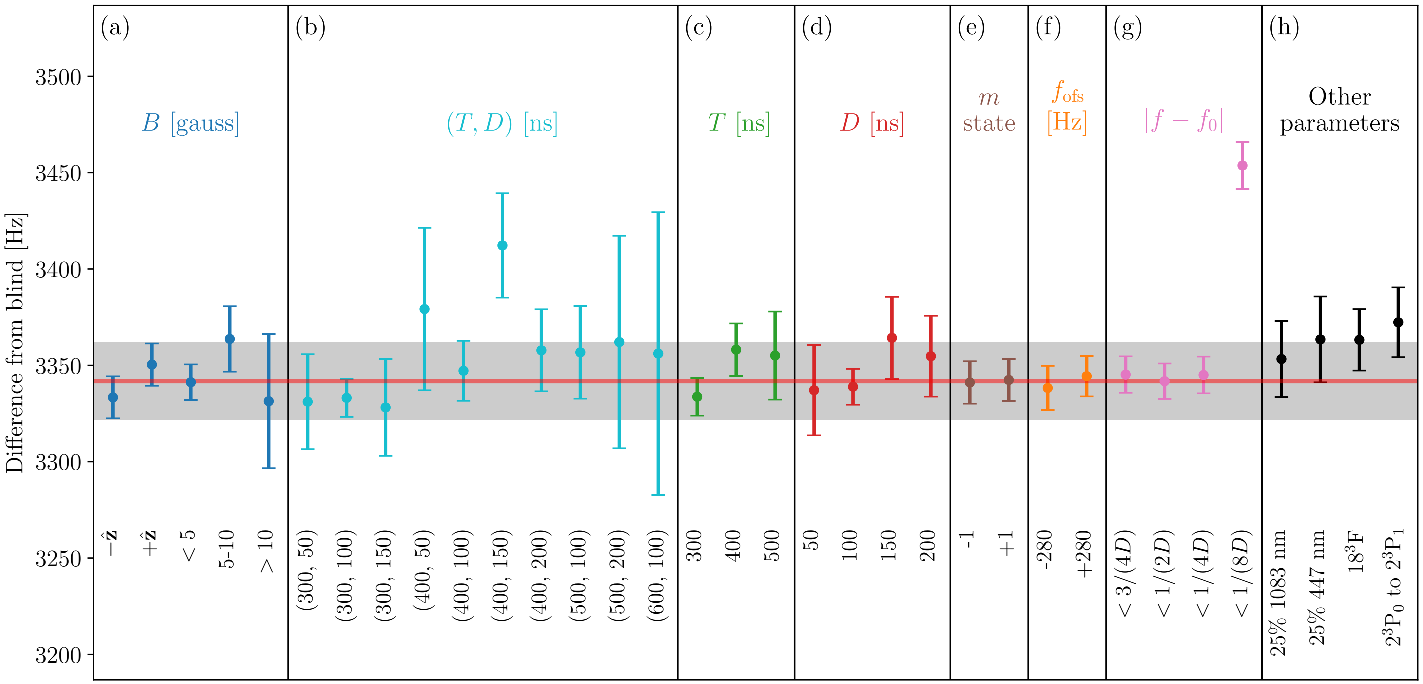

Figure 4.1: Summary plot of results from this measurement. (a) shows linecentres measured for different magnetic field parameters. (b)-(d) show the results of different microwave pulse timing parameters. (e) shows the two optical pumping directions. (f) shows positive and negative offset frequencies. (g) shows the results of restricting the analysis to different frequency ranges around f_0. (h) shows low laser powers, Rydberg detection state, and microwave transition directions. The grey band covers ±20 Hz, corresponding to the uncertainty goal for this measurement.

analysis. When analyzing the data these logs can then be used to check for systematic effects by plotting the linecentres as a function of the parameter in question, and seeing whether there is any relationship between them.

In this measurement, many systematic effects have been tested for and confirmed to be controlled to a level sufficient for a measurement at a precision of 20 Hz. However, one systematic effect remains as a major concern. When the data is reanalyzed by excluding data taken at frequencies further than $1/(8D)$ from the centre of the transition, Fig. 4.1(g) shows that the linecentre shifts by approximately 100 Hz for the centres obtained with analyses using wider frequency ranges. Investigations into the cause of this shift are described in Sec. 4.15, though the cause of this discrepancy was not resolved during the course of the research for this dissertation.

4.2 Power Shifts and Extrapolation

In this FOSOF measurement there is a large class of systematic shifts that are approximately proportional to microwave power and thus extrapolate to zero shift at zero power. These shifts include the ac Stark shift and ac Zeeman shift caused by the oscillating microwave electric and magnetic fields, as well as shifts caused by a wide range of possible imperfections in the microwave pulses. Numerical simulations were performed to verify that the pulse imperfections cause shifts which are linear in microwave power and extrapolate to zero shift at zero power, and are described in Sec. 5.2.

Because the line shifts are expected to be proportional to microwave power, all results in the experiment are determined by extrapolating the linecentre to zero power. In both experiment and simulation it is found that the shifts are proportional to P/T, which can be used as the extrapolation parameter. Extrapolating against P/T

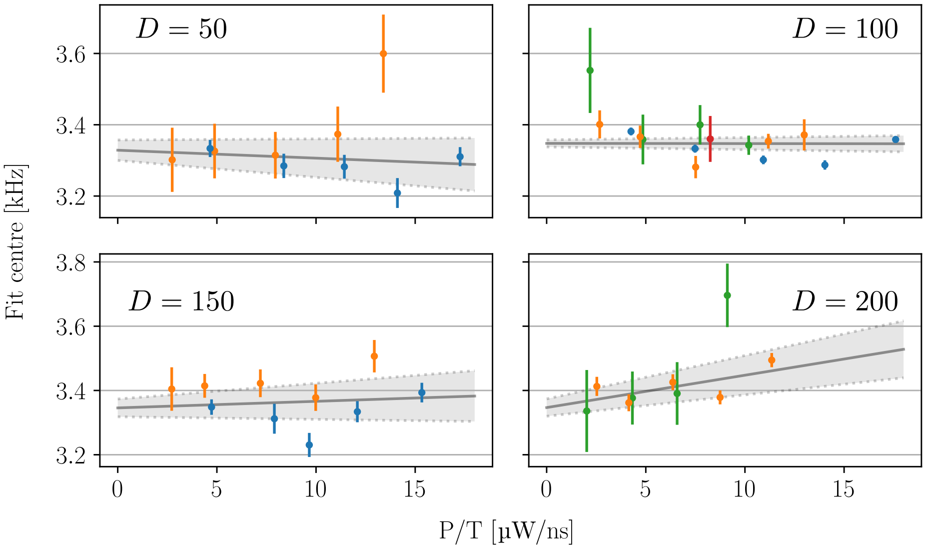

Figure 4.2: Power extrapolations for the data of all T values at a given D value combined. In all plots, blue is $T = 300$ data, orange is $T = 400$, green is $T = 500$ and red is $T = 600$. The shaded areas show the uncertainty in the linear fit for each D.

allows all data for a given value of D to be analyzed together, which enhances the determination of the extrapolation slope and thus decreases the overall uncertainty of the measurement. The final analysis to determine the linecentre consists of finding the P/T extrapolation slope for each D value, using this slope to correct the linecentres obtained in each data run, and then taking a weighted average of these centres. The table of data in Appendix A shows the results of the extrapolation correction process for each configuration of experiment parameters. When restricting the data to isolate a given parameter as in Table 4.1 and Fig. 4.1, the correction to remove the power shift is calculated by performing the extrapolation including all data, and only restricting the data to that taken with a particular parameter value when taking the weighted average.

In the previous 2^3P_2-to-2^3P_1 experiment [20], the analysis was performed with a varying cutoff of the saturation parameter PD^2 in order to verify that the data included in the analysis was far enough below saturation intensity and pulse length for the linear extrapolation to hold. In the current experiment much less power reaches the atoms (1 W vs. 75 W, see Sec. 3.3.1), so that even the highest combinations of P and D used are still far from saturating the microwave transition and so it is not necessary to apply this cut.

4.3 Microwave Power Imperfections

In a typical spectroscopy experiment, it is essential to ensure that the power driving the measured transition does not change as the frequency is varied, because power varying with frequency can skew the lineshape and shift the measured centre of the line. In a FOSOF experiment, the sensitivity to this effect is decreased because the phase of the atomic response is measured, rather than the amplitude. The main effect of non-constant power over frequency is to change the slope of the power extrapolation, so it is still important to minimize the power variation versus frequency (power flatness) as much as possible, especially so that there is not a significantly different power flatness at different nominal power settings. The results of the simulations in Sec. 5.2.1 show that it takes a significantly larger error in power flatness at different powers than is present here to skew the linecentre (when extrapolated to zero power) from the true centre frequency.

It is also important to have equal power in the microwave pulses which originate from each generator (i.e. equal amplitudes of the two pulses shown in Fig. 2.1), and to have accurately determined relative power levels (e.g. 20%, 40%, 60%, 80% and 100% of the maximum power which can be obtained from the amplifier) to record data at, so that the extrapolation of linecentres to zero power described in Sec. 4.2

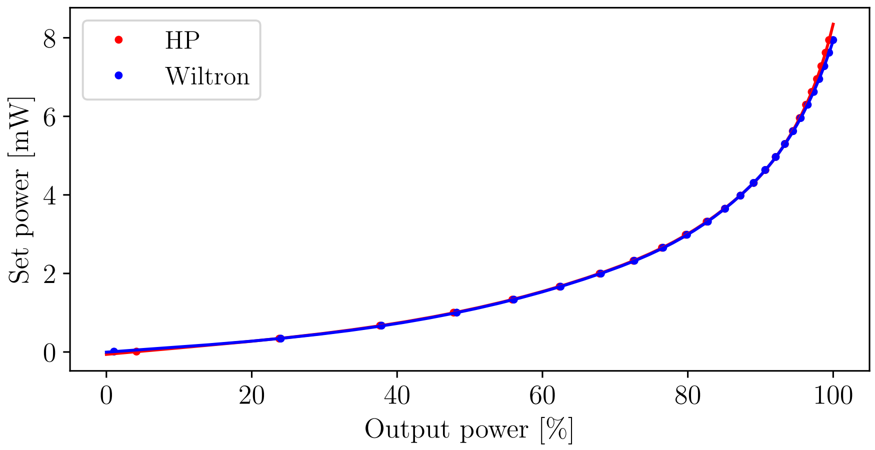

Figure 4.3: Power calibration curves as recorded at the end of the microwave system (by the diode with output labelled ‘To data logger’ in Fig. 3.12), with interpolating splines. The slope increases to the right as the amplifier nears saturation. This plot gives the required generator power setting as a function of the desired output power.

can be performed.

4.3.1 Microwave Power Calibration

Because every microwave component has frequency-dependent transmission and reflection properties, a calibration must be performed to determine what power to set on each microwave generator in order to obtain approximately flat power across the range of frequencies used in the experiment and equal power in the pulses from the two generators at each frequency. To obtain a set of accurate relative powers, the reduction of the microwave amplifier’s gain as it approaches its saturation power limit must be accounted for.

To achieve these goals (flat power across the microwave frequency range used in the experiment, a set of well-calibrated relative power levels, and equal power in both pulses), first the power for each generator is separately scanned over its range of power settings at the centre frequency, with the output power measured on the diode at the

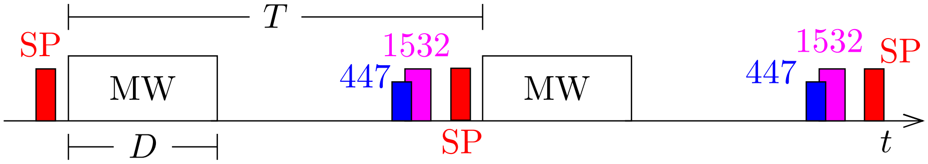

Figure 4.4: Timing diagram for the pulse sequence used in testing power flatness with atomic data. MW = microwaves, SP = state-preparation pulse, 447 = 447 nm laser, 1532 = 1532 nm laser.

end of the experiment's microwave chain (the diode with output labelled 'To data logger' in Fig. 3.12). The results of this measurement are shown in Fig. 4.3. Then, for each power setting from 20% to 100% (in 20% increments), the power is measured for a range of frequencies covering the span which will be used in the measurement. Based on these measurements, the set powers for each frequency are adjusted by the amount which will give flat power according to the calibration curve from Fig. 4.3. A spline which interpolates across frequencies is then saved for each power level with these flattened power settings.

This procedure is imperfect as the saturation curve varies slightly with frequency, but the process can be repeated iteratively to increase the precision. Typically two iterations are sufficient to reach the 0.01 dBm resolution to which both generators are limited.

4.3.2 Verification of Power Flatness From Atomic Signal

Because the power measured at the diode may not exactly correspond to the power seen by the atoms (due to losses and reflections in the microwave system between these two locations), an experiment was performed to verify the power flatness using the transition strength of $\Delta m_J = \pm 1$ microwave transitions. The experiment was carried out by switching off the main experiment solenoid (Main Helmholtz coils in Fig. 3.10) and instead running large currents through the external background-cancelling coils

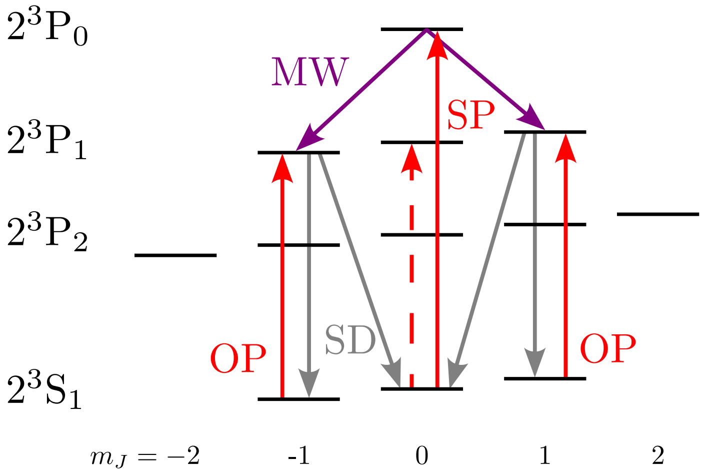

Figure 4.5: Transitions used in experiment to measure power flatness from the atomic signal. OP = optical pumping, SD = spontaneous decay, SP = state-preparation laser, MW = microwaves. Dashed arrow represents forbidden transition. Atoms will accumulate in the $2^3S_1(m_J = 0)$ state while exposed to only the optical pumping laser, as there are decay paths into this state but no excitation paths out of it. During the experiment the population in 2^3P_0 is recorded with the usual detection scheme of Fig. 3.3 while the frequency of microwaves depopulating it is scanned through the two Zeeman-shifted transitions shown.

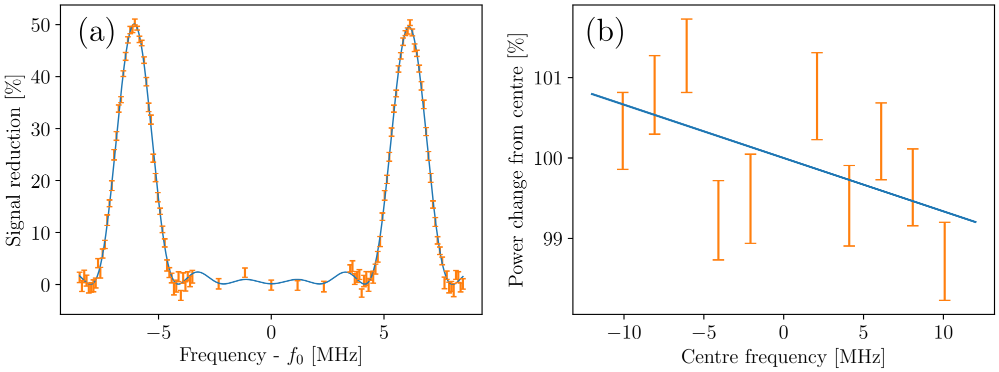

Figure 4.6: (a) A scan through microwave frequencies at a dc magnetic field of 2.857 G, with 500 ns microwave pulses separated by 3 µs. The overlaid fit is a sum of two sinc^2 functions. The scale on the y axis is percentage of atomic signal depleted by turning microwave pulses on. Each point is the average of 20 repeats, error bars are standard error of the mean. (b) Power determinations at a range of B fields, which cause different Zeeman shifts of the peaks shown in (a). The linear fit shown gives a slope of $-0.066(23)$ %/MHz.

in order to generate magnetic fields in the $\hat{\mathbf{x}}$ or $\hat{\mathbf{y}}$ direction, so that the microwaves in the waveguide (which are always polarized along $\hat{\mathbf{z}}$) are now polarized perpendicular to the magnetic field and can thus drive $\Delta m_J = \pm 1$ transitions.

Applying the magnetic field along another axis also changes the transitions which are driven by the lasers. The optical pumping beam (sent in along the z axis from above) has its polarization changed to linearly polarized parallel to the dc magnetic field along the x or y axis (as defined in Fig. 3.8) to drive $\Delta m_J = 0$ transitions (as shown in Fig. 4.5). This laser is tuned to excite atoms into $2^3\mathrm{P}_1$, as doing so allows for optically pumping atoms into $2^3\mathrm{S}_1(m_J = 0)$. This optical pumping scheme works because transitions where both $\Delta J = 0$ and $m_J = 0 \to 0$ are forbidden, and so $2^3\mathrm{S}_1(m_J = 0)$ is a dark state to this laser configuration, as can be seen in Fig. 4.5. Because it is a dark state, atoms can radiatively decay to it but cannot be excited out of it, and eventually almost all of the atoms will end up in $2^3\mathrm{S}_1(m_J = 0)$.

After this optical pumping scheme, a pulse from the state-preparation laser (SP in Fig. 4.4) drives the $2^3\mathrm{S}_1(m_J = 0)$-to-$2^3\mathrm{P}_0(m_J = 0)$ transition, and then a pulse from one of the microwave generators drives some of the population out of $2^3\mathrm{P}_0$. The $\Delta m_J = \pm 1$ transitions are shifted from the centre frequency by $\mp(2.101\,\mathrm{MHz/G})|\mathbf{B}|$, and so scanning across microwave frequencies shows two peaks, which shift with the applied field (as shown in Fig. 4.6(a)). Because the height of these peaks is proportional to the microwave power in the pulse, their heights can be used to measure how different the power is at the two resonant frequencies. Because the detection laser transitions are all from $2^3\mathrm{P}_0$, there is no concern of different matrix elements for the detection lasers biasing the results as there would be if the populations in $2^3\mathrm{P}_1(m_J = \pm 1)$ were measured directly. There is however a small difference in magnetic dipole matrix elements M between the two Zeeman-shifted transitions, with the ratio of their squares given by [29]

$$\frac{M(2^3\mathrm{P}_0(m_J=0)\leftrightarrow 2^3\mathrm{P}_1(m_J=-1))^2}{M(2^3\mathrm{P}_0(m_J=0)\leftrightarrow 2^3\mathrm{P}_1(m_J=+1))^2}=1+\frac{6\mu_\mathrm{B}B_x}{h\Delta f_{10}}, \tag{4.1}$$

where μ_B is the Bohr magneton, h is Planck's constant, B_x is the dc magnetic field strength in the $\hat{\mathbf{x}}$ direction, and Δf_{10} is the frequency difference between the $2^3\mathrm{P}_1$ and $2^3\mathrm{P}_0$ states. The effect of the different matrix elements is corrected for by dividing the height of the $2^3\mathrm{P}_0(m_J=0)\rightarrow 2^3\mathrm{P}_1(m_J=-1)$ peak by the ratio of the squared matrix elements.

To carry out this experiment, a long microwave pulse ($D=500\,\mathrm{ns}$) is used in order to give a large signal, and a large separation between pulses ($T=3\,\mu\mathrm{s}$) ensures that atoms which are exposed to multiple microwave pulses do not contribute significantly to the signal. In order to account for drifts in signal intensity, the signal size was recorded with microwaves on and then immediately after with microwaves off, and the depopulation given by the ratio between the microwave on and microwave off signal sizes. Using this ratio accounts for any slow drifts in signal size, as well as controlling for the reduced CEM efficiency at larger magnetic fields. This process was repeated 20 times for each frequency (of Fig. 4.6), with the order of frequencies randomized between each repeat. A function of the form

$$S(f)=A_1\,\mathrm{sinc}^2\left(\frac{f-f_1}{w}\right)+A_2\,\mathrm{sinc}^2\left(\frac{f-f_2}{w}\right) \tag{4.2}$$

is fit to the data, where A_i, f_i, and w are fit parameters.

Similar measurements are performed for a range of magnetic field values. The results of these measurements are shown in Fig. 4.6(b), demonstrating that the power seen by the atoms varies at a rate of less than 0.1 %/MHz at the 1σ level.

4.4 Magnetic Fields in the Experiment

In Sec. 3.2.7, the three pairs of coils used to cancel out the background dc magnetic field are described, as well as the Helmholtz coils used to generate the dc bias field for the experiment. The current sources for all of these coil pairs are calibrated in order to ensure that the only magnetic field component in the small volume ($<1\,\mathrm{mm}^3$) in which atoms are exposed to microwave pulses is in the $\hat{\mathbf{z}}$ direction, and that the value of this component is precisely known in order to correct for the Zeeman shift due to this field.

4.4.1 Zeeman Shifts

When a helium atom is exposed to a dc magnetic field, the orbital and spin angular momenta of the electrons create magnetic dipole moments which can raise or lower the energy of atomic states, lifting the degeneracy of the m_J sublevels.

In a magnetic field, the potential energy of a magnetic dipole is given by

$$U = -\mu \cdot \mathbf{B}, \tag{4.3}$$

with the additional quadratic part of the interaction being negligible at the small fields used for this measurement. The total dipole moment of a helium atom is given by a combination of a part due to the orbital angular momentum of the electrons,

$$\mu_{\mathrm{orbital}} = \frac{-g_L \mu_B}{\hbar} \hat{L}, \tag{4.4}$$

(where the Bohr magneton $\mu_B = \frac{e\hbar}{2m_e}$) and a part due to the intrinsic spin of the electrons

$$\mu_{\text{spin}} = -g_s \mu_B \frac{\hat{S}}{\hbar}. \tag{4.5}$$

Thus the energy shift due to the external magnetic field contributes a magnetic term to the Hamiltonian

$$\hat{H}_B = \frac{\mu_B}{\hbar} \left(g_L \hat{L} + g_S \hat{S} \right). \tag{4.6}$$

In the low-field regime, this energy is small compared to the energy splitting between the states, and so the shifts can be accurately calculated with perturbation theory. For the $2^3\mathrm{P}_1(m_J = 0)$-to-$2^3\mathrm{P}_0(m_J = 0)$ transition being studied, both states have zero linear shift rate because the diagonal matrix elements of $\vec{\mu} \cdot \vec{B}$ are zero, but there is still a small quadratic shift of $197.741\,\mathrm{Hz/G}^2$[30] from second-order perturbations.

4.4.2 Magnetic Field Coil Calibration

The initial calibration of all coils was done with a three-axis gaussmeter as described in Sec. 2.10 of [23]. This calibration is imperfect because the probe cannot be placed exactly where the atomic microwave transition occurs. However, the scheme used to measure the microwave power flatness in Sec. 4.3.1 can also be used to calibrate the $\hat{\mathbf{x}}$ and $\hat{\mathbf{y}}$ magnetic field coils by measuring the linear Zeeman shift of the $\Delta m_J = \pm 1$ microwave transitions and performing an extrapolation to the applied current value which results in zero Zeeman shift for each particular set of coils. Fig. 4.7(a) shows the separation between the two peaks (see Fig. 4.6(a)) versus current through the x axis background field-cancelling coil pair. The current required to cancel the background magnetic field component along the x axis is found at the x intercept of the linear fit (where the peak separation is zero), shown at a magnified scale in Fig. 4.7(b). This is

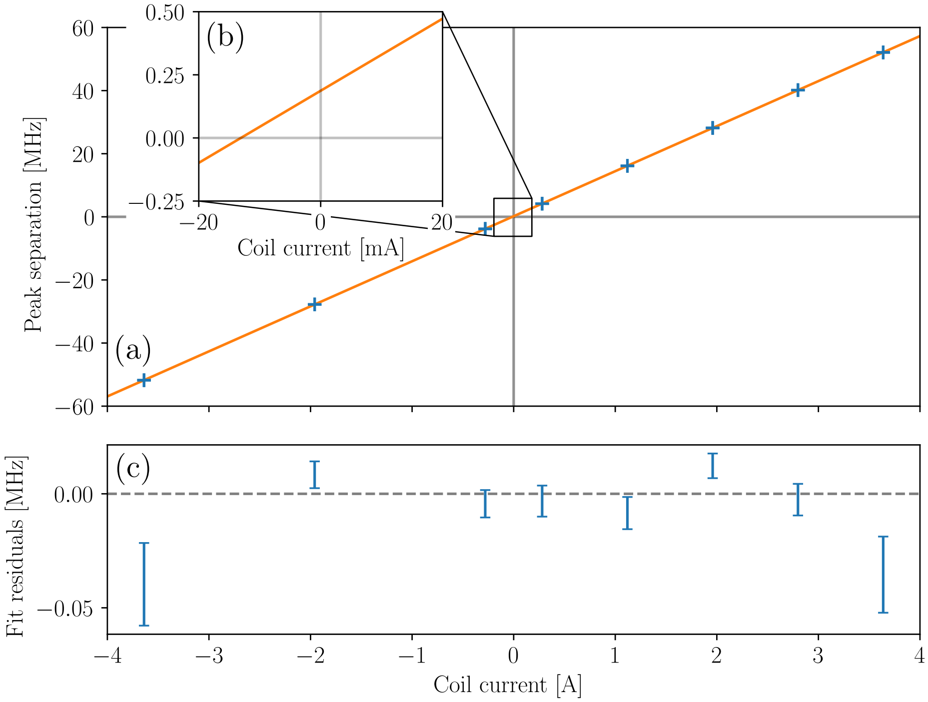

Figure 4.7: (a): Atomic calibration data for x axis background field cancelling coil, showing frequency separation between the $\Delta m_J = \pm 1$ transitions as a function of applied current. The inset (b) shows the x intercept of a straight line fit. The residuals of the fit are shown in (c).

the current which the coils are set to during the main experiment in order to cancel out the components of the background magnetic field at the point where the helium atoms interact with the microwaves.

The calibration of the y-axis cancelling coil uses the exact scheme shown in Fig. 4.5. For the x-axis cancelling coil, however, the state-preparation laser cannot drive $\Delta m_J = 0$ transitions as it travels along the same axis to which the magnetic field is now aligned. To drive these transitions, the fibre which carries the optical pumping beam from the EOM is moved from above the experiment (allowing the optical pumping beam to travel along $\hat{\mathbf{z}}$) to beside it (allowing the optical pumping beam to travel along $\hat{\mathbf{x}}$), so that the same optical pumping and state-preparation scheme as the regular experiment (Fig. 3.3) can be used (σ^+ or σ^- optical pumping beam along the bias field axis, state-preparation laser on $\Delta m_J = \pm 1$).

The results of this procedure for x and y axes are given in Table 4.2, with the field zeroed to better than 1 mG. These uncertainties are on the same scale as the individual components of earth's magnetic field vary over a year [31].

For the $\hat{\mathbf{z}}$ cancelling coils a similar procedure driving the $\Delta m_J = \pm 1$ transitions with the microwaves cannot be used, as the coils are aligned with the waveguide's polarization axis and so only the $\Delta m_J = 0$ transition can be driven. However, using the 197.741 kHz/G^2 quadratic Zeeman shift of the $2^3\mathrm{P}_0(m_J = 0) \rightarrow 2^3\mathrm{P}_1(m_J = 0)$ transition, FOSOF data taken with a range of bias fields applied by the cancelling coils (instead of the main solenoid) can be used to find the current which cancels out the background field component in the $\hat{\mathbf{z}}$ direction. This is accomplished by fitting a quadratic function to the recorded linecentres versus cancelling coil current, and setting the current to the value at the turning point of the quadratic fit. With eight hours of FOSOF data, this component was zeroed to a precision of 10 mG. This precision is limited by the smaller shift rate compared to the linear case for x and y axes (resulting in a shift approximately one thousand times smaller at the maximum ∼12 G which each pair of cancelling coils can apply).

Similarly, FOSOF data taken during regular experiment runs can be used to calibrate the current-to-field factor for the main experiment solenoid, giving $k = 10.859(10)$ G/A, which can then be used to correct for the quadratic Zeeman shift at any applied B field using the current value recorded on the shunt resistor.

Due to the possibility of the atomic microwave excitations occurring at slightly different positions depending on laser alignment (and thus different fields), a 0.1 % uncertainty is assigned to the Zeeman shift correction, as was done for the $2^3\mathrm{P}_2$-to-$2^3\mathrm{P}_1$ measurement (as described in detail in Sec. 4.1.2 of [23]).

The consistency between data taken at <5 G and that taken at high magnetic

Coil Axis	Zero-Field Current [mA]	Current-to-Field Factor [mG/A]	Uncertainty in Zeroed Field [mG]
$\hat{\mathbf{x}}$	13.67(13)	3396.91(24)	0.44
$\hat{\mathbf{y}}$	67.77(19)	3189.60(42)	0.61
$\hat{\mathbf{z}}$	142.3(32)	3050.3(54)	9.8

Table 4.2: Currents required to cancel background field components as determined from fits of atomic data such as that shown in Fig. 4.7.

fields as shown in Fig. 4.1 and Table 4.1 shows that the Zeeman shift is well-controlled at the 20 Hz level.

4.5 Calculation of Linecentres

To generate the final stage of results which are presented in Figs. 4.1 and 4.19 and Table 4.1 while incorporating the error due to the Zeeman shift uncertainty (Sec. 4.4) and the uncertainty due to the power extrapolation described in Sec. 4.2, a weighted average of the linecentres is taken after they are corrected for both the Zeeman shift and the power extrapolation. The weights for this weighted average are found by first grouping each set of experimental runs with the same $T, D, P, |B|, m_J,$ and f_{ofs} values, assigning a weight to each of these categories, and performing an optimization routine to find the set of weights which minimizes the total uncertainty (including the uncorrelated statistical uncertainties and the correlated Zeeman and extrapolation uncertainties) of the weighted average. The set of all combinations of experiment parameters and their associated data is listed in Appendix A, along with the corresponding uncertainties and weights determined from this process which are used to calculate the weighted average linecentre.

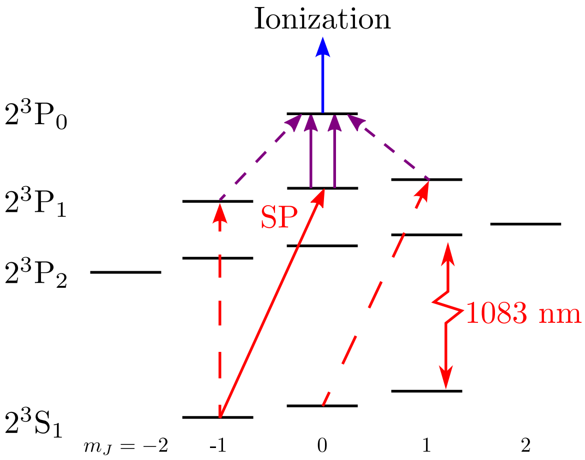

Figure 4.8: Level diagram showing possible unwanted transitions with dashed arrows. Red = state-preparation laser (SP), purple = microwaves, blue = detection lasers.

4.6 Imperfect Laser Polarization and Optical Pumping

A potential systematic effect can be caused by a combination of imperfect optical pumping, imperfect polarization of the state-preparation laser, and imperfect alignment of the microwave waveguide with the dc magnetic field. Ideally, the experiment sequence starts with all of the atoms in $2^3S_1(m_J = -1)$ (or $2^3S_1(m_J = 1)$). The state-preparation laser, which is polarized along the y axis and travels along the x axis (see Fig. 3.8 for definition of axes), can then only drive the $\Delta m_J = +1$ transition to $2^3P_1(m_J = 0)$. However, as shown in Fig. 4.8, if there is any population left over in $2^3S_1(m_J = 0)$, this laser can drive that population into $2^3P_1(m_J = +1)$ as it has a not too dissimilar Zeeman shift compared to that of the intended transition. Even if the optical pumping is perfect, a component of the state-preparation laser polarization along $\hat{\mathbf{z}}$ will allow it to drive the $\Delta m_J = 0$ transition from $2^3S_1(m_J = -1)$ to $2^3P_1(m_J = -1)$. This $\Delta m_J = 0$ transition probability is magnified if the state-preparation transition is driven beyond saturation, as the population transfer due to the unintended $\Delta m_J = 0$ transitions will continue to grow while the main transition does not due to saturation. Because of this effect, the power and duration of the state-preparation laser pulse are carefully adjusted to slightly below its saturation level.

If any population ends up in $2^3\mathrm{P}_1(m_J = \pm 1)$ through these paths, it might be driven into the detection state $2^3\mathrm{P}_0$ via close-to-resonance $\Delta m_J = \pm 1$ transitions from the microwave pulses, which have a linear Zeeman shift of 2.101 MHz/G. These Δm_J transitions could only be driven if the waveguide is not perfectly aligned with the magnetic field-generating solenoid, so that there is some component of the microwave polarization along $\hat{\mathbf{y}}$. This combination of imperfections would result in quantum interference between the intended and unintended microwave transitions, which would shift the measured linecentre, especially at low dc magnetic fields, as is simulated in Sec. 5.2.4.

4.6.1 Calibrating State-Preparation Laser Polarization

The optical-pumping configuration and an experiment scheme similar to that described in Sec. 4.3.2 can be used to calibrate the polarization of the state-preparation laser. This laser drives atoms from $2^3\mathrm{S}_1$ to $2^3\mathrm{P}_1$, travels in the $\hat{\mathbf{x}}$ direction and should be linearly polarized along $\hat{\mathbf{y}}$ so that it drives only $\Delta m_J = \pm 1$ transitions and not $\Delta m_J = 0$ transitions. The calibration scheme is realized by optically pumping into $2^3\mathrm{S}_1(m_J = 0)$ and tuning the state-preparation and detection lasers to transitions to and from $2^3\mathrm{P}_0$, respectively, as shown in Fig. 4.9(a). As the state-preparation laser frequency is varied with a large (∼30 G) magnetic field applied to separate the transitions by their Zeeman shifts, the orientations of the linear polarizer and quarter-wave plate (QWP, to compensate for vacuum viewport birefringence) of Fig.

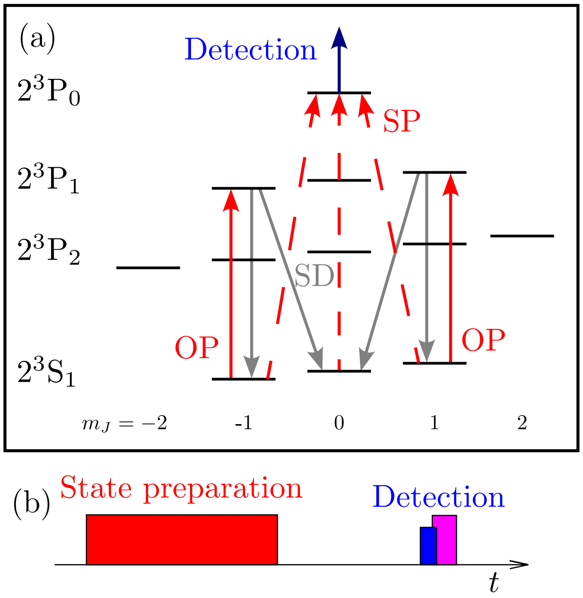

Figure 4.9: Scheme used to calibrate state-preparation laser polarization. (a) Levels and transitions used in the experiment. Dashed lines indicate transitions which should not be driven in the ideal case: the $\Delta m_J = 0$ transition because the polarization of SP should not allow it, and the $\Delta m_J = \pm 1$ transitions because there should be no population in the $2^3S_1(m_J = \pm 1)$ states. SP = state-preparation laser, OP = optical pumping, SD = spontaneous decay. (b) Timing of laser pulses used in the experiment.

3.23 are adjusted to minimize the signal due to $\Delta m_J = 0$ transitions originating from $2^3S_1(m_J = 0)$. Minimizing this signal ensures that the state-preparation laser is polarized along the y axis, perpendicular to the magnetic field along the z axis.

To carry out this calibration a very long state-preparation pulse (200 ns) is used, as shown in Fig. 4.9(b), in order to oversaturate the transitions and enhance the visibility of the signal from the unintended polarization component. A large ∼30 G dc magnetic field is also applied to separate the $\Delta m_J = \pm 1$ transitions by their linear Zeeman shifts of ±2.101 MHz/G relative to the $\Delta m_J = 0$ transition. It is also necessary to use the 1083 nm laser B tuned to the $2^3S_1 \rightarrow 2^3P_1$ transition to optically pump, as laser A must be tuned to the $2^3S_1 \rightarrow 2^3P_0$ transition for the state-preparation pulse and laser C must also be tuned to that transition to act as the laser stabilization reference for the 1532 nm laser. Tuning laser B to $2^3S_1 \rightarrow 2^3P_1$ rather than its usual

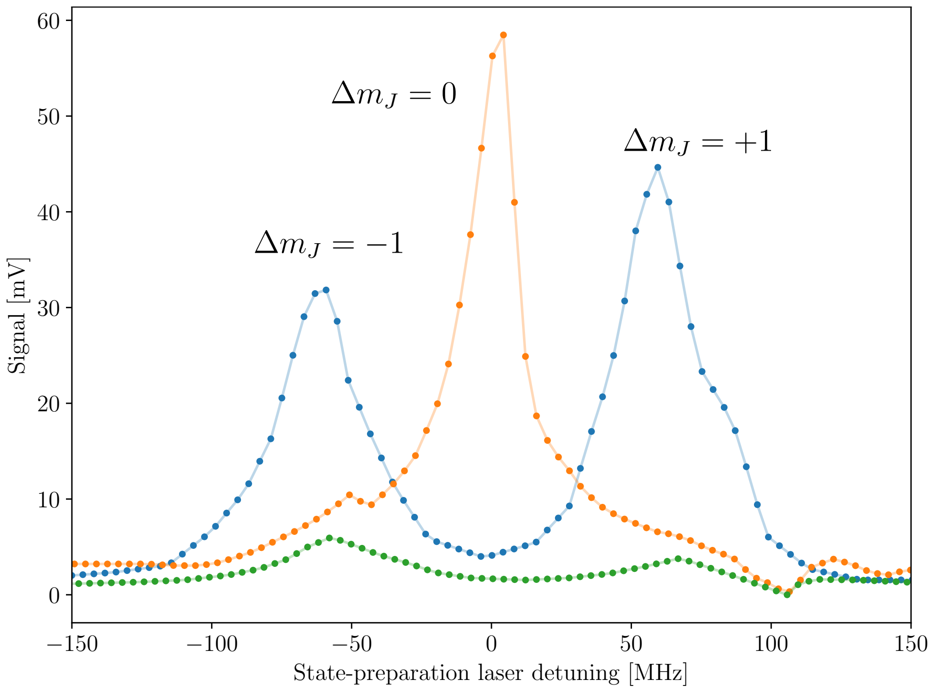

Figure 4.10: Atomic signals recorded as the frequency of the state-preparation (SP) laser was scanned during the calibration of its polarization. The blue data was recorded with approximately the correct SP polarization (which suppresses the $\Delta m_J = 0$ transition) but no optical pumping. The orange data was recorded with optical pumping on, but the SP polarization intentionally misaligned by 10°. The green data was recorded with optical pumping on after setting the calibrated SP polarizer and QWP angles.

$2^3\mathrm{S}_1 \rightarrow 2^3\mathrm{P}_2$ reduces the effectiveness of the 2DMOT, decreasing the signal by a factor of approximately three. Effective optical pumping is required in this scheme must be effective because, if it is poor, there will be a significant population remaining in the $2^3\mathrm{S}_1(m_J = \pm 1)$ states. Any population in these states will be driven efficiently to $2^3\mathrm{P}_0$, as these are allowed transitions when the polarization is set correctly, resulting in large Zeeman-shifted peaks which partially overlap with and obscure the $\Delta m_J = 0$ peak which is being minimized by tuning the polarization. Using this procedure, the results of Fig. 4.10 were obtained, showing very effective suppression of this unintended transition.

Evidence that the effect of unintended transitions due to imperfect polarization is negligible is provided by the consistency of linecentres measured at different dc magnetic fields (discussed in Sec. 4.4), because the shift in linecentre is strongly dependent on this field, as will be shown in Fig. 5.5. The consistency of linecentres determined from experiments performed with the microwave transition driven from $2^3\mathrm{P}_0$ to $2^3\mathrm{P}_1$ discussed in Sec. 4.10 is also evidence that this imperfect polarization effect is well-controlled, as these experiments should be much less sensitive to this effect. It would also be expected that decreasing the state-preparation laser power as described in Sec. 4.7 would decrease the size of this imperfect polarization effect. The shifts from the polarization effect would be lessened because the intended transition ($2^3\mathrm{S}_1(m_J = \pm 1)$ to $2^3\mathrm{P}_1(m_J = 0)$) is close to saturation at the usual operating state-preparation laser power and pulse duration but the unintended transitions ($2^3\mathrm{S}_1(m_J = \pm 1)$ to $2^3\mathrm{P}_1(m_J = \pm 1)$) are far from saturation, and so the intended transition will decrease in strength less than the unintended transitions when reducing laser power. No such shift is seen as the laser power is lowered, as also seen in Table 4.1. We conclude from all of these tests that no significant systematic effects are present due to unintended transitions being driven.

4.7 AC Shifts due to Laser Fields

The presence of laser light can shift the resonant frequency of a transition via the ac Stark shift. In this experiment, due to the laser and microwave pulse timing shown in Fig. 3.4, the atoms are never exposed to lasers during the microwave FOSOF sequence, and so there should be no effect of laser-induced shifts on the linecentre of the microwave transition. However, it was found that placing the laser pulses too close in time to the microwave pulses (as viewed on the oscilloscope shown in Fig. 3.12) resulted in a significant shift in the measured linecentre. After shifting the laser pulses

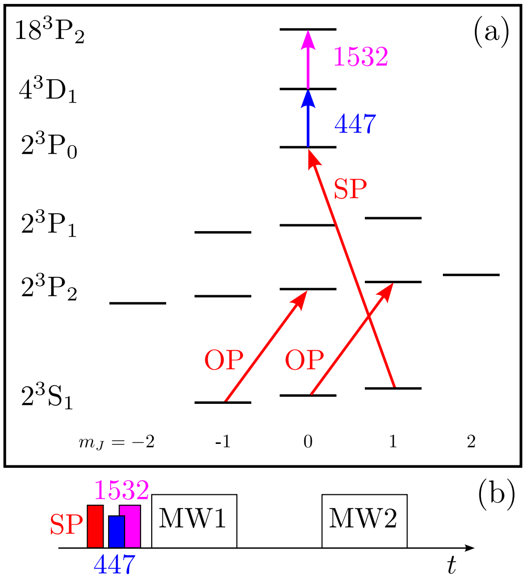

Figure 4.11: (a) The level scheme used for Rydberg quenching tests. Atoms are optically pumped (OP) into $2^3S_1(m_J = \pm 1)$, and then driven directly to 2^3P_0 by the state-preparation laser (SP), after which they are driven to the $n = 18$ Rydberg state. (b) The timing sequence used in Rydberg quenching experiments. Atoms are only exposed to microwaves after being excited to the Rydberg state.

to be at least 25 ns away from the microwave pulses, linecentre shifts consistent with zero were seen when taking data with the 1083 nm or 447 nm laser power reduced to 25% of their regular power, as shown in Table 4.1 and Fig. 4.1 (which are derived from the results labelled L447P and LSPP in the table of Appendix A). Assuming that the shift due to laser fields is proportional to the laser power, the shift at 100 % 1083 nm laser power is 29(29) Hz, and −15(27) Hz for 100 % 447 nm laser power. These results show that there are no laser field-induced AC shifts at the 30 Hz level of precision.

4.8 Rydberg State Quenching by Microwaves

When exposed to ac electric fields, the population of Rydberg atoms can be depleted by ac Stark ionization and off-resonance transitions. If the microwave pulses cause a significant depopulation due to this effect, it could result in a spurious signal component

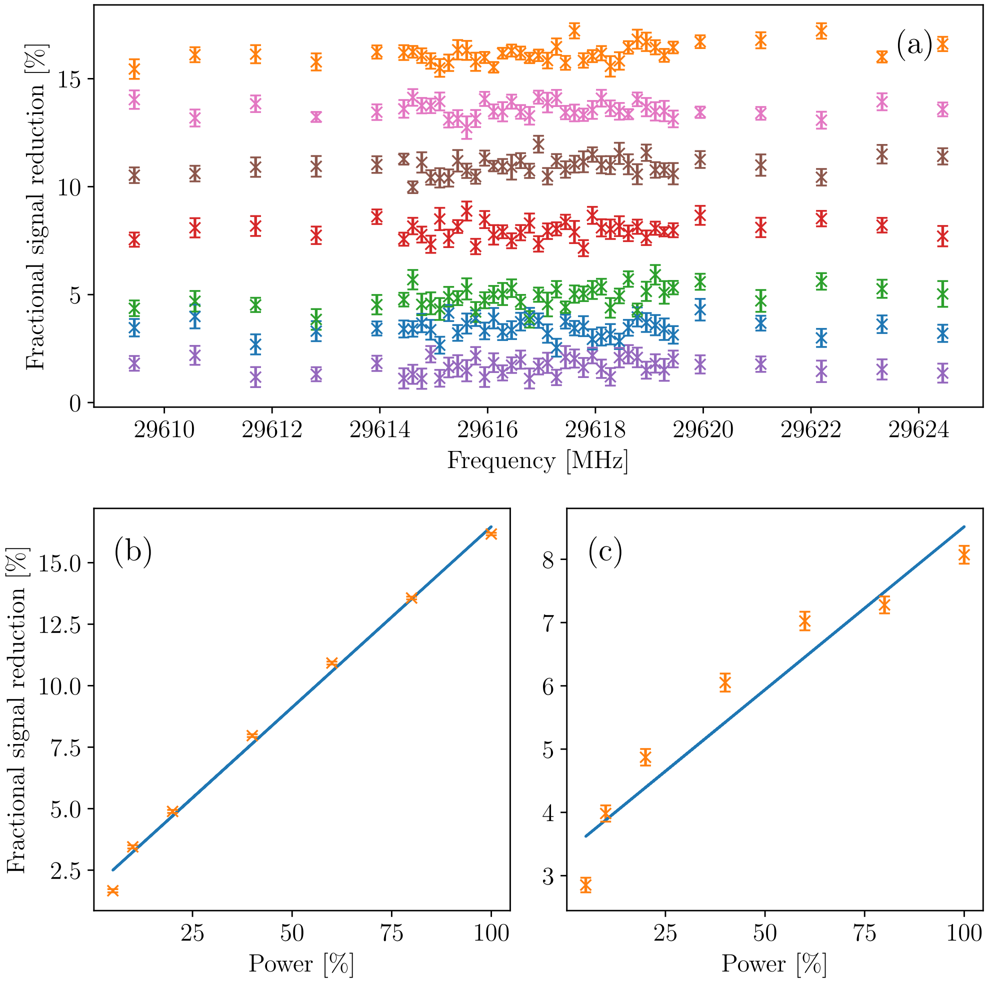

Figure 4.12: Rydberg state population loss due to microwave pulses. (a): Scans across frequency for 18^3P atoms at 5 (purple), 10 (blue), 20 (green), 40 (red), 60 (brown), 80 (pink), and 100% (orange) power, displaying no significant frequency dependence across this range. Error bars are standard error of 20 repeated measurements. (b): The weighted average of the points in (a) for each power setting as a function of power, with a linear fit. (c): The same as in (b), but for 18^3F Rydberg atoms.

at the offset frequency which could be out of phase with the 2^3P_1-to-2^3P_0 FOSOF signal, potentially skewing the measured linecentre.

In principle, there should be no microwave electric field at the point where the helium beam passes through the waveguide (due to the half-wavelength spacing between the waveguide short and the hole described in Sec. 3.2.5 resulting in an electric-field node at the location of the hole, 7.204 mm from the short). However, the nonzero width of the hole allows atoms away from the centre of the hole to be exposed to a small microwave electric field. Additionally, the position of the node shifts slightly at microwave frequencies away from the centre of the atomic transition. Decreasing the size of this effect (to the level shown here) was one reason why the diameter of the helium access hole in the waveguide was reduced from 1 mm to 0.5 mm.

To determine the size of this effect, a test was carried out by tuning both the state-preparation and detection lasers to drive transitions to and from the 2^3P_0 state, respectively, as shown in Fig. 4.11(a). The laser pulses were shifted as shown in Fig. 4.11(b) so that the detection lasers were immediately after the state-preparation pulse, followed by a pair of $T = 600\,\text{ns}, D = 200\,\text{ns}$ microwave pulses. The frequencies of the two microwave pulses were set 280 Hz apart as they are in regular FOSOF experiments. With this scheme, any reduction in signal caused by the microwaves being turned on must be due to removal of atoms from the $n = 18$ Rydberg state. The time-averaged results of this test (averaged over many cycles of the 280 Hz offset frequency) are shown in Fig. 4.12, indicating up to a 15 % loss in Rydberg population at maximum microwave power.

In order to determine whether this Rydberg quenching effect could have any influence on the phase of the atomic FOSOF signal, an analysis of the frequency component from this quenching experiment at the 280 Hz offset frequency was performed using the inner product method described in Sec. 3.5. No evidence of any nonzero signal at this frequency was found with a noise floor approximately 10^3 times smaller than the typical FOSOF signal amplitude.

The consistency between measured FOSOF linecentres obtained when using the two different Rydberg states (18^3P and 18^3F), described in Sec. 4.9 (despite the factor of two difference in quenching seen in Fig. 4.12(b,c)), gives the strongest evidence that this quenching effect does not cause any significant shift in the linecentre.

4.9 Rydberg Detection States

There are two Rydberg states accessible with the 1532 nm laser from the 4^3D_1 state: the 18^3P and 18^3F states. The latter is more sensitive to electric fields, and so a comparison of the linecentres measured using the two states gives an indication of whether any effect due to the interaction of microwaves or any stray dc electric fields with Rydberg atoms causes a shift in the measured linecentre. The difference in linecentres obtained from experiments using the 18^3P and 18^3F states (with summaries shown in Fig. 4.1 and Table 4.1, and the results for each experiment configuration given in Appendix A) is 21(16) Hz, which is consistent with no shift at the 20 Hz level of precision. This analysis assumes that the power extrapolation slope is the same for all data taken at a given value of D. Being more conservative in our analysis by allowing for the possibility of different power extrapolation slopes for the two Rydberg states (by separately fitting for these two slopes), the difference between linecentres for the two states is 62(48) Hz, which constrains any possible shift to be smaller than 110 Hz.

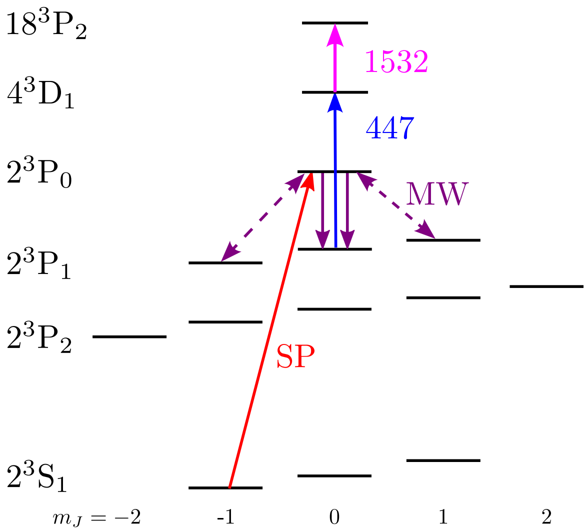

Figure 4.13: Level schematic showing the alternate experiment configuration (compared to Fig. 3.3), where atoms are initially excited to 2^3P_0 and then undergo a microwave transition to $2^3P_1(m_J = 0)$ before being excited by the detection laser and ionized. Dashed arrows indicate the possible presence of unwanted transitions that could result from imperfect microwave polarization.

4.10 Direction of Microwave Transition

The experiment is usually run with the state-preparation laser exciting atoms from $2^3S_1(m_J = \pm 1)$ to $2^3P_1(m_J = 0)$, with the microwaves then driving atoms to 2^3P_0 (see Fig. 3.3). By re-tuning the lasers it can also be run with atoms first excited into 2^3P_0 and then driven into $2^3P_1(m_J = 0)$ by the microwaves, as shown in Fig. 4.13. This configuration is less susceptible to the imperfect polarization issues discussed in Sec. 4.6, as, unlike in the case when the state-preparation laser drives atoms to $2^3P_1(m_J = 0)$, there are no near-resonance $m_J = \pm 1$ states for 2^3P_0. The only way that $\Delta m_J = \pm 1$ microwave transitions from $2^3P_1(m_J = \pm 1)$ can contribute is if the errant horizontal polarization component of the microwaves drives atoms there from 2^3P_0 and back again, which is very unlikely as even the intended $\Delta m_J = 0$ transition is far from saturation in our usual experiment timing, and only a small fraction of

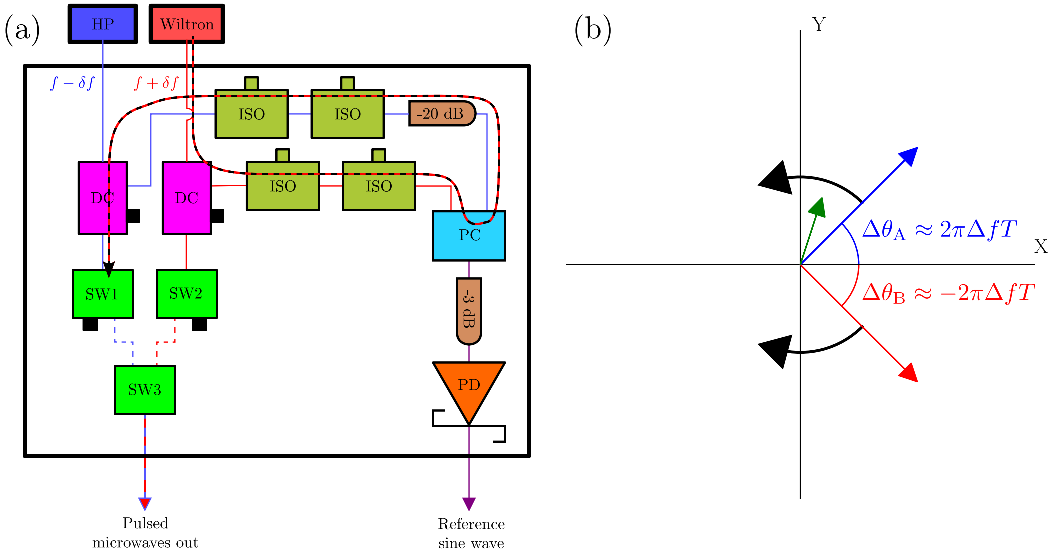

Figure 4.14: (a) A possible microwave leakage path through the microwave pulsing system, shown as red and black dashed line. (b) A phasor representation of the two FOSOF experiment types (A and B are blue and red), and an interfering phasor (green). The FOSOF phasors are rotated and scaled according to the lineshape function Eqn. (2.27) as the detuning Δf is varied, but the interfering phasor will vary in a different manner.

this power is horizontally polarized and available to drive the $\Delta m_J = \pm 1$ transitions.

If the power extrapolations for $2^3\mathrm{P}_0 \to 2^3\mathrm{P}_1$ and $2^3\mathrm{P}_1 \to 2^3\mathrm{P}_0$ are carried out separately, the difference between the linecentres obtained is 4(97) Hz, which is consistent with zero shift but at a low level of precision. If the data is combined and one extrapolation slope is used, the difference in linecentres is 21(12) Hz. Consistency in the measured linecentre between this configuration and the regular configuration is a further indication that the possible imperfect polarization issues do not skew the measured linecentre from the true value.

4.11 Microwave Isolation

In a FOSOF experiment, it is critical to have a very high level of isolation between the two paths which generate the microwave pulses at $f - f_{\mathrm{ofs}}/2$ and $f + f_{\mathrm{ofs}}/2$. If a small amount of power from the HP generator couples into the path of the Wiltron generator (or vice versa, see Fig. 4.14(a)), it will cause interference, and the amplitude of the microwave in these pulses will oscillate at the offset frequency. This oscillating microwave amplitude results in an added modulation of the atomic signal, which can be thought of as a phasor which adds with the desired FOSOF response, as shown in Fig. 4.14(b). This additional phasor would have a phase which varies with the microwave frequency differently than the phase of the atomic FOSOF signal phasor, causing a distortion of the FOSOF lineshape.

The FOSOF phase is approximately given by $\Delta\theta_{\mathrm{A}} = 2\pi T \Delta f$ (Eqn. (2.13)), or, when the order of the microwave pulses is reversed for the cancellation of erroneous phases described in Sec. 2.1.2, $\Delta\theta_{\mathrm{B}} = -2\pi T \Delta f$. From these expressions, it can be seen that for $T = 300\,\mathrm{ns}$ a 5 Hz error corresponds to approximately 10^{-5} rad. In the worst case, the interference phasor is 90° out of phase with the FOSOF phasor, and will cause a 5 Hz shift if it is 10^{-5} times as large as the FOSOF phasor. This corresponds to 50 dB in amplitude or 100 dB in power.

One of the possible leakage paths is shown in Fig. 4.14(a). To determine how well the pulses from the two generators are isolated from this path, one can compare the attenuation of a microwave signal travelling along this interference path relative to the direct microwave path. First, the directional coupler couples 13 dB of the microwave power. Then each of the two isolators has 1.25 dB of insertion loss, and the isolation between ports 1 and 2 of the power combiner (PC) is 18 dB in the 30 GHz frequency band. The 20 dB attenuator at one of the power combiner inputs adds another 20 dB of isolation, and the isolators are specified to 20 dB each. Entering the SW1 path through the coupled port of the directional coupler adds another 26 dB of isolation. These factors add to a total of 119.5 dB of isolation. To compare to the direct SW1 path, this 119.5 dB of isolation must be reduced by the 2.2 dB insertion loss of the directional coupler, so the relative isolation between the direct path to SW1 from the HP generator relative to this leakage path from the Wiltron generator is approximately 117 dB. The cables used within the box are rated to 110 dB of shielding, as are the 2.92 mm connectors, and so direct cable-to-cable coupling via radiation should not be a concern either.

Microwave leakage is also possible where the two signals are combined at SW3 of Fig. 4.14. Each switch is specified to 50 dB of isolation (defined as the attenuation of a path through the switch in the off state), and the switching topology used means that this combines to 100 dB as there are two switches in each path (with SW3 common to both). This 100 dB isolation only applies to isolation of the two paths from each other during pulses; in the time between pulses the isolation between the input of SW1 (or SW2) and the output of SW3 is only 50 dB, as SW3 is always open to one of the two paths. This lower attenuation for one path is not expected to skew FOSOF results however, as it only applies to one microwave frequency at a time and will not contribute to the atomic signal at the offset frequency.

The consistency of results obtained with different T values is evidence that the level of microwave isolation achieved in this measurement is sufficient. If T is doubled, so is the slope of the FOSOF phase $\Delta\theta = 2\pi T \Delta f$ (Eqn. (2.13)), and so a phasor which causes the same phase shift will have its effect on shifting the measured linecentre halved. Simulations of the effect of poor isolation on the measured linecentre are described in Sec. 5.2.5.

4.12 Offset Frequency

Because the HP microwave generator can only have its frequency set in 1 kHz steps, the offset frequency is set such that $f_{\text{Wiltron}} = f_{\text{HP}} + f_{\text{ofs}}$, and the recorded frequency is f_{HP}. The derivation leading to the FOSOF lineshape of Eqn. (2.27) assumes the frequencies of the two generators are set to $f - f_{\mathrm{ofs}}/2$ and $f + f_{\mathrm{ofs}}/2$, and so a correction which consists of adding $f_{\mathrm{ofs}}/2$ to the recorded frequency must be applied during the analysis.

The majority of the experiment configurations (listed in Appendix A) were recorded as pairs of $f_{\mathrm{ofs}} = 280\,\mathrm{Hz}$ and $f_{\mathrm{ofs}} = -280\,\mathrm{Hz}$ data. The experiment was also performed with offset frequencies ranging from $-2800\,\mathrm{Hz}$ to $2800\,\mathrm{Hz}$ in order to test for any systematic effects. The range of linecentres determined over this span of offset frequencies was 83(56) Hz, which constrains any possible effect (assuming an effect linear in offset frequency) at $|f_{\mathrm{ofs}}| = 280\,\mathrm{Hz}$ to 8(6) Hz. This result confirms that the offset frequency is properly corrected for and does not cause any unaccounted for systematic effect.

4.13 Doppler Shifts

If a helium atom travelling through the microwave waveguide has a velocity component along the axis of the waveguide (the direction along which the microwaves travel, x in Fig. 3.8), the Doppler effect will cause a frequency shift of

$$\Delta f_{\mathrm{Doppler}} = \frac{v_x}{c} f = \frac{|\mathbf{v}| \sin(\theta)}{c} f, \tag{4.7}$$

where $\mathbf{v}$ is the velocity of the atom, f is the frequency of the microwaves, and c is the speed of light. With an 1100 m/s beam, a misalignment of only one milliradian would cause a 110 Hz shift at $f = 29.6\,\mathrm{GHz}$. Based on the machining tolerances of the screw holes used to mount the base of the ionizer and waveguide assembly, this misalignment could be as much as ±3 mrad. In addition to this, in Sec. 4.6 of Ref.

[23] the possible misalignment is conservatively estimated at ±5 mrad. Combining the possible alignment errors in quadrature gives a range of ±6 mrad, and a Doppler shift of ±660 Hz. However, the standing wave in the waveguide caused by the short will mostly cancel this Doppler shift, as the transition will be driven by two waves of almost equal power travelling in opposite directions. This will in effect cause the lineshape to be the sum of one line centred at $f_0 + \Delta f_{\text{Doppler}}$ and another at $f_0 - \Delta f_{\text{Doppler}}$. Because $\Delta f_{\text{Doppler}}$ is much smaller than the width of the line, this will cause a very small broadening effect and would lead to a shift in the resulting linecentre only if there were unequal powers in the two waves. The experiment described in Sec. 4.13.1 indicates that the power in the two waves may differ by approximately 4 % at $f = 29.6$ GHz. A 96 % cancellation of an up to 660 Hz Doppler shift would leave a residual shift of 26 Hz, which is larger than the anticipated precision of this measurement. A calculation of the expected Ohmic losses due to surface currents in the waveguide as the microwaves travel from the helium access hole, to the short, and back to the access hole again gives a value of 0.4% loss for a gold-plated waveguide, which leads to a Doppler shift of <2.6 Hz.

One planned test for any effect due to Doppler shifts is to run the source at a higher temperature by using a coolant other than liquid nitrogen, which will increase the speed of the beam and thus amplify any existing net shift. For example a mixture of dry ice and isopropyl alcohol will stay at 195 K (the sublimation point of CO_2) as long as solid dry ice remains, a factor of ∼2.5 higher than the 77 K boiling point of liquid nitrogen. As the RMS speed of a gas is proportional to $\sqrt{T}$, this would increase the speed and thus Doppler shift by a factor of ∼1.6. Higher temperatures are also possible, such as an ice water bath at 273 K giving a factor of 1.9, but it is important to ensure that the source stays well below 430 K because the indium used to improve thermal conductivity will melt into the turbopump below the source at

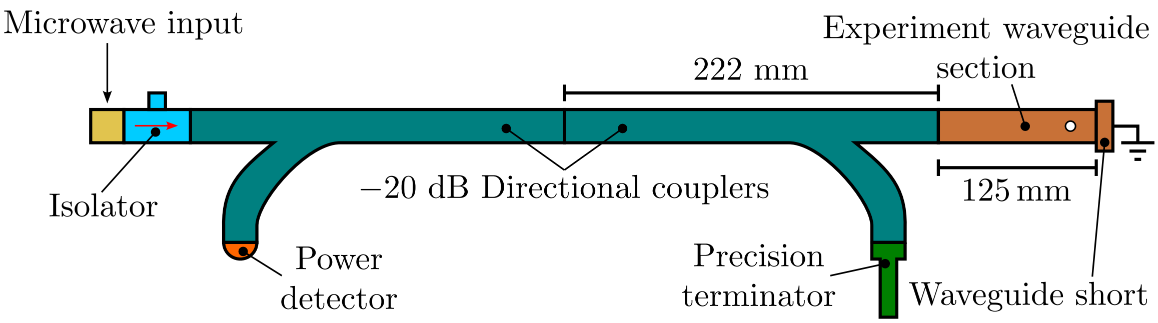

Figure 4.15: Setup to measure waveguide short reflectivity. This configuration measures reflected power, the terminator and detector are swapped (without moving the directional couplers) to measure incident power.

this temperature. Reversing the direction of microwave propagation by disassembling the experiment region (Fig. 3.8) and installing the waveguide section in the opposite orientation is another proposed test which is possible without otherwise altering the components, and should reverse the sign of any possible Doppler shift.

The shift caused by the relativistic transverse Doppler effect (caused by time dilation) is given by

$$\frac{\Delta f_{\mathrm{TD}}}{f_0} = \sqrt{1 - \frac{v^2}{c^2}} - 1, \tag{4.8}$$

which is on the order of a part in 10^{11} at a speed of 1100 m/s. This shift is insignificant for the ~1 ppb precision goal of this experiment.

4.13.1 Waveguide Short Reflectivity Measurements

To determine how perfectly the Doppler shift is cancelled by the reflection from the waveguide short, an attempt was made to measure the reflectivity of the waveguide short using the thermal microwave power meter (HP 436A meter with R8486A thermocouple sensor).

Fig. 4.15 shows the setup which was used for this measurement. Microwaves from one of the generators are coupled in through a 2.92 mm coaxial line-to-WR-28 adapter, pass through an isolator, two 20 dB directional couplers combined to make a bidirectional coupler, then enter the waveguide section from the experiment and are reflected from the short. The reflected microwaves then travel through the combined couplers again and the power is measured on the coupled port of the coupler on the left in the figure. This measurement was repeated with the positions of the detector and terminator swapped to measure the coupled portion of the power which was incident on the short, and the reflectivity of the short can be deduced from the ratio of these values.

The main imperfections of this reflectivity measurement are that the attenuation of the microwaves due to nonzero resistance in the waveguide walls is not negligible over these distances, and that reflections of unknown phase from each component leading to constructive or destructive interference at the power sensor can be significant. The attenuation can be approximately accounted for by measuring the length of each section of waveguide and correcting by the known attenuation per unit length for waveguides of a given conductor. The directional couplers are made of silver-coated brass, which has 0.6 dB/m of attenuation at 29.6 GHz [32], and the experiment waveguide is gold-coated copper, which has a loss of 0.74 dB/m at the same frequency. These attenuation values are calculated using the resistivity of pure silver and gold, and may be higher in practice due to various imperfections, such as corrosion and impurities increasing the surface resistance of the metals. The effect of microwave reflections on this measurement can be accounted for to some extent by repeating the measurement over a wide range of frequencies, such that the interference varies from constructive to destructive, and then taking the average of the constructive and destructive values. Possible reflections are why the incident power needs to be measured from the coupled port of the directional coupler instead of simply putting the power detector in place of the waveguide section: the very different reflectivities of

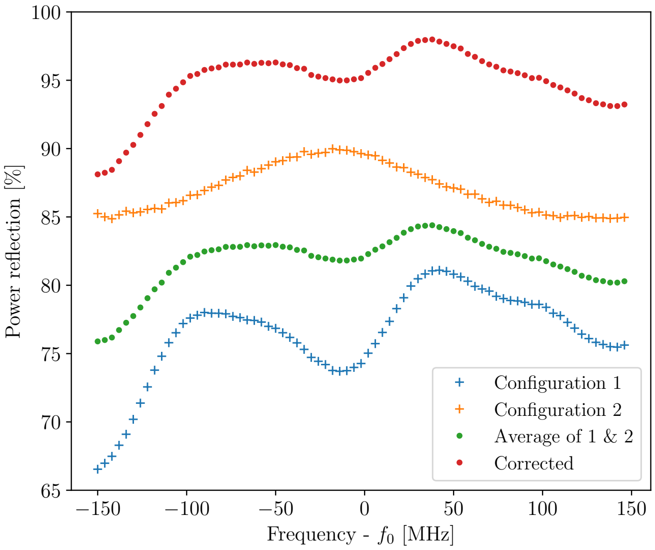

Figure 4.16: Results of reflectivity measurements. Configurations 1 & 2 differ by interchanging the directional couplers in Fig. 4.15. "Corrected" refers to correcting for waveguide attenuation as described in the text. Each point is the average of 3 repeats, with the order of frequencies randomized for each repeat.

the two components would cause different standing wave patterns, and so the power at the detector would not correspond to the power incident upon the waveguide. The measurement was also repeated with the directional couplers swapped in order to account for their coupling efficiency (which is specified to a mean accuracy over the 26.5–40 GHz frequency band of ±0.7 dB, and 0.6 dB of variation within this band) differing from the nominal values, and the results of the two configurations averaged.

The results of the measurements are shown in Fig. 4.16, indicating that the overall reflectivity of the waveguide section (which has holes drilled through it for helium beam access) and short (which has a hole drilled through for laser access) is determined to be on the order of 95%. The difference in paths between the input power measurement and the reflected power measurement is two passes through the main arm of a directional coupler and two passes through the experiment waveguide section, which combine to give a correction factor of 0.46 dB. The two configurations show markedly different power levels, likely due to different levels of reflections from waveguide components introduced when reassembling the equipment to obtain the four configurations (measuring incident and reflected power, and repeating each measurement with the couplers interchanged). This measurement is most likely an underestimate of the actual reflectivity as the only loss is assumed to be the attenuation of ideal waveguides, while in practice other loss mechanisms will exist (e.g. leakage from imperfect joints between waveguide sections). For the possible 6 mrad misalignment from above, a 96% cancellation would reduce the 660 Hz shift to about 26 Hz. This shift is similar in magnitude to the 20 Hz precision goal of the experiment. However, this measurement is far from perfect (for example, different reflections could be introduced when reassembling the components shown in Fig. 4.15 due to misaligned waveguide flanges, making the averaging of the data shown in Fig. 4.16 ineffective at cancelling out the effects of the reflections), and so the results are unlikely to be accurate at even the 10% scale.

The waveguide short is held to the polished end face of the waveguide under pressure applied by screws, and so it is plausible that the electrical contact could depend on how these screws are tightened, changing each time these parts were assembled. To test this, the reflectivity was measured as the screws were loosened progressively, giving the results shown in Fig. 4.17, which shows that loosening the screws a significant amount causes only a small decrease in reflectivity. The fact that the reflectivity does not strongly depend on the pressure applied to the short suggests that the calculated result (which assumes a grounded conductive plane is in perfect contact with the end faces of the waveguide walls) of 0.4% power mismatch between incident and reflected waves is an accurate description of the physical system, and the net shift due to almost-perfectly cancelled Doppler shifts at up to 6 mrad of misalignment between the atomic beam and microwave propagation direction is under

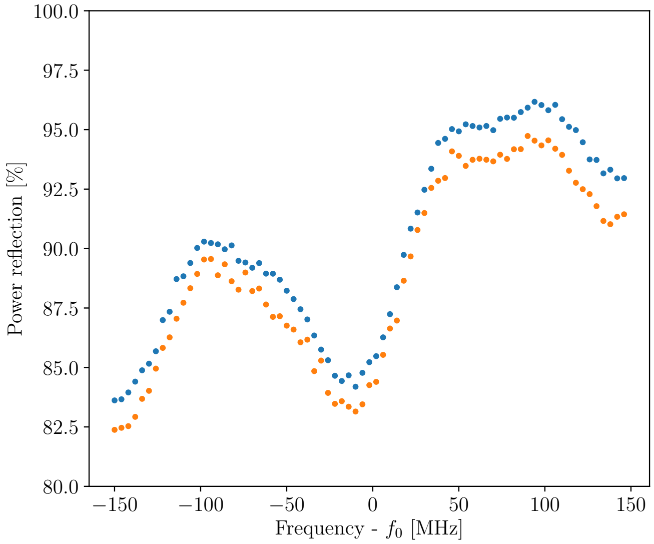

Figure 4.17: Results of reflectivity measurements of the waveguide short to test the effect of contact pressure between short and waveguide. Blue points are data taken with all screws tightened, orange points are data taken after loosening all screws 1/8th of a turn.

2.6 Hz.

4.14 Frequency Reference

As discussed in Sec. 3.3.4, a stable, high-precision clock is required to determine the applied microwave frequency to the precision required for our uncertainty goal. The Trimble Thunderbolt E GPS-disciplined oscillator used is specified to have an Allan deviation of less than 2×10^{-11} over averaging times up to 10^4 seconds, corresponding to a frequency stability of 0.6 Hz at 29.6 GHz, and has a specified accuracy of 1.16×10^{-12} when averaged over a day. Thus its contribution to the error budget should be negligible, as long as data collected while the clock does not have a GPS signal is excluded, as described in Sec. 3.3.4.

4.15 Systematic Effect of Undetermined Origin

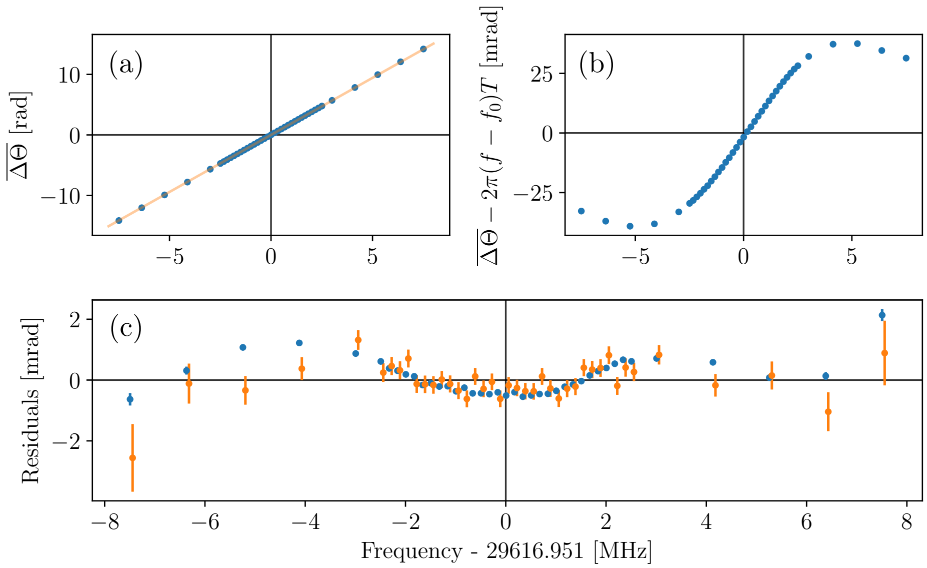

Figure 4.18: Averaged fit information for all $T = 300\,\mathrm{ns}, D = 100\,\mathrm{ns}$, and $P = 100\%$ data. (a) Averaged FOSOF phase after reversal ($\overline{\Delta\Theta} = (\Delta\theta_\mathrm{A} - \Delta\theta_\mathrm{B})/2$ from Eqn. (2.26)) as a function of microwave frequency (blue dots) and line corresponding to predicted TDPT FOSOF lineshape $\overline{\Delta\Theta} = 2\pi T(f - f_0)$. (b) Difference between the experimental points and the line in (a), corresponding to Fig. 2.6(b). Error bars are not shown as they would be smaller than the points. (c) Average of the residuals for the fit to Eqn. (2.27) for all of the selected subset of data (blue) and extrapolation of the residuals to zero power (orange).

After taking the majority of the data required to complete a measurement of the $2^3\mathrm{P}_1$-to-$2^3\mathrm{P}_0$ transition frequency (totalling 904 different configurations of experiment parameters, which are listed in Appendix A), and eliminating many potential systematic effects, it was found that re-analyzing the results by excluding data taken at microwave frequencies further from the linecentre resulted in a shift in measured linecentre of approximately 100 Hz, significantly more than the 20 Hz precision goal as shown by the $|f - f_0| < 1/(8D)$ point in Fig. 4.1(g). Such a large shift shows that there is an uncontrolled systematic effect which must be eliminated or corrected for in order to complete a measurement with a precision of 20 Hz.

The analysis using only the central frequencies (within $1/(8D)$ of the resonant frequency), also eliminated the consistency between data taken at different T and D values, which can be seen by comparing the analysis including data taken at microwave frequencies out to $f_0 \pm 1/(2D)$ in Fig. 4.1 to that taken using only the central frequencies in Fig. 4.19. It would be expected that data recorded far from the centre frequency, where the amplitude of the signal is lower, would be more susceptible to systematic shifts, but this inconsistency for only the narrow frequency range analysis suggests that may not be the case here.

Because the width of the transition is proportional to $1/D$ (with the first zeros of the approximately sinc^2 amplitude lineshape of Eqn. (2.11) occurring at $f_0 \pm 1/D$), in order to combine data taken at different D values, the frequency range is defined as a fraction of $1/D$, i.e. $|f - f_0| < 1/(2D)$, $|f - f_0| < 1/(4D)$ etc.

More detailed information about the nature of this problem can be determined from the averaged fit residuals in Fig. 4.18(c), where an obvious shape is visible after averaging 400 hours of $T = 300\,\mathrm{ns}, D = 100\,\mathrm{ns}, P = 100\,\%$ data. If the fitting function Eqn. (2.27) accurately described the data, the residuals would be randomly scattered around, and consistent with, zero. Due to the power extrapolation used to determine linecentres, the effect of these residuals on the lincentre would also be negated if the residuals extrapolated linearly to zero at zero power, however, as the orange points in Fig. 4.18(c) show, they do not. The effect of these residuals not extrapolating to zero is visible in Fig. 4.20, which shows how the linecentre extrapolations as a function of power differ when restricting the frequency range of the analysis to $|f - f_0| < 1/(8D)$.

In the remainder of this section, various avenues are investigated in an attempt to determine the origin of this residual effect.

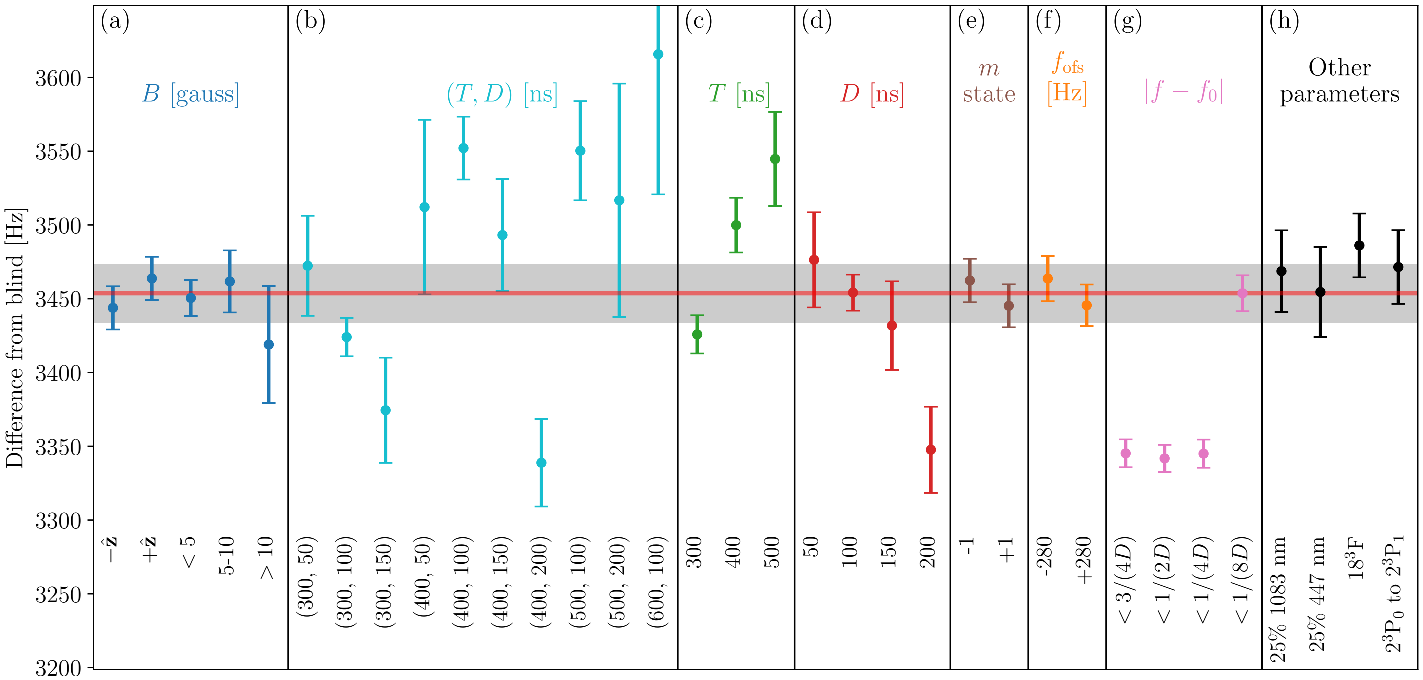

Figure 4.19: Summary plot of results from this measurement, when only using the narrow frequency range data with $|f - f_0| < 1/(8D)$. (a) shows linecentres measured for different magnetic field parameters. (b)-(d) show the results of different microwave pulse timing parameters. (e) shows the two optical pumping directions. (f) shows restricting the analysis to different frequency ranges around the centre. (g) shows laser, Rydberg detection state, and microwave transition directions. The grey band covers ±20 Hz, corresponding to the uncertainty goal for this measurement. The inconsistencies shown in (b)-(d) are in contrast with Fig. 4.1, which uses $|f - f_0| < 3/(4D)$

4.15.1 Varying Experiment Parameters

Separating the data from the experiment according to various parameters and averaging the corresponding residuals (found from fitting the data from each experiment run to Eqn. (2.27)) gives the plots shown in Fig. 4.21. The consistency of the shape of the residuals across all of these parameters rules out a wide range of possible causes of the effect.

For offset frequency in Fig. 4.21(a), frequency-dependent effects in either the reference arm or the atomic FOSOF signal arm of the system would be expected to result in different residuals at different offset frequencies. These effects could result from phase shifts due to the amplifiers in each arm, if the phase cancellation under the pulse order reversal described in Sec. 2.1.2 is not perfect.

The residuals for different optical pumping states in Fig. 4.21(b) could show effects due to optical pumping into one state being less complete than the other, or elliptical polarization of the state-preparation laser. These effects are described in detail in Sec. 4.6.

In Fig. 4.21(d), consistent residuals are shown between data from the current data collection period and data taken during a previous period when temporal overlap of the laser and microwave pulses caused a shift in the linecentre (discussed in Sec. 4.7). This consistency shows that the undetermined systematic effect is not due to incomplete elimination of the shift due to laser-microwave overlap.

The two microwave transition directions in Fig. 4.21(e) ($2^3\mathrm{P}_1$ to $2^3\mathrm{P}_0$ and $2^3\mathrm{P}_0$ to $2^3\mathrm{P}_1$) would be expected to show different results if the unknown effect was caused by the imperfect microwave polarization described in Sec. 4.6.

The two Rydberg states in Fig. 4.21(f) would show different residuals if the quenching of the Rydberg states by the microwaves described in Sec. 4.8 were involved

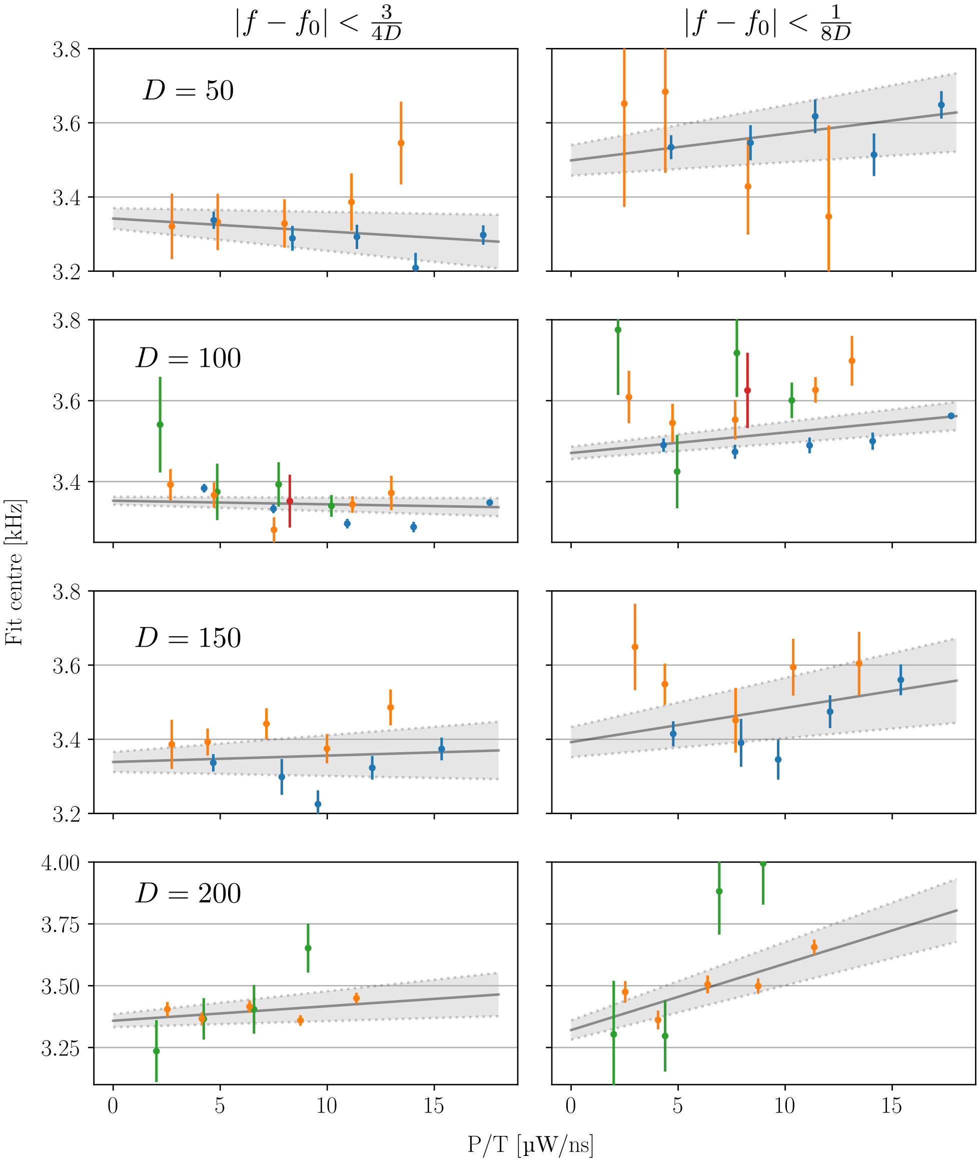

Figure 4.20: Power extrapolations for all T values at a given D value, for full (left column, $f_0 \pm 3/(4D)$) and narrow (right column, $f_0 \pm 1/(8D)$) frequency ranges. In all plots, blue is $T = 300$ data, orange is $T = 400$, green is $T = 500$ and red is $T = 600$. The average of the data for each (T, D, P) combination is shown. The power used is that measured at the diode labelled "To data logger" in Fig. 3.12. The shaded areas show the uncertainty in the linear fit for each D.

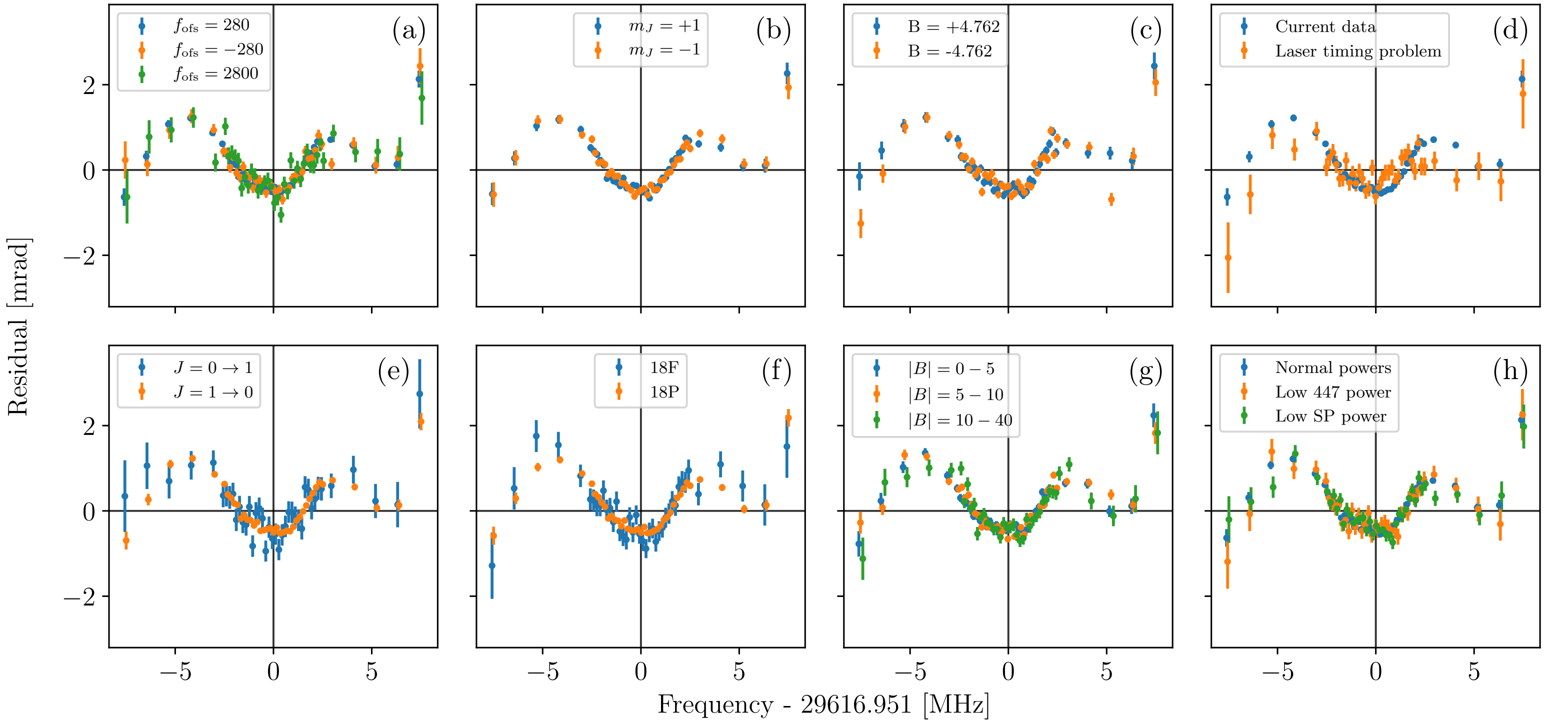

Figure 4.21: Residual plots for data restricted to various different parameters, showing consistency in every case. (a): Offset frequencies, (b): m_J states at the start of the experiment cycle (see Fig. 3.3), (c): Reversed magnetic field sign, (d): Data where overlap between laser and microwave pulses caused a shift, (e): Reversed direction of microwave transition (see Fig. 4.13), (f): Alternate Rydberg detection state, (g): Magnetic field magnitude ranges (both positive and negative fields included), (h): Laser powers decreased to 25% (and thus signal size by a similar ratio). SP = state preparation. All plots show $T = 300\,\text{ns}, D = 100\,\text{ns}, P = 100\%$ data.

in this effect, as the 18^3F state would be more strongly affected due to its higher sensitivity to electric fields.

The consistency between data taken with lower laser powers in Fig. 4.21(h) is again evidence against the light shifts from overlapping laser and microwave pulses, and incorrect state-preparation laser polarization. The reduced signal in this case also rules out effects where an independent phasor interferes with the FOSOF one, which could be caused by imperfections in the microwave system. In these experiments the FOSOF signal amplitude is reduced due to the decreased laser power, and so the interfering phasor's amplitude would increase relative to the FOSOF phasor's amplitude, magnifying any possible interference effect.

4.15.2 Fitting Procedure

As a check against an error being made in the data analysis, the Mathematica code which generates the initial fits was rewritten in Python 3 by myself (the original Mathematica code was written by Kosuke Kato). A slightly larger number of the runs failed to fit in the Python program because the fitting module used (`lmfit`) is less robust than Mathematica's `NonLineaModelFit`, so the averaged residuals are not numerically identical between the two cases, but the differences are at the microradian level. The data fitting step of the analysis outputs the residuals which are averaged to generate the plots in this section, so if there is any problem in the analysis it must be before this point. The only analysis performed before the fitting is performed is the generation of the initial inner products as described in Sec. 3.5, which is unchanged from the previous 2.3 GHz measurement [20], and has also been checked carefully for errors.

4.15.3 Microwave Pulse Imperfections

Phase and amplitude imperfections in the microwave pulses are potential sources of systematic effects in a FOSOF experiment, as the derivation of the FOSOF lineshape of Sec. 2.1.2 assumes perfectly rectangular amplitude profiles for the pulses (i.e., sudden turn-on and turn-off) and uniform phase within each pulse.

The main cause of pulse imperfections is reflections throughout the microwave system due to impedance mismatches. The largest of these is the intentional near-100% reflection from the waveguide short a half wavelength (14.4 mm) from the helium access hole in the waveguide. The speed of 29.6 GHz microwaves in WR-28 waveguide is $0.702c$, and so it takes

$$\frac{2 \times 7.20\,\mathrm{mm}}{0.702c} = 0.068\,\mathrm{ns} \tag{4.9}$$

from the time a microwave wavefront hits the helium beam to when its reflection passes back through the beam again and a standing wave is established. This delay is a very small fraction of even the shortest 50 ns pulses used in the experiment, and should be approximately cancelled by the opposite process at the end of the pulse, so the impact of this effect is expected to be negligible.

Other reflections from multiple points separated by metre-scale distances in the microwave system can lead to multi-nanosecond delays between the initial and reflected waves, and more significant pulse distortions. The reflected wave has a different phase to the initial wave, and so there is a phase shift in the resulting wave at the time when the reflection reaches the atoms.

In order to directly characterize the amplitude and phase profiles of the microwave pulses (as was done in the previous 2.3 GHz experiment [20] and is described in Sec. 4.2.4 of [23]), the 29.6 GHz microwaves must be sampled by an oscilloscope with a sufficiently high bandwidth and sample rate. Because the Tektronix DPO7354 oscilloscope used in this experiment only has a bandwidth of 3.5 GHz, indirect methods must be used.

The simplest of these indirect techniques is looking at oscilloscope traces of the output of the Schottky diode power detector (shown in Fig. 3.12), as these traces are recorded at every frequency for every run of the experiment. The traces do not directly carry phase information, but the effect of constructive or destructive interference from reflections can be seen as a step up or down in power near the start and/or end of a pulse. There is no obvious sign of such interference, even in heavily averaged oscilloscope traces in the current experiment, but the 1.5 ns response time of the Schottky diode power detector limits the time resolution for observing the interference on short time scales.

Other techniques rely on mixing down the pulse signal to a frequency which is within the bandwidth of the oscilloscope. This technique was first attempted by directly using a mixer (Minicircuits MDB-44H+), with one generator's CW output fed into the mixer's local oscillator port and the pulse train (sampled at a range of points throughout the microwave system) connected to the rf port. The mixer then outputs a pulsed signal at the frequency difference of the two generators, which can be set such that the beat period is an integer multiple of the oscilloscope's sample period. The beat signal can be recorded on the oscilloscope and analyzed with the inner product method described in Sec. 3.5 to determine phase and power profiles throughout the pulse, as shown in the left column of Fig. 4.22.

In order to verify that the results obtained with the mixer are representative of the pulses, a method utilizing a more direct beat note between the CW signal and the pulsed signal was also used. To accomplish this, the two signals were fed into the two input ports of a power combiner, with the output connected to a Schottky

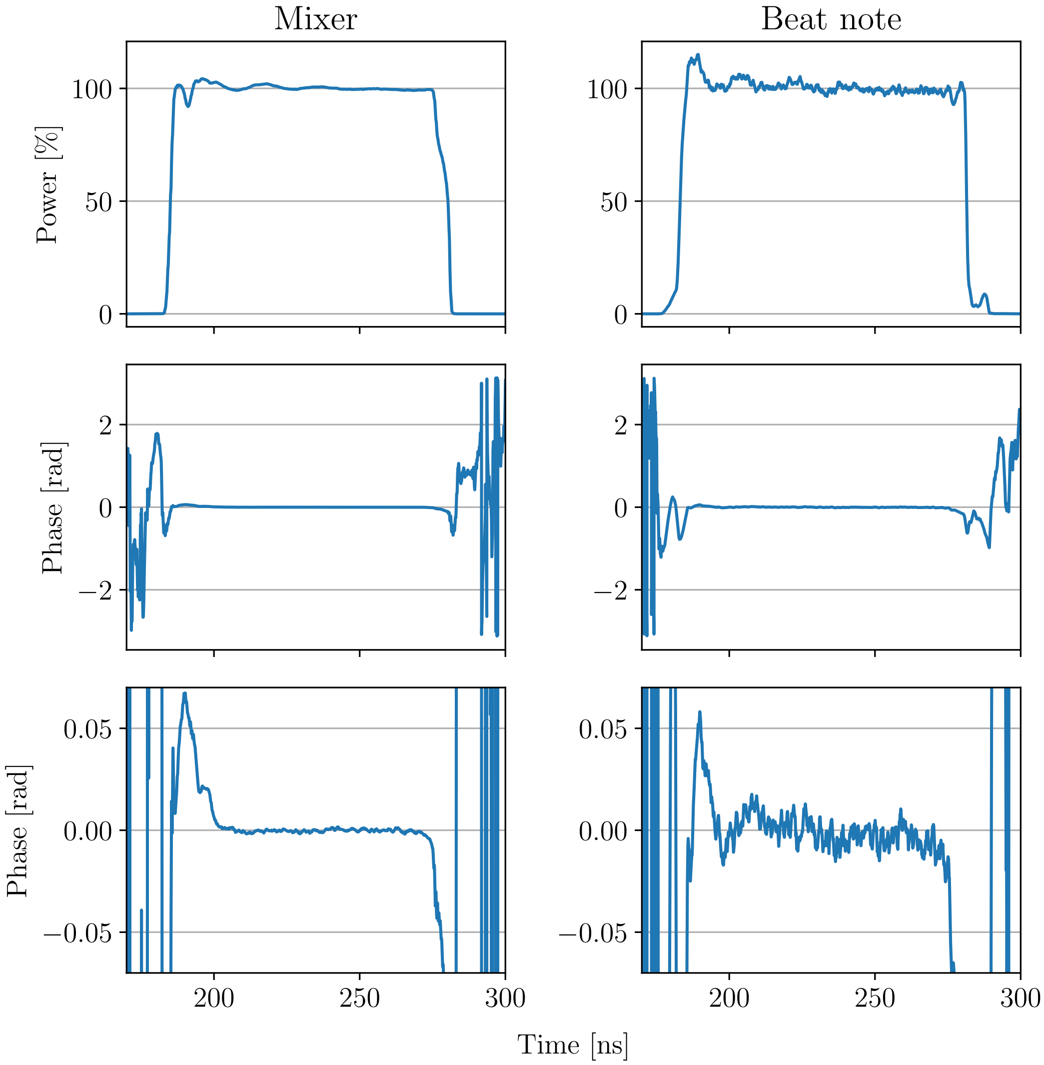

Figure 4.22: Microwave pulse profiles from the current experiment, derived with two different methods which are described in the text. In both cases the pulses are recorded after travelling through the entire microwave system and being reflected off the short, then coupled out through the directional coupler. The data shown is the average of 100 traces for the mixer and 1000 for the beat note. Both sets of data are taken with the pulses at the centre frequency and the reference microwaves 1 GHz below it. The bottom row is a zoomed-in copy of the middle row.

diode power detector, the response of which was recorded on the oscilloscope. This is essentially the same configuration as the one used to generate the FOSOF reference signal described in Sec. 3.3.2, where it is described in greater detail. The signal from the Schottky diode power detector can again be analyzed with the inner product method, and repeated for many traces (with the phase for each trace referenced to zero in the middle of the pulse) and averaged together. The results of this analysis are shown in the right column of Fig. 4.22.

Comparing the profiles of Fig. 4.22 obtained from the two methods shows that they are generally similar. However, they do have some obvious differences, most significantly a different turn-on profile and a small bump in power after the end of the pulse in the beat note profile. A significant effort was made to obtain more precise profiles for the phases and amplitudes of the pulses with different methods (and different parameters, such as powers, offset frequencies, and frequency of microwaves in the pulse), but eventually higher precision was determined to be unachievable without an unwarranted investment of time and equipment. What is clear is that the phase chirps at the edges of the pulse, though large, mostly take place when no significant power is present. Ultimately these measurements were used to motivate simulating a wide range of pulse amplitude and phase profiles, as described in Sec. 5.2.3. These simulations show that regardless of the exact profiles of amplitudes and phases within the pulses, there is no significant effect on the linecentre when extrapolated to zero microwave power.

5 Numerical Modelling of the Experiment

5.1 Description of the Model

Due to the discovery of systematic shifts proportional to the microwave power level in the previous measurement of the 2.3 GHz 2^3P_2-to-2^3P_1 interval [20], a numerical simulation of the experiment was developed. The simulation consists of a parallelized Modern Fortran program which directly integrates the Schrödinger equation using the fourth-order Runge-Kutta method for a nine-level atom (all 2^3P states, with magnetic sublevels) subjected to two pulses of microwave radiation. This simulation is used to investigate the shifts in linecentre due to a wide range of imperfections in the experiment, in order to estimate the magnitudes of the shifts and verify that they extrapolated to zero shift at zero microwave power. Source code for the simulation is provided in Appendix B.

5.1.1 Derivation of the Equations to be Solved

The time-evolution of the quantum-mechanical state of an atom is described by the time-dependent Schrödinger equation

$$i\hbar\frac{d}{dt}\left|\mathbf{\Psi}(t)\right\rangle = \hat{H}\left|\mathbf{\Psi}(t)\right\rangle, \tag{5.1}$$

where $\mathbf{\Psi(t)}$ is the state vector of the atom and $\hat{H}$ is the Hamiltonian of the system. For a magnetic-dipole transition like the one measured in this experiment, the time-varying part of the Hamiltonian is given by

$$\hat{H}_B = \frac{\mu_B}{\hbar}\left(g_L\hat{\mathbf{L}} + g_S\hat{\mathbf{S}}\right)\cdot\mathbf{B}(t), \tag{5.2}$$

where μ_B is the Bohr magneton, g_L is the orbital angular momentum g-factor, g_S is the spin g-factor, and $\hat{\mathbf{L}}$ and $\hat{\mathbf{S}}$ are the orbital angular momentum and spin operators. The total Hamiltonian is then $\hat{H} = \hat{H}_0 + \hat{H}_B$, where $\hat{H}_0$ is the unperturbed Hamiltonian given by Eqn. (1.2). If the atom were a two-level system in a general superposition with time-varying coefficients $c_1(t)$ and $c_2(t)$, the Schrödinger equation could be written as

$$i\hbar\frac{d}{dt}\begin{pmatrix} c_1(t)\left|\psi_1\right\rangle \\ c_2(t)\left|\psi_2\right\rangle \end{pmatrix} = \left(\begin{pmatrix} E_1 & 0 \\ 0 & E_2 \end{pmatrix} + \hat{H}_B\right)\begin{pmatrix} c_1(t)\left|\psi_1\right\rangle \\ c_2(t)\left|\psi_2\right\rangle \end{pmatrix}, \tag{5.3}$$

where $\left|\psi_k\right\rangle$ are the different atomic states which can be labelled with $n^{2S+1}L_J(m_J)$ as described in Sec. 1.2.1, and E_k is the energy of the k-th state. This represents a pair of coupled linear ordinary differential equations:

$$\begin{aligned} i\hbar\dot{c}_1(t)\left|\psi_1\right\rangle &= (E_1 + \hat{H}_B)c_1(t)\left|\psi_1\right\rangle + \hat{H}_B c_2(t)\left|\psi_2\right\rangle \\ i\hbar\dot{c}_2(t)\left|\psi_2\right\rangle &= (E_2 + \hat{H}_B)c_2(t)\left|\psi_2\right\rangle + \hat{H}_B c_1(t)\left|\psi_1\right\rangle. \end{aligned} \tag{5.4}$$

The coefficients can be isolated by applying $\langle\psi_1|$ and $\langle\psi_2|$ to both sides of the first and second equations respectively to give

$$\begin{aligned} \dot{c}_1 &= \tfrac{-i}{\hbar}\left(c_1\left(E_1 + \langle\psi_1|\,\hat{H}_B\,|\psi_1\rangle\right) + c_2\,\langle\psi_1|\,\hat{H}_B\,|\psi_2\rangle\right) \\ \dot{c}_2 &= \tfrac{-i}{\hbar}\left(c_2\left(E_2 + \langle\psi_2|\,\hat{H}_B\,|\psi_2\rangle\right) + c_1\,\langle\psi_2|\,\hat{H}_B\,|\psi_1\rangle\right), \end{aligned} \tag{5.5}$$

which use the matrix elements

$$\langle\psi_2|\hat{H}_B|\psi_1\rangle = \langle\psi_2|\frac{\mu_B}{\hbar}\left(g_L\hat{L} + g_S\hat{S}\right)\cdot\mathbf{B}(t)|\psi_1\rangle = V_{12}. \tag{5.6}$$

These matrix elements have been calculated for the relevant states of helium in Ref. [33]. This pair of equations can be extended to all nine 2^3P states by simply extending the $|\mathbf{\Psi}\rangle$ vectors and Hamiltonian to add the relevant matrix elements for coupling each state to every other state, providing a set of equations which can be straightforwardly translated to code for numerical integration with the fourth-order Runge-Kutta method.

5.1.2 Implementation Details

In an ideal FOSOF experiment, the microwave pulses switch on and off instantly and the phase is constant throughout each pulse. Both conditions are impossible to realize in an actual experiment due to the imperfect nature of microwave switches and partial reflections of the pulses from discontinuities in the microwave path, as discussed in Sec. 4.15.3. The idealized amplitude and phase profiles shown in Fig. 5.1 can be used as inputs to the simulation, as can profiles constructed to test specific phase and amplitude imperfections. The profiles made from measurements of the microwave pulses in the experiment shown in Fig. 4.22 can also be used.

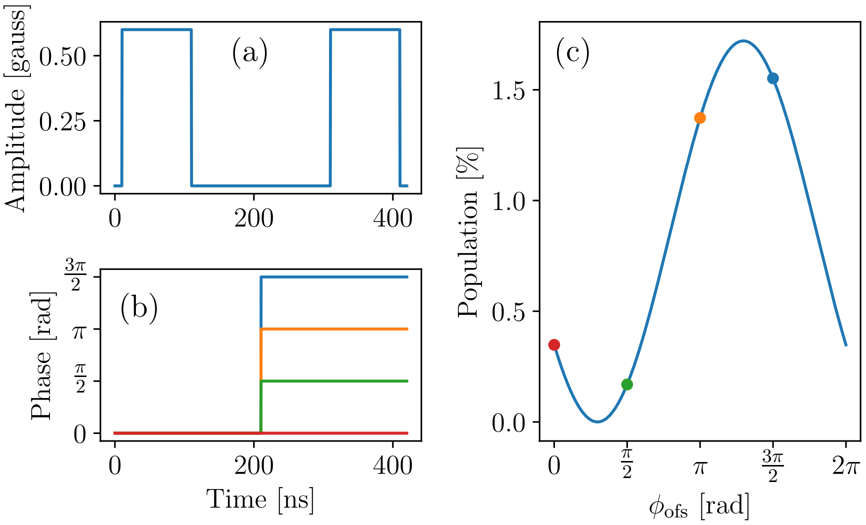

Figure 5.1: Example amplitude (a) and phase (b) profiles with ideal rectangular pulses and uniform phase within each pulse. The four different phase values for the second pulse correspond to different times during a period of the offset frequency. Panel (c) shows the numerical solution to these four ideal cases, with a fit that shows the sinusoidal variation of the resulting final population as a function of the offset in phase between the two pulses.

The primary output of each run of the simulation is the simulated atomic signal, which corresponds to the fraction of the population which is in the upper state of the FOSOF transition after both microwave pulses, $|c_2(t = t_{\mathrm{Final}})|^2$ from Eqn. (5.3). The effect of the FOSOF frequency offset is represented by adding an extra phase ϕ_{ofs} to one of the microwave pulses. Both configurations described in Sec. 2.1.2 must be simulated, which is done by switching the microwave pulse which ϕ_{ofs} is added to (the second pulse in configuration A, and the first pulse in configuration B). To simulate different points in time during a recorded trace of the experiment (like those shown in Fig. 3.28), the simulation is re-run with different values of ϕ_{ofs} to represent the different phases sampled throughout a period of the offset frequency. A set of $|c_2(t = t_{\mathrm{Final}})|^2$ values calculated at a range of offset phases ϕ_{ofs} corresponds to an experiment digitizer trace with a trace length of exactly one period of the offset frequency. Different numbers of offset phase ϕ_{ofs} samples used within $(0, 2\pi]$ showed no difference in calculated atomic signal phase so long as the the minimum of three samples required to determine the phase of a cosine with known frequency but unknown amplitude is used. To be cautious, the simulation was run with four phases ϕ_{ofs} sampled in all simulations.

In order to determine the linecentre of the simulated experiment, the process of running the simulation at multiple ϕ_{ofs} values to assemble a trace is repeated to obtain simulated traces at the same set of microwave frequencies as used in the experiment. The traces can then be analyzed in exactly the same way as described in Sec. 3.5: The phase of the simulated atomic signal relative to the offset phase ϕ_{ofs} is calculated using the inner product method, the phases are stitched into a nearly-straight line by removing the discontinuities, and then the lineshape function Eqn. (2.27) is fit to the phases as a function of microwave frequency.

5.1.3 Simulation Parameters

Time Step

The scale of the time step needed for the simulation is determined by the centre frequency of the transition, which corresponds to a period of approximately 30 ps. The time step h used in the simulation must be significantly smaller than 30 ps, but exactly how much smaller is best determined by running the simulation repeatedly while decreasing the step size and seeing where it converges with the known centre, as shown in Fig. 5.2. Based on this data, a time step of $h = 50\,\text{fs}$ was used.

Magnetic Fields

A dc background field of $B_x = B_y = 0, B_z = 4.762\,\text{G}$ was used in all integrations, except when explicitly stated otherwise. For the ac magnetic field, the amplitude of the vertical component of B at the centre of the waveguide for the fundamental TE_{10}

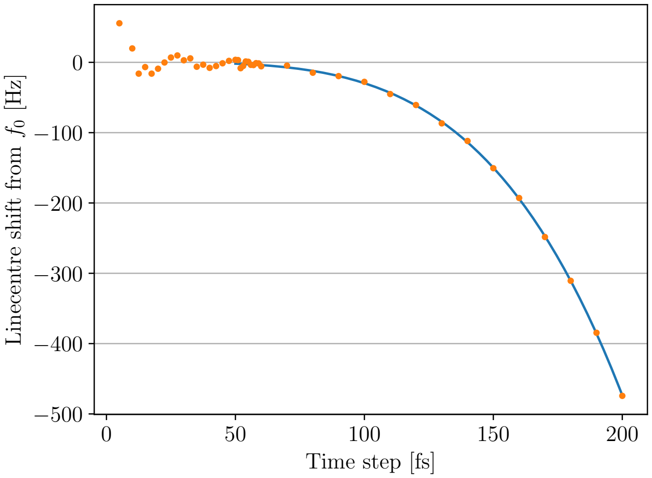

Figure 5.2: Convergence of the linecentre extracted from the simulation with perfect pulses as the time step h is reduced, with a fit to $f(h) = ah^4$ for $h \geq 50\,\mathrm{fs}$ shown. This is the expected shape: at large h, the global truncation error (which is proportional to h^4 for fourth-order Runge-Kutta) is the dominant source of error. At very small h, errors due to the finite precision of floating point numbers become dominant.

mode in WR-28 waveguide is given by [32]

$$B = \left[\frac{4P}{ab}\frac{\mu_0}{c}\left(1 - \frac{f_\mathrm{c}^2}{f^2}\right)^{-\frac{1}{2}}\right]^{\frac{1}{2}}, \tag{5.7}$$

where $a = 3.556\,\mathrm{mm}$ and $b = 7.112\,\mathrm{mm}$ are the waveguide dimensions, c is the speed of light, μ_0 is the vacuum permeability, and f and f_c are the microwave frequency and TE_{10} cutoff frequency respectively ($f_\mathrm{c} = 21.077\,\mathrm{GHz}$ for WR-28). Assuming that approximately 1 W reaches the atoms from the 15 W microwave amplifier (as described in Sec. 3.3.1), this gives $B = 0.3\,\mathrm{G}$ at 100% power and $f = 29.6\,\mathrm{GHz}$. This value is doubled at the position that the atoms pass through the waveguide due to the reflection caused by the waveguide short that is a half wavelength from this location.

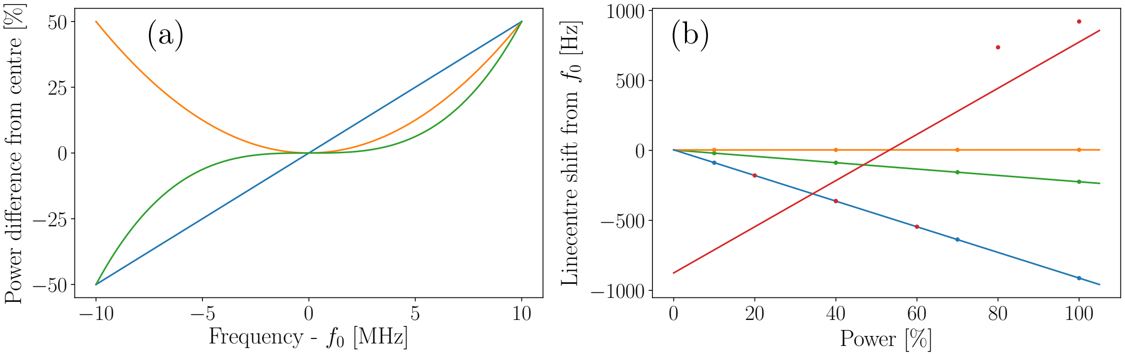

Figure 5.3: (a) Curves used to test the effect of power flatness in the simulation. All forms are chosen to give a very large 50% power difference 10 MHz from the centre in order to exaggerate any possible effect. (b) Linear power extrapolations for simulated $T = 300\,\text{ns}, D = 100\,\text{ns}$ experiments. In both panels blue is linear, orange is quadratic, and green is cubic. The red points show linear power flatness with the same magnitude of slope as blue, but with the sign reversed for $P \geq 80\%$.

5.2 Simulations

5.2.1 Power Flatness

A variety of forms of power variation versus frequency were tested, including linear, quadratic, and cubic, with some specific forms tested shown in Fig. 5.3(a) and results given in Table 5.1.Such power variations do not shift the linecentre (when extrapolated to zero power) at the ~5 Hz precision of the simulation. The small shifts are despite the fact that Fig. 5.3(a) shows exaggerated variations, with 50 % differences in power between the centre frequency and $f_0 \pm 10$ MHz, or 5 %/MHz in the linear case compared to the <0.1 %/MHz level of power flatness determined with atomic data from the experiment in Sec. 4.3.2.

To illustrate the relative insensitivity of a FOSOF phase measurement to an atomic signal amplitude measurement, the simulation can also be fit to the amplitude lineshape for a FOSOF pulse sequence (the $P(t) \propto \text{sinc}^2(D\Delta\omega/2)$ part of Eqn. (2.11)).

Power Flatness Shape	Shift in f_0 at 100% Power [Hz]	Zero-Power Extrapolated Centre [Hz]
Linear	-917	4
Quadratic	1	3
Cubic	-227	3
Linear, Reversing Sign	774	-876

Table 5.1: Results of simulations with the power curves shown in Fig. 5.3. The determined linecentres as a function of microwave power are shown in Fig. 5.3(b).

Fitting the data to this amplitude lineshape results in shifts of tens of kHz in the linecentre (compared to <5 Hz for FOSOF) for the power variation functions which are antisymmetric around the centre frequency. There is no net skew in the quadratic case, because the effect is the same on either side of f_0.

One possibility which can skew the extrapolated FOSOF linecentre is if the power flatness is not the same at different power levels. Then, the points lie on different extrapolation lines as shown by the red data in Fig. 5.3(b), and the zero-power extrapolated linecentre does not coincide with the true linecentre. However, this type of change of power flatness versus power cannot be an issue in the experiment, as the power flattening procedure is verified with atomic data to be effective to at worst 0.1 %/MHz in Sec. 4.3.2 at 100% microwave power.

Furthermore, it is also very unlikely for the power slope at different nominal microwave power settings to vary significantly. Although the measurements of microwave power used in the power flattening method described in Sec. 4.3.1 are subject to reflections within the microwave system which cause frequency-dependent offsets of the measured microwave power from the true value, the measured power at any given frequency is still proportional to the power seen by the atoms for the reasons discussed in Sec. 3.3.3 (i.e. the relationship is $P_{\text{Measured}}(f) = k(f)P_{\text{Actual}}(f)$, where k varies with microwave frequency but not power level). Therefore, the method used to flatten the microwave power as a function of frequency will perform equally well at every nominal power setting, and if there is any error in the power flatness it will be of the same form at every power setting.

5.2.2 Imbalanced Pulse Power

The difference in zero-power extrapolated linecentres between the FOSOF simulations with no imperfections and those with the power in one of the two pulses reduced to 50% was less than 0.01 Hz, indicating that this parameter is not a significant concern. This result holds independently for experiment types A and B of Fig. 2.3, i.e. it does not depend on the pulse order reversal to cancel the imperfection.

5.2.3 Amplitude and Phase Distortions in Microwave Pulses

Microwave switches are known to cause phase chirps in the transmitted signal as they switch states, with the duration of the chirp being approximately the same as the switching time. This chirp effect has been observed directly in the 2^3P_2-to-2^3P_1 measurement, and indirectly in the current measurement, as described in Sec. 4.15.3. It is plausible that this chirp could cause a systematic effect in a FOSOF experiment since the relative phases of the pulses are of critical importance. A set of simulated chirps is shown in Fig. 5.4. These chirps are exaggerated (compared to those from the experiment shown in Fig. 4.22) by shifting the time when they occur to significantly overlap with the period where the pulse amplitude is still a significant fraction of the peak amplitude (compared to the experiment data where the large phase shifts occur only when the pulse amplitude is nearly zero). They are also exaggerated in the particular form they take: if all four chirps are equal, their effects cancel and they do not cause any shift. The second row of Fig. 4.22 shows that this is approximately the

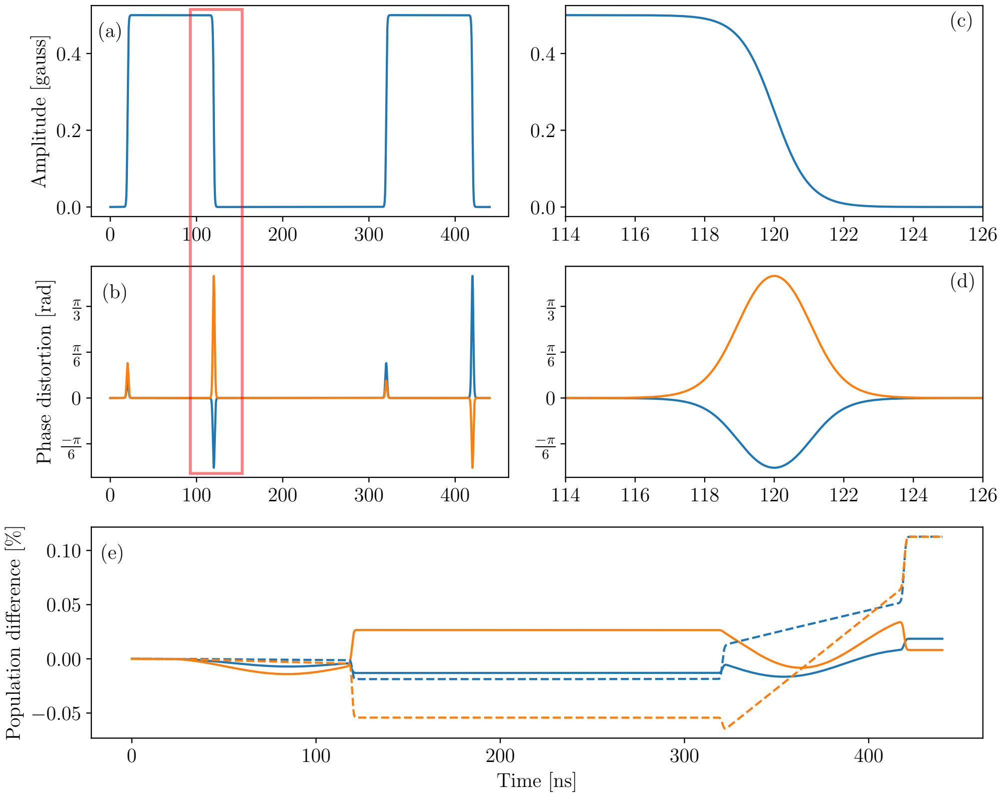

Figure 5.4: (a) and (b): Constructed amplitude and phase profiles for the simulation with large phase chirps at the beginnings and ends of pulses. (c) and (d): Amplitude and phase profiles zoomed in on the end of the first pulse, as highlighted in red on (a) and (b). Note that the amplitude profile has a gradual turn-off, rather than instantaneous. In all plots the orange and blue lines represent the two pulse orders of a FOSOF experiment. The amplitude profile is the same for both pulse orders. (e): The difference in population evolution between the cases with and without phase chirps, as a percentage of the total population. The solid traces were simulated at $f = f_0 - 7.5\,\text{MHz}$, close to the first zero of the $D = 100$ amplitude lineshape at $f_0 - 10\,\text{MHz}$. The dashed traces are on resonance, where both pulse orders cause the same deviation from the ideal case.

case in the experiment. Other simulations show that if the chirps differ between the two pulses, they cause a large (~10 kHz) shift which is removed by the pulse order reversal shown in Fig. 2.3. The simulated chirps shown in Fig. 5.4 differ significantly both within each pulse and between pulses, exaggerating the shift in two separate ways.

When simulating the chirps shown in Fig. 5.4, if the pulse order reversal (described in Sec. 2.1.2) is not performed, the zero-power extrapolated centre is shifted by approximately 8.7 kHz. This shift goes to zero when the pulse order reversal is included, returning the same extrapolated centre as the ideal case and a 0-100% power shift of only 29 Hz. Many other chirp patterns were simulated, including randomizing the magnitudes of the chirps (between -1 and 1 rad) at each frequency, but there were no significant differences in the results compared to the case shown here.

5.2.4 Imperfect Polarizations

In order to simulate the effects of having both imperfect state-preparation laser and microwave polarization, simulations were run with a starting state which had some population in $2^3\mathrm{P}_1$ $m_J = \pm 1$ and $m_J = 0$ and a component of the microwave field along the y axis corresponding to a specified angle between the waveguide polarization axis and the dc magnetic field.

As an extreme case, the simulation was run starting with one third of the population in each of the three m_J sublevels of $2^3\mathrm{P}_1$, and the polarization of the microwaves rotated 5° away from the z axis towards the y axis. This imperfection causes very large shifts which strongly depend on the dc magnetic field strength as shown in Fig. 5.5. The effect is more pronounced at low fields, as the Δm_J transitions are Zeeman shifted less and move closer in frequency to the $\Delta m_J = 0$ resonance. Simulations run

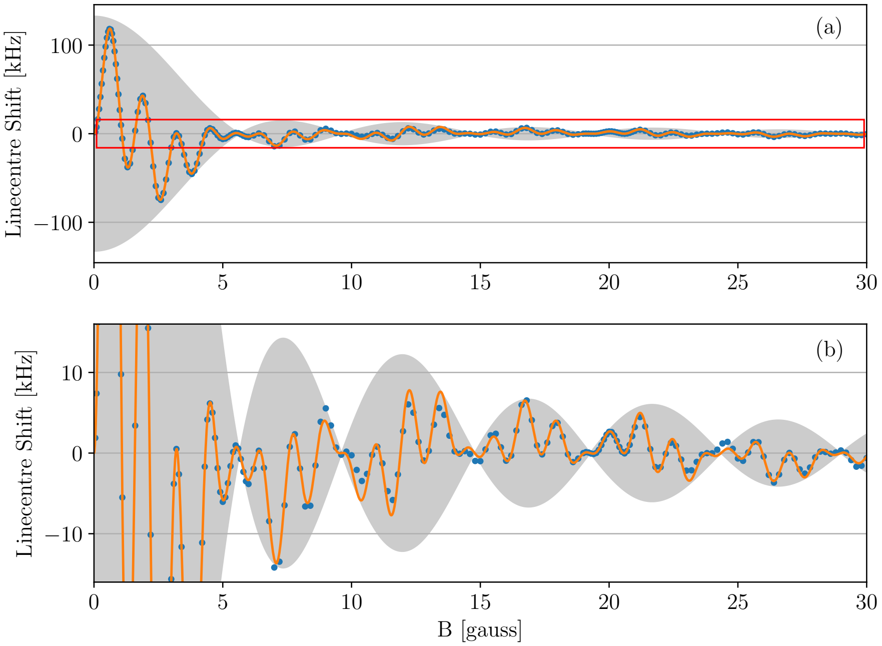

Figure 5.5: (a): The results of a simulation with microwave polarization misaligned with the dc magnetic field. For these runs, the polarization is rotated 5° in the $\hat{\mathbf{y}}$ direction, and the initial population is equally distributed between the three m_J sublevels of $2^3\mathrm{P}_1$. (b): a zoomed-in view of the area highlighted in (a). Blue dots: simulation results, orange line: a fit to Eqn. (5.8), shaded area: the envelope described by the first term of Eqn. (5.8).

with either of these polarization imperfections removed do not show this effect, as expected. The effect also disappears if the matrix elements for the transitions from $2^3\mathrm{P}_1(m_J = \pm 1)$ to $2^3\mathrm{P}_0$ are set to zero, which verifies that these transitions cause this shift. Simulations run with different parameters show that changing the polarization angle of the microwaves or the population in the $m_J = \pm 1$ states only changes the scale of these oscillations, and have no effect on the shape as a function of B.

The frequency shift as a function of dc magnetic field is approximately described by the empirically determined relationship

$$\Delta f(B) = \left[A_1 \operatorname{sinc}\left(\frac{B}{\tau_1}\right) + A_2 \operatorname{sinc}^2\left(\frac{B}{\tau_2}\right)\right] \times \\ \left[\frac{1}{2}\left(\sin\left(2\pi\frac{B-B_1}{T_1}\right) + \sin\left(2\pi\frac{B-B_2}{T_2}\right)\right)\right], \quad (5.8)$$

where the subscripted variables are floating fit parameters, and $\operatorname{sinc}(x) = \sin(x)/(x)$.

In the experiment, unwanted population in the $m_J = \pm 1$ states can be eliminated by perfect optical pumping and maintaining perfect state-preparation laser polarization, and efforts have been made to ensure that both of these parameters are close to perfect in the experiment, as described in Sec. 4.6.1. Further investigation of this interference effect would allow magnetic fields to be chosen in the experiment for each T, D combination which correspond to zero interference shift. However, the 20 Hz-level consistency between data taken at different B field values (Fig. 4.1), and the consistency when driving the microwave transition from $2^3\mathrm{P}_1$ to $2^3\mathrm{P}_0$ and vice versa (Sec. 4.10) indicate that this effect is sufficiently well-controlled.

5.2.5 Microwave Isolation

In order to determine the effect of coupling between the two arms of the microwave system, as described in Sec. 4.11, simulations were run for the scenario of a single switch allowing some of the microwave power through both paths at all times, as illustrated in Fig. 5.6. This imperfection corresponds to a perturbation of

$$H'_{\mathrm{lu}}(t) = \begin{cases} \epsilon_{\mathrm{L}} B_0(\cos(\omega t + \phi_{\mathrm{S}}) + \cos(\omega t + \phi_{\mathrm{ofs}} + \phi_{\mathrm{S}})) & \text{In between pulses} \\ B_0(\cos(\omega t) + \epsilon_{\mathrm{L}} \cos(\omega t + \phi_{\mathrm{ofs}} + \phi_{\mathrm{S}})) & \text{During first pulse} \\ B_0(\cos(\omega t + \phi_{\mathrm{ofs}}) + \epsilon_{\mathrm{L}} \cos(\omega t + \phi_{\mathrm{S}})) & \text{During second pulse} \end{cases} \quad (5.9)$$

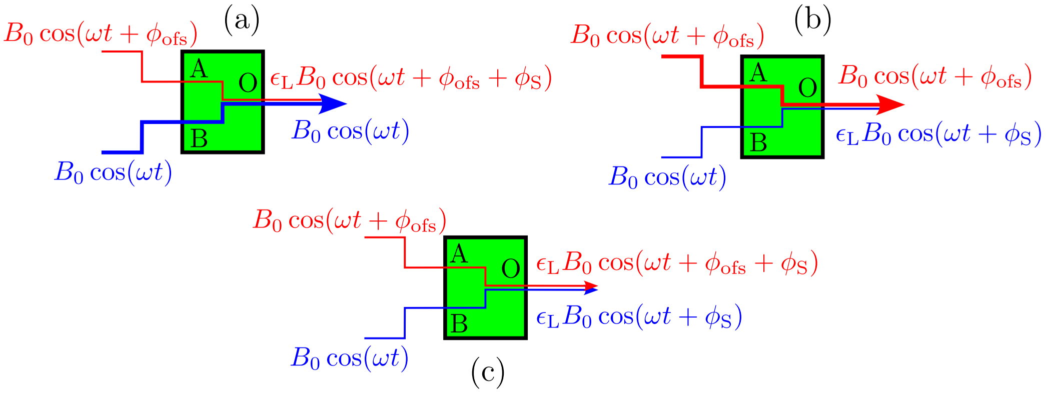

Figure 5.6: An illustration of the interference paths corresponding to the cases in Eqn. (5.9). Green rectangles are switches with two input ports (A and B) and one output (O). In (a), the path AO is disabled, allowing only a small fraction of the microwave power at A to reach O. Path BO is transmitting, and treated as lossless. This configuration corresponds to the first pulse (second case of Eqn. (5.9)). (b) is the reverse of (a), corresponding to the second pulse (third case of Eqn. (5.9)). (c) has both paths disabled, corresponding to the times when both pulses are off (first case of Eqn. (5.9)).

where $\phi_{\rm ofs}$ represents the offset phase as described in Sec. 5.1.2, $\epsilon_{\rm L}$ is a small amplitude of leakage through the switches (see Fig. 5.6), and $\phi_{\rm S}$ represents the phase difference of microwaves which travel a different path to reach the output of the switch. For experiment type B (of Fig. 2.3), $\phi_{\rm ofs}$ is shifted to the other cosine in every case.

The simulation is run at a range of $\phi_{\rm S}$ values, and three microwave powers at each $\phi_{\rm S}$ in order to extrapolate the linecentre to zero microwave power in each case. Simulated shifts for the zero-power extrapolation are similar to the 100% power shifts, as shown in Fig. 5.7. The leakage amplitude of $\epsilon_{\rm L} = 10^{-2}$ (corresponding to 40 dB of attenuation) is highly exaggerated compared to the leakage expected from our 100 dB of isolation (as discussed in Sec. 4.11), which would lead to $\epsilon_{\rm L} = 10^{-5}$.

The effect of this leakage is almost independent of power (to within 15 Hz). This effect is not cancelled out by the FOSOF reversal of Fig. 2.3. The shift as a function

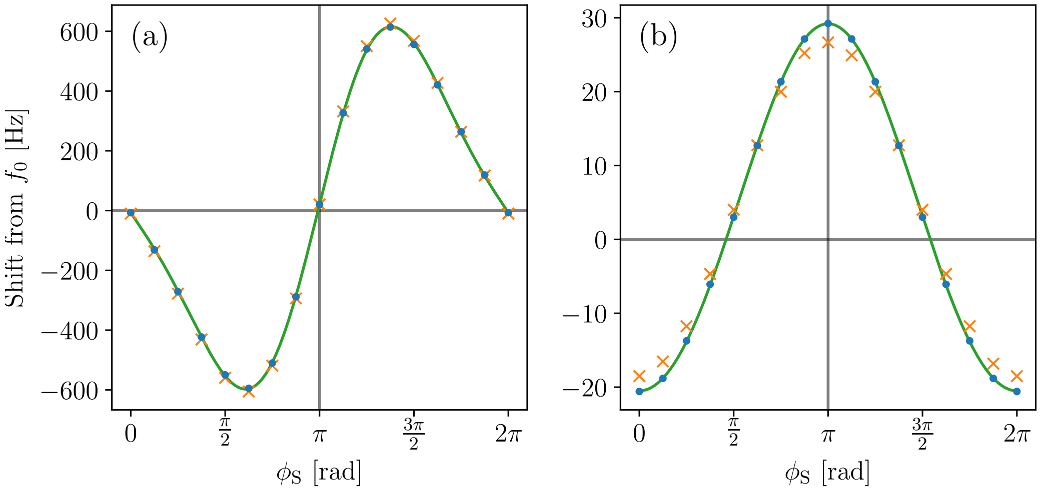

Figure 5.7: (a) Results of simulations run for a range of ϕ_S values for $\epsilon_L = 10^{-2}$. (b) Results of simulations run with the same conditions as (a), but $\epsilon_L = 0$ when the pulses are off (case 1 of Eqn. (5.9)). In both cases the orange crosses are the 100% microwave power linecentres, the blue dots are zero-power extrapolated linecentres, and the green lines are fits of the extrapolated linecentres to Eqn. (5.10), with values provided in Table 5.2.

Case	A_1[Hz]	A_2[Hz]	ϕ_1[rad]/π	ϕ_2[rad]/π
(a)	557	-129	0.993	0.497
(b)	24.8	-0.616	0.500	0.250

Table 5.2: Fits to Eqn. (5.10) for cases (a) and (b) of Fig. 5.7.

of ϕ_S is described by

$$\Delta f(\phi_S) = A_1 \sin(\phi_S - \phi_1) + A_2 \sin(\phi_S - \phi_2), \tag{5.10}$$

where the A_i and ϕ_i are fit parameters, with values provided in Table 5.2. Further simulations show that the size of the linecentre shift due to this effect is proportional to ϵ_L. The magnitude of this shift for the always-on case (Eqn. (5.9) as written) is strongly dependent on the frequency range used in the analysis, as discussed in Sec. 5.3.

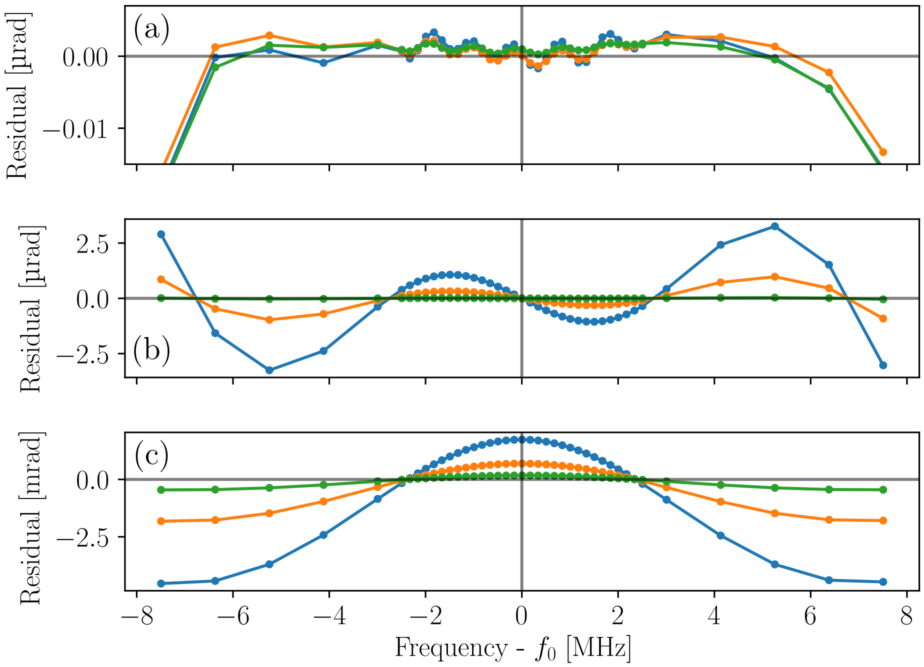

Figure 5.8: Residuals from fitting simulation results to Eqn. (2.27). Note the factor of 1000 difference in y axis units for (c). In each plot, the 100% power residuals are blue, the 55% power residuals are orange, and 10% power is green. (a) shows the results from simulating the perfect pulses of Fig. 5.1, (b) for pulses with a 50% power difference between them (as in Sec. 5.2.2), and (c) for a 5 %/MHz linear power slope (as in Sec. 5.2.1).

5.3 Relationship to Systematic Effect of Unknown Origin

The systematic effect of unknown origin described in Sec. 4.15 is evident in experiment data as a shift in the linecentre when we exclude from the analysis data recorded at frequencies further than $1/(8D)$ from the linecentre, even when extrapolating to zero power. This behaviour implies that the fit residuals have a component which is symmetric around the linecentre, and such a structure is visible in Fig. 4.18(c). This relationship between symmetric residuals and frequency-dependent shifts exists because the fitting procedure minimizes the uncertainty-weighted sum of squared errors,

$$\chi^2 = \sum_{i=1}^{N} \left(\frac{y_i - f(x_i, \mathbf{p})}{\sigma_i} \right)^2 , \tag{5.11}$$

where (x_i, y_i) are the data points, σ_i are the corresponding uncertainties, $f(x_i, \mathbf{p})$ is the function to be fit, and $\mathbf{p}$ is the list of fit parameters which are adjusted to minimize Eqn. (5.11). For the FOSOF lineshape, Eqn. (2.27), adjusting the values of V and D only affects the small nonlinear part of the lineshape shown in Fig. 2.6(b). Adjusting value of T changes the slope, and adjusting the value of f_0 translates the function along the x axis (which, for an approximately straight line, is equivalent to a translation along the y axis scaled by the slope $2\pi T$). Therefore, adding a constant phase ϕ' to the phase determined at every frequency will shift the linecentre determined from the fit by $\Delta f = \phi'/(2\pi T) = 530\,\mathrm{Hz/mrad}$ for $T = 300\,\mathrm{ns}$. In an approximate sense, adding a residual which is symmetric around the linecentre has the effect of adding a constant phase which varies depending on the frequency range used in the fit, because the main change it will cause to the calculated fit parameters (when considering the scale of T, D, V, and shifts in f_0 which are relevant to this experiment) is to shift the linecentre determined from the fit.

The residuals for fits to simulated experiments in Fig. 5.8 show a range of behaviours, and illustrate again why these effects cannot be responsible for the frequency range-dependent shift in the experiment data. In case (a), corresponding to a simulation with no intentional imperfections, the residuals are extremely small ($0.01\,\mu\mathrm{rad}$ corresponds to a shift of $0.005\,\mathrm{Hz}$ at $T = 300\,\mathrm{ns}$), and are attributable to errors in the simulation due to the finite precision of floating point numbers. In case (b) (strongly imbalanced pulse powers), the residuals are still very small, and are also antisymmetric around the linecentre, so that decreasing the frequency range does not shift the measured linecentre. In addition to this, the residuals extrapolate to zero at zero power. In

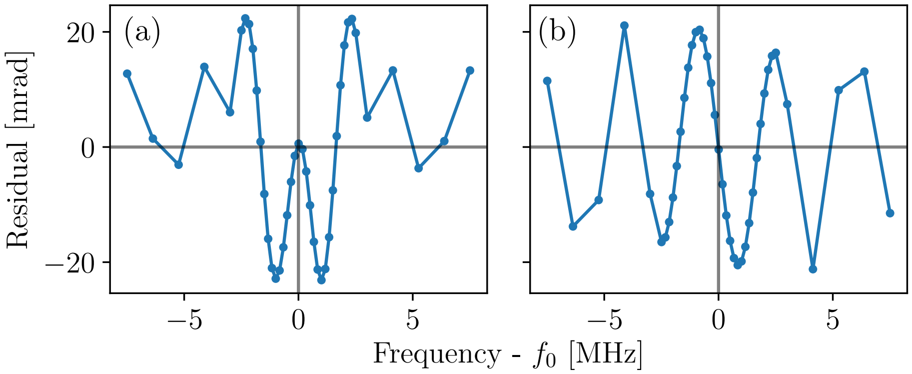

Figure 5.9: Residuals from fitting simulation results with poor switch isolation to Eqn. (2.27). Case (a) corresponds to the $\phi_\mathrm{S} = \pi/2$ point of Fig. 5.7(a) (ϵ_L always on), and (b) corresponds to the $\phi_\mathrm{S} = \pi$ point of Fig. 5.7(b) (ϵ_L only on during pulses).

case (c) (very poor 5 %/MHz power flatness), the magnitude of the residuals is large (1 mrad corresponds to 530 Hz), and the residuals are symmetric so that reducing the frequency range will alter how much they shift the linecentre. However, the residuals again extrapolate to zero at zero microwave power, and so do not cause a shift in the extrapolated linecentre.

Fig. 5.9 shows the residuals from simulating the poor switch isolation described in Sec. 5.2.5. Both cases have residuals at a very large scale (20 mrad corresponds to 10.6 kHz), but in case (b) the residuals are fortuitously antisymmetric around the linecentre and do not cause a significant net shift at any frequency range. In the residuals of case (a), however, all problems are present: The residuals are very large, they are symmetric around f_0, and they do not extrapolate to zero at zero power (they are almost completely independent of power). These properties illustrate why this potential systematic effect is the most dangerous, and why care is taken to ensure that the two microwave paths are isolated to at least 100 dB. Even with this level of isolation, if the analysis is restricted to $|f - f0| \leq 1/(8D)$, the values of A_1 and A_2 from Table 5.2 increase to 7437 Hz and 202 Hz, respectively (the ϕ_i values are unchanged). To conservatively estimate the size of the shift due to this effect in the current experiment, we take the 20 mrad (10.6 kHz) maximum magnitude of the residuals, and scale from the simulated $\epsilon_{\mathrm{L}} = 10^{-2}$ to the value for the 100 dB of isolation we have in our experiment, $\epsilon_{\mathrm{L}} = 10^{-5}$. This gives a maximum shift in the experiment of 10.6 Hz, which is half of the 20 Hz precision goal (and corresponds closely to the 5 Hz maximum shift due to 100 dB of isolation estimated in Sec. 4.11), and shows that the isolation between microwave paths must be controlled to a very high level to complete a measurement at this level of precision. If any such problem exists in a measurement, it should show as a frequency range-dependent shift in the linecentre, though even this conservative estimate gives a maximum shift an order of magnitude smaller than the one seen in the current experiment.

6 Conclusion

Significant progress has been made towards a 20 Hz-precision measurement of the $2^3\mathrm{P}_1$-to-$2^3\mathrm{P}_0$ fine-structure interval in helium using the frequency-offset separated oscillatory fields (FOSOF) technique. The FOSOF technique is described in Chapter 2. The investigation of a large number of systematic effects is described in Chapter 4, with the results of most of these investigations summarized in Fig. 4.1 and Table 4.1. A shift in the measured linecentre observed when excluding data recorded at microwave frequencies farther than $f_0 \pm 1/(8D)$ from the resonant frequency of the transition from the analysis remains as an unresolved problem, after numerous avenues of investigation were explored, as described in Sec. 4.15. The development of a numerical model to simulate the experiment is described in Chapter 5. This model is used to estimate the magnitudes of shifts caused by various imperfections in the experiment, to determine whether the shifts caused by these imperfections extrapolate to zero at zero microwave power, and show that the modelled imperfections are too small to be responsible for the unresolved systematic effect described in Sec. 4.15.

In order to complete a measurement of the $2^3\mathrm{P}_1$-to-$2^3\mathrm{P}_0$ interval in helium to a precision of 20 Hz, the unresolved frequency range-dependent systematic effect must be controlled. The microwave system described in Sec. 3.3.1 could be improved to potentially reduce the size of the systematic effect by further improving isolation between the two microwave paths, and to increase the size of the atomic signal by reducing losses incurred between the output of the amplifier and the point where the atoms interact with the microwaves. Recent advances in solid-state microwave amplifiers in the 29.6 GHz band have also enabled an order of magnitude more power to be obtained within our research budget. Increased signal size will improve the rate at which statistical uncertainty in the linecentre can be reduced, and therefore the pace at which systematic effects can be tested.

Subsequent to the work described in this dissertation, a measurement of the 2^3P_1-to-2^3P_0 interval to a precision of 60 Hz was submitted for publication[34] by our group. I continued to contribute to this effort, and am listed as an author on that submission. This measurement follows the framework for testing systematic effects which I developed. The final value obtained for the frequency of the 2^3P_1-to-2^3P_0 interval is 29 616 955 018(60) Hz, with all systematic effects well-controlled and the residuals of the fits to the FOSOF lineshape consistent with zero with no underlying structure (and therefore the determined linecentre does not depend on the analysis frequency range). This result is consistent with both the wide frequency range linecentre (which is 41 Hz below the final value, and shown by the horizontal red line in Fig. 4.1) and narrow frequency range linecentre (which is 56 Hz above the final value, and shown as the red horizontal line in Fig. 4.19) from this work.

A completed 20 Hz measurement of the 29.6 GHz 2^3P_1-to-2^3P_0 interval could be combined with our already-completed[20] 25 Hz measurement of the 2.3 GHz 2^3P_2-to-2^3P_1 interval to obtain a 1 ppb determination of the combined 31.9 GHz 2^3P_2-to-2^3P_0 interval. When combined with a sufficiently precise theoretical calculation of the same interval, a 0.5 ppb determination of the fine-structure constant could be obtained for the first time ever in a multi-electron system, allowing tests of multi-electron QED and multiple effects of physics beyond the Standard Model.

A Table of Condensed Experiment Data

The total number of experiment runs collected during the research presented in this dissertation exceeds 8000, and so only a condensed summary table of the data is presented here. The data is condensed by defining a combination of T, D, P, B, m_J, and f_{ofs} as one configuration of the experiment, and taking the weighted (by the linecentre fit uncertainty) average of all the data in each configuration. The acronyms used to describe special data types for systematic tests in the final column are:

- NR: Normal Run
- LSPP: Low State-Preparation Power (laser power reduced to 25%)
- L447P: Low 447 nm Power (laser power reduced to 25%)
- 18F: Data taken using the 18F Rydberg state for detection
- MWDR: Microwave Direction Reversed (driving the FOSOF transition from 2^3P_0 to 2^3P_1).

The "Relative fit centre" column is the corrected (Zeeman and extrapolation slope) linecentre relative to the average calculated by multiplying the fit centre for each configuration with the corresponding value in the weight column and summing them. The weights are calculated with an optimization routine described in Sec. 4.4.2.

Table A.1: Summary of Experiment Runs

Experiment number N_{Exp}	Pulse separation T [ns]	Pulse duration D [ns]	Microwave power P [%]	Magnetic field B [G]	Optical pumping m_J state	Offset frequency f_{ofs} [Hz]	Relative fit centre ν_{Fit} [Hz]	Total error $\Delta\nu_0$ [Hz]	Fit uncertainty $\Delta\nu_{\mathrm{Fit}}$ [Hz]	Slope error $\Delta\nu_{\mathrm{Slope}}$ [Hz]	Zeeman shift error $\Delta\nu_{\mathrm{B}}$ [Hz]	Experiment duration D_{Exp} [h]	Weight W [%]	Data type
1	300	50	20	−4.762	−1	−280	125	139	138	8.8	4.5	2.1	0.0880	NR
2	300	50	20	−4.762	−1	280	−93	93	93	8.8	4.5	7.3	0.2018	NR
3	300	50	20	−4.762	1	280	−169	81	80	8.8	4.5	9.9	0.2605	NR
4	300	50	20	4.762	−1	280	59	88	88	8.8	4.5	10.1	0.2187	NR
5	300	50	20	4.762	1	−280	30	147	147	8.8	4.5	2.1	0.0795	NR
6	300	50	20	4.762	1	280	131	89	89	8.8	4.5	8.7	0.2126	NR
7	300	50	40	−4.762	−1	−280	119	153	152	17.6	4.5	1.4	0.0003	NR
8	300	50	40	−4.762	−1	280	−166	101	99	17.6	4.5	3.2	0.0006	NR
9	300	50	40	−4.762	1	280	−114	86	84	17.6	4.5	5.7	0.0002	NR
10	300	50	40	4.762	−1	280	114	98	97	17.6	4.5	5.6	0.0001	NR
11	300	50	40	4.762	1	−280	271	133	132	17.6	4.5	1.4	0.0002	NR
12	300	50	40	4.762	1	280	175	114	113	17.6	4.5	3.0	0.0002	NR
13	300	50	60	−4.762	−1	−280	296	136	133	26.4	4.5	0.8	0.0006	NR
14	300	50	60	−4.762	−1	280	−182	114	110	26.4	4.5	1.9	0.0006	NR
15	300	50	60	−4.762	1	−280	77	320	319	26.4	4.5	0.2	0.0005	NR
16	300	50	60	−4.762	1	280	−95	95	92	26.4	4.5	3.8	0.0001	NR
17	300	50	60	4.762	−1	−280	−309	357	356	26.4	4.5	0.2	0.0001	NR
18	300	50	60	4.762	−1	280	−16	103	99	26.4	4.5	3.7	0.0006	NR
19	300	50	60	4.762	1	−280	−6	162	160	26.4	4.5	0.8	0.0004	NR
20	300	50	60	4.762	1	280	−107	124	121	26.4	4.5	1.8	0.0001	NR
21	300	50	80	−4.762	−1	−280	124	146	141	35.2	4.5	0.8	0.0005	NR
22	300	50	80	−4.762	−1	280	−209	112	106	35.2	4.5	1.7	0.0003	NR
23	300	50	80	−4.762	1	280	−48	95	88	35.2	4.5	3.5	0.0005	NR
24	300	50	80	4.762	−1	280	−225	93	86	35.2	4.5	3.4	0.0008	NR
25	300	50	80	4.762	1	−280	−42	126	120	35.2	4.5	0.8	0.0000	NR
26	300	50	80	4.762	1	280	−39	108	102	35.2	4.5	1.9	0.0005	NR
27	300	50	100	−4.762	−1	−280	−177	123	115	44.0	4.5	0.8	0.0005	NR
28	300	50	100	−4.762	−1	280	42	85	72	44.0	4.5	2.7	0.0000	NR
29	300	50	100	−4.762	1	280	−95	84	72	44.0	4.5	3.9	0.0001	NR
30	300	50	100	4.762	−1	280	90	91	80	44.0	4.5	3.7	0.0005	NR
31	300	50	100	4.762	1	−280	−31	126	118	44.0	4.5	0.8	0.0006	NR
32	300	50	100	4.762	1	280	154	84	71	44.0	4.5	3.3	0.0001	NR
33	300	100	20	−19.048	−1	280	884	732	728	2.5	71.9	0.4	0.0004	NR
34	300	100	20	−14.286	1	280	53	193	189	2.5	40.5	1.2	0.0007	NR
35	300	100	20	−9.524	−1	−280	36	104	102	2.5	18.0	1.4	0.0002	NR
36	300	100	20	−9.524	−1	280	−53	115	114	2.5	18.0	1.9	0.0001	NR
37	300	100	20	−9.524	1	−280	108	169	168	2.5	18.0	1.2	0.0001	NR
38	300	100	20	−9.524	1	280	154	120	119	2.5	18.0	2.8	0.0000	NR
39	300	100	20	−8.248	−1	−280	−234	121	121	2.5	13.5	1.1	0.0523	NR
40	300	100	20	−8.248	−1	280	95	126	126	2.5	13.5	1.1	0.0513	NR
41	300	100	20	−8.248	1	−280	28	132	131	2.5	13.5	1.8	0.0463	NR
42	300	100	20	−8.248	1	280	242	129	129	2.5	13.5	1.7	0.0457	NR
43	300	100	20	−6.734	−1	−280	140	123	122	2.5	9.0	1.1	0.1961	NR
44	300	100	20	−6.734	−1	280	37	128	128	2.5	9.0	1.1	0.1786	NR
45	300	100	20	−6.734	1	−280	−95	108	107	2.5	9.0	1.7	0.2489	NR
46	300	100	20	−6.734	1	280	−267	131	131	2.5	9.0	1.7	0.1666	NR
47	300	100	20	−5.000	−1	−280	−733	828	828	2.5	5.0	2.5	0.0095	NR
48	300	100	20	−5.000	−1	280	−1086	1261	1261	2.5	5.0	1.5	0.0052	NR
49	300	100	20	−5.000	1	−280	210	719	719	2.5	5.0	2.6	0.0105	NR
50	300	100	20	−5.000	1	280	803	866	866	2.5	5.0	1.4	0.0072	NR
51	300	100	20	−4.762	−1	−280	−2	42	42	2.5	4.5	15.3	2.8015	NR
52	300	100	20	−4.762	−1	280	44	36	35	2.5	4.5	24.4	4.0124	NR
53	300	100	20	−4.762	1	−280	−20	47	47	2.5	4.5	14.5	2.2757	NR
54	300	100	20	−4.762	1	280	10	37	37	2.5	4.5	23.3	3.6381	NR
55	300	100	20	4.762	−1	−280	34	49	49	2.5	4.5	14.6	2.0523	NR

Table continues on next page

Table A.1: Continued from previous page

N_{Exp}	T [ns]	D [ns]	P [%]	B [G]	m_J	f_{ofs} [Hz]	ν_{Fit} [Hz]	$\Delta\nu_0$ [Hz]	$\Delta\nu_{\mathrm{Fit}}$ [Hz]	$\Delta\nu_{\mathrm{Slope}}$ [Hz]	$\Delta\nu_{\mathrm{B}}$ [Hz]	D_{Exp} [h]	W [%]	Data type
56	300	100	20	4.762	−1	280	88	40	40	2.5	4.5	22.7	3.1439	NR
57	300	100	20	4.762	1	−280	11	43	43	2.5	4.5	15.1	2.7288	NR
58	300	100	20	4.762	1	280	51	35	35	2.5	4.5	23.6	4.1042	NR
59	300	100	20	5.000	−1	−280	−599	653	653	2.5	5.0	1.6	0.0135	NR
60	300	100	20	5.000	−1	280	−69	663	663	2.5	5.0	1.6	0.0114	NR
61	300	100	20	5.000	1	−280	857	763	763	2.5	5.0	3.0	0.0119	NR
62	300	100	20	5.000	1	280	−7	755	755	2.5	5.0	2.7	0.0098	NR
63	300	100	20	6.734	−1	−280	92	132	131	2.5	9.0	1.7	0.1714	NR
64	300	100	20	6.734	−1	280	202	135	134	2.5	9.0	1.7	0.1537	NR
65	300	100	20	6.734	1	−280	−5	128	128	2.5	9.0	1.1	0.1783	NR
66	300	100	20	6.734	1	280	32	123	122	2.5	9.0	1.1	0.1894	NR
67	300	100	20	8.248	−1	−280	110	119	118	2.5	13.6	1.7	0.0558	NR
68	300	100	20	8.248	−1	280	99	132	131	2.5	13.6	1.7	0.0519	NR
69	300	100	20	8.248	1	−280	214	128	128	2.5	13.6	1.1	0.0458	NR
70	300	100	20	8.248	1	280	183	116	115	2.5	13.6	1.1	0.0629	NR
71	300	100	20	9.524	−1	−280	41	135	134	2.5	18.0	1.2	0.0003	NR
72	300	100	20	9.524	−1	280	201	115	113	2.5	18.0	3.1	0.0004	NR
73	300	100	20	9.524	1	−280	129	109	108	2.5	18.0	1.4	0.0005	NR
74	300	100	20	9.524	1	280	87	109	108	2.5	18.0	1.8	0.0004	NR
75	300	100	20	14.286	−1	280	−514	294	291	2.5	40.6	1.0	0.0004	NR
76	300	100	20	19.048	1	280	35	493	488	2.5	72.1	0.4	0.0006	NR
77	300	100	40	−19.048	−1	280	−463	795	792	5.1	71.9	0.2	0.0008	NR
78	300	100	40	−14.286	1	280	129	191	187	5.1	40.5	1.0	0.0002	NR
79	300	100	40	−9.524	−1	−280	182	112	110	5.1	18.0	1.0	0.0003	NR
80	300	100	40	−9.524	−1	280	−106	107	105	5.1	18.0	1.2	0.0003	NR
81	300	100	40	−9.524	1	−280	148	170	169	5.1	18.0	0.5	0.0000	NR
82	300	100	40	−9.524	1	280	−58	113	112	5.1	18.0	1.7	0.0006	NR
83	300	100	40	−8.248	−1	−280	−51	131	130	5.1	13.5	0.7	0.0008	NR
84	300	100	40	−8.248	−1	280	−68	123	123	5.1	13.5	0.7	0.0008	NR
85	300	100	40	−8.248	1	−280	84	116	116	5.1	13.5	1.0	0.0001	NR
86	300	100	40	−8.248	1	280	59	127	126	5.1	13.5	1.0	0.0005	NR
87	300	100	40	−6.734	−1	−280	30	129	129	5.1	9.0	0.5	0.0969	NR
88	300	100	40	−6.734	−1	280	69	160	160	5.1	9.0	0.5	0.0668	NR
89	300	100	40	−6.734	1	−280	19	110	110	5.1	9.0	1.0	0.1330	NR
90	300	100	40	−6.734	1	280	−98	123	122	5.1	9.0	1.0	0.1125	NR
91	300	100	40	−5.000	−1	−280	181	523	523	5.1	5.0	2.7	0.0132	NR
92	300	100	40	−5.000	−1	280	−1458	462	462	5.1	5.0	3.4	0.0172	NR
93	300	100	40	−5.000	1	−280	−1005	431	431	5.1	5.0	5.1	0.0203	NR
94	300	100	40	−5.000	1	280	−771	426	426	5.1	5.0	4.9	0.0217	NR
95	300	100	40	−4.762	−1	−280	−2	40	40	5.1	4.5	10.1	2.2828	NR
96	300	100	40	−4.762	−1	280	−52	37	36	5.1	4.5	13.2	2.8504	NR
97	300	100	40	−4.762	1	−280	−7	44	44	5.1	4.5	8.9	1.9501	NR
98	300	100	40	−4.762	1	280	6	40	39	5.1	4.5	12.3	2.3929	NR
99	300	100	40	4.762	−1	−280	−52	45	44	5.1	4.5	9.9	1.8545	NR
100	300	100	40	4.762	−1	280	−80	40	40	5.1	4.5	12.0	2.3076	NR
101	300	100	40	4.762	1	−280	−37	44	44	5.1	4.5	8.9	1.9245	NR
102	300	100	40	4.762	1	280	28	37	37	5.1	4.5	13.1	2.7589	NR
103	300	100	40	5.000	−1	−280	−328	406	406	5.1	5.0	4.1	0.0216	NR
104	300	100	40	5.000	−1	280	−1116	429	429	5.1	5.0	3.7	0.0197	NR
105	300	100	40	5.000	1	−280	41	423	422	5.1	5.0	4.4	0.0194	NR
106	300	100	40	5.000	1	280	−291	498	498	5.1	5.0	3.1	0.0152	NR
107	300	100	40	6.734	−1	−280	−49	157	156	5.1	9.0	1.0	0.0649	NR
108	300	100	40	6.734	−1	280	−186	138	137	5.1	9.0	1.0	0.0835	NR
109	300	100	40	6.734	1	−280	−74	116	115	5.1	9.0	0.5	0.1139	NR
110	300	100	40	6.734	1	280	−103	127	127	5.1	9.0	0.5	0.0971	NR
111	300	100	40	8.248	−1	−280	−202	135	134	5.1	13.6	1.0	0.0006	NR
112	300	100	40	8.248	−1	280	1	113	112	5.1	13.6	1.0	0.0006	NR
113	300	100	40	8.248	1	−280	−170	110	110	5.1	13.6	0.7	0.0007	NR
114	300	100	40	8.248	1	280	−27	135	134	5.1	13.6	0.7	0.0008	NR
115	300	100	40	9.524	−1	−280	452	184	183	5.1	18.0	0.5	0.0002	NR

Table continues on next page

Table A.1: Continued from previous page

N_{Exp}	T [ns]	D [ns]	P [%]	B [G]	m_J	f_{ofs} [Hz]	ν_{Fit} [Hz]	$\Delta\nu_0$ [Hz]	$\Delta\nu_{\mathrm{Fit}}$ [Hz]	$\Delta\nu_{\mathrm{Slope}}$ [Hz]	$\Delta\nu_{\mathrm{B}}$ [Hz]	D_{Exp} [h]	W [%]	Data type
116	300	100	40	9.524	−1	280	−5	116	114	5.1	18.0	1.9	0.0008	NR
117	300	100	40	9.524	1	−280	23	98	96	5.1	18.0	1.0	0.0003	NR
118	300	100	40	9.524	1	280	81	103	101	5.1	18.0	1.2	0.0008	NR
119	300	100	40	14.286	−1	280	−91	203	199	5.1	40.6	1.2	0.0006	NR
120	300	100	40	19.048	1	280	−308	520	515	5.1	72.1	0.2	0.0002	NR
121	300	100	60	−19.048	−1	280	−606	844	841	7.6	71.9	0.1	0.0001	NR
122	300	100	60	−14.286	1	280	−450	209	205	7.6	40.5	0.6	0.0007	NR
123	300	100	60	−9.524	−1	−280	80	145	144	7.6	18.0	0.5	0.0007	NR
124	300	100	60	−9.524	−1	280	−87	118	117	7.6	18.0	0.6	0.0006	NR
125	300	100	60	−9.524	1	−280	126	169	167	7.6	18.0	0.5	0.0004	NR
126	300	100	60	−9.524	1	280	97	122	121	7.6	18.0	1.2	0.0001	NR
127	300	100	60	−8.248	−1	−280	19	120	119	7.6	13.5	0.7	0.0006	NR
128	300	100	60	−8.248	−1	280	168	96	95	7.6	13.5	0.7	0.0008	NR
129	300	100	60	−8.248	1	−280	−32	131	130	7.6	13.5	0.6	0.0001	NR
130	300	100	60	−8.248	1	280	−159	143	142	7.6	13.5	0.6	0.0006	NR
131	300	100	60	−6.734	−1	−280	−61	122	121	7.6	9.0	0.6	0.0188	NR
132	300	100	60	−6.734	−1	280	−78	115	115	7.6	9.0	0.5	0.0180	NR
133	300	100	60	−6.734	1	−280	−49	126	125	7.6	9.0	0.6	0.0148	NR
134	300	100	60	−6.734	1	280	−31	126	125	7.6	9.0	0.7	0.0155	NR
135	300	100	60	−5.000	−1	−280	−438	506	506	7.6	5.0	2.1	0.0093	NR
136	300	100	60	−5.000	−1	280	−688	473	473	7.6	5.0	1.9	0.0106	NR
137	300	100	60	−5.000	1	−280	−1088	422	422	7.6	5.0	3.5	0.0142	NR
138	300	100	60	−5.000	1	280	−824	399	398	7.6	5.0	3.3	0.0132	NR
139	300	100	60	−4.762	−1	−280	−125	47	46	7.6	4.5	6.0	1.1074	NR
140	300	100	60	−4.762	−1	280	−33	43	42	7.6	4.5	7.1	1.3060	NR
141	300	100	60	−4.762	1	−280	−122	49	48	7.6	4.5	5.9	1.0252	NR
142	300	100	60	−4.762	1	280	−56	44	43	7.6	4.5	7.2	1.2587	NR
143	300	100	60	4.762	−1	−280	−32	49	48	7.6	4.5	6.0	0.9837	NR
144	300	100	60	4.762	−1	280	−22	42	42	7.6	4.5	7.1	1.3423	NR
145	300	100	60	4.762	1	−280	−111	48	47	7.6	4.5	5.4	1.0839	NR
146	300	100	60	4.762	1	280	−13	40	39	7.6	4.5	7.5	1.4945	NR
147	300	100	60	5.000	−1	−280	−467	403	403	7.6	5.0	3.1	0.0130	NR
148	300	100	60	5.000	−1	280	−58	389	389	7.6	5.0	3.3	0.0140	NR
149	300	100	60	5.000	1	−280	−788	497	497	7.6	5.0	2.3	0.0106	NR
150	300	100	60	5.000	1	280	−1526	458	458	7.6	5.0	2.1	0.0129	NR
151	300	100	60	6.734	−1	−280	90	129	129	7.6	9.0	0.6	0.0141	NR
152	300	100	60	6.734	−1	280	−92	122	121	7.6	9.0	0.6	0.0140	NR
153	300	100	60	6.734	1	−280	−231	113	112	7.6	9.0	0.5	0.0192	NR
154	300	100	60	6.734	1	280	98	111	110	7.6	9.0	0.5	0.0204	NR
155	300	100	60	8.248	−1	−280	−115	126	125	7.6	13.6	0.6	0.0005	NR
156	300	100	60	8.248	−1	280	−68	133	132	7.6	13.6	0.6	0.0001	NR
157	300	100	60	8.248	1	−280	−15	113	112	7.6	13.6	0.6	0.0002	NR
158	300	100	60	8.248	1	280	−25	109	108	7.6	13.6	0.8	0.0000	NR
159	300	100	60	9.524	−1	−280	28	133	131	7.6	18.0	0.5	0.0008	NR
160	300	100	60	9.524	−1	280	97	128	126	7.6	18.0	1.2	0.0003	NR
161	300	100	60	9.524	1	−280	157	113	111	7.6	18.0	0.5	0.0002	NR
162	300	100	60	9.524	1	280	−9	114	113	7.6	18.0	0.6	0.0000	NR
163	300	100	60	14.286	−1	280	−230	292	289	7.6	40.6	0.4	0.0007	NR
164	300	100	60	19.048	1	280	514	569	564	7.6	72.3	0.1	0.0003	NR
165	300	100	80	−19.048	−1	280	−282	690	686	10.1	71.7	0.1	0.0002	NR
166	300	100	80	−14.286	1	280	−237	198	193	10.1	40.5	0.5	0.0006	NR
167	300	100	80	−9.524	−1	−280	−84	106	104	10.1	18.0	0.5	0.0005	NR
168	300	100	80	−9.524	−1	280	66	107	105	10.1	18.0	0.6	0.0001	NR
169	300	100	80	−9.524	1	−280	239	147	146	10.1	18.0	0.4	0.0007	NR
170	300	100	80	−9.524	1	280	−121	114	113	10.1	18.0	1.3	0.0004	NR
171	300	100	80	−8.248	−1	−280	−10	118	117	10.1	13.5	0.4	0.0008	NR
172	300	100	80	−8.248	−1	280	−203	127	126	10.1	13.5	0.4	0.0001	NR
173	300	100	80	−8.248	1	−280	172	105	103	10.1	13.5	0.6	0.0003	NR
174	300	100	80	−8.248	1	280	64	109	108	10.1	13.5	0.6	0.0001	NR
175	300	100	80	−6.734	−1	−280	66	123	122	10.1	9.0	0.4	0.0002	NR

Table continues on next page

Table A.1: Continued from previous page

N_{Exp}	T [ns]	D [ns]	P [%]	B [G]	m_J	f_{ofs} [Hz]	ν_{Fit} [Hz]	$\Delta\nu_0$ [Hz]	$\Delta\nu_{\text{Fit}}$ [Hz]	$\Delta\nu_{\text{Slope}}$ [Hz]	$\Delta\nu_{\text{B}}$ [Hz]	D_{Exp} [h]	W [%]	Data type
176	300	100	80	−6.734	−1	280	116	120	119	10.1	9.0	0.4	0.0007	NR
177	300	100	80	−6.734	1	−280	30	126	125	10.1	9.0	0.5	0.0000	NR
178	300	100	80	−6.734	1	280	−64	118	118	10.1	9.0	0.5	0.0006	NR
179	300	100	80	−5.000	−1	−280	267	546	546	10.1	5.0	1.0	0.0047	NR
180	300	100	80	−5.000	−1	280	−800	847	847	10.1	5.0	0.5	0.0070	NR
181	300	100	80	−5.000	1	−280	−567	539	539	10.1	5.0	1.0	0.0065	NR
182	300	100	80	−5.000	1	280	−1406	408	407	10.1	5.0	1.6	0.0056	NR
183	300	100	80	−4.762	−1	−280	−160	48	47	10.1	4.5	4.8	0.4694	NR
184	300	100	80	−4.762	−1	280	−78	42	40	10.1	4.5	6.3	0.6095	NR
185	300	100	80	−4.762	1	−280	−59	46	44	10.1	4.5	4.8	0.5096	NR
186	300	100	80	−4.762	1	280	−89	42	41	10.1	4.5	6.1	0.6108	NR
187	300	100	80	4.762	−1	−280	−64	46	45	10.1	4.5	5.4	0.4892	NR
188	300	100	80	4.762	−1	280	−42	40	39	10.1	4.5	7.1	0.6755	NR
189	300	100	80	4.762	1	−280	−54	42	41	10.1	4.5	5.1	0.5843	NR
190	300	100	80	4.762	1	280	−84	42	41	10.1	4.5	6.1	0.5853	NR
191	300	100	80	5.000	−1	−280	−1044	461	461	10.1	5.0	0.8	0.0085	NR
192	300	100	80	5.000	−1	280	−958	492	492	10.1	5.0	1.1	0.0033	NR
193	300	100	80	5.000	1	−280	−1676	684	684	10.1	5.0	0.9	0.0060	NR
194	300	100	80	5.000	1	280	−355	596	596	10.1	5.0	1.0	0.0025	NR
195	300	100	80	6.734	−1	−280	167	138	137	10.1	9.0	0.6	0.0006	NR
196	300	100	80	6.734	−1	280	−42	121	120	10.1	9.0	0.5	0.0002	NR
197	300	100	80	6.734	1	−280	−74	121	120	10.1	9.0	0.4	0.0005	NR
198	300	100	80	6.734	1	280	−128	114	113	10.1	9.0	0.4	0.0000	NR
199	300	100	80	8.248	−1	−280	−66	118	117	10.1	13.6	0.6	0.0006	NR
200	300	100	80	8.248	−1	280	−59	121	120	10.1	13.6	0.6	0.0005	NR
201	300	100	80	8.248	1	−280	41	119	118	10.1	13.6	0.4	0.0001	NR
202	300	100	80	8.248	1	280	188	118	117	10.1	13.6	0.4	0.0003	NR
203	300	100	80	9.524	−1	−280	−114	167	166	10.1	18.0	0.4	0.0001	NR
204	300	100	80	9.524	−1	280	172	104	102	10.1	18.0	1.4	0.0004	NR
205	300	100	80	9.524	1	−280	155	107	105	10.1	18.0	0.5	0.0005	NR
206	300	100	80	9.524	1	280	−6	108	106	10.1	18.0	0.6	0.0005	NR
207	300	100	80	14.286	−1	280	124	196	192	10.1	40.6	0.8	0.0006	NR
208	300	100	80	19.048	1	280	−1556	515	510	10.1	72.2	0.1	0.0000	NR
209	300	100	100	−23.810	−1	280	−274	255	229	12.6	112.4	1.0	0.0001	NR
210	300	100	100	−23.810	1	280	103	297	274	12.6	112.4	1.0	0.0003	NR
211	300	100	100	−19.048	−1	280	−244	162	144	12.6	71.9	2.2	0.0008	NR
212	300	100	100	−19.048	1	280	−28	106	76	12.6	71.9	5.3	0.0001	NR
213	300	100	100	−14.286	−1	280	−95	152	146	12.6	40.5	0.9	0.0002	NR
214	300	100	100	−14.286	1	280	32	74	61	12.6	40.5	5.1	0.0001	NR
215	300	100	100	−11.905	−1	280	11	43	30	12.6	28.1	10.8	0.0003	NR
216	300	100	100	−11.905	1	280	−11	48	37	12.6	28.1	7.6	0.0002	NR
217	300	100	100	−9.524	−1	280	42	36	28	12.6	18.0	14.0	0.0000	NR
218	300	100	100	−9.524	1	280	28	42	36	12.6	18.0	10.0	0.0004	NR
219	300	100	100	−8.248	−1	−280	241	145	144	12.6	13.5	0.3	0.0004	NR
220	300	100	100	−8.248	−1	280	−127	129	128	12.6	13.5	0.3	0.0003	NR
221	300	100	100	−8.248	1	−280	−50	126	125	12.6	13.5	0.5	0.0006	NR
222	300	100	100	−8.248	1	280	177	105	103	12.6	13.5	0.5	0.0006	NR
223	300	100	100	−7.143	−1	280	5	32	27	12.6	10.1	10.8	0.0003	NR
224	300	100	100	−7.143	1	280	121	38	34	12.6	10.1	7.5	0.0008	NR
225	300	100	100	−6.734	−1	−280	−112	122	121	12.6	9.0	0.3	0.0002	NR
226	300	100	100	−6.734	−1	280	−37	163	162	12.6	9.0	0.3	0.0001	NR
227	300	100	100	−6.734	1	−280	−363	99	97	12.6	9.0	0.5	0.0007	NR
228	300	100	100	−6.734	1	280	61	100	98	12.6	9.0	0.5	0.0006	NR
229	300	100	100	−5.000	−1	−280	−1352	512	512	12.6	5.0	1.2	0.0005	NR
230	300	100	100	−5.000	−1	280	−715	505	504	12.6	5.0	1.1	0.0000	NR
231	300	100	100	−5.000	1	−280	−913	356	356	12.6	5.0	1.7	0.0004	NR
232	300	100	100	−5.000	1	280	−1523	385	385	12.6	5.0	1.8	0.0001	NR
233	300	100	100	−4.762	−1	−2800	119	96	95	12.6	4.5	2.0	0.0000	NR
234	300	100	100	−4.762	−1	−280	−66	44	42	12.6	4.5	4.7	0.0003	NR
235	300	100	100	−4.762	−1	−40	18	53	51	12.6	4.5	4.4	0.0002	NR

Table continues on next page

Table A.1: Continued from previous page

N_{Exp}	T [ns]	D [ns]	P [%]	B [G]	m_J	f_{ofs} [Hz]	ν_{Fit} [Hz]	$\Delta\nu_0$ [Hz]	$\Delta\nu_{\text{Fit}}$ [Hz]	$\Delta\nu_{\text{Slope}}$ [Hz]	$\Delta\nu_{\text{B}}$ [Hz]	D_{Exp} [h]	W [%]	Data type
236	300	100	100	−4.762	−1	30	131	149	148	12.6	4.5	1.2	0.0006	NR
237	300	100	100	−4.762	−1	40	118	54	52	12.6	4.5	4.4	0.0004	NR
238	300	100	100	−4.762	−1	280	−33	36	33	12.6	4.5	9.1	0.0008	NR
239	300	100	100	−4.762	−1	2800	128	97	96	12.6	4.5	1.9	0.0003	NR
240	300	100	100	−4.762	1	−280	−110	38	36	12.6	4.5	7.0	0.0005	NR
241	300	100	100	−4.762	1	−40	−141	114	113	12.6	4.5	0.7	0.0004	NR
242	300	100	100	−4.762	1	40	75	126	125	12.6	4.5	1.0	0.0002	NR
243	300	100	100	−4.762	1	280	−7	29	25	12.6	4.5	18.2	0.0005	NR
244	300	100	100	4.762	−1	−280	−35	39	37	12.6	4.5	7.2	0.0002	NR
245	300	100	100	4.762	−1	−40	196	130	129	12.6	4.5	0.7	0.0007	NR
246	300	100	100	4.762	−1	40	166	106	106	12.6	4.5	1.0	0.0004	NR
247	300	100	100	4.762	−1	280	−28	30	27	12.6	4.5	16.8	0.0001	NR
248	300	100	100	4.762	1	−2800	26	100	99	12.6	4.5	1.9	0.0002	NR
249	300	100	100	4.762	1	−280	−40	45	43	12.6	4.5	4.3	0.0005	NR
250	300	100	100	4.762	1	−40	119	54	52	12.6	4.5	4.3	0.0008	NR
251	300	100	100	4.762	1	30	33	128	127	12.6	4.5	1.7	0.0006	NR
252	300	100	100	4.762	1	40	141	55	54	12.6	4.5	4.4	0.0006	NR
253	300	100	100	4.762	1	280	−11	34	32	12.6	4.5	8.9	0.0001	NR
254	300	100	100	4.762	1	2800	125	92	91	12.6	4.5	1.9	0.0001	NR
255	300	100	100	5.000	−1	−280	−1018	273	273	12.6	5.0	1.7	0.0006	NR
256	300	100	100	5.000	−1	280	−7	271	270	12.6	5.0	1.5	0.0005	NR
257	300	100	100	5.000	1	−280	−737	501	501	12.6	5.0	1.0	0.0007	NR
258	300	100	100	5.000	1	280	−973	434	434	12.6	5.0	1.3	0.0000	NR
259	300	100	100	6.734	−1	−280	86	112	111	12.6	9.0	0.5	0.0007	NR
260	300	100	100	6.734	−1	280	−31	115	114	12.6	9.0	0.5	0.0004	NR
261	300	100	100	6.734	1	−280	7	145	144	12.6	9.0	0.3	0.0007	NR
262	300	100	100	6.734	1	280	−113	103	101	12.6	9.0	0.3	0.0007	NR
263	300	100	100	7.143	−1	280	−47	39	35	12.6	10.2	7.5	0.0002	NR
264	300	100	100	7.143	1	280	94	30	25	12.6	10.2	10.8	0.0001	NR
265	300	100	100	8.248	−1	−280	−14	136	134	12.6	13.6	0.5	0.0007	NR
266	300	100	100	8.248	−1	280	−43	110	108	12.6	13.6	0.5	0.0008	NR
267	300	100	100	8.248	1	−280	149	138	137	12.6	13.6	0.3	0.0006	NR
268	300	100	100	8.248	1	280	64	137	136	12.6	13.6	0.3	0.0002	NR
269	300	100	100	9.524	−1	280	70	44	39	12.6	18.0	9.5	0.0007	NR
270	300	100	100	9.524	1	280	−11	34	26	12.6	18.0	14.7	0.0003	NR
271	300	100	100	11.905	−1	280	28	51	41	12.6	28.2	7.5	0.0008	NR
272	300	100	100	11.905	1	280	−41	41	26	12.6	28.2	10.9	0.0005	NR
273	300	100	100	14.286	−1	280	57	81	68	12.6	40.6	5.7	0.0003	NR
274	300	100	100	14.286	1	280	188	131	124	12.6	40.6	0.9	0.0003	NR
275	300	100	100	19.048	−1	280	−36	116	90	12.6	72.1	5.3	0.0006	NR
276	300	100	100	19.048	1	280	64	121	96	12.6	72.1	2.3	0.0005	NR
277	300	100	100	23.810	−1	280	−67	437	422	12.6	112.6	1.0	0.0007	NR
278	300	100	100	23.810	1	280	83	214	182	12.6	112.6	1.0	0.0005	NR
279	300	150	20	−4.762	−1	−280	−162	128	128	8.5	4.5	1.4	0.1106	NR
280	300	150	20	−4.762	−1	280	74	106	105	8.5	4.5	2.3	0.1703	NR
281	300	150	20	−4.762	1	−280	−20	100	99	8.5	4.5	1.5	0.1896	NR
282	300	150	20	−4.762	1	280	−60	74	73	8.5	4.5	3.8	0.3547	NR
283	300	150	20	4.762	−1	−280	203	109	109	8.5	4.5	1.9	0.1522	NR
284	300	150	20	4.762	−1	280	−81	84	84	8.5	4.5	3.8	0.2611	NR
285	300	150	20	4.762	1	−280	71	100	100	8.5	4.5	1.4	0.1854	NR
286	300	150	20	4.762	1	280	135	97	97	8.5	4.5	2.0	0.1942	NR
287	300	150	40	−4.762	−1	−280	−73	117	116	17.0	4.5	1.0	0.0000	NR
288	300	150	40	−4.762	−1	280	−50	96	95	17.0	4.5	1.6	0.0002	NR
289	300	150	40	−4.762	1	−280	52	103	101	17.0	4.5	0.8	0.0006	NR
290	300	150	40	−4.762	1	280	−16	70	68	17.0	4.5	2.9	0.0006	NR
291	300	150	40	4.762	−1	−280	−5	85	83	17.0	4.5	1.4	0.0003	NR
292	300	150	40	4.762	−1	280	−38	78	76	17.0	4.5	2.7	0.0005	NR
293	300	150	40	4.762	1	−280	39	102	100	17.0	4.5	1.0	0.0001	NR
294	300	150	40	4.762	1	280	−37	85	83	17.0	4.5	1.6	0.0005	NR
295	300	150	60	−4.762	−1	−280	−89	118	115	25.6	4.5	0.5	0.0005	NR

Table continues on next page

Table A.1: Continued from previous page

N_{Exp}	T [ns]	D [ns]	P [%]	B [G]	m_J	f_{ofs} [Hz]	ν_{Fit} [Hz]	$\Delta\nu_0$ [Hz]	$\Delta\nu_{\mathrm{Fit}}$ [Hz]	$\Delta\nu_{\mathrm{Slope}}$ [Hz]	$\Delta\nu_{\mathrm{B}}$ [Hz]	D_{Exp} [h]	W [%]	Data type
296	300	150	60	−4.762	−1	280	−269	102	99	25.6	4.5	1.0	0.0007	NR
297	300	150	60	−4.762	1	−280	−139	88	84	25.6	4.5	1.1	0.0003	NR
298	300	150	60	−4.762	1	280	43	82	78	25.6	4.5	1.8	0.0001	NR
299	300	150	60	4.762	−1	−280	285	117	114	25.6	4.5	0.8	0.0001	NR
300	300	150	60	4.762	−1	280	−83	96	92	25.6	4.5	1.8	0.0003	NR
301	300	150	60	4.762	1	−280	−152	149	147	25.6	4.5	0.5	0.0004	NR
302	300	150	60	4.762	1	280	−93	106	103	25.6	4.5	1.0	0.0007	NR
303	300	150	80	−4.762	−1	−280	−141	112	107	34.1	4.5	0.5	0.0006	NR
304	300	150	80	−4.762	−1	280	−51	104	98	34.1	4.5	0.8	0.0003	NR
305	300	150	80	−4.762	1	−280	−38	87	80	34.1	4.5	0.8	0.0007	NR
306	300	150	80	−4.762	1	280	−81	79	71	34.1	4.5	1.4	0.0000	NR
307	300	150	80	4.762	−1	−280	−78	94	87	34.1	4.5	0.8	0.0008	NR
308	300	150	80	4.762	−1	280	102	86	79	34.1	4.5	1.3	0.0002	NR
309	300	150	80	4.762	1	−280	0	117	112	34.1	4.5	0.5	0.0002	NR
310	300	150	80	4.762	1	280	−29	92	85	34.1	4.5	0.8	0.0006	NR
311	300	150	100	−4.762	−1	−280	144	108	99	42.6	4.5	0.5	0.0000	NR
312	300	150	100	−4.762	−1	280	53	98	88	42.6	4.5	0.8	0.0005	NR
313	300	150	100	−4.762	1	−280	−94	93	83	42.6	4.5	0.6	0.0008	NR
314	300	150	100	−4.762	1	280	19	85	73	42.6	4.5	1.1	0.0007	NR
315	300	150	100	4.762	−1	−280	147	106	97	42.6	4.5	0.6	0.0001	NR
316	300	150	100	4.762	−1	280	29	84	72	42.6	4.5	1.1	0.0001	NR
317	300	150	100	4.762	1	−280	−84	110	102	42.6	4.5	0.5	0.0008	NR
318	300	150	100	4.762	1	280	232	102	93	42.6	4.5	0.8	0.0000	NR
319	400	50	20	−4.762	−1	−280	153	320	320	6.6	4.5	2.4	0.0332	NR
320	400	50	20	−4.762	−1	280	−184	346	346	6.6	4.5	2.3	0.0260	NR
321	400	50	20	−4.762	1	−280	31	274	273	6.6	4.5	4.3	0.0386	NR
322	400	50	20	−4.762	1	280	−217	256	255	6.6	4.5	4.8	0.0426	NR
323	400	50	20	4.762	−1	−280	−14	249	249	6.6	4.5	5.3	0.0525	NR
324	400	50	20	4.762	−1	280	321	255	255	6.6	4.5	5.3	0.0490	NR
325	400	50	20	4.762	1	−280	158	298	298	6.6	4.5	2.8	0.0316	NR
326	400	50	20	4.762	1	280	−85	320	319	6.6	4.5	2.4	0.0292	NR
327	400	50	40	−4.762	−1	−280	55	248	248	13.2	4.5	2.9	0.0008	NR
328	400	50	40	−4.762	−1	280	−35	226	226	13.2	4.5	2.9	0.0003	NR
329	400	50	40	−4.762	1	−280	−124	225	225	13.2	4.5	4.2	0.0008	NR
330	400	50	40	−4.762	1	280	−155	213	213	13.2	4.5	4.8	0.0000	NR
331	400	50	40	4.762	−1	−280	−200	207	207	13.2	4.5	4.5	0.0001	NR
332	400	50	40	4.762	−1	280	−14	213	213	13.2	4.5	5.2	0.0005	NR
333	400	50	40	4.762	1	−280	69	221	221	13.2	4.5	3.0	0.0003	NR
334	400	50	40	4.762	1	280	278	214	214	13.2	4.5	3.1	0.0005	NR
335	400	50	60	−4.762	−1	−280	13	249	248	19.8	4.5	1.4	0.0006	NR
336	400	50	60	−4.762	−1	280	264	225	224	19.8	4.5	1.6	0.0004	NR
337	400	50	60	−4.762	1	−280	128	232	231	19.8	4.5	2.4	0.0006	NR
338	400	50	60	−4.762	1	280	−228	207	206	19.8	4.5	2.6	0.0004	NR
339	400	50	60	4.762	−1	−280	−73	207	206	19.8	4.5	2.4	0.0003	NR
340	400	50	60	4.762	−1	280	279	231	231	19.8	4.5	2.5	0.0001	NR
341	400	50	60	4.762	1	−280	−406	269	268	19.8	4.5	1.4	0.0002	NR
342	400	50	60	4.762	1	280	34	241	240	19.8	4.5	1.5	0.0001	NR
343	400	50	80	−4.762	−1	−280	154	202	200	26.4	4.5	1.1	0.0003	NR
344	400	50	80	−4.762	−1	280	−30	261	259	26.4	4.5	1.1	0.0006	NR
345	400	50	80	−4.762	1	−280	165	237	235	26.4	4.5	1.3	0.0003	NR
346	400	50	80	−4.762	1	280	−165	280	279	26.4	4.5	1.3	0.0002	NR
347	400	50	80	4.762	−1	−280	289	162	159	26.4	4.5	2.1	0.0007	NR
348	400	50	80	4.762	−1	280	−156	271	270	26.4	4.5	1.4	0.0006	NR
349	400	50	80	4.762	1	−280	−119	226	225	26.4	4.5	1.1	0.0001	NR
350	400	50	80	4.762	1	280	−53	190	189	26.4	4.5	1.3	0.0004	NR
351	400	50	100	−4.762	−1	−280	314	231	229	33.0	4.5	0.6	0.0008	NR
352	400	50	100	−4.762	−1	280	342	238	235	33.0	4.5	0.9	0.0008	NR
353	400	50	100	−4.762	1	−280	267	191	188	33.0	4.5	1.4	0.0008	NR
354	400	50	100	−4.762	1	280	84	257	255	33.0	4.5	1.3	0.0004	NR
355	400	50	100	4.762	−1	−280	249	215	212	33.0	4.5	1.0	0.0007	NR

Table continues on next page

Table A.1: Continued from previous page

N_{Exp}	T [ns]	D [ns]	P [%]	B [G]	m_J	f_{ofs} [Hz]	ν_{Fit} [Hz]	$\Delta\nu_0$ [Hz]	$\Delta\nu_{\mathrm{Fit}}$ [Hz]	$\Delta\nu_{\mathrm{Slope}}$ [Hz]	$\Delta\nu_{\mathrm{B}}$ [Hz]	D_{Exp} [h]	W [%]	Data type
356	400	50	100	4.762	−1	280	−250	208	205	33.0	4.5	1.4	0.0005	NR
357	400	50	100	4.762	1	−280	117	282	280	33.0	4.5	0.9	0.0004	NR
358	400	50	100	4.762	1	280	−12	268	266	33.0	4.5	0.9	0.0004	NR
359	400	100	20	−4.762	−1	−280	9	125	125	1.9	4.5	3.1	0.3328	NR
360	400	100	20	−4.762	−1	280	113	110	110	1.9	4.5	5.9	0.4508	NR
361	400	100	20	−4.762	1	−280	97	145	145	1.9	4.5	4.8	0.2671	NR
362	400	100	20	−4.762	1	280	−87	119	119	1.9	4.5	9.4	0.3784	NR
363	400	100	20	4.762	−1	−280	245	159	159	1.9	4.5	4.8	0.2072	NR
364	400	100	20	4.762	−1	280	−132	121	121	1.9	4.5	8.6	0.3557	NR
365	400	100	20	4.762	1	−280	47	119	119	1.9	4.5	3.1	0.3770	NR
366	400	100	20	4.762	1	280	251	96	95	1.9	4.5	5.8	0.5776	NR
367	400	100	40	−4.762	−1	−280	−71	111	111	3.8	4.5	2.0	0.3558	NR
368	400	100	40	−4.762	−1	280	112	88	88	3.8	4.5	4.0	0.5598	NR
369	400	100	40	−4.762	1	−280	32	139	139	3.8	4.5	3.2	0.2209	NR
370	400	100	40	−4.762	1	280	133	109	109	3.8	4.5	6.3	0.3689	NR
371	400	100	40	4.762	−1	−280	−26	150	150	3.8	4.5	2.8	0.1905	NR
372	400	100	40	4.762	−1	280	6	140	140	3.8	4.5	5.2	0.2195	NR
373	400	100	40	4.762	1	−280	−51	103	102	3.8	4.5	2.2	0.4068	NR
374	400	100	40	4.762	1	280	−154	83	83	3.8	4.5	4.4	0.6262	NR
375	400	100	60	−4.762	−1	−280	−163	141	141	5.7	4.5	1.0	0.1623	NR
376	400	100	60	−4.762	−1	280	−33	83	83	5.7	4.5	3.8	0.5025	NR
377	400	100	60	−4.762	1	−280	56	152	152	5.7	4.5	1.7	0.1450	NR
378	400	100	60	−4.762	1	280	−105	97	97	5.7	4.5	4.8	0.3644	NR
379	400	100	60	4.762	−1	−280	−362	174	173	5.7	4.5	1.2	0.1098	NR
380	400	100	60	4.762	−1	280	−132	99	98	5.7	4.5	5.1	0.3437	NR
381	400	100	60	4.762	1	−280	−4	141	141	5.7	4.5	1.1	0.1634	NR
382	400	100	60	4.762	1	280	31	77	77	5.7	4.5	3.8	0.5705	NR
383	400	100	80	−4.762	−1	−280	170	109	109	7.6	4.5	1.1	0.1890	NR
384	400	100	80	−4.762	−1	280	137	86	86	7.6	4.5	2.3	0.3206	NR
385	400	100	80	−4.762	1	−280	−36	128	127	7.6	4.5	1.7	0.1419	NR
386	400	100	80	−4.762	1	280	191	108	108	7.6	4.5	3.1	0.1963	NR
387	400	100	80	4.762	−1	−280	−61	129	129	7.6	4.5	1.4	0.1469	NR
388	400	100	80	4.762	−1	280	−117	105	105	7.6	4.5	3.3	0.2138	NR
389	400	100	80	4.762	1	−280	−32	110	110	7.6	4.5	1.1	0.1995	NR
390	400	100	80	4.762	1	280	−28	81	80	7.6	4.5	2.4	0.3595	NR
391	400	100	100	−4.762	−1	−280	8	110	110	9.5	4.5	0.8	0.1160	NR
392	400	100	100	−4.762	−1	280	39	103	102	9.5	4.5	1.8	0.1308	NR
393	400	100	100	−4.762	1	−280	25	108	107	9.5	4.5	0.9	0.1173	NR
394	400	100	100	−4.762	1	280	3	89	88	9.5	4.5	4.0	0.1740	NR
395	400	100	100	4.762	−1	−280	97	111	110	9.5	4.5	0.9	0.1141	NR
396	400	100	100	4.762	−1	280	−20	92	92	9.5	4.5	4.0	0.1591	NR
397	400	100	100	4.762	1	−280	−7	113	112	9.5	4.5	0.8	0.1066	NR
398	400	100	100	4.762	1	280	158	87	86	9.5	4.5	2.0	0.1747	NR
399	400	150	20	−4.762	−1	−280	242	178	178	6.4	4.5	3.3	0.0881	NR
400	400	150	20	−4.762	−1	280	−70	108	107	6.4	4.5	6.7	0.2493	NR
401	400	150	20	−4.762	1	−280	471	370	370	6.4	4.5	0.5	0.0231	NR
402	400	150	20	−4.762	1	280	57	85	84	6.4	4.5	6.2	0.4198	NR
403	400	150	20	4.762	−1	−280	221	314	314	6.4	4.5	0.5	0.0304	NR
404	400	150	20	4.762	−1	280	74	92	92	6.4	4.5	6.5	0.3418	NR
405	400	150	20	4.762	1	−280	−254	183	182	6.4	4.5	3.3	0.0840	NR
406	400	150	20	4.762	1	280	86	107	107	6.4	4.5	6.2	0.2599	NR
407	400	150	40	−4.762	−1	−280	173	178	177	12.8	4.5	2.3	0.0005	NR
408	400	150	40	−4.762	−1	280	77	110	109	12.8	4.5	3.6	0.0007	NR
409	400	150	40	−4.762	1	−280	385	328	328	12.8	4.5	0.3	0.0002	NR
410	400	150	40	−4.762	1	280	207	98	97	12.8	4.5	3.4	0.0003	NR
411	400	150	40	4.762	−1	−280	189	391	391	12.8	4.5	0.3	0.0006	NR
412	400	150	40	4.762	−1	280	−48	107	106	12.8	4.5	3.3	0.0007	NR
413	400	150	40	4.762	1	−280	66	162	161	12.8	4.5	2.3	0.0002	NR
414	400	150	40	4.762	1	280	69	118	118	12.8	4.5	3.3	0.0007	NR
415	400	150	60	−4.762	−1	−280	197	143	141	19.2	4.5	1.4	0.0003	NR

Table continues on next page

Table A.1: Continued from previous page

N_{Exp}	T [ns]	D [ns]	P [%]	B [G]	m_J	f_{ofs} [Hz]	ν_{Fit} [Hz]	$\Delta\nu_0$ [Hz]	$\Delta\nu_{\text{Fit}}$ [Hz]	$\Delta\nu_{\text{Slope}}$ [Hz]	$\Delta\nu_{\text{B}}$ [Hz]	D_{Exp} [h]	W [%]	Data type
416	400	150	60	−4.762	−1	280	−192	124	122	19.2	4.5	1.9	0.0002	NR
417	400	150	60	−4.762	1	−280	216	135	133	19.2	4.5	1.1	0.0008	NR
418	400	150	60	−4.762	1	280	63	98	96	19.2	4.5	2.3	0.0000	NR
419	400	150	60	4.762	−1	−280	−41	156	154	19.2	4.5	1.3	0.0004	NR
420	400	150	60	4.762	−1	280	121	104	102	19.2	4.5	2.4	0.0002	NR
421	400	150	60	4.762	1	−280	65	150	149	19.2	4.5	1.5	0.0003	NR
422	400	150	60	4.762	1	280	188	120	118	19.2	4.5	1.7	0.0003	NR
423	400	150	80	−4.762	−1	−280	18	168	166	25.6	4.5	1.1	0.0000	NR
424	400	150	80	−4.762	−1	280	−121	127	124	25.6	4.5	1.7	0.0005	NR
425	400	150	80	−4.762	1	−280	122	172	170	25.6	4.5	0.7	0.0007	NR
426	400	150	80	−4.762	1	280	27	98	94	25.6	4.5	1.9	0.0006	NR
427	400	150	80	4.762	−1	−280	−83	194	192	25.6	4.5	0.6	0.0006	NR
428	400	150	80	4.762	−1	280	−4	108	105	25.6	4.5	1.9	0.0003	NR
429	400	150	80	4.762	1	−280	104	160	158	25.6	4.5	1.1	0.0000	NR
430	400	150	80	4.762	1	280	54	113	110	25.6	4.5	1.5	0.0003	NR
431	400	150	100	−4.762	−1	−280	−99	166	163	32.0	4.5	0.7	0.0006	NR
432	400	150	100	−4.762	−1	280	159	122	117	32.0	4.5	1.3	0.0003	NR
433	400	150	100	−4.762	1	−280	281	195	192	32.0	4.5	0.4	0.0005	NR
434	400	150	100	−4.762	1	280	163	94	89	32.0	4.5	1.8	0.0008	NR
435	400	150	100	4.762	−1	−280	375	257	255	32.0	4.5	0.4	0.0006	NR
436	400	150	100	4.762	−1	280	135	113	108	32.0	4.5	1.8	0.0002	NR
437	400	150	100	4.762	1	−280	273	161	158	32.0	4.5	0.7	0.0006	NR
438	400	150	100	4.762	1	280	149	114	109	32.0	4.5	1.7	0.0001	NR
439	400	200	20	−4.762	−1	−280	−344	192	192	7.6	4.5	3.0	0.0656	NR
440	400	200	20	−4.762	−1	280	−104	98	98	7.6	4.5	7.0	0.2488	NR
441	400	200	20	−4.762	1	−280	29	200	200	7.6	4.5	2.1	0.0568	NR
442	400	200	20	−4.762	1	280	33	97	97	7.6	4.5	5.3	0.2485	NR
443	400	200	20	4.762	−1	−280	−237	158	157	7.6	4.5	3.2	0.0944	NR
444	400	200	20	4.762	−1	280	58	119	119	7.6	4.5	5.0	0.1645	NR
445	400	200	20	4.762	1	−280	−112	212	211	7.6	4.5	2.9	0.0546	NR
446	400	200	20	4.762	1	280	−52	104	104	7.6	4.5	6.6	0.2170	NR
447	400	200	40	−4.762	−1	−280	92	188	187	15.2	4.5	1.9	0.0006	NR
448	400	200	40	−4.762	−1	280	−105	117	116	15.2	4.5	3.6	0.0003	NR
449	400	200	40	−4.762	1	−280	280	221	221	15.2	4.5	0.6	0.0001	NR
450	400	200	40	−4.762	1	280	188	91	89	15.2	4.5	2.8	0.0002	NR
451	400	200	40	4.762	−1	−280	−43	267	266	15.2	4.5	0.6	0.0001	NR
452	400	200	40	4.762	−1	280	116	108	107	15.2	4.5	2.8	0.0002	NR
453	400	200	40	4.762	1	−280	0	179	178	15.2	4.5	2.3	0.0007	NR
454	400	200	40	4.762	1	280	70	115	114	15.2	4.5	3.6	0.0002	NR
455	400	200	60	−4.762	−1	−280	−225	169	168	22.8	4.5	1.6	0.0008	NR
456	400	200	60	−4.762	−1	280	71	120	118	22.8	4.5	2.2	0.0005	NR
457	400	200	60	−4.762	1	−280	350	161	159	22.8	4.5	0.9	0.0002	NR
458	400	200	60	−4.762	1	280	−4	107	105	22.8	4.5	2.0	0.0003	NR
459	400	200	60	4.762	−1	−280	164	192	191	22.8	4.5	0.9	0.0005	NR
460	400	200	60	4.762	−1	280	−4	124	122	22.8	4.5	2.1	0.0006	NR
461	400	200	60	4.762	1	−280	185	178	177	22.8	4.5	1.5	0.0001	NR
462	400	200	60	4.762	1	280	−17	115	113	22.8	4.5	2.5	0.0003	NR
463	400	200	80	−4.762	−1	−280	−202	159	156	30.4	4.5	1.2	0.0001	NR
464	400	200	80	−4.762	−1	280	101	122	118	30.4	4.5	1.8	0.0003	NR
465	400	200	80	−4.762	1	−280	−69	173	170	30.4	4.5	0.5	0.0004	NR
466	400	200	80	−4.762	1	280	−15	97	92	30.4	4.5	1.8	0.0000	NR
467	400	200	80	4.762	−1	−280	−94	184	182	30.4	4.5	0.5	0.0005	NR
468	400	200	80	4.762	−1	280	−136	124	120	30.4	4.5	1.5	0.0000	NR
469	400	200	80	4.762	1	−280	−168	147	144	30.4	4.5	1.2	0.0000	NR
470	400	200	80	4.762	1	280	−129	125	121	30.4	4.5	2.0	0.0003	NR
471	400	200	100	−4.762	−1	−280	788	236	233	38.0	4.5	0.3	0.0003	NR
472	400	200	100	−4.762	−1	280	225	112	105	38.0	4.5	1.5	0.0002	NR
473	400	200	100	−4.762	1	−280	37	238	235	38.0	4.5	0.3	0.0007	NR
474	400	200	100	−4.762	1	280	−12	104	96	38.0	4.5	1.5	0.0005	NR
475	400	200	100	4.762	−1	−280	257	196	192	38.0	4.5	0.3	0.0003	NR

Table continues on next page

Table A.1: Continued from previous page

N_{Exp}	T [ns]	D [ns]	P [%]	B [G]	m_J	f_{ofs} [Hz]	ν_{Fit} [Hz]	$\Delta\nu_0$ [Hz]	$\Delta\nu_{\mathrm{Fit}}$ [Hz]	$\Delta\nu_{\mathrm{Slope}}$ [Hz]	$\Delta\nu_{\mathrm{B}}$ [Hz]	D_{Exp} [h]	W [%]	Data type
476	400	200	100	4.762	−1	280	−25	116	109	38.0	4.5	1.4	0.0002	NR
477	400	200	100	4.762	1	−280	−257	305	303	38.0	4.5	0.3	0.0001	NR
478	400	200	100	4.762	1	280	−46	116	110	38.0	4.5	1.5	0.0002	NR
479	500	100	20	−4.762	−1	−280	−156	472	472	1.5	4.5	1.9	0.0246	NR
480	500	100	20	−4.762	−1	280	−263	474	474	1.5	4.5	1.9	0.0244	NR
481	500	100	20	−4.762	1	−280	965	397	397	1.5	4.5	1.9	0.0358	NR
482	500	100	20	−4.762	1	280	−52	318	318	1.5	4.5	2.8	0.0532	NR
483	500	100	20	4.762	−1	−280	425	387	387	1.5	4.5	1.9	0.0361	NR
484	500	100	20	4.762	−1	280	132	388	388	1.5	4.5	2.3	0.0358	NR
485	500	100	20	4.762	1	−280	346	331	331	1.5	4.5	2.3	0.0504	NR
486	500	100	20	4.762	1	280	−81	283	283	1.5	4.5	4.2	0.0688	NR
487	500	100	40	−4.762	−1	−280	88	369	369	3.0	4.5	1.3	0.0351	NR
488	500	100	40	−4.762	−1	280	51	292	292	3.0	4.5	3.1	0.0581	NR
489	500	100	40	−4.762	1	−280	271	313	313	3.0	4.5	1.6	0.0514	NR
490	500	100	40	−4.762	1	280	−174	287	287	3.0	4.5	1.6	0.0600	NR
491	500	100	40	4.762	−1	−280	142	292	292	3.0	4.5	1.7	0.0551	NR
492	500	100	40	4.762	−1	280	−240	271	271	3.0	4.5	1.4	0.0640	NR
493	500	100	40	4.762	1	−280	289	366	366	3.0	4.5	1.2	0.0341	NR
494	500	100	40	4.762	1	280	200	248	248	3.0	4.5	3.1	0.0772	NR
495	500	100	60	−4.762	−1	−280	−232	310	310	4.6	4.5	1.1	0.0402	NR
496	500	100	60	−4.762	−1	280	−147	302	302	4.6	4.5	2.0	0.0468	NR
497	500	100	60	−4.762	1	−280	−258	231	231	4.6	4.5	1.4	0.0759	NR
498	500	100	60	−4.762	1	280	156	257	257	4.6	4.5	1.4	0.0636	NR
499	500	100	60	4.762	−1	−280	87	290	290	4.6	4.5	1.4	0.0499	NR
500	500	100	60	4.762	−1	280	−135	236	236	4.6	4.5	1.5	0.0711	NR
501	500	100	60	4.762	1	−280	514	262	261	4.6	4.5	1.2	0.0555	NR
502	500	100	60	4.762	1	280	51	199	199	4.6	4.5	2.2	0.1002	NR
503	500	100	80	−4.762	−1	−280	188	289	288	6.1	4.5	0.7	0.0381	NR
504	500	100	80	−4.762	−1	280	−185	225	224	6.1	4.5	1.4	0.0630	NR
505	500	100	80	−4.762	1	−280	340	203	203	6.1	4.5	1.4	0.0727	NR
506	500	100	80	−4.762	1	280	338	232	232	6.1	4.5	1.4	0.0593	NR
507	500	100	80	4.762	−1	−280	150	218	217	6.1	4.5	1.4	0.0640	NR
508	500	100	80	4.762	−1	280	−5	218	218	6.1	4.5	1.4	0.0673	NR
509	500	100	80	4.762	1	−280	26	239	239	6.1	4.5	0.7	0.0565	NR
510	500	100	80	4.762	1	280	−25	197	197	6.1	4.5	1.8	0.0805	NR
511	500	100	100	−4.762	−1	−280	95	171	171	7.6	4.5	1.6	0.0826	NR
512	500	100	100	−4.762	−1	280	−44	102	102	7.6	4.5	6.4	0.2266	NR
513	500	100	100	−4.762	1	−280	−406	191	191	7.6	4.5	1.6	0.0673	NR
514	500	100	100	−4.762	1	280	−108	102	102	7.6	4.5	5.7	0.2289	NR
515	500	100	100	4.762	−1	−280	−53	183	183	7.6	4.5	1.5	0.0702	NR
516	500	100	100	4.762	−1	280	227	114	113	7.6	4.5	5.8	0.1828	NR
517	500	100	100	4.762	1	−280	−28	176	176	7.6	4.5	1.6	0.0773	NR
518	500	100	100	4.762	1	280	−39	89	88	7.6	4.5	6.5	0.2901	NR
519	500	200	20	−4.762	−1	280	−165	706	706	6.1	4.5	0.6	0.0069	NR
520	500	200	20	−4.762	1	−280	−546	342	341	6.1	4.5	1.2	0.0272	NR
521	500	200	20	−4.762	1	280	207	320	320	6.1	4.5	1.7	0.0334	NR
522	500	200	20	4.762	−1	−280	626	309	309	6.1	4.5	1.2	0.0343	NR
523	500	200	20	4.762	−1	280	−863	293	293	6.1	4.5	1.7	0.0346	NR
524	500	200	20	4.762	1	−280	−696	750	750	6.1	4.5	0.6	0.0077	NR
525	500	200	40	−4.762	−1	−280	408	369	368	12.1	4.5	0.9	0.0005	NR
526	500	200	40	−4.762	−1	280	65	453	453	12.1	4.5	0.9	0.0002	NR
527	500	200	40	−4.762	1	−280	−27	365	364	12.1	4.5	1.0	0.0001	NR
528	500	200	40	−4.762	1	280	−551	306	306	12.1	4.5	1.5	0.0008	NR
529	500	200	40	4.762	−1	−280	182	390	390	12.1	4.5	0.8	0.0008	NR
530	500	200	40	4.762	−1	280	368	309	309	12.1	4.5	1.7	0.0006	NR
531	500	200	40	4.762	1	−280	262	380	380	12.1	4.5	1.2	0.0001	NR
532	500	200	40	4.762	1	280	−135	408	408	12.1	4.5	1.2	0.0007	NR
533	500	200	60	−4.762	−1	−280	−615	442	442	18.2	4.5	0.8	0.0002	NR
534	500	200	60	−4.762	−1	280	1609	555	555	18.2	4.5	0.8	0.0007	NR
535	500	200	60	−4.762	1	−280	138	189	188	18.2	4.5	1.7	0.0001	NR

Table continues on next page

Table A.1: Continued from previous page

N_{Exp}	T [ns]	D [ns]	P [%]	B [G]	m_J	f_{ofs} [Hz]	ν_{Fit} [Hz]	$\Delta\nu_0$ [Hz]	$\Delta\nu_{\mathrm{Fit}}$ [Hz]	$\Delta\nu_{\mathrm{Slope}}$ [Hz]	$\Delta\nu_{\mathrm{B}}$ [Hz]	D_{Exp} [h]	W [%]	Data type
536	500	200	60	−4.762	1	280	57	241	240	18.2	4.5	1.2	0.0005	NR
537	500	200	60	4.762	−1	−280	−172	231	230	18.2	4.5	1.5	0.0007	NR
538	500	200	60	4.762	−1	280	−583	253	252	18.2	4.5	2.0	0.0000	NR
539	500	200	60	4.762	1	−280	−624	509	509	18.2	4.5	0.5	0.0000	NR
540	500	200	60	4.762	1	280	159	364	364	18.2	4.5	0.8	0.0005	NR
541	500	200	80	−4.762	−1	−280	103	334	333	24.3	4.5	0.5	0.0008	NR
542	500	200	80	−4.762	−1	280	−435	419	418	24.3	4.5	0.5	0.0000	NR
543	500	200	80	−4.762	1	−280	−384	325	324	24.3	4.5	0.9	0.0002	NR
544	500	200	80	−4.762	1	280	−135	291	290	24.3	4.5	0.9	0.0003	NR
545	500	200	80	4.762	−1	−280	122	288	287	24.3	4.5	0.7	0.0007	NR
546	500	200	80	4.762	−1	280	−285	307	306	24.3	4.5	0.9	0.0000	NR
547	500	200	80	4.762	1	−280	371	330	330	24.3	4.5	0.5	0.0004	NR
548	500	200	80	4.762	1	280	−120	389	388	24.3	4.5	0.5	0.0000	NR
549	500	200	100	−4.762	−1	−280	8	319	318	30.4	4.5	0.6	0.0007	NR
550	500	200	100	−4.762	−1	280	−385	407	406	30.4	4.5	0.6	0.0001	NR
551	500	200	100	−4.762	1	−280	231	253	252	30.4	4.5	0.9	0.0005	NR
552	500	200	100	−4.762	1	280	−8	265	264	30.4	4.5	1.0	0.0004	NR
553	500	200	100	4.762	−1	−280	321	271	269	30.4	4.5	0.9	0.0008	NR
554	500	200	100	4.762	−1	280	423	245	243	30.4	4.5	0.9	0.0003	NR
555	500	200	100	4.762	1	−280	747	313	311	30.4	4.5	0.7	0.0007	NR
556	500	200	100	4.762	1	280	443	259	258	30.4	4.5	0.6	0.0007	NR
557	600	100	100	−4.762	−1	−280	142	220	220	6.3	4.5	3.3	0.0611	NR
558	600	100	100	−4.762	−1	280	−54	226	226	6.3	4.5	3.8	0.0599	NR
559	600	100	100	−4.762	1	−280	287	227	227	6.3	4.5	3.8	0.0592	NR
560	600	100	100	−4.762	1	280	−183	311	311	6.3	4.5	1.8	0.0315	NR
561	600	100	100	4.762	−1	−280	−347	199	199	6.3	4.5	4.3	0.0734	NR
562	600	100	100	4.762	−1	280	−93	211	211	6.3	4.5	4.7	0.0700	NR
563	600	100	100	4.762	1	−280	−16	195	194	6.3	4.5	3.8	0.0798	NR
564	600	100	100	4.762	1	280	289	181	181	6.3	4.5	3.8	0.0940	NR
565	300	100	20	−4.762	−1	−280	766	268	268	2.5	4.5	0.9	0.0682	MWDR
566	300	100	20	−4.762	−1	280	−154	226	226	2.5	4.5	1.4	0.0962	MWDR
567	300	100	20	−4.762	1	−280	−134	316	316	2.5	4.5	0.4	0.0508	MWDR
568	300	100	20	−4.762	1	280	144	287	287	2.5	4.5	0.4	0.0607	MWDR
569	300	100	20	4.762	−1	−280	817	360	360	2.5	4.5	0.4	0.0389	MWDR
570	300	100	20	4.762	−1	280	45	345	345	2.5	4.5	0.4	0.0444	MWDR
571	300	100	20	4.762	1	−280	−29	266	266	2.5	4.5	1.2	0.0703	MWDR
572	300	100	20	4.762	1	280	166	215	215	2.5	4.5	1.8	0.1088	MWDR
573	300	100	40	−4.762	−1	−280	−320	212	212	5.1	4.5	0.7	0.0826	MWDR
574	300	100	40	−4.762	−1	280	367	180	180	5.1	4.5	0.9	0.1150	MWDR
575	300	100	40	−4.762	1	−280	−22	276	276	5.1	4.5	0.4	0.0498	MWDR
576	300	100	40	−4.762	1	280	−89	236	236	5.1	4.5	0.4	0.0687	MWDR
577	300	100	40	4.762	−1	−280	−203	246	246	5.1	4.5	0.4	0.0631	MWDR
578	300	100	40	4.762	−1	280	−317	245	245	5.1	4.5	0.4	0.0629	MWDR
579	300	100	40	4.762	1	−280	−80	196	196	5.1	4.5	0.9	0.0940	MWDR
580	300	100	40	4.762	1	280	−214	204	204	5.1	4.5	0.7	0.0904	MWDR
581	300	100	60	−4.762	−1	−280	−14	209	209	7.6	4.5	0.7	0.0567	MWDR
582	300	100	60	−4.762	−1	280	158	229	228	7.6	4.5	0.5	0.0441	MWDR
583	300	100	60	−4.762	1	−280	201	278	278	7.6	4.5	0.2	0.0318	MWDR
584	300	100	60	−4.762	1	280	286	305	304	7.6	4.5	0.2	0.0257	MWDR
585	300	100	60	4.762	−1	−280	−80	280	280	7.6	4.5	0.2	0.0326	MWDR
586	300	100	60	4.762	−1	280	19	260	260	7.6	4.5	0.2	0.0348	MWDR
587	300	100	60	4.762	1	−280	350	211	211	7.6	4.5	1.0	0.0524	MWDR
588	300	100	60	4.762	1	280	−204	300	300	7.6	4.5	0.5	0.0250	MWDR
589	300	100	80	−4.762	−1	−280	298	185	185	10.1	4.5	0.4	0.0305	MWDR
590	300	100	80	−4.762	−1	280	154	177	177	10.1	4.5	0.4	0.0312	MWDR
591	300	100	80	−4.762	1	−280	156	292	292	10.1	4.5	0.1	0.0140	MWDR
592	300	100	80	−4.762	1	280	591	360	360	10.1	4.5	0.1	0.0087	MWDR
593	300	100	80	4.762	−1	−280	−282	277	277	10.1	4.5	0.1	0.0173	MWDR
594	300	100	80	4.762	−1	280	−231	352	352	10.1	4.5	0.1	0.0160	MWDR
595	300	100	80	4.762	1	−280	150	276	276	10.1	4.5	0.4	0.0134	MWDR

Table continues on next page

Table A.1: Continued from previous page

N_{Exp}	T [ns]	D [ns]	P [%]	B [G]	m_J	f_{ofs} [Hz]	ν_{Fit} [Hz]	$\Delta\nu_0$ [Hz]	$\Delta\nu_{\text{Fit}}$ [Hz]	$\Delta\nu_{\text{Slope}}$ [Hz]	$\Delta\nu_{\text{B}}$ [Hz]	D_{Exp} [h]	W [%]	Data type
596	300	100	80	4.762	1	280	−110	264	264	10.1	4.5	0.4	0.0155	MWDR
597	300	100	100	−9.524	−1	−280	−44	123	121	12.6	18.0	1.3	0.0006	MWDR
598	300	100	100	−9.524	−1	280	−215	119	117	12.6	18.0	1.4	0.0006	MWDR
599	300	100	100	−9.524	1	−280	307	117	115	12.6	18.0	0.9	0.0002	MWDR
600	300	100	100	−9.524	1	280	50	128	126	12.6	18.0	0.8	0.0003	MWDR
601	300	100	100	−8.248	−1	−280	−86	147	146	12.6	13.5	1.0	0.0006	MWDR
602	300	100	100	−8.248	−1	280	60	125	123	12.6	13.5	1.0	0.0007	MWDR
603	300	100	100	−8.248	1	−280	210	121	120	12.6	13.5	0.8	0.0008	MWDR
604	300	100	100	−8.248	1	280	212	134	133	12.6	13.5	0.8	0.0001	MWDR
605	300	100	100	−6.734	−1	−280	123	124	123	12.6	9.0	1.2	0.0005	MWDR
606	300	100	100	−6.734	−1	280	48	122	121	12.6	9.0	1.3	0.0003	MWDR
607	300	100	100	−6.734	1	−280	−61	120	119	12.6	9.0	0.7	0.0002	MWDR
608	300	100	100	−6.734	1	280	128	118	117	12.6	9.0	0.7	0.0007	MWDR
609	300	100	100	−4.762	−1	−280	312	267	266	12.6	4.5	0.3	0.0002	MWDR
610	300	100	100	−4.762	−1	280	399	286	286	12.6	4.5	0.3	0.0005	MWDR
611	300	100	100	−4.762	1	−280	117	286	286	12.6	4.5	0.1	0.0004	MWDR
612	300	100	100	−4.762	1	280	−209	389	389	12.6	4.5	0.1	0.0006	MWDR
613	300	100	100	4.762	−1	−280	42	371	371	12.6	4.5	0.1	0.0007	MWDR
614	300	100	100	4.762	−1	280	168	258	258	12.6	4.5	0.1	0.0002	MWDR
615	300	100	100	4.762	1	−280	131	251	250	12.6	4.5	0.3	0.0005	MWDR
616	300	100	100	4.762	1	280	158	268	267	12.6	4.5	0.3	0.0006	MWDR
617	300	100	100	6.734	−1	−280	−113	132	131	12.6	9.0	0.7	0.0005	MWDR
618	300	100	100	6.734	−1	280	158	112	110	12.6	9.0	0.6	0.0006	MWDR
619	300	100	100	6.734	1	−280	133	109	107	12.6	9.0	1.2	0.0007	MWDR
620	300	100	100	6.734	1	280	215	108	107	12.6	9.0	1.2	0.0005	MWDR
621	300	100	100	8.248	−1	−280	167	147	146	12.6	13.6	0.9	0.0004	MWDR
622	300	100	100	8.248	−1	280	−206	124	123	12.6	13.6	0.9	0.0004	MWDR
623	300	100	100	8.248	1	−280	23	126	124	12.6	13.6	1.0	0.0004	MWDR
624	300	100	100	8.248	1	280	80	126	124	12.6	13.6	0.9	0.0007	MWDR
625	300	100	100	9.524	−1	−280	105	139	137	12.6	18.0	0.8	0.0007	MWDR
626	300	100	100	9.524	−1	280	70	126	124	12.6	18.0	0.8	0.0000	MWDR
627	300	100	100	9.524	1	−280	−132	134	132	12.6	18.0	1.3	0.0002	MWDR
628	300	100	100	9.524	1	280	−131	109	106	12.6	18.0	1.3	0.0004	MWDR
629	400	100	20	−4.762	−1	−280	−71	195	195	1.9	4.5	3.1	0.1403	MWDR
630	400	100	20	−4.762	−1	280	136	208	207	1.9	4.5	2.9	0.1255	MWDR
631	400	100	20	−4.762	1	−280	225	210	210	1.9	4.5	1.8	0.1201	MWDR
632	400	100	20	−4.762	1	280	−317	216	216	1.9	4.5	1.8	0.1156	MWDR
633	400	100	20	4.762	−1	−280	364	196	196	1.9	4.5	1.8	0.1365	MWDR
634	400	100	20	4.762	−1	280	260	209	209	1.9	4.5	1.7	0.1188	MWDR
635	400	100	20	4.762	1	−280	3	182	182	1.9	4.5	2.2	0.1581	MWDR
636	400	100	20	4.762	1	280	−185	209	209	1.9	4.5	2.1	0.1250	MWDR
637	400	100	40	−4.762	−1	−280	196	173	173	3.8	4.5	2.0	0.1472	MWDR
638	400	100	40	−4.762	−1	280	195	267	267	3.8	4.5	1.3	0.0635	MWDR
639	400	100	40	−4.762	1	−280	155	192	192	3.8	4.5	1.3	0.1160	MWDR
640	400	100	40	−4.762	1	280	−444	170	170	3.8	4.5	1.2	0.1439	MWDR
641	400	100	40	4.762	−1	−280	446	180	180	3.8	4.5	1.2	0.1349	MWDR
642	400	100	40	4.762	−1	280	−199	179	179	3.8	4.5	1.3	0.1385	MWDR
643	400	100	40	4.762	1	−280	298	227	227	3.8	4.5	1.5	0.0801	MWDR
644	400	100	40	4.762	1	280	16	186	186	3.8	4.5	1.5	0.1195	MWDR
645	400	100	60	−4.762	−1	−280	49	154	154	5.7	4.5	1.6	0.1438	MWDR
646	400	100	60	−4.762	−1	280	−91	181	181	5.7	4.5	1.4	0.1016	MWDR
647	400	100	60	−4.762	1	−280	−256	156	156	5.7	4.5	1.0	0.1386	MWDR
648	400	100	60	−4.762	1	280	−151	160	160	5.7	4.5	1.0	0.1272	MWDR
649	400	100	60	4.762	−1	−280	−131	178	178	5.7	4.5	1.0	0.1093	MWDR
650	400	100	60	4.762	−1	280	91	164	164	5.7	4.5	1.0	0.1230	MWDR
651	400	100	60	4.762	1	−280	17	148	148	5.7	4.5	1.5	0.1507	MWDR
652	400	100	60	4.762	1	280	−91	144	144	5.7	4.5	1.4	0.1576	MWDR
653	400	100	80	−4.762	−1	−280	−47	152	152	7.6	4.5	1.5	0.1045	MWDR
654	400	100	80	−4.762	−1	280	32	187	186	7.6	4.5	1.3	0.0695	MWDR
655	400	100	80	−4.762	1	−280	−245	187	187	7.6	4.5	0.5	0.0715	MWDR

Table continues on next page

Table A.1: Continued from previous page

N_{Exp}	T [ns]	D [ns]	P [%]	B [G]	m_J	f_{ofs} [Hz]	ν_{Fit} [Hz]	$\Delta\nu_0$ [Hz]	$\Delta\nu_{\mathrm{Fit}}$ [Hz]	$\Delta\nu_{\mathrm{Slope}}$ [Hz]	$\Delta\nu_{\mathrm{B}}$ [Hz]	D_{Exp} [h]	W [%]	Data type
656	400	100	80	−4.762	1	280	−113	212	211	7.6	4.5	0.5	0.0550	MWDR
657	400	100	80	4.762	−1	−280	69	215	215	7.6	4.5	0.5	0.0514	MWDR
658	400	100	80	4.762	−1	280	−14	212	211	7.6	4.5	0.5	0.0541	MWDR
659	400	100	80	4.762	1	−280	−15	154	154	7.6	4.5	1.1	0.0994	MWDR
660	400	100	80	4.762	1	280	114	165	165	7.6	4.5	1.1	0.0909	MWDR
661	400	100	100	−4.762	−1	−280	−87	153	152	9.5	4.5	1.0	0.0582	MWDR
662	400	100	100	−4.762	−1	280	318	155	155	9.5	4.5	1.1	0.0620	MWDR
663	400	100	100	−4.762	1	−280	−155	169	169	9.5	4.5	0.5	0.0569	MWDR
664	400	100	100	−4.762	1	280	−212	173	173	9.5	4.5	0.5	0.0454	MWDR
665	400	100	100	4.762	−1	−280	−150	201	200	9.5	4.5	0.5	0.0356	MWDR
666	400	100	100	4.762	−1	280	9	180	180	9.5	4.5	0.5	0.0463	MWDR
667	400	100	100	4.762	1	−280	−144	205	205	9.5	4.5	0.9	0.0369	MWDR
668	400	100	100	4.762	1	280	−81	187	187	9.5	4.5	0.8	0.0426	MWDR
669	400	200	20	−4.762	−1	−280	84	134	133	7.6	4.5	5.1	0.1300	MWDR
670	400	200	20	−4.762	−1	280	−48	137	136	7.6	4.5	5.4	0.1261	MWDR
671	400	200	20	−4.762	1	−280	293	141	141	7.6	4.5	3.6	0.1174	MWDR
672	400	200	20	−4.762	1	280	−120	132	132	7.6	4.5	3.7	0.1331	MWDR
673	400	200	20	4.762	−1	−280	213	138	137	7.6	4.5	3.7	0.1216	MWDR
674	400	200	20	4.762	−1	280	103	141	140	7.6	4.5	3.7	0.1161	MWDR
675	400	200	20	4.762	1	−280	257	118	118	7.6	4.5	5.1	0.1657	MWDR
676	400	200	20	4.762	1	280	9	119	119	7.6	4.5	4.7	0.1652	MWDR
677	400	200	40	−4.762	−1	−280	−99	122	121	15.2	4.5	3.3	0.0003	MWDR
678	400	200	40	−4.762	−1	280	−87	113	112	15.2	4.5	3.7	0.0004	MWDR
679	400	200	40	−4.762	1	−280	94	122	121	15.2	4.5	2.5	0.0001	MWDR
680	400	200	40	−4.762	1	280	97	134	133	15.2	4.5	2.7	0.0005	MWDR
681	400	200	40	4.762	−1	−280	−78	142	141	15.2	4.5	2.6	0.0007	MWDR
682	400	200	40	4.762	−1	280	96	131	130	15.2	4.5	2.6	0.0001	MWDR
683	400	200	40	4.762	1	−280	93	108	106	15.2	4.5	3.7	0.0004	MWDR
684	400	200	40	4.762	1	280	−73	116	115	15.2	4.5	3.6	0.0002	MWDR
685	400	200	60	−4.762	−1	−280	10	121	119	22.8	4.5	2.4	0.0004	MWDR
686	400	200	60	−4.762	−1	280	283	148	146	22.8	4.5	1.9	0.0007	MWDR
687	400	200	60	−4.762	1	−280	77	134	132	22.8	4.5	1.6	0.0004	MWDR
688	400	200	60	−4.762	1	280	−146	128	126	22.8	4.5	1.6	0.0003	MWDR
689	400	200	60	4.762	−1	−280	−2	128	125	22.8	4.5	1.6	0.0002	MWDR
690	400	200	60	4.762	−1	280	−140	135	133	22.8	4.5	1.7	0.0006	MWDR
691	400	200	60	4.762	1	−280	−147	114	112	22.8	4.5	2.4	0.0004	MWDR
692	400	200	60	4.762	1	280	196	131	129	22.8	4.5	2.2	0.0002	MWDR
693	400	200	80	−4.762	−1	−280	−76	109	104	30.4	4.5	2.6	0.0008	MWDR
694	400	200	80	−4.762	−1	280	−133	104	100	30.4	4.5	2.9	0.0001	MWDR
695	400	200	80	−4.762	1	−280	−35	83	78	30.4	4.5	3.7	0.0002	MWDR
696	400	200	80	−4.762	1	280	−60	74	67	30.4	4.5	4.7	0.0007	MWDR
697	400	200	80	4.762	−1	−280	−8	87	81	30.4	4.5	4.0	0.0004	MWDR
698	400	200	80	4.762	−1	280	−26	83	77	30.4	4.5	4.7	0.0000	MWDR
699	400	200	80	4.762	1	−280	111	106	101	30.4	4.5	2.7	0.0003	MWDR
700	400	200	80	4.762	1	280	−74	109	105	30.4	4.5	2.8	0.0006	MWDR
701	400	200	100	−4.762	−1	−280	102	107	99	38.0	4.5	2.0	0.0007	MWDR
702	400	200	100	−4.762	−1	280	−2	116	110	38.0	4.5	2.0	0.0002	MWDR
703	400	200	100	−4.762	1	−280	−64	78	68	38.0	4.5	4.0	0.0008	MWDR
704	400	200	100	−4.762	1	280	−25	81	72	38.0	4.5	3.7	0.0000	MWDR
705	400	200	100	4.762	−1	−280	36	94	86	38.0	4.5	3.1	0.0008	MWDR
706	400	200	100	4.762	−1	280	123	83	74	38.0	4.5	4.0	0.0007	MWDR
707	400	200	100	4.762	1	−280	144	114	108	38.0	4.5	1.9	0.0003	MWDR
708	400	200	100	4.762	1	280	57	115	109	38.0	4.5	1.7	0.0005	MWDR
709	500	100	80	−4.762	−1	−280	−236	199	199	6.1	4.5	1.4	0.0837	MWDR
710	500	100	80	−4.762	−1	280	−256	229	229	6.1	4.5	1.2	0.0617	MWDR
711	500	100	80	−4.762	1	−280	151	256	255	6.1	4.5	1.2	0.0499	MWDR
712	500	100	80	−4.762	1	280	357	255	255	6.1	4.5	1.2	0.0498	MWDR
713	500	100	80	4.762	−1	−280	−29	256	256	6.1	4.5	1.3	0.0493	MWDR
714	500	100	80	4.762	−1	280	−283	224	224	6.1	4.5	1.2	0.0701	MWDR
715	500	100	80	4.762	1	−280	48	198	198	6.1	4.5	1.4	0.0826	MWDR

Table continues on next page

Table A.1: Continued from previous page

N_{Exp}	T [ns]	D [ns]	P [%]	B [G]	m_J	f_{ofs} [Hz]	ν_{Fit} [Hz]	$\Delta\nu_0$ [Hz]	$\Delta\nu_{\text{Fit}}$ [Hz]	$\Delta\nu_{\text{Slope}}$ [Hz]	$\Delta\nu_{\text{B}}$ [Hz]	D_{Exp} [h]	W [%]	Data type
716	500	100	80	4.762	1	280	303	240	240	6.1	4.5	1.2	0.0539	MWDR
717	500	100	100	−4.762	−1	−280	189	148	148	7.6	4.5	3.6	0.1048	MWDR
718	500	100	100	−4.762	−1	280	49	145	145	7.6	4.5	3.4	0.1112	MWDR
719	500	100	100	−4.762	1	−280	141	215	214	7.6	4.5	1.4	0.0504	MWDR
720	500	100	100	−4.762	1	280	−59	188	188	7.6	4.5	1.4	0.0685	MWDR
721	500	100	100	4.762	−1	−280	33	199	198	7.6	4.5	1.4	0.0584	MWDR
722	500	100	100	4.762	−1	280	322	191	191	7.6	4.5	1.4	0.0625	MWDR
723	500	100	100	4.762	1	−280	10	144	144	7.6	4.5	2.9	0.1155	MWDR
724	500	100	100	4.762	1	280	−279	132	132	7.6	4.5	2.9	0.1333	MWDR
725	300	100	100	−4.762	−1	−280	39	52	50	12.6	4.5	5.6	0.0008	LSPP
726	300	100	100	−4.762	−1	280	5	55	53	12.6	4.5	5.6	0.0000	LSPP
727	300	100	100	−4.762	1	−280	−3	36	34	12.6	4.5	8.0	0.0008	LSPP
728	300	100	100	−4.762	1	280	81	35	33	12.6	4.5	8.0	0.0002	LSPP
729	300	100	100	4.762	−1	−280	1	41	39	12.6	4.5	8.0	0.0001	LSPP
730	300	100	100	4.762	−1	280	−55	44	42	12.6	4.5	8.0	0.0004	LSPP
731	300	100	100	4.762	1	−280	16	48	46	12.6	4.5	5.8	0.0003	LSPP
732	300	100	100	4.762	1	280	−23	47	45	12.6	4.5	5.7	0.0007	LSPP
733	300	100	100	−4.762	−1	280	−129	40	38	12.6	4.5	7.5	0.0000	L447P
734	300	100	100	−4.762	1	−280	−111	159	159	12.6	4.5	0.5	0.0002	L447P
735	300	100	100	−4.762	1	280	61	37	35	12.6	4.5	9.8	0.0007	L447P
736	300	100	100	4.762	−1	−280	202	242	242	12.6	4.5	0.5	0.0002	L447P
737	300	100	100	4.762	−1	280	82	36	34	12.6	4.5	9.9	0.0008	L447P
738	300	100	100	4.762	1	280	56	40	38	12.6	4.5	8.1	0.0007	L447P
739	300	50	20	−4.762	−1	−280	−98	133	133	8.8	4.5	2.9	0.1012	18F
740	300	50	20	−4.762	−1	280	126	129	128	8.8	4.5	2.9	0.1097	18F
741	300	50	20	−4.762	1	−280	−240	132	132	8.8	4.5	2.9	0.0968	18F
742	300	50	20	−4.762	1	280	3	136	136	8.8	4.5	2.9	0.0918	18F
743	300	50	20	4.762	−1	−280	−34	139	139	8.8	4.5	2.9	0.0829	18F
744	300	50	20	4.762	−1	280	82	140	140	8.8	4.5	2.9	0.0858	18F
745	300	50	20	4.762	1	−280	4	136	136	8.8	4.5	2.9	0.0973	18F
746	300	50	20	4.762	1	280	37	134	134	8.8	4.5	2.9	0.1005	18F
747	300	50	40	−4.762	−1	−280	−165	147	146	17.6	4.5	1.6	0.0000	18F
748	300	50	40	−4.762	−1	280	138	129	128	17.6	4.5	1.6	0.0002	18F
749	300	50	40	−4.762	1	−280	−52	126	124	17.6	4.5	1.8	0.0008	18F
750	300	50	40	−4.762	1	280	−48	164	163	17.6	4.5	1.2	0.0006	18F
751	300	50	40	4.762	−1	−280	−147	128	127	17.6	4.5	1.9	0.0007	18F
752	300	50	40	4.762	−1	280	10	118	117	17.6	4.5	1.7	0.0001	18F
753	300	50	40	4.762	1	−280	253	138	137	17.6	4.5	1.5	0.0002	18F
754	300	50	40	4.762	1	280	−1	128	126	17.6	4.5	1.6	0.0007	18F
755	300	50	60	−4.762	−1	−280	−83	143	140	26.4	4.5	1.2	0.0007	18F
756	300	50	60	−4.762	−1	280	−21	140	138	26.4	4.5	1.2	0.0001	18F
757	300	50	60	−4.762	1	−280	29	128	125	26.4	4.5	1.2	0.0003	18F
758	300	50	60	−4.762	1	280	−100	132	130	26.4	4.5	1.2	0.0004	18F
759	300	50	60	4.762	−1	−280	−89	115	112	26.4	4.5	1.2	0.0006	18F
760	300	50	60	4.762	−1	280	−97	135	133	26.4	4.5	1.2	0.0004	18F
761	300	50	60	4.762	1	−280	−75	137	134	26.4	4.5	1.2	0.0000	18F
762	300	50	60	4.762	1	280	95	140	137	26.4	4.5	1.2	0.0005	18F
763	300	50	80	−4.762	−1	−280	−176	123	117	35.2	4.5	1.1	0.0006	18F
764	300	50	80	−4.762	−1	280	−119	128	123	35.2	4.5	1.1	0.0004	18F
765	300	50	80	−4.762	1	−280	−129	140	136	35.2	4.5	1.0	0.0003	18F
766	300	50	80	−4.762	1	280	34	136	132	35.2	4.5	0.7	0.0006	18F
767	300	50	80	4.762	−1	−280	169	133	129	35.2	4.5	1.0	0.0004	18F
768	300	50	80	4.762	−1	280	44	131	126	35.2	4.5	1.0	0.0006	18F
769	300	50	80	4.762	1	−280	78	159	155	35.2	4.5	1.0	0.0008	18F
770	300	50	80	4.762	1	280	99	160	156	35.2	4.5	1.1	0.0000	18F
771	300	50	100	−4.762	−1	−280	−8	120	111	44.0	4.5	1.0	0.0007	18F
772	300	50	100	−4.762	−1	280	60	116	108	44.0	4.5	1.0	0.0004	18F
773	300	50	100	−4.762	1	−280	−88	127	119	44.0	4.5	1.1	0.0002	18F
774	300	50	100	−4.762	1	280	128	121	112	44.0	4.5	1.2	0.0005	18F
775	300	50	100	4.762	−1	−280	−155	152	145	44.0	4.5	0.9	0.0004	18F

Table continues on next page

Table A.1: Continued from previous page

N_{Exp}	T [ns]	D [ns]	P [%]	B [G]	m_J	f_{ofs} [Hz]	ν_{Fit} [Hz]	$\Delta\nu_0$ [Hz]	$\Delta\nu_{\mathrm{Fit}}$ [Hz]	$\Delta\nu_{\mathrm{Slope}}$ [Hz]	$\Delta\nu_{\mathrm{B}}$ [Hz]	D_{Exp} [h]	W [%]	Data type
776	300	50	100	4.762	−1	280	−233	150	144	44.0	4.5	0.9	0.0001	18F
777	300	50	100	4.762	1	−280	144	163	157	44.0	4.5	1.0	0.0008	18F
778	300	50	100	4.762	1	280	77	146	139	44.0	4.5	1.0	0.0007	18F
779	300	100	20	−4.762	−1	−280	56	101	101	2.5	4.5	1.9	0.4855	18F
780	300	100	20	−4.762	−1	280	−76	127	127	2.5	4.5	1.4	0.3050	18F
781	300	100	20	−4.762	1	−280	240	130	130	2.5	4.5	2.0	0.2988	18F
782	300	100	20	−4.762	1	280	59	124	123	2.5	4.5	2.0	0.3327	18F
783	300	100	20	4.762	−1	−280	272	123	123	2.5	4.5	1.9	0.3178	18F
784	300	100	20	4.762	−1	280	−243	117	117	2.5	4.5	1.9	0.3666	18F
785	300	100	20	4.762	1	−280	166	131	130	2.5	4.5	1.7	0.3023	18F
786	300	100	20	4.762	1	280	208	133	133	2.5	4.5	1.4	0.2862	18F
787	300	100	40	−4.762	−1	−280	−60	115	115	5.1	4.5	1.0	0.2755	18F
788	300	100	40	−4.762	−1	280	161	108	108	5.1	4.5	1.0	0.3157	18F
789	300	100	40	−4.762	1	−280	16	136	136	5.1	4.5	1.0	0.2048	18F
790	300	100	40	−4.762	1	280	−86	139	139	5.1	4.5	1.0	0.1880	18F
791	300	100	40	4.762	−1	−280	−201	130	129	5.1	4.5	1.0	0.2153	18F
792	300	100	40	4.762	−1	280	−54	126	126	5.1	4.5	1.0	0.2349	18F
793	300	100	40	4.762	1	−280	−16	112	111	5.1	4.5	1.0	0.2940	18F
794	300	100	40	4.762	1	280	403	162	162	5.1	4.5	1.0	0.1433	18F
795	300	100	60	−4.762	−1	−280	−92	94	94	7.6	4.5	1.0	0.2580	18F
796	300	100	60	−4.762	−1	280	76	120	120	7.6	4.5	0.8	0.1594	18F
797	300	100	60	−4.762	1	−280	91	134	134	7.6	4.5	0.7	0.1306	18F
798	300	100	60	−4.762	1	280	104	116	115	7.6	4.5	0.7	0.1746	18F
799	300	100	60	4.762	−1	−280	−38	124	123	7.6	4.5	0.8	0.1653	18F
800	300	100	60	4.762	−1	280	85	119	119	7.6	4.5	0.8	0.1702	18F
801	300	100	60	4.762	1	−280	80	102	102	7.6	4.5	1.0	0.2326	18F
802	300	100	60	4.762	1	280	133	107	107	7.6	4.5	1.0	0.2073	18F
803	300	100	80	−4.762	−1	−280	57	97	97	10.1	4.5	1.1	0.1134	18F
804	300	100	80	−4.762	−1	280	171	79	79	10.1	4.5	1.1	0.1687	18F
805	300	100	80	−4.762	1	−280	−45	143	142	10.1	4.5	0.5	0.0520	18F
806	300	100	80	−4.762	1	280	−416	129	128	10.1	4.5	0.5	0.0671	18F
807	300	100	80	4.762	−1	−280	23	152	151	10.1	4.5	0.5	0.0448	18F
808	300	100	80	4.762	−1	280	−136	121	120	10.1	4.5	0.5	0.0725	18F
809	300	100	80	4.762	1	−280	69	84	84	10.1	4.5	1.4	0.1485	18F
810	300	100	80	4.762	1	280	28	81	80	10.1	4.5	1.3	0.1605	18F
811	300	100	100	−9.524	−1	−280	152	133	131	12.6	18.0	0.5	0.0003	18F
812	300	100	100	−9.524	−1	280	−3	129	127	12.6	18.0	0.5	0.0005	18F
813	300	100	100	−9.524	1	−280	118	136	134	12.6	18.0	0.5	0.0007	18F
814	300	100	100	−9.524	1	280	−161	112	110	12.6	18.0	0.5	0.0004	18F
815	300	100	100	−8.248	−1	−280	−29	128	127	12.6	13.5	0.6	0.0005	18F
816	300	100	100	−8.248	−1	280	−114	136	134	12.6	13.5	0.6	0.0004	18F
817	300	100	100	−8.248	1	−280	81	139	138	12.6	13.5	0.4	0.0003	18F
818	300	100	100	−8.248	1	280	−192	119	117	12.6	13.5	0.4	0.0003	18F
819	300	100	100	−6.734	−1	−280	−135	144	143	12.6	9.0	0.2	0.0001	18F
820	300	100	100	−6.734	−1	280	226	157	156	12.6	9.0	0.2	0.0001	18F
821	300	100	100	−6.734	1	−280	−22	114	113	12.6	9.0	0.4	0.0006	18F
822	300	100	100	−6.734	1	280	68	111	110	12.6	9.0	0.4	0.0007	18F
823	300	100	100	−4.762	−1	−280	−171	229	229	12.6	4.5	0.1	0.0004	18F
824	300	100	100	−4.762	−1	280	−115	153	153	12.6	4.5	0.4	0.0004	18F
825	300	100	100	−4.762	1	−280	−8	115	115	12.6	4.5	0.5	0.0001	18F
826	300	100	100	−4.762	1	280	−53	110	109	12.6	4.5	0.5	0.0003	18F
827	300	100	100	4.762	−1	−280	−27	130	129	12.6	4.5	0.5	0.0004	18F
828	300	100	100	4.762	−1	280	196	129	129	12.6	4.5	0.5	0.0002	18F
829	300	100	100	4.762	1	−280	58	93	92	12.6	4.5	0.6	0.0006	18F
830	300	100	100	4.762	1	280	175	154	153	12.6	4.5	0.4	0.0002	18F
831	300	100	100	6.734	−1	−280	171	120	119	12.6	9.0	0.4	0.0003	18F
832	300	100	100	6.734	−1	280	9	122	121	12.6	9.0	0.4	0.0007	18F
833	300	100	100	6.734	1	−280	−67	161	160	12.6	9.0	0.2	0.0003	18F
834	300	100	100	6.734	1	280	188	121	120	12.6	9.0	0.2	0.0008	18F
835	300	100	100	8.248	−1	−280	266	122	121	12.6	13.6	0.4	0.0006	18F

Table continues on next page

Table A.1: Continued from previous page

N_{Exp}	T [ns]	D [ns]	P [%]	B [G]	m_J	f_{ofs} [Hz]	ν_{Fit} [Hz]	$\Delta\nu_0$ [Hz]	$\Delta\nu_{\text{Fit}}$ [Hz]	$\Delta\nu_{\text{Slope}}$ [Hz]	$\Delta\nu_{\text{B}}$ [Hz]	D_{Exp} [h]	W [%]	Data type
836	300	100	100	8.248	−1	280	5	148	146	12.6	13.6	0.4	0.0008	18F
837	300	100	100	8.248	1	−280	165	93	91	12.6	13.6	0.7	0.0005	18F
838	300	100	100	8.248	1	280	57	121	119	12.6	13.6	0.6	0.0004	18F
839	300	100	100	9.524	−1	−280	65	135	134	12.6	18.0	0.5	0.0000	18F
840	300	100	100	9.524	−1	280	−16	118	115	12.6	18.0	0.5	0.0005	18F
841	300	100	100	9.524	1	−280	−11	108	106	12.6	18.0	0.5	0.0003	18F
842	300	100	100	9.524	1	280	−17	148	146	12.6	18.0	0.5	0.0002	18F
843	400	100	100	−4.762	−1	−280	−237	108	107	9.5	4.5	1.5	0.1284	18F
844	400	100	100	−4.762	−1	280	55	100	99	9.5	4.5	1.6	0.1419	18F
845	400	100	100	−4.762	1	−280	−98	99	98	9.5	4.5	1.2	0.1325	18F
846	400	100	100	−4.762	1	280	183	103	103	9.5	4.5	1.2	0.1238	18F
847	400	100	100	4.762	−1	−280	−14	101	101	9.5	4.5	1.2	0.1304	18F
848	400	100	100	4.762	−1	280	79	96	95	9.5	4.5	1.2	0.1495	18F
849	400	100	100	4.762	1	−280	22	107	106	9.5	4.5	1.6	0.1187	18F
850	400	100	100	4.762	1	280	−107	106	105	9.5	4.5	1.6	0.1244	18F
851	400	200	20	−4.762	−1	−280	341	142	142	7.6	4.5	3.4	0.1150	18F
852	400	200	20	−4.762	−1	280	17	136	136	7.6	4.5	3.7	0.1269	18F
853	400	200	20	−4.762	1	−280	−43	125	125	7.6	4.5	3.4	0.1515	18F
854	400	200	20	−4.762	1	280	−12	133	133	7.6	4.5	3.4	0.1377	18F
855	400	200	20	4.762	−1	−280	178	142	142	7.6	4.5	3.6	0.1186	18F
856	400	200	20	4.762	−1	280	72	138	137	7.6	4.5	3.5	0.1213	18F
857	400	200	20	4.762	1	−280	106	126	126	7.6	4.5	3.5	0.1451	18F
858	400	200	20	4.762	1	280	−128	133	133	7.6	4.5	3.4	0.1368	18F
859	400	200	40	−4.762	−1	−280	−270	147	147	15.2	4.5	1.6	0.0005	18F
860	400	200	40	−4.762	−1	280	−83	133	133	15.2	4.5	1.6	0.0001	18F
861	400	200	40	−4.762	1	−280	−286	139	138	15.2	4.5	2.0	0.0002	18F
862	400	200	40	−4.762	1	280	106	130	129	15.2	4.5	2.0	0.0001	18F
863	400	200	40	4.762	−1	−280	−278	144	143	15.2	4.5	2.0	0.0008	18F
864	400	200	40	4.762	−1	280	172	137	136	15.2	4.5	1.9	0.0004	18F
865	400	200	40	4.762	1	−280	−14	144	143	15.2	4.5	1.6	0.0002	18F
866	400	200	40	4.762	1	280	85	142	141	15.2	4.5	1.6	0.0002	18F
867	400	200	60	−4.762	−1	−280	96	140	139	22.8	4.5	1.4	0.0001	18F
868	400	200	60	−4.762	−1	280	−200	148	147	22.8	4.5	1.4	0.0003	18F
869	400	200	60	−4.762	1	−280	127	131	129	22.8	4.5	1.6	0.0001	18F
870	400	200	60	−4.762	1	280	5	127	125	22.8	4.5	1.7	0.0001	18F
871	400	200	60	4.762	−1	−280	−101	135	133	22.8	4.5	1.6	0.0006	18F
872	400	200	60	4.762	−1	280	−92	122	120	22.8	4.5	1.6	0.0000	18F
873	400	200	60	4.762	1	−280	−177	131	129	22.8	4.5	1.3	0.0006	18F
874	400	200	60	4.762	1	280	20	114	112	22.8	4.5	1.3	0.0003	18F
875	400	200	80	−4.762	−1	−280	52	124	120	30.4	4.5	1.1	0.0006	18F
876	400	200	80	−4.762	−1	280	−87	142	138	30.4	4.5	1.1	0.0005	18F
877	400	200	80	−4.762	1	−280	−312	137	133	30.4	4.5	1.3	0.0006	18F
878	400	200	80	−4.762	1	280	−168	140	136	30.4	4.5	1.3	0.0006	18F
879	400	200	80	4.762	−1	−280	132	139	135	30.4	4.5	1.3	0.0002	18F
880	400	200	80	4.762	−1	280	−181	135	131	30.4	4.5	1.3	0.0001	18F
881	400	200	80	4.762	1	−280	−23	131	127	30.4	4.5	1.1	0.0008	18F
882	400	200	80	4.762	1	280	17	138	134	30.4	4.5	1.1	0.0008	18F
883	400	200	100	−4.762	−1	−280	−110	145	140	38.0	4.5	0.9	0.0004	18F
884	400	200	100	−4.762	−1	280	286	143	138	38.0	4.5	0.9	0.0006	18F
885	400	200	100	−4.762	1	−280	34	131	125	38.0	4.5	1.1	0.0005	18F
886	400	200	100	−4.762	1	280	−13	109	102	38.0	4.5	1.2	0.0000	18F
887	400	200	100	4.762	−1	−280	160	136	131	38.0	4.5	1.1	0.0001	18F
888	400	200	100	4.762	−1	280	−161	135	130	38.0	4.5	1.1	0.0007	18F
889	400	200	100	4.762	1	−280	−5	134	128	38.0	4.5	0.9	0.0004	18F
890	400	200	100	4.762	1	280	130	119	112	38.0	4.5	0.9	0.0008	18F
891	500	100	100	−4.762	−1	−280	−48	112	112	7.6	4.5	4.6	0.1860	18F
892	500	100	100	−4.762	−1	280	178	110	109	7.6	4.5	4.5	0.1991	18F
893	500	100	100	−4.762	1	−280	−12	122	122	7.6	4.5	3.1	0.1643	18F
894	500	100	100	−4.762	1	280	111	118	117	7.6	4.5	3.1	0.1664	18F
895	500	100	100	4.762	−1	−280	−79	162	162	7.6	4.5	2.4	0.0877	18F

Table continues on next page

Table A.1: Continued from previous page

N_{Exp}	T [ns]	D [ns]	P [%]	B [G]	m_J	f_{ofs} [Hz]	ν_{Fit} [Hz]	$\Delta\nu_0$ [Hz]	$\Delta\nu_{\mathrm{Fit}}$ [Hz]	$\Delta\nu_{\mathrm{Slope}}$ [Hz]	$\Delta\nu_{\mathrm{B}}$ [Hz]	D_{Exp} [h]	W [%]	Data type
896	500	100	100	4.762	−1	280	−68	151	151	7.6	4.5	2.4	0.1045	18F
897	500	100	100	4.762	1	−280	80	116	116	7.6	4.5	4.6	0.1796	18F
898	500	100	100	4.762	1	280	−165	110	110	7.6	4.5	4.5	0.1916	18F
899	600	100	100	−4.762	−1	−280	−414	657	657	6.3	4.5	0.7	0.0089	18F
900	600	100	100	−4.762	1	−280	7	503	503	6.3	4.5	1.2	0.0130	18F
901	600	100	100	−4.762	1	280	−645	544	544	6.3	4.5	1.2	0.0123	18F
902	600	100	100	4.762	−1	−280	406	1024	1024	6.3	4.5	0.5	0.0037	18F
903	600	100	100	4.762	1	−280	1231	761	761	6.3	4.5	0.4	0.0072	18F
904	600	100	100	4.762	1	280	245	1087	1087	6.3	4.5	0.4	0.0030	18F

End of table

B Source Code for Numerical Simulation of the Experiment

The code presented in this appendix was written for the Fortran 2008 standard and compiled using the Intel Fortran Compiler. The compiler flags were set to the `O2` optimization level, with function inlining allowed (`Ob2`), and with all improved floating-point precision flags enabled. The `QxHost` flag to optimize code for the processor of the computer on which it was compiled and run (Intel Core i5-4690) was also enabled.

```fortran
program schrodSim
   use iso_fortran_env, only: int16, int32, real64
   use ifport
   use omp_lib
   implicit none

   integer, parameter :: RK=real64, Ishort=int16, Ilong=int32

   !Units: GHz, ns, J, gauss, mm
   integer(Ilong) :: nFreqs, nPhis_overall, folStat, nPhis, nStates=9, nTracePts, tInd, nThreadsNative, nThreadsToUse
   integer(Ilong) :: init_i, i_freq, f0Ind, j_phis, j_switchPhis, expNum, parLoopInd, nFreqsDone, saveFreqInd
   complex(RK), parameter :: ci=(0.0_RK,1.0_RK), c0=(0.0_RK,0.0_RK), c1=(1.0_RK,0.0_RK)
   real(RK), dimension(:), allocatable :: phis, phis_overall, phis_coupling, switchPhis_deg, Bt, freqs_loop, phis_loop, loopArr, chirpScales
```

```
  real(RK), dimension(2) :: amp_coupling, phi_coupling
  real(RK), parameter :: pi=4.0_RK*ATAN(1.0_RK)
  real(RK), parameter :: h_planck=6.626070040E-25_RK, hbar=h_planck/2.0_RK/pi !CODATA, J/GHz
  real(RK), parameter :: muB=9.274009994E-28_RK !CODATA, J/gauss
  real(RK), parameter :: freq01=29.616951_RK, freq12=2.29117659_RK, EJ1=0.0_RK, EJ0=h_planck*freq01+EJ1, EJ2 = EJ1-h_planck*freq12
  real(RK), parameter :: gS=2.00231930436182_RK, gL=0.9998629_RK !CODATA
! real(RK), parameter :: gS=2.00223886745683_RK, gL=0.9998736_RK !Drake (1994) Corrections
  real(RK), parameter :: chi=muB*(gS+gL), xi=muB*(gS-gL), saveStep = 0.01_RK, t0=20.0_RK
  real(RK) :: t_max, h, t, t_step, t_halfStep, tT, tD, freqRF, amp, PSlope, PQuad, PCube, PImbal, k_amp
  real(RK) :: centreT, Bz0, nPhis_overall_float, theta_MW, powerLvl, ampScale, loopVar, chirpStretch
  complex(RK), dimension(:,:), allocatable :: psi, psi_new, k, k1, k2, k3, k4, psi_sum
  complex(RK), dimension(:), allocatable :: psi_vec
  real(RK), dimension(:,:), allocatable :: B, B_step, B_halfStep, B_background, pops_out, trace, pops
  character(len=*), parameter :: resultsStem='C:\CodeBlocks Fortran projects\30 GHz parallel bad switch\results', resultsDesc = 'vary coupling always on'
  character(len=*), parameter :: printFmtStr='(I2.1,A,I2.1,A,I2,A,I2,A,I2,F7.3,A,F5.3)'
  character(len=5) :: switchPhiStr
  character(len=100) :: loopStr
  character(len=260) :: resultsDir, fullSaveDir
  character(len=1), dimension(2) :: expTypes=['A','B']
! character(len=1), dimension(1) :: expTypes=['A']
  character(len=1) :: expType

  h = 5.0E-5_RK !Good step size
  tT = 300.0_RK !Experiment period, ns
  tD = 100.0_RK !Pulse duration, ns

  Bz0 = 4.762_RK !DC B field
  theta_MW = 0.0_RK !Microwave polarisation angle, degrees
  PSlope = 0.0_RK !Power slope, %/MHz.
! PQuad = 0.5_RK !Quadratic power shift, %/MHz^2. Also a nantucket whaling ship
! PCube = 0.05_RK !Cubic power shift, %/MHz^3
  PImbal = 1.0_RK !Drops the power of one pulse to this fraction (value for no effect = 1)
```

```
! k_amp = 1.0E-2 !Coupling between generators, in terms of amplitude

   chirpStretch = 1.0_RK !Larger = wider chirp
! chirpScales = [1, -4, 2, 7]/6.0_RK !Scale individual chirps
   chirpScales = [0, 0, 0, 0]*1.0_RK

   powerLvl = 100.0_RK

   loopArr = [5.0E-3]*1.0_RK

! loopArr = [10,55,100]*1.0_RK !For a power scan
! loopArr = [10,100]*1.0_RK
! loopArr = [100]*1.0_RK

! t_max = tT + tD + 2*t0
! centreT = t_max/2.0_RK
   t_max = 2*tT !Integrate over a whole two-pulse period of the experiment cycle. Use this if something is happening when pulses are "off"
   centreT = t0 + (tT+tD)/2.0_RK !Centre time is halfway between the pulses

   phis_overall = [0:2]*2.0_RK*pi/3.0_RK !For averaging over global phase. Works as an extra dimension for most arrays, which is then averaged over.
! switchPhis_deg = [0:16]*22.5_RK
   switchPhis_deg = [120]*1.0_RK

! psi_vec = SQRT([c0, 1*c1, 1*c1, 1*c1, c0, c0, c0, c0, c0]) !Start with mixed population
   psi_vec = SQRT([c0, c0, c1, c0, c0, c0, c0, c0, c0]) !Start with perfect population

   nPhis = 4
   phis_loop = [0:nPhis-1]*2.0_RK*pi/nPhis !FOSOF phases sampled throughout offset period

! freqs_loop = [-7:7]/1.0_RK !For testing with smaller number of frequencies
! freqs_loop = freqs_loop*1.0E-3_RK + freq01

   freqs_loop = [29609.458, 29610.583, 29611.708, 29612.833, 29613.958, 29614.458,& !Freqs used in exp for D=100
            & 29614.625, 29614.791, 29614.958, 29615.125, 29615.291, 29615.458,&
            & 29615.625, 29615.791, 29615.958, 29616.125, 29616.291, 29616.458,&
            & 29616.625, 29616.791, 29616.958, 29617.125, 29617.291, 29617.458,&
```

```
            & 29617.625, 29617.791, 29617.958, 29618.125, 29618.291, 29618.458,&
            & 29618.625, 29618.791, 29618.958, 29619.125, 29619.291, 29619.458,&
            & 29619.958, 29621.083, 29622.208, 29623.333, 29624.458]*1.0E-3_RK

   freqs_loop = (freqs_loop - freq01)*100.0_RK/tD + freq01 !Rescale frequency list appropriately for when D is not 100 ns

   nFreqs = SIZE(freqs_loop)
   f0Ind = NINT(nFreqs/2.0_RK)
   saveFreqInd = f0ind
   nPhis_overall = SIZE(phis_overall)
   nPhis_overall_float = REAL(nPhis_overall,RK)
   psi_vec = psi_vec/SQRT(SUM(ABS(psi_vec)**2)) !Normalise wavefunction

   !Use enough threads such that you're never running fewer threads than number of cores
   !(eg 41 freqs with 16 threads would use 16 then 16 then 9, which would waste CPU time)
   !I think this is optimal but have not yet tested to be sure
! nThreadsNative = omp_get_num_procs()
! nThreadsToUse = nThreadsNative
! if (nFreqs.LT.nThreadsNative) then
! nThreadsToUse = nFreqs
! else if (nFreqs.LE.2*nThreadsNative) then
! nThreadsToUse = NINT(nFreqs/2.0_RK)
! else
! do while(mod(nFreqs,nThreadsToUse) .LT. nThreadsNative)
! nThreadsToUse = nThreadsToUse + 1
! end do
! end if
! CALL omp_set_num_threads(nThreadsToUse)

   allocate(pops_out(nFreqs,1+nPhis))
   allocate(psi_new(nPhis_overall,nStates), psi(nPhis_overall,nStates))
   allocate(B_background(nPhis_overall,3), B(nPhis_overall,3), B_step(nPhis_overall,3), B_halfStep(nPhis_overall,3))
   allocate(phis(nPhis_overall), phis_coupling(nPhis_overall), Bt(nPhis_overall))
   nTracePts = CEILING(t_max/saveStep) !For saving decimated trace data, skip t=0
   allocate(trace(nTracePts,3), pops(nTracePts,5))

   do j_switchPhis=1,size(switchPhis_deg)
```

```fortran
      do parLoopInd=1,SIZE(loopArr) !Whole run loop for changing parameters
         loopVar = loopArr(parLoopInd)

                  !Select which parameter is being varied in the loop
! theta_MW = loopVar
! Bz0 = loopVar
! powerLvl = loopVar
! h = loopVar
! PSlope = 0.05_RK*powerLvl !5%/MHz at 100%, 0.5%/MHz at 10%
! nPhis = NINT(loopVar)
! phis_loop = [0:nPhis-1]*2.0_RK*pi/nPhis !FOSOF
! allocate(pops_out(nFreqs,1+nPhis))

         k_amp = loopVar

         write(loopStr, '(E25.17)') loopVar
         write(switchPhiStr, '(F5.1)') switchPhis_deg(j_switchPhis)
         B_background(1:nPhis_overall, 1) = 0.0_RK !Residual background B field (x,y,z)
         B_background(1:nPhis_overall, 2) = 0.0_RK
         B_background(1:nPhis_overall, 3) = 0.0_RK

         resultsDir = resultsStem//'/'//resultsDesc//' '//switchPhiStr//'deg'
         fullSaveDir = trim(adjustl(resultsDir))//'/'//trim(adjustl(loopStr))
         folStat = MAKEDIRQQ(trim(adjustl(resultsDir)))
         folStat = MAKEDIRQQ(trim(adjustl(fullSaveDir)))

         do expNum=1,size(expTypes) !A/B experiment loop, for reversing order of pulses
            expType = expTypes(expNum)
            open(20, file=trim(adjustl(fullSaveDir))//'/'//expType//'.bin', form='unformatted', status='unknown')
            do j_phis=1,nPhis !Pulse phase loop, this is the FOSOF part
               nFreqsDone = 1
                              ! OpenMP parallel variable assignment. Must make most variables private so that different threads do not interfere, by default they are public
               !$OMP PARALLEL FIRSTPRIVATE(j_phis, parLoopInd, loopVar, powerLvl) &
               !$OMP& PRIVATE(freqRF, ampScale, amp, phis, phi_coupling, amp_coupling, &
               !$OMP& & t, t_halfStep, t_step, B, Bt, B_halfStep, B_step, psi, psi_sum, psi_new, k1, k2, k3, k4, k, tInd)
```

```fortran
            !$OMP DO
            do i_freq=1,nFreqs !Microwave frequency loop
               freqRF = freqs_loop(i_freq)
               ampScale = 0.5_RK*SQRT(powerLvl/100.0_RK)*SQRT(1.0_RK + (freqRF-freq01)*10.0_RK*PSlope) !Linear, *10 instead of /100 because GHz/MHz conversion
! ampScale = 0.5_RK*SQRT(powerLvl/100.0_RK)*SQRT(1.0_RK + (freqRF-freq01)*10.0_RK*PSlope*SIGN(1.0_RK, powerLvl - 79.9_RK)) !Linear, reverse slope at 80%
! ampScale = 0.5_RK*SQRT(powerLvl/100.0_RK)*SQRT(1.0_RK + (1.0E3_RK*(freqRF-freq01))**2.0_RK*PCube*0.01_RK) !Quadratic
! ampScale = 0.5_RK*SQRT(powerLvl/100.0_RK)*SQRT(1.0_RK + (1.0E3_RK*(freqRF-freq01))**3.0_RK*PCube*0.01_RK) !Cubic

               !SIGN is a 2-arg function, SIGN(x,y) returns |x|*y/|y| (magnitude of x, sign of y)
! ampScale = 0.5_RK*SQRT(powerLvl/100.0_RK)*SQRT(1.0_RK+SIGN((1.0E3_RK*(freqRF-freq01)**2.0_RK*PSlope*0.01_RK),freqRF-freq01))

               !Runge-Kutta initialising
               t = 0.0_RK
               amp = 0.0_RK
               phis = [1:nPhis_overall]*0.0_RK
               phis_coupling = [1:nPhis_overall]*0.0_RK
               Bt = [1:nPhis_overall]*0.0_RK

               do init_i=1,nPhis_overall
                  psi_new(init_i, 1:nStates) = psi_vec
               end do
               B_step(1:nPhis_overall, 1) = 0.0_RK
               B_step(1:nPhis_overall, 2) = 0.0_RK
               B_step(1:nPhis_overall, 3) = Bz0
               B_step = B_step + B_background

               if((j_phis.EQ.nPhis).AND.(i_freq.EQ.saveFreqInd)) then
                  open(11, file=trim(adjustl(fullSaveDir))//'/'//'trace_'//expType//'.bin', form='unformatted', status='unknown')
                  open(12, file=trim(adjustl(fullSaveDir))//'/'//'pops_'//expType//'.bin', form='unformatted', status='unknown')
               end if
```

```
                  do while (t.LT.t_max) !Runge-Kutta loop
                     t_halfStep = t + h/2.0_RK
                     t_step = t + h

                     psi = psi_new
                     !z-polarised microwaves with some y component, and z-aligned DC B field. Use previous iteration to maybe save on calculations
                     B = B_step

                     call getAmpPhi(t_halfStep, ampScale, amp, phis, chirpStretch, chirpScales, amp_coupling, phi_coupling)
                     !Changing shapes of amp_coupling(1) and (2) for A/B is done in getAmpPhi. This gives the right A/B switch
                     Bt = amp*COS(2*pi*freqRF*t_halfStep + phis) + ampScale*(amp_coupling(1)* &
                        COS(2*pi*freqRF*t_halfStep + phis_overall + phis_loop(j_phis) + &
                         phi_coupling(1)) + amp_coupling(2)*COS(2*pi*freqRF*t_halfStep + phis_overall + phi_coupling(2)))
                     B_halfStep(1:nPhis_overall, 1) = 0.0_RK
                     B_halfStep(1:nPhis_overall, 2) = Bt*SIND(theta_MW)
                     B_halfStep(1:nPhis_overall, 3) = Bz0 + Bt*COSD(theta_MW)
                     B_halfStep = B_halfStep + B_background

                     call getAmpPhi(t_step, ampScale, amp, phis, chirpStretch, chirpScales, amp_coupling, phi_coupling)
                     Bt = amp*COS(2*pi*freqRF*t_step + phis) + ampScale*(amp_coupling(1)* &
                        COS(2*pi*freqRF*t_step + phis_overall + phis_loop(j_phis) + &
                        phi_coupling(1)) + amp_coupling(2)*COS(2*pi*freqRF*t_step + phis_overall + phi_coupling(2)))
                     B_step(1:nPhis_overall, 1) = 0.0_RK
                     B_step(1:nPhis_overall, 2) = Bt*SIND(theta_MW)
                     B_step(1:nPhis_overall, 3) = Bz0 + Bt*COSD(theta_MW)
                     B_step = B_step + B_background

                     !Summing variables in arguments of function calls leads to a compiler warning about temp arrays, this is just making the temp arrays (for RK summands) explicitly
                     k1 = schrodStep(EJ0, EJ1, EJ2, psi, B)
```

```

                  psi_sum = psi+h*k1/2.0_RK
                  k2 = schrodStep(EJ0, EJ1, EJ2, psi_sum, B_halfStep)

                  psi_sum = psi+h*k2/2.0_RK
                  k3 = schrodStep(EJ0, EJ1, EJ2, psi_sum, B_halfStep)

                  psi_sum = psi+h*k3
                  k4 = schrodStep(EJ0, EJ1, EJ2, psi_sum, B_step)

                  k = (k1 + 2.0_RK*k2 + 2.0_RK*k3 + k4)/6.0_RK

                  psi_new = psi + h*k
                  t = t_step

                                       !Only one thread can access "critical" part at a time:
                  !$OMP CRITICAL
! INQUIRE(UNIT=11, OPENED=isOpen)
                  if ((j_phis.EQ.nPhis).AND.(i_freq.EQ.saveFreqInd).AND.(mod(t,saveStep).LT.h)) then
                     tInd = NINT(t/saveStep)! + 1 !Arrays start at 1, mod(0,x) = 0 BUT subtract 1 because time already stepped
                                             !Save decimated amplitude/phase profiles
                     trace(tInd,1) = t
                     trace(tInd,2) = amp
                     trace(tInd,3) = phis(2)

                                             !Write populations over time to variable to save for debugging/illustration
                     pops(tInd,1) = t
                     pops(tInd,2) = sum(abs(psi_new(1:nPhis_overall,1))**2)/nPhis_overall_float
                     pops(tInd,3) = sum(abs(psi_new(1:nPhis_overall,2))**2)/nPhis_overall_float
                     pops(tInd,4) = sum(abs(psi_new(1:nPhis_overall,3))**2)/nPhis_overall_float
                     pops(tInd,5) = sum(abs(psi_new(1:nPhis_overall,4))**2)/nPhis_overall_float
```

```fortran
                     end if
                     !$OMP END CRITICAL

                  end do !Runge-Kutta time loop
                                    !Only let one thread write to files at a time
                  !$OMP CRITICAL
                  if((j_phis.EQ.nPhis).AND.(i_freq.EQ.saveFreqInd)) then
                     write(11) trace
                     write(12) pops
                     close(11)
                     close(12)
                  end if
                  pops_out(i_freq,1) = freqRF
                  pops_out(i_freq,1+j_phis) = sum(abs(psi_new(1:nPhis_overall,1))**2)/nPhis_overall_float
                  write(*,printFmtStr) parLoopInd, '/', SIZE(loopArr), ' '//expType//' ', j_phis, '/', nPhis, ' ', nFreqsDone, (freqRF-freq01)*1.0E3_RK, ' ', 100*(ampScale*2)**2/powerLvl
                  !$OMP END CRITICAL
                  nFreqsDone = nFreqsDone + 1
               end do !Freqs loop
               !$OMP END DO
               !$OMP END PARALLEL
            end do !Phis pulse loop
            write(20) pops_out !Write populations in each state at end of experiment period. The important output
            close(20)
! deallocate(pops_out)
         end do !A/B exp type loop
      end do !Whole run loop for changing parameters
! write(*,*) pops_out
   end do !j_switchPhis loop

contains
   SUBROUTINE getAmpPhi(t, ampScale, amp, phis, chirpStretch, chirpScales, amp_coupling, phi_coupling)
      REAL(RK), INTENT(IN) :: t, ampScale, chirpStretch
      REAL(RK), DIMENSION(:), INTENT(IN) :: chirpScales
      REAL(RK), INTENT(OUT) :: amp
```

```
      REAL(RK), DIMENSION(2), INTENT(OUT) :: amp_coupling, phi_coupling
      REAL(RK) :: phi, phi_chirp
      REAL(RK), DIMENSION(nPhis_overall), INTENT(OUT) :: phis

      !Uncomment for rectangular pulses
      if(expType .EQ. 'A') then
         if (t .LT. t0) then
            amp = 0.0_RK
            amp_coupling = k_amp !*0
            phi_coupling = switchPhis_deg(j_switchPhis)*pi/180.0_RK
         else if (t .LT. t0+tD) then
            amp = SQRT(PImbal)*1.0_RK
            amp_coupling(1) = k_amp
            amp_coupling(2) = 0.0_RK +k_amp
            phi_coupling(1) = switchPhis_deg(j_switchPhis)*pi/180.0_RK
            phi_coupling(2) = 0.0_RK
         else if (t .LT. t0+tT) then
            amp = 0.0_RK
            amp_coupling = k_amp !*0
            phi_coupling = switchPhis_deg(j_switchPhis)*pi/180.0_RK
         else if (t .LT. t0+tT+tD) then
            amp = 1.0_RK
            amp_coupling(1) = 0.0_RK +k_amp
            amp_coupling(2) = k_amp
            phi_coupling(1) = 0.0_RK
            phi_coupling(2) = switchPhis_deg(j_switchPhis)*pi/180.0_RK
         else
            amp = 0.0_RK
            amp_coupling = k_amp !*0
            phi_coupling = switchPhis_deg(j_switchPhis)*pi/180.0_RK
         end if
      else
         if (t .LT. t0) then
            amp = 0.0_RK
            amp_coupling = k_amp !*0
            phi_coupling = switchPhis_deg(j_switchPhis)*pi/180.0_RK
         else if (t .LT. t0+tD) then
            amp = 1.0_RK
            amp_coupling(1) = 0.0_RK +k_amp
```

```
            amp_coupling(2) = k_amp
            phi_coupling(1) = 0.0_RK
            phi_coupling(2) = switchPhis_deg(j_switchPhis)*pi/180.0_RK
         else if (t .LT. t0+tT) then
            amp = 0.0_RK
            amp_coupling = k_amp !*0
            phi_coupling = switchPhis_deg(j_switchPhis)*pi/180.0_RK
         else if (t .LT. t0+tT+tD) then
            amp = SQRT(PImbal)*1.0_RK
            amp_coupling(1) = k_amp
            amp_coupling(2) = 0.0_RK +k_amp
            phi_coupling(1) = switchPhis_deg(j_switchPhis)*pi/180.0_RK
            phi_coupling(2) = 0.0_RK
         else
            amp = 0.0_RK
            amp_coupling = k_amp !*0
            phi_coupling = switchPhis_deg(j_switchPhis)*pi/180.0_RK
         end if
      end if

! amp_coupling = k_amp !Uncomment to have both couplings on always

! Uncomment for pulses with turn-on time
! if (expType .EQ. 'A') then
! amp = (SQRT(PImbal)*(TANH(t-t0)-TANH(t-tD-t0)) + (TANH(t-tT-t0)-TANH(t-tT-tD-t0)))/2.0_RK
! else if (expType .EQ. 'B') then
! amp = ((TANH(t-t0)-TANH(t-tD-t0)) + SQRT(PImbal)*(TANH(t-tT-t0)-TANH(t-tT-tD-t0)))/2.0_RK
! end if
!
      amp = amp*ampScale


      !Exptype A: FOSOF phase difference is in 2nd pulse
      if (t.LT.centreT) then
         if (expType .EQ. 'A') then
            phi = 0.0_RK
         else
```

```
            phi = phis_loop(j_phis)
         end if
      else if (t .GT. centreT) then
         if (expType .EQ. 'A') then
            phi = phis_loop(j_phis)
         else
            phi = 0.0_RK
         end if

      end if

      !Exptype A: FOSOF phase difference is in 2nd pulse, coupling is from 2nd pulse. switchPhi due to diff path in switch for isolated arm, assumed symmetric
      if (expType .EQ. 'A') then
! phis_coupling = phis_overall + phis_loop(j_phis) - switchPhis_deg(j_switchPhis)*pi/180.0_RK
         phi_chirp = pi/2*(chirpScales(1)*((0.5+0.5*TANH((t-t0+1)/chirpStretch)) - (0.5+0.5*TANH((t-t0-1)/chirpStretch))) + &
                chirpScales(2)*((0.5+0.5*TANH((t-(tD+t0-1))/chirpStretch)) - (0.5+0.5*TANH((t-(tD+t0+1))/chirpStretch))) + &
                chirpScales(3)*((0.5+0.5*TANH((t-(tT+t0-1))/chirpStretch)) - (0.5+0.5*TANH((t-(tT+t0+1))/chirpStretch))) + &
                chirpScales(4)*((0.5+0.5*TANH((t-(tT+tD+t0-1))/chirpStretch)) - (0.5+0.5*TANH((t-(tT+tD+t0+1))/chirpStretch))))
      else
! phis_coupling = phis_overall - switchPhis_deg(j_switchPhis)*pi/180.0_RK
         phi_chirp = pi/2*(chirpScales(3)*((0.5+0.5*TANH((t-t0+1)/chirpStretch)) - (0.5+0.5*TANH((t-t0-1)/chirpStretch))) + &
                chirpScales(4)*((0.5+0.5*TANH((t-(tD+t0-1))/chirpStretch)) - (0.5+0.5*TANH((t-(tD+t0+1))/chirpStretch))) + &
                chirpScales(1)*((0.5+0.5*TANH((t-(tT+t0-1))/chirpStretch)) - (0.5+0.5*TANH((t-(tT+t0+1))/chirpStretch))) + &
                chirpScales(2)*((0.5+0.5*TANH((t-(tT+tD+t0-1))/chirpStretch)) - (0.5+0.5*TANH((t-(tT+tD+t0+1))/chirpStretch))))
      end if

      phis = phi + phis_overall + phi_chirp
   END SUBROUTINE

```

```
   function schrodStep(EJ0, EJ1, EJ2, psi, B)
   !Calculate the 9-level Schrodinger eqn from the matrix elements
      real(RK), intent(in) :: EJ0, EJ1, EJ2
      real(RK), dimension(nPhis_overall, 3), intent(in) :: B
            real(RK), dimension(nPhis_overall) :: Bx, By, Bz
      complex(RK), dimension(nPhis_overall, nStates), intent(in) :: psi
      complex(RK), dimension(nPhis_overall, nStates) :: schrodStep
      complex(RK), dimension(nPhis_overall) :: psiJ0m0, psiJ1mn1, psiJ1m0, psiJ1m1, psiJ2mn2, psiJ2mn1, psiJ2m0, psiJ2m1, psiJ2m2

            !Rename components of input variables for convenience:
            Bx = B(1:nPhis_overall, 1)
            By = B(1:nPhis_overall, 2)
            Bz = B(1:nPhis_overall, 3)

            psiJ0m0 = psi(1:nPhis_overall, 1)
            psiJ1mn1 = psi(1:nPhis_overall, 2)
            psiJ1m0 = psi(1:nPhis_overall, 3)
            psiJ1m1 = psi(1:nPhis_overall, 4)
            psiJ2mn2 = psi(1:nPhis_overall, 5)
            psiJ2mn1 = psi(1:nPhis_overall, 6)
            psiJ2m0 = psi(1:nPhis_overall, 7)
            psiJ2m1 = psi(1:nPhis_overall, 8)
            psiJ2m2 = psi(1:nPhis_overall, 9)

            !Calculate the time evolution of each substate:

      schrodStep(1:nPhis_overall, 1) = (xi*psiJ1mn1*(Bx-ci*By)/SQRT(3.0_RK) - xi*psiJ1m1*(Bx+ci*By)/SQRT(3.0_RK) &
      + SQRT(2.0_RK/3.0_RK)*xi*psiJ1m0*Bz + psiJ0m0*EJ0)*-ci/hbar

      schrodStep(1:nPhis_overall, 2) = (0.5_RK*xi*psiJ2mn2*(Bx-ci*By) + xi*psiJ0m0*(Bx+ci*By)/SQRT(3.0_RK) &
      + chi*psiJ1m0*(Bx+ci*By)/SQRT(8.0_RK) - xi*psiJ2m0*(Bx+ci*By)/SQRT(24.0_RK) + 0.5_RK*xi*psiJ2mn1*Bz &
      + psiJ1mn1*(EJ1-chi*Bz/2.0_RK))*-ci/hbar

            schrodStep(1:nPhis_overall, 3) = (chi*psiJ1mn1*(Bx-ci*By)/SQRT(8.0_RK) + xi*psiJ2mn1*(Bx-ci*By)/SQRT(8.0_RK) &
```

```
            + chi*psiJ1m1*(Bx+ci*By)/SQRT(8.0_RK) - xi*psiJ2m1*(Bx+ci*By)/SQRT(8.0_RK) +
                SQRT(2.0_RK/3.0_RK)*xi*psiJ0m0*Bz &
            + xi*psiJ2m0*Bz/SQRT(3.0_RK) + psiJ1m0*EJ1)*-ci/hbar

            schrodStep(1:nPhis_overall, 4) = (-xi*psiJ0m0*(Bx-ci*By)/SQRT(3.0_RK) + chi*
                psiJ1m0*(Bx-ci*By)/SQRT(8.0_RK) &
            + xi*psiJ2m0*(Bx-ci*By)/SQRT(24.0_RK) - 0.5_RK*xi*psiJ2m2*(Bx+ci*By) + 0.5_RK*
                xi*psiJ2m1*Bz &
            + psiJ1m1*(EJ1+chi*Bz/2.0_RK))*-ci/hbar

            schrodStep(1:nPhis_overall, 5) = (0.5_RK*xi*psiJ1mn1*(Bx+ci*By) + 0.5_RK*chi*
                psiJ2mn1*(Bx+ci*By) &
            + psiJ2mn2*(EJ2-chi*Bz))*-ci/hbar

            schrodStep(1:nPhis_overall, 6) = (0.5_RK*chi*psiJ2mn2*(Bx-ci*By) + xi*psiJ1m0
                *(Bx+ci*By)/SQRT(8.0_RK) &
            + SQRT(3.0_RK/8.0_RK)*chi*psiJ2m0*(Bx+ci*By) + 0.5*xi*psiJ1mn1*Bz + psiJ2mn1*(
                EJ2-chi*Bz/2.0_RK))*-ci/hbar

            schrodStep(1:nPhis_overall, 7) = (-xi*psiJ1mn1*(Bx-ci*By)/SQRT(24.0_RK) &
            + SQRT(3.0_RK/8.0_RK)*chi*psiJ2mn1*(Bx-ci*By) + xi*psiJ1m1*(Bx+ci*By)/SQRT
                (24.0_RK) &
            + SQRT(3.0_RK/8.0_RK)*chi*psiJ2m1*(Bx+ci*By) + xi*psiJ1m0*Bz/SQRT(3.0_RK) +
                psiJ2m0*EJ2)*-ci/hbar

            schrodStep(1:nPhis_overall, 8) = (-xi*psiJ1m0*(Bx-ci*By)/SQRT(8.0_RK) + SQRT
                (3.0_RK/8.0_RK)*chi*psiJ2m0*(Bx-ci*By) &
            + 0.5_RK*chi*psiJ2m2*(Bx+ci*By) + 0.5_RK*xi*psiJ1m1*Bz + psiJ2m1*(EJ2 + chi*Bz
                /2.0_RK))*-ci/hbar

            schrodStep(1:nPhis_overall, 9) = (-0.5_RK*xi*psiJ1m1*(Bx-ci*By) + 0.5_RK*chi*
                psiJ2m1*(Bx-ci*By) &
      + psiJ2m2*(EJ2 + chi*Bz))*-ci/hbar

   end function

end program
```

Bibliography

1. Kragh, H. Magic Number: A Partial History of the Fine-Structure Constant. *Archive for History of Exact Sciences* **57,** 395–431. ISSN: 00039519, 14320657. `http://www.jstor.org/stable/41134170` (2003).
2. Tiesinga, E., Mohr, P. J., Newell, D. B. & Taylor, B. N. *The 2018 CODATA Recommended Values of the Fundamental Physical Constants* National Institute of Standards and Technology, Gaithersburg, MD 20899. `http://physics.nist.gov/constants`.
3. BIPM. *Le Système international d'unités / The International System of Units ('The SI Brochure')* Ninth. ISBN: 978-92-822-2272-0. `http://www.bipm.org/en/si/si_brochure/` (Bureau international des poids et mesures, 2019).
4. Morel, L., Yao, Z., Cladé, P. & Guellati-Khélifa, S. Determination of the fine-structure constant with an accuracy of 81 parts per trillion. *Nature* **588,** 61–65 (Dec. 2020).
5. Parker, R. H., Yu, C., Zhong, W., Estey, B. & Müller, H. Measurement of the fine-structure constant as a test of the Standard Model. *Science* **360,** 191–195. ISSN: 0036-8075. eprint: `https://science.sciencemag.org/content/360/6385/191.full.pdf`. `https://science.sciencemag.org/content/360/6385/191` (2018).

6. Fan, X., Myers, T. G., Sukra, B. A. D. & Gabrielse, G. Measurement of the Electron Magnetic Moment. *Phys. Rev. Lett.* **130,** 071801. `https://link.aps.org/doi/10.1103/PhysRevLett.130.071801` (7 Feb. 2023).
7. Aoyama, T., Kinoshita, T. & Nio, M. Theory of the Anomalous Magnetic Moment of the Electron. *Atoms* **7.** ISSN: 2218-2004. `https://www.mdpi.com/2218-2004/7/1/28` (2019).
8. Jeffery, A. *et al.* Determination of the von Klitzing constant and the fine-structure constant through a comparison of the quantized Hall resistance and the ohm derived from the NIST calculable capacitor. *Metrologia* **35,** 83–96. `https://doi.org/10.1088%2F0026-1394%2F35%2F2%2F3` (Apr. 1998).
9. Smiciklas, M. & Shiner, D. Determination of the Fine Structure Constant Using Helium Fine Structure. *Phys. Rev. Lett.* **105,** 123001. `https://link.aps.org/doi/10.1103/PhysRevLett.105.123001` (12 Sept. 2010).
10. Pachucki, K. & Yerokhin, V. A. Fine Structure of Heliumlike Ions and Determination of the Fine Structure Constant. *Phys. Rev. Lett.* **104,** 070403. `https://link.aps.org/doi/10.1103/PhysRevLett.104.070403` (7 Feb. 2010).
11. George, M. C., Lombardi, L. D. & Hessels, E. A. Precision Microwave Measurement of the $2^3P_1 - 2^3P_0$ Interval in Atomic Helium: A Determination of the Fine-Structure Constant. *Phys. Rev. Lett.* **87,** 173002. `https://link.aps.org/doi/10.1103/PhysRevLett.87.173002` (17 Oct. 2001).
12. Giusfredi, G. *et al.* Present status of the fine-structure frequencies of the 2^3P helium level. *Canadian Journal of Physics* **83,** 301–310. eprint: `https://doi.org/10.1139/p04-075`. `https://doi.org/10.1139/p04-075` (2005).

13. Zelevinsky, T., Farkas, D. & Gabrielse, G. Precision Measurement of the Three 2^3P_J Helium Fine Structure Intervals. *Phys. Rev. Lett.* **95,** 203001. `https://link.aps.org/doi/10.1103/PhysRevLett.95.203001` (20 Nov. 2005).

14. Zheng, X. *et al.* Laser Spectroscopy of the Fine-Structure Splitting in the 2^3P_J Levels of ^{4}He. *Phys. Rev. Lett.* **118,** 063001. `https://link.aps.org/doi/10.1103/PhysRevLett.118.063001` (6 Feb. 2017).

15. Marsman, A., Horbatsch, M. & Hessels, E. A. The Effect of Quantum-Mechanical Interference on Precise Measurements of the n = 2 Triplet P Fine Structure of Helium. *Journal of Physical and Chemical Reference Data* **44,** 031207. eprint: `https://doi.org/10.1063/1.4922796`. `https://doi.org/10.1063/1.4922796` (2015).

16. Schwartz, C. Fine Structure of Helium. *Phys. Rev.* **134,** A1181–A1187. `https://link.aps.org/doi/10.1103/PhysRev.134.A1181` (5A June 1964).

17. Kponou, A., Hughes, V. W., Johnson, C. E., Lewis, S. A. & Pichanick, F. M. J. Precise Measurement of the $2^3P_0 - 2^3P_1$ Fine-Structure Interval of Helium. *Phys. Rev. Lett.* **26,** 1613–1616. `https://link.aps.org/doi/10.1103/PhysRevLett.26.1613` (26 June 1971).

18. Ficek, F. *et al.* Constraints on exotic spin-dependent interactions between electrons from helium fine-structure spectroscopy. *Phys. Rev. A* **95,** 032505. `https://link.aps.org/doi/10.1103/PhysRevA.95.032505` (3 Mar. 2017).

19. Ringwald, A. *Alternative dark matter candidates: Axions* in *Neutrino Oscillation Workshop* **283** (2017), 081.

20. Kato, K., Skinner, T. D. G. & Hessels, E. A. Ultrahigh-Precision Measurement of the $n = 2$ Triplet P Fine Structure of Atomic Helium Using Frequency-Offset Separated Oscillatory Fields. *Phys. Rev. Lett.* **121,** 143002. `https://link.aps.org/doi/10.1103/PhysRevLett.121.143002` (14 Oct. 2018).

21. Vutha, A. C. & Hessels, E. A. Frequency-offset separated oscillatory fields. *Phys. Rev. A* **92,** 052504. `https://link.aps.org/doi/10.1103/PhysRevA.92.052504` (5 Nov. 2015).

22. Ramsey, N. F. A New Molecular Beam Resonance Method. *Phys. Rev.* **76,** 996–996. `https://link.aps.org/doi/10.1103/PhysRev.76.996` (7 Oct. 1949).

23. Kato, K. *Precision Microwave Frequency-offset Separated-oscillatory-fields Measurement of the* 2^3P_1*-to-*2^3P_2 *Fine-structure Interval in Atomic Helium* PhD thesis (York University, 2019).

24. Griffiths, D. J. *Introduction to Quantum Mechanics (2nd Ed.)* 2nd ed. (Pearson Prentice Hall, 2005).

25. Lombardi, M. A. The Use of GPS Disciplined Oscillators as Primary Frequency Standards for Calibration and Metrology Laboratories. *NCSLI Measure* **3,** 56–65. eprint: `https://doi.org/10.1080/19315775.2008.11721437`. `https://doi.org/10.1080/19315775.2008.11721437` (2008).

26. Beica, H. *Improved Laser Locking Techniques for Realizing an Enhanced Measurement of the Helium 2 Triplet P Fine Structure* MA thesis (York University, 2013).

27. Harris, M. L., Cornish, S. L., Tripathi, A. & Hughes, I. G. Optimization of sub-Doppler DAVLL on the rubidium D2 line. *Journal of Physics B: Atomic, Molecular and Optical Physics* **41,** 085401. `https://dx.doi.org/10.1088/0953-4075/41/8/085401` (Apr. 2008).

28. Choi, G.-W. & Noh, H.-R. Sub-Doppler DAVLL spectra of the D1 line of rubidium: a theoretical and experimental study. *Journal of Physics B: Atomic, Molecular and Optical Physics* **48,** 115008. `https://dx.doi.org/10.1088/0953-4075/48/11/115008` (May 2015).

29. George, M. C. *Precision Measurements of the* $n = 2^3P$ *Intervals of Atomic Helium: A Determination of the Fine-Structure Constant* PhD thesis (York University, 2003).

30. Yan, Z.-C. & Drake, G. W. F. Eigenvalues and expectation values for the $1s^22s^2S$, $1s^22p^2P$, and $1s^23d^2D$ states of lithium. *Phys. Rev. A* **52,** 3711–3717. `https://link.aps.org/doi/10.1103/PhysRevA.52.3711` (5 Nov. 1995).

31. Wardinski, I. & Holme, R. A time-dependent model of the Earth's magnetic field and its secular variation for the period 1980–2000. *Journal of Geophysical Research: Solid Earth* **111.** `https://agupubs.onlinelibrary.wiley.com/doi/abs/10.1029/2006JB004401` (2006).

32. Pozar, D. M. *Microwave Engineering (4th Ed.)* ISBN: 978-0-470-63155-3 (2012).

33. Borbely, J. *Seperated Oscillatory Field Microwave Measurement of the* $n = 2^3P_1$*-to-*$n = 2^3P_2$ *Fine-Structure Interval of Helium* PhD thesis (York University, 2009).

34. Heydarizadmotlagh, F., Skinner, T. D. G., Kato, K., George, M. C. & Hessels, E. A. Precision measurement of the n=2 triplet P J=1-to-J=0 fine structure of atomic helium using frequency-offset separated oscillatory fields. arXiv: `2310.17040 [physics.atom-ph]` (2023).